



TECHNISCHE
UNIVERSITÄT
WIEN
Vienna University of Technology

DISSERTATION

DEVELOPMENT OF A MULTI-SENSOR INTEGRATED ORGAN-ON-A-CHIP PLATFORM FOR STUDYING PARKINSON'S DISEASE

carried out for the purpose of obtaining the degree of Doctor technicae (Dr. techn.),
submitted at TU Wien, Faculty of Technical Chemistry,

by

Dipl.-Ing. Sarah Spitz

Mat.Nr.: 01140105

under the supervision of

Univ. Prof. Dipl.-Ing. Dr. Peter Ertl


Institute of Applied Synthetic Chemistry and Institute of Chemical Technologies and
Analytics

Vienna, August 2022

Affidavit

I declare in lieu of oath, that I wrote this thesis and performed the associated research myself, using only literature cited in this volume. If text passages from sources are used literally, they are marked as such. I confirm that this work is original and has not been submitted elsewhere for any examination, nor is it currently under consideration for a thesis elsewhere.

Vienna, August 2022



Signature

ACKNOWLEDGMENTS

First and foremost, I would like to express my sincerest gratitude to all former and existing members of the CellChipGroup for their friendship and tremendous support during the past five years. I want to specifically thank my supervisor, Prof. Peter Ertl, for taking me on as his Ph.D. student and introducing me to the world of organ-on-a-chip technology. Thank you for your guidance and continuous support throughout my last five years at the CellChipGroup! In addition, I would like to thank Prof. Jens Schwamborn and Dr. Silvia Bolognin, without whose continued support, my Ph.D. project would not have been possible.

I want to thank Dr. Barbara Bachmann, Dr. Christoph Eilenberger, and Dr. Helene Zirath for introducing me to the CellChipGroup (herein specific thanks go to Barbara Bachmann for her outstanding persuasiveness at the BOKU Sommerfest) and all the fun days that ensued, including the time we nearly got lost in Amsterdam. Furthermore, I would like to thank Dipl. Ing. Selina Schweinberger, Dipl. Ing. Silvia Schobesberger, Dipl. Ing. Florian Selinger and Dipl. Ing. Konstanze Brandauer for their support and ensuring I was always stocked up on savory snacks. Dear Chippos and Chipporellas, thank you for the fun times we had both inside and outside the shielded laboratory spaces in the BZ EG. Many thanks also go to the Austrian Marshall Plan Foundation, the OeAD-GmbH, the Austrian Federal Ministry of Education, Science and Research (BMBWF), and the Vienna University of Technology, who enabled me to spend the last part of my Ph.D. at the Massachusetts Institute of Technology. In this context, I would also like to express my sincere gratitude to Prof. Roger Kamm and all Kammsters for welcoming me to the laboratories at MIT BE. Lastly, I would like to thank my family (including my extended Austrian family) and friends for their continuous and loving support over my entire academic education. Thank you very much!

*“When you have eliminated the impossible, whatever remains,
however improbable, must be the truth.”*

Sherlock Holmes

ABSTRACT

Organoid technology describes a scientific field that concentrates on the *in vitro* generation of miniaturized tissue analogs capable of emulating intricate organotypic characteristics on both a structural and functional level. As such, it has become an indispensable tool in many scientific disciplines, from biological engineering to pharmaceutical development. One specific example constitutes the field of Parkinson's disease, a neurodegenerative disorder that, to this date, remains restricted to symptomatic control due to a persistent lack of neuroprotective and disease-modifying treatment strategies. Despite the recent progress that has been accomplished by modeling Parkinson's disease employing midbrain organoids, three key limitations hinder the technology from reaching its full potential. These drawbacks include (i) the omission of critical biophysical cues such as interstitial fluid flow, (ii) nutrient-deficiency-based growth restrictions resulting from the organoids' intrinsic structure, and the concomitant lack of vasculature, as well as (iii) low analytical accessibility impeding time-resolved monitoring. In this doctoral study, a multi-sensor integrated organ-on-a-chip platform for the long-term cultivation and non-invasive monitoring of human midbrain organoids was developed. While the development, characterization, and subsequent integration of optical, electrical, and electrochemical sensors enabled the non-invasive monitoring of vital physiological aspects *in vitro*, including oxygen demand, electrophysiological activity, and dopamine release, the dynamic cultivation milieu, could markedly enhance organoid viability and differentiation. Key pathological phenotypes encompassing impaired mitochondrial activity, reduced numbers of dopaminergic neurons, and aggregated α -synuclein were emulated when cultivating organoids derived from a Parkinson's patient. Upon exposing the midbrain organoids to the repurposed excipient 2-hydroxypropyl- β -cyclodextrin, marked rescue effects were observed, highlighting the platform's applicability for drug screening purposes.

KURZFASSUNG

Organoid-Technologie beschreibt ein wissenschaftliches Feld, das sich auf die Erzeugung miniaturisierter Gewebeanaloga konzentriert, die in der Lage sind, komplizierte organotypische Eigenschaften sowohl auf struktureller als auch auf funktioneller Ebene *in vitro* zu emulieren. Als solches ist es zu einem unverzichtbaren Werkzeug in einer Vielzahl von wissenschaftlichen Disziplinen geworden, die von der Biotechnik bis zur pharmazeutischen Entwicklung reichen. Ein konkretes Beispiel stellt das wissenschaftliche Feld um Parkinson dar, eine neurodegenerative Erkrankung, die aufgrund des anhaltenden Mangels an neuroprotektiven und krankheitsmodifizierenden Behandlungsstrategien bis heute auf eine symptomatische Behandlung beschränkt ist. Trotz erheblicher Fortschritte im Modellieren von Parkinson mittels sogenannter Mittelhirn-Organoiden hindern drei wesentliche Faktoren die Technologie daran, ihr volles Potenzial auszuschöpfen. Zu diesen Nachteilen gehören (i) die Vernachlässigung biophysikalischer Stimuli wie dem interstitiellen Flüssigkeitsfluss, ein wesentlicher Akteur bei der Gewebemöostase (ii) Wachstumsbeschränkungen aufgrund von Nährstoffmangel, die sich aus der intrinsischen Struktur der Organoiden und einem damit einhergehenden Mangel an Gefäßen ergeben sowie (iii) geringe analytische Zugänglichkeit, die eine zeitaufgelöste Überwachung erschwert. Im Zuge dieser Doktorarbeit wurde eine Multisensor-integrierte Organ-on-a-Chip-Plattform für die langfristige Kultivierung und nicht-invasive Überwachung von Organoiden des menschlichen Mittelhirns entwickelt. Die Entwicklung, Charakterisierung und anschließende Integration optischer, elektrischer und elektrochemischer Sensoren ermöglichte die nicht-invasive Messung kritischer physiologischer Aspekte wie dem Sauerstoffbedarf, der elektrophysiologischen Aktivität sowie der Ausschüttung von Dopamin *in vitro*. Zudem begünstigte ein dynamisches Kultivierungsmilieu die Differenzierung und Viabilität humaner Mittelhirn Organoiden. Charakteristische pathologische Phänotypen, darunter eine beeinträchtigte mitochondriale

Aktivität, eine verringerte Anzahl dopaminerger Neuronen und aggregiertes α -Synuclein wurden bei der Kultivierung von Patienten-spezifischen Organoiden emuliert. Zudem konnten nach Behandlung der Mikrogewebe mit dem umfunktionierten Zuckermolekül 2-Hydroxypropyl- β -Cyclodextrin phänotypische Rettungseffekte beobachtet werden, die die Anwendbarkeit der Plattform für Wirkstoff-Screening-Zwecke unterstreicht.

TABLE OF CONTENTS

ABSTRACT	5
KURZFASSUNG	6
TABLE OF CONTENTS	8
LIST OF FIGURES	10
LIST OF TABLES	10
LIST OF ABBREVIATIONS	11
1. PROBLEM AND MOTIVATION	14
1.1 PARKINSON’S DISEASE.....	14
1.1.1 <i>Parkinson’s Disease: Its Pathological Hallmarks, Symptoms, and Etiology</i>	14
1.1.2 <i>Experimental Models of PD and the Unmet Need for Neuroprotective and Disease-Modifying Strategies</i>	20
1.2 A PERSONALIZED APPROACH TO PARKINSON’S DISEASE – HUMAN MIDBRAIN ORGANOID	
ORGANOIDS.....	24
1.3 FROM MICROFLUIDICS TO BRAIN-ON-A-CHIP TECHNOLOGY	29
1.4 TACKLING THE ISSUE OF LOW ANALYTICAL ACCESSIBILITY – SENSING STRATEGIES IN ORGAN-ON-A-CHIP TECHNOLOGY	37
1.4.1 <i>Electrical Sensors</i>	38
1.4.2 <i>Electrochemical Sensors</i>	40
1.4.3 <i>Optical Sensors</i>	41
1.4.4 <i>Multiple-Sensor Integrated OoC Platforms</i>	44
2. AIMS, RESULTS, AND CONCLUSION	52
2.1 AIMS OF THE THESIS	52
2.2 OVERVIEW OF RESEARCH ARTICLES	53
2.2.1 <i>MANUSCRIPT #1</i>	53
2.2.2 <i>MANUSCRIPT #2</i>	54
2.2.3 <i>MANUSCRIPT #3</i>	55

2.2.4 MANUSCRIPT #4.....	57
2.3 SCIENTIFIC CONTRIBUTION OF THE DISSERTATION, CONCLUSION, AND OUTLOOK.....	59
3. ORIGINAL RESEARCH ARTICLES.....	64
3.1 MANUSCRIPT #1 – ARTICLE	64
3.2 MANUSCRIPT #1 – SUPPLEMENTARY INFORMATION	76
3.1 MANUSCRIPT #2 - ARTICLE.....	80
3.4 MANUSCRIPT #2 – SUPPLEMENTARY INFORMATION	93
3.5 MANUSCRIPT #3 - ARTICLE.....	99
3.5 MANUSCRIPT #3 – SUPPLEMENTARY INFORMATION	110
3.6 MANUSCRIPT #4 - ARTICLE.....	121
3.7 MANUSCRIPT #4 – SUPPLEMENTARY INFORMATION	123
BIBLIOGRAPHY	153

LIST OF FIGURES

<i>FIGURE 1: GRAPHICAL SUMMARY OF PD-ASSOCIATED MOTOR- AND NON-MOTOR MANIFESTATIONS.</i> ^{5,6}	15
<i>FIGURE 2: GRAPHICAL REPRESENTATION OF THE TWO MAJOR HALLMARKS ASSOCIATED WITH PD.</i>	16
<i>FIGURE 3: GRAPHICAL REPRESENTATION OF THE KEY ENVIRONMENTAL AND GENETIC RISK FACTORS LINKED TO PD.</i> ..	18
<i>FIGURE 4: GRAPHICAL ILLUSTRATION DEMONSTRATING THE GROWTH OF THE FIELD OF ORGANOID AND BRAIN ORGANOID TECHNOLOGY BETWEEN 2011 AND 2021.</i>	24
<i>FIGURE 5: GRAPHICAL ILLUSTRATIONS ON OOC TECHNOLOGY</i>	30
<i>FIGURE 6: REPRESENTATIVE OVERVIEW OF TISSUE-SPECIFIC OOC PLATFORMS.</i>	33
<i>FIGURE 7: REPRESENTATION OF BRAIN ORGANOID-ON-A-CHIP PLATFORMS.</i>	36
<i>FIGURE 8: SCHEMATIC OVERVIEW OF THE THREE DIFFERENT SENSING PRINCIPLES FOUND IN OOC PLATFORMS.</i>	37
<i>FIGURE 9: REPRESENTATIVE EXAMPLES OF SENSOR INTEGRATED OOC PLATFORMS.</i>	42

LIST OF TABLES

<i>TABLE 1: ADVANTAGES AND DISADVANTAGES OF CURRENT PD IN VIVO MODELS.</i>	21
<i>TABLE 2: COMPREHENSIVE OVERVIEW OF STUDIES ON HMO-BASED IN VITRO MODELS.</i>	27
<i>TABLE 3: COMPREHENSIVE OVERVIEW OF SENSOR INTEGRATED OOC PLATFORMS.</i>	46

LIST OF ABBREVIATIONS

2D	Two-dimensional
3D	Three-dimensional
3xSNCA	Triplication mutation of the alpha-synuclein gene
6-OHDA	6-hydroxy-dopamine
ALS	Amyotrophy lateral sclerosis
BBB	Blood-brain-barrier
CFD	Computational fluid dynamics
CHCHD2	Coiled-coil-helix-coiled-coil-helix domain-containing protein 2
CK-MB	Creatine kinase-MB
CNC	Computer numerical control
COC	Cyclic olefin copolymer
DA	Dopamine
DO	Dissolved oxygen
DJ-1	Parkinson disease protein 7
ECM	Extracellular matrix
EIS	Electrochemical impedance spectroscopy
FACS	Fluorescence-activated single cell sorting
FOXA2	Forkhead Box A2
GBA	Glucosylceramidase beta
GST- α	Glutathione transferase alpha
GWAS	Genome wide association studies
hMO	Human midbrain organoid
HP- β -CD	2-Hydroxypropyl-beta-cyclodextrin
HPLC	High performance liquid chromatography
HTS	High throughput screening

Ion-sensitive field-effect transistors	ISFET
iPSC	Induced pluripotent stem cell
L-Dopa	Levodopa
LIS1	Lissencephaly-1
LRRK2	Leucin-rich-repeat kinase 2
MAPT	Microtubule associated protein tau
MEA	Multi electrode array
Mox	Metal oxide
MPP+	1-methyl-4-phenylpyridinium
MPTP	1-methyl-4-phenyl-1,2,3,6-tetrahydropyridine
MRM-MS	Multiple reaction monitoring-mass spectrometry
NO	Nitric oxide
OoC	Organ-on-a-chip
PD	Parkinson's disease
PDMS	Poly(dimethylsiloxane)
PINK1	PTEN induced kinase 1
PLA2G6	Phospholipase A2 Group 6
PMMA	Polymethyl methacrylate
PRKN	Parkin
Ref.	Reference
REM	Rapid eye movement
ROS	Reactive oxygen species
TEER	Transepithelial electrical resistance
TXNIP	Thioredoxin interacting protein
VSP13C	Vacuolar protein sorting 13 homolog C
WNT	Wingless-related integration site

1. PROBLEM AND MOTIVATION

1.1 PARKINSON'S DISEASE

1.1.1 Parkinson's Disease: Its Pathological Hallmarks, Symptoms, and Etiology

First described in 1817 by the general medical practitioner James Parkinson in a monograph titled “*An Essay on the Shaking Palsy*,” Parkinson’s disease (PD) today constitutes the fastest-growing neurodegenerative disease worldwide.^{1,2} According to a Global Burden of Disease study, at present, 9.4 million patients live with PD, a number which is expected to double by the year 2040.^{3,4} While PD can occur as early as in the third decade of life, the average age of onset is 60 years or older, rendering age one of the biggest risk factors linked to the disease.⁵ PD is a multifactorial disorder that has been associated with a variety of highly debilitating motor and non-motor symptoms (see Figure 1). Among others, motor symptoms include bradykinesia, rigidity, and resting tremors that, to this date, both individually and collectively provide the only indication for clinical diagnosis. Motor manifestations, however, often are preceded by non-motor symptoms such as depression, anxiety, constipation, olfactory dysfunction, and rapid eye movement (REM) behavior disorder, which can occur even decades before the actual diagnosis of the disease.^{6,7} Unfortunately, these non-motor symptoms often remain overlooked, despite the resulting constraints arising therefrom.⁷⁻⁹ In fact, a recent study by *Hermanowicz et al.*, encompassing 700 individuals (PD patients and caregivers), pointed out that around 50% of the interviewed cohort classified non-motor symptoms as a greater challenge in day-to-day life as opposed to motor symptoms.¹⁰ Overall, PD-related symptoms significantly impair the quality of everyday life and impose a great economic and emotional burden on patients, their families, as well as the healthcare system.^{2,10} A situation that is further worsened by comorbidities encompassing infections, cardiac and gastrointestinal disorders, fall-related injuries, and most importantly, the persistent lack of neuroprotective and disease-

altering therapeutics. To this date, PD is still exclusively treated symptomatically, with motor manifestations constituting the primary target and levodopa (L-DOPA), a compound known for its severe side effects (e.g., confusion, vomiting, dyskinesia), remaining the most prescribed medication and biggest hope for a short-term remedy.^{11,12}

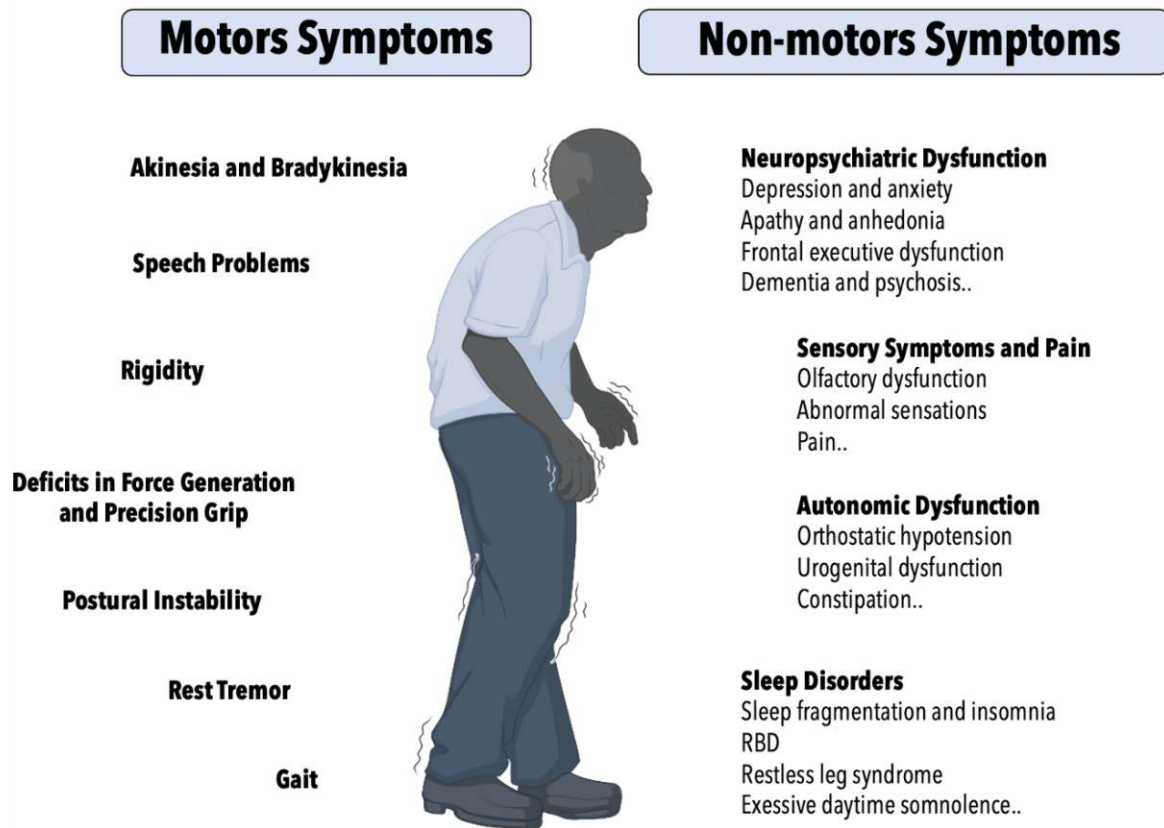


Figure 1: Graphical summary of PD-associated motor- and non-motor manifestations. Images were generated using Biorender. ^{6,7}

From a neuropathological point of view, PD is characterized by two distinctive hallmarks: i) the progressive loss of dopaminergic neurons in the *substantia nigra* of the human midbrain and ii) the accumulation of aggregated α -synuclein in the form of so-called Lewy-Bodies. The degeneration of dopaminergic neurons in the *substantia nigra* results in dopamine (DA) depletion within the nigrostriatal pathway, an essential part of the basal ganglia motor loop that controls locomotor activity.^{7,13} The onset of motor manifestations has been linked to a 50-80%

loss of dopaminergic neurons, indicating an initial compensatory mechanism in early stages of the disease.^{14,15} The presence of non-motor symptoms further supports the involvement of other neurotransmitters, next to DA, including neurotransmitters of the glutamatergic, cholinergic, serotonergic, and adrenergic systems, as well as the neuromodulators adenosine and enkephalins.¹⁶ Lewy-Bodies are considered a major hallmark in PD, PD dementia, and Lewy-body dementia and have been detected in several rare genetic disorders. They are intracellular cytoplasmic aggregates primarily comprised of the protein α -synuclein and lipids. They are characterized by a spherical morphology and radially organized fibrils and have been associated with neurodegeneration-associated lesions. Their formation is secondary to a malfunctioning of the ubiquitin-proteasome system and involves an excessive production of misfolded forms of ubiquitin proteins.¹⁷

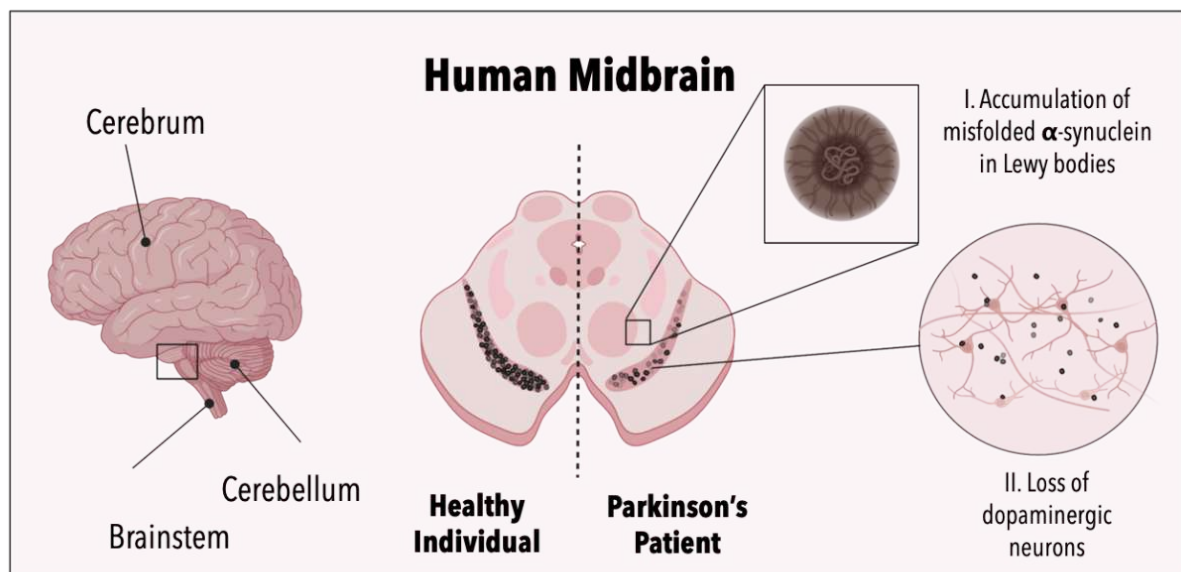


Figure 2: Graphical representation of the two major hallmarks associated with PD. The accumulation of misfolded α -synuclein. (I) The loss of dopaminergic neurons in the substantia nigra (II). Images were generated using Biorender.

The landmark discovery in 1983 that 1-methyl-4-phenyl-1,2,3,6-tetrahydropyridine (MPTP) causes selective injury to dopaminergic neurons resulting in PD-like manifestations, reinforced the conception that, first and foremost, PD is of environmental origin. MPTP, a structural and mechanistic analog to several pesticides, was derived by accident in synthesizing 3-

desmethylprodine, an opioid analgesic drug.^{18,19} Since then, rural living and well water consumption have been identified as the predominant environmental risk factors of PD, as they constitute surrogates for agricultural chemicals and pesticides. Specific pesticides, including rotenone and paraquat, have been successfully linked to PD in humans and parkinsonism in animals; the latter has rendered them an indispensable tool in the establishment of *in vivo* PD models. Other neurotoxicants associated with PD include chlorinated solvents (e.g., dry cleaning) and polychlorinated biphenyls (e.g., lubricants and coolants). Although these compounds have already been banned, they remain in soil and water due to their high environmental persistence.^{7,20} Next to chemical risk factors, also mild to moderate head injury and bacterial and viral infections have been associated with an increased risk of developing PD. On the other hand, smoking and caffeine/theine intake have been shown to reduce the risk of acquiring PD. Studies have found that current smokers have less than half the risk of developing PD when compared with nonsmokers and that male high coffee drinkers exhibit a nearly 60% reduction in risk as opposed to non-drinkers. While the exact mode of action has not been identified yet, studies could show that the alkaloid nicotine most likely infers the reduction observed in smokers.^{21,22} Moreover, physical activity, specific dietary patterns, and certain drugs, including nonsteroidal anti-inflammatory agents and calcium channel blockers, have been associated with a lower risk of acquiring PD.²³

In parallel to the identification of environmental risk factors, significant progress has been made in the discovery of genetic predispositions to PD.²² In the mid-1990s, a connection was drawn between PD and genetics for the first time. Before then, PD was assumed to be of sporadic origin, with age and environmental impacts constituting the main two risk factors. Nonetheless, only 15 % of PD patients report a family history of PD symptoms, rendering 85 % of all cases sporadic.

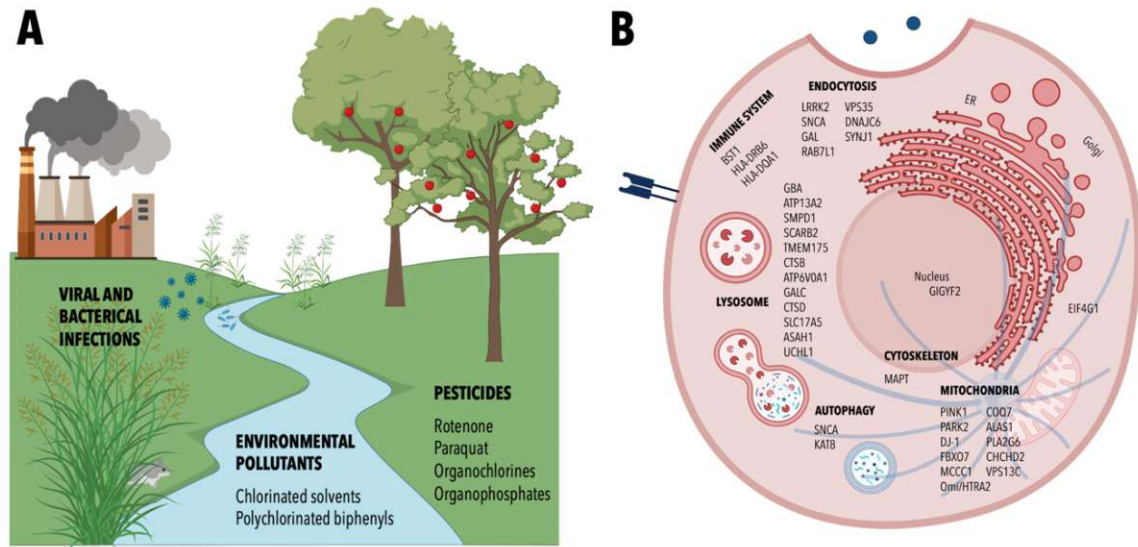


Figure 3: Graphical representation of the key environmental and genetic risk factors linked to PD. Images were generated using Biorender²⁴⁻²⁶

The distinction between genetic predispositions within familial and sporadic PD has to be taken with caution, however, as it is very likely that multiple genetic risk factors synergistically increase the chances of acquiring PD in both cases.²⁴ This hypothesis is underlined by the growing number of genome-wide association studies (GWAS) and genetic studies that have led to the identification of more than 40 novel risk loci associated with sporadic PD.²⁷ Interestingly, these studies have shown that the most common PD-related mutations display the lowest PD penetrance. In contrast, the rarest mutations, such as mutations in SNCA, PRKN, and LRRK2 (often associated with familial PD), pose the highest risk of clinical manifestation, with PRKN, LRRK2(G2019S), GBA, and CHCHD2 (P2L)¹ constituting the most penetrant mutations increasing the risk by 14, 10, 8 and 5% respectively.²⁴ While the most common genetic predispositions only account for a small proportion of PD cases; their analysis has shed light on common cellular processes that appear to be implicated in the neurodegenerative disorder PD (see Figure 3B).²⁸ Many genetic risk factors (e.g., CHCHD2, PRKN, PLA2G6,

¹ Abbreviations of the respective genes are first introduced in the list of abbreviations on page 10-11.

VSP13C, PINK1, LRRK2) have been linked to mitochondrial respiration and recycling.²⁴ This correlation is further supported by studies employing patient-derived cells (e.g., LRRK2, PRKN, PINK1, GBA, and SNCA) exhibiting morphologically aberrant mitochondria and impaired cellular respiration.^{29–34} Moreover, mutations in LRRK2, PRKN, PINK1, GBA, DJ-1, and SNCA have been linked to increased reactive oxygen species (ROS) levels and higher susceptibilities to cell death, pointing towards impaired oxidative stress-buffering capacity.^{35–40} While protein aggregation (α -synuclein and tau protein) was accounted for in several patient-derived cell lines with mutations in LRRK2, PRKN, PINK1, GBA, SNCA, and MAPT, impaired protein degradation resulting from both compromised autolysosome formation and maturation as well as decreased lysosomal enzymatic activities were linked to the genetic risk factors: LRRK2, PRKN, GBA, SNCA, PINK1, and DJ-1.^{24,34,46–51,35,36,38,41–45} For example, a study showed that the G2019S mutation in LRRK2 resulted in the binding of the kinase (LRRK2) to the lysosomal membrane, thus impairing chaperone-mediated autophagy.⁴³ On the other hand, protein aggregates in cells carrying a genetic predisposition in the MAPT gene impaired axonal mitochondrial movement and resulted in aberrant neurites.^{52,53} In addition, mutations in LRRK2, SNCA, GBA, and PRKN have been linked to synaptic dysregulation, including impaired electrophysiological activity, decreased calcium-mediated DA release, and impaired DA reuptake – the latter two both increasing DA-mediated neurotoxicity.^{34,47,54–58} Upon co-culture with T-lymphocytes, cells derived from sporadic patients displayed increased cell death via IL17-mediated signaling cascades, underlining previous notions on a neuroinflammatory role in PD.⁵⁹ Genetic and GWAS studies have significantly accelerated the progress in the field of PD over the last years, underlining the highly heterogeneous nature of PD and its multifactorial etiology. While this data points to the necessity of shifting the focus onto personalized approaches and improved substratification strategies, it also sheds light on several commonalities in cellular susceptibilities to PD, including mitochondrial dysfunction,

impaired protein degradation, and synaptic malfunction, as well as altered responses to neuroinflammation and oxidative stress. As a consequence, rare genetic alterations such as mutations in SNCA and LRRK2 provide an ideal basis for studying the implicated cellular pathways in PD and thus identifying potential new routes of therapeutic interference, despite their overall low incidence.^{24,28}

1.1.2 Experimental Models of PD and the Unmet Need for Neuroprotective and Disease-Modifying Strategies

An ideal experimental model for studying PD should feature the two key pathological hallmarks of the disease, namely i) the presence of Lewy bodies and ii) the loss of dopaminergic neurons. Moreover, the model must be progressive in its nature, including a time-dependent onset of PD-related phenotypes. In other words, the optimal experimental model of PD should provide a gradual onset of pathophysiological phenotypes that only after pathological manifestation would be employed for assessing a drug's or neuroprotective agent's effectiveness.^{60,61} Due to the restricted access to primary/patient-derived neuronal cell sources and the intrinsic limitations to primary cell cultures, specific attention in PD research has been directed toward developing animal-based models. Many experimental animal models have been developed so far, ranging from fruit flies and nematodes over rodents up to cats, dogs, and non-human primates.⁶² While small animal models do not recapitulate most clinical manifestations and are restricted in emulating pathological hallmarks, ethical concerns and high costs have limited the research on larger animals, including non-human primates, despite their often superior characteristics. As such, rodent-based experimental models that are readily available, genetically malleable, and low in cost constitute the predominant platform in PD research.⁶³ However, it must be noted that PD is restricted to humans and does not naturally occur within animals.⁶⁴ Therefore, pathological phenotypes must first be induced within the

models, forming the basis of model classification.⁶² As such, animal-based PD models can be separated into toxin-based and genetic models. Toxin-based models employ toxins such as 6-hydroxy-dopamine (6-OHDA) or 1-methyl-4-phenyl-1,2,3,6-tetrahydropyridine (MPTP) to induce nigrostriatal dopaminergic lesions predominantly through inhibiting mitochondrial function.⁶⁵

Table 1: Advantages and disadvantages of current PD in vivo models

Type of Experimental Animal Model	Mode of Action / Observations	Advantages	Disadvantages	Ref.
Toxin	6-OHDA	<ul style="list-style-type: none"> - ROS induce mitochondrial dysfunction - Induces major and consistent behavioral deficits 	<ul style="list-style-type: none"> - Does not penetrate the BBB - Acute toxicity - Lacks Lewy body formation 	60,66
	MPTP	<ul style="list-style-type: none"> - Inhibition of complex I in mitochondrial respiration 	<ul style="list-style-type: none"> - Penetrates the BBB - Progressive neuronal loss when administered continuously in low doses - Decreased DA levels in the striatum - Emulates the topography of dopaminergic neuron loss 	67,68
	Rotenone	<ul style="list-style-type: none"> - Insecticide - Inhibition of complex I - Targets catecholaminergic neurons 	<ul style="list-style-type: none"> - Degeneration of dopaminergic neurons - Behavioral impairment 	69,70
	Paraquat	<ul style="list-style-type: none"> - Widely used herbicide - Structurally similar to MPTP - Inhibition of complex I 	<ul style="list-style-type: none"> - Induces age-dependent neuronal cell loss - Induces Lewy Body formation 	62,70
Genetic	SNCA	<ul style="list-style-type: none"> - Accumulation of synuclein 	<ul style="list-style-type: none"> - Capable of emulating synuclein mediated pathological phenotypes 	71,72

	- Motor deficits		- Non-physiological topography of dopaminergic neuron loss	
LRRK2	- Motor deficits and axonal pathology - Dopaminergic degeneration	- Assessment of LRRK2-mediated functions	- Limited dopaminergic neuron degeneration - No accumulation of synuclein	71,73,74
PINK1	- Complete suppression can induce age-dependent DA reduction and decreased locomotor activity	- Assessment of the Parkin/PINK 1 pathway - Reduced locomotor activity and DA levels in drosophila and G309D-PINK1 mice	- Most models do not display a significant impairment of dopaminergic neurons	71,73,75
PRKN	- Overexpression elicits neuroprotective effects after treatment with MPTP and 6-OHDA	- Assessment of Parkin-mediated functions	- Lacks characteristic PD related phenotypes	62,71
DJ-1	- DJ-1 knock-out mice display hypersensitivity towards MPTP and rotenone	- Useful for combinatorial studies employing neurotoxins	- Lacks characteristic PD related phenotypes	71,76

While these models are considered the most thoroughly studied, results obtained from these models rarely translate into the clinic successfully. One potential explanation for this is the acute onset mediated by the administration of toxins, which significantly differs from the degenerative processes observed in humans. As an alternative to toxin-based models, genetic PD models have been developed by either generating null mutations or overexpressing genes of potential interest. Genetic models have provided valuable information on the involvement

of PD-related genes; however, they rarely emulate all pathologically relevant hallmarks.^{62,63,65,77} Table 1 provides an overview of the different models, highlighting their respective advantages and disadvantages. Overall, it remains indisputable that experimental animal models have provided valuable insights into the underlying mechanisms of PD. However, physiological differences, most notably the absence of PD in animals, that have not brought forth any neuroprotective or disease-modifying treatment strategies raise the question of whether animal models will suffice to tackle the remaining hurdles in understanding and fighting PD.¹¹ This is of particular importance considering the increasing socioeconomic burden associated with PD. In the US alone, PD-related costs have been estimated at \$51.9 billion. A recent study by *Yang et al.* calculated that this total economic burden consists of \$25.4 billion in direct medical costs and \$26.5 billion in indirect and non-medical costs (including an indirect cost of \$14.2 billion related to PD patients and caregiver burden).² Based on a projected PD prevalence of 1.6 million, the study postulates that the burden in the US alone would surpass \$79 billion by 2037. Despite these prospects and the significant gain in knowledge obtained over recent years, the demand for disease-modifying and neuroprotective strategies remains unmet.

In summary, the limitations of current PD models, which are reflected by the high failure rates of clinical trials, underline the urgent need for new and alternative strategies that better replicate the pathological features of this highly heterogeneous disorder.⁷⁸ One attractive alternative constitutes organoid technology, a rapidly evolving field focusing on the *in vitro* recreation of miniaturized tissue analogs. The usage of reprogrammed cells derived from easily accessible skin or blood samples not only allows for the recreation of (patho-)physiological tissue models but opens new routes from patient-specific models to personalized medicine.

1.2 A PERSONALIZED APPROACH TO PARKINSON'S DISEASE – HUMAN MIDBRAIN ORGANOID

With the emergence of induced pluripotent stem cell (iPSC)-technology in 2006, for the first time, tangible opportunities for physiologically relevant and personalized *in vitro* models have opened up in the form of so-called "organoids."⁷⁹ Organoids denote *in vitro* derived microtissues that, by undergoing some level of self-organization, can recapitulate fundamental physiological facets of *in vivo* organs.⁸⁰ Several organoid-based models have been developed so far, including, among others, organoids of the skin, the intestine, the liver, and the heart.^{81–84} Moreover, as illustrated by Figure 4, tremendous efforts have been directed toward establishing brain organoids, encompassing microtissues of the forebrain, the hindbrain, and the midbrain, the afflicted region in PD.^{85–88}

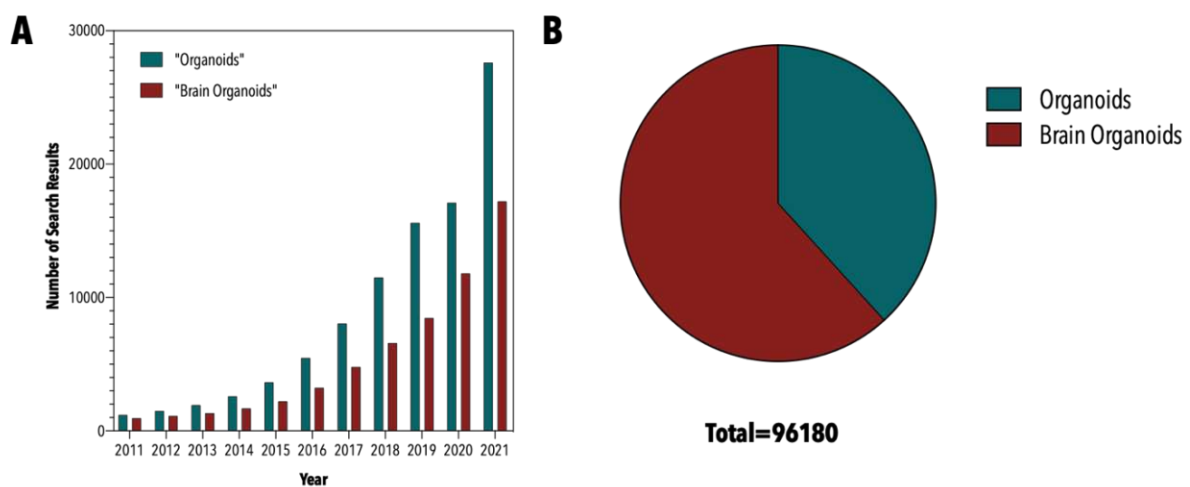


Figure 4: Graphical illustration demonstrating the growth of the field of organoid and brain organoid technology between 2011 and 2021. Exponential increase in search results obtained for both "organoids" and "brain organoids" between 2011 and 2021 (A). Graphical representation of the percentage that brain organoid search results make up in all search results related to organoids (B). Note: Number of search results refers to the number of hits obtained in Google Scholar in response to the query "organoids" and "brain organoids".

Human midbrain organoids (hMOs) have been shown to mimic essential features of the tissue's three-dimensional (3D) cytoarchitectural arrangement and function and, more importantly, mirror pathological hallmarks of PD including α -synuclein aggregation and dopaminergic

neurodegeneration. So far, 15 studies have been published on hMOs; a comprehensive overview is given in Table 2. Starting from regionally patterned neuroepithelial stem cells, *Monzel et al.* were able to generate hMOs that display characteristic spatially patterned groups of dopaminergic neurons and robust glia differentiation into astrocytes and oligodendrocytes after 61 days of culture.⁸⁷ Both A10 and A9 midbrain dopaminergic neurons, a subpopulation predominantly affected in PD, were present in the reported hMO model. In addition to electrophysiological activity, neuromelanin deposition, void in commonly used animal models, could be observed after 149 days in culture. Employing an alternative differentiation protocol, *Jo et al.* observed accelerated neuromelanin formation, starting at around 80 days of culture. In agreement with the human midbrain, where neuromelanin is accumulated within the *substantia nigra* postnatal, fluorescence-activated single-cell sorting (FACS) analysis revealed that neuromelanin-containing cells were enriched in the vulnerable A9 midbrain dopaminergic neuron subpopulation.⁸⁸ Due to the inherent size of the mesencephalic microtissues, encompassing several millimeters, and the concomitant lack of vasculature, organoids are prone to develop necrotic cores a fundamental limitation of organoid technology. While *Berger et al.* were able to slightly reduce the size of the formed necrotic cores by cultivating hMOs in a millifluidic set-up, *Nickels et al.* addressed the limitation by shortening the expansion phases of the organoid differentiation protocol resulting in an overall reduced size of the midbrain microtissues and thus optimized diffusion properties.^{89,90} *Sabaté et al.* expanded the latter model by microglia, the predominant immune component of the brain, resulting in altered synaptic gene expression and improved neuronal excitability.⁹¹ In a study by *Renner et al.*, specific focus was directed towards the establishment of a high throughput screening- (HTS-) compatible hMO protocol, allowing for an automatable process starting from hMO generation up to microtissue analysis.⁹² In addition to the development of healthy hMO models, over the last three years, significant progress has been made too in establishing PD patient-specific

models. Two studies demonstrated the emulation of pathological hallmarks of PD, such as reduced numbers and limited complexity of midbrain dopaminergic neurons, by generating midbrain organoids from patient-derived cells containing an LRRK2-G2019 mutation.⁹³ Employing patient-derived cells carrying a PRKN mutation, *Kano et al.* could replicate reduced astrocyte activity as observed in post-mortem samples of the iPSC-donors.⁹⁴ In a recent study by *Jarazao et al.*, pathological hallmarks, including impaired mitochondrial activity and reduced numbers of dopaminergic neurons, were emulated by generating hMOs from patient-derived cells carrying a mutation in the PINK1 gene.⁵¹ Most importantly, the authors were able to elicit a significant rescue of these phenotypes after treating the hMOs with the repurposed excipient 2-hydroxypropyl-beta-cyclodextrin (HP- β -CD), demonstrating the applicability of hMOs for drug screening purposes. By generating hMOs from patient-derived cells carrying a 3xSNCA mutation, two recently published preprints could mimic pathological phenotypes ranging from dopaminergic neurodegeneration and α -synuclein aggregation to synaptic decline.^{58,95} Finally, *Jo et al.* were able to recapitulate for the first time in a midbrain organoid model the presence of Lewy bodies, the second most important hallmark of PD, by generating dual perturbation organoids carrying 3xSNCA and GBA mutations.⁹⁶ Altogether, the substantial progress in midbrain organoid technology has undoubtedly proven that patient-specific organoid models provide a valuable tool in PD research, capable of emulating the disorder's key pathological hallmarks. However, despite these significant advancements, several challenges persist, including the tissue's immaturity, organoid variability, lack of specific cell types (e.g., microvascular endothelial cells), and nutrient deficiency-based growth restrictions. In addition, organoid technology still strongly relies on unphysiological cultivation conditions that omit critical biophysical cues (e.g., interstitial fluid flow). Brain-specific interstitial fluid flow has been linked to a variety of essential functions, including the delivery of nutrients, the removal of metabolic and neurotoxic waste, non-synaptic cell-cell

communication, tissue homeostasis as well as cell migration.⁹⁷ Moreover, as part of the so-called "glymphatic system" – a glial-mediated clearance system of the human brain – interstitial fluid flow has been linked to exacerbated protein deposition in models of Alzheimer's disease and one model of PD as well as to the delivery and clearance of drugs, making it of considerable importance in the context of pharmacological screening applications.^{98,99} Furthermore, hMO technology still strongly depends on the use of invasive endpoint analysis that restricts the investigation of continuous events such as tissue maturation and disease progression. In fact, only 1 out of all 15 studies (see Table 2) employed non-invasive sensing strategies to monitor alterations in the hMOs' electrophysiological properties during maturation.

In summary, to further increase the technology's predictive power and its ability to provide a genuine alternative to animal models, the next generation of hMO models will need to address (a) crucial biophysical stimuli, (b) analytical accessibility, and (c) lacking cellular interactions (endothelial cells).

Table 2: Comprehensive overview of studies on hMO-based in vitro models.

Characteristics of the hMO model	Application/ Findings	Analysis	Cultivation Condition	Ref.
Healthy hMO	Development of a differentiation protocol resulting in spatially organized dopaminergic neurons, astrocytes, oligodendrocytes, occasional neuromelanin formation, and electrophysiological activity.	Invasive endpoint analysis	Wellplate/shaker	87
Healthy hMO	Development of a differentiation protocol resulting in dopaminergic neurons, functional electrically active synapses, and pronounced neuromelanin formation.	Invasive endpoint analysis	Wellplate/shaker	88
Healthy hMO	Development of a differentiation protocol.	Invasive endpoint analysis	Wellplate/shaker	100
Healthy hMO	Development of an HTS-compatible protocol for the differentiation and analysis of hMOs.	Invasive endpoint analysis	Wellplate/shaker	92

Healthy hMO	Optimized differentiation protocol results in reduced necrotic core formation.	Invasive endpoint analysis	Invasive endpoint analysis	90
Healthy hMO	Millifluidic cultivation reduces necrotic core formation.	Invasive endpoint analysis	Millifluidic	89
Healthy hMO	Integration of microglia into the hMO model.	Invasive endpoint analysis	Invasive endpoint analysis	91
PINK1 mutation	Model reveals altered energetic profiles, apoptosis, mitophagy and reduced dopaminergic differentiation. Treatment with the repurposed excipient HP- β -CD rescues PD phenotypes by improving mitophagic capacity.	Invasive endpoint analysis	Wellplate/shaker	51
3xSNCA	Model recapitulates α -synuclein aggregation, dopaminergic neurodegeneration, impaired astrocyte differentiation and synaptic function.	Non-invasive recording of electrophysiological activity	Wellplate/shaker	58
3xSNCA	Model recapitulates α -synuclein aggregation in neurons and glial populations.	Invasive endpoint analysis	Wellplate/shaker	95
PRKN mutation	Comparison of post-mortem samples and hMOs reveals reduced numbers of astrocytes in PRKN patients.	Invasive endpoint analysis	Wellplate/shaker	94
GBA and SNCA mutation	Model recapitulates α -synuclein aggregation and Lewy Body formation.	Invasive endpoint analysis	Wellplate/shaker	96
G2019S-LRRK2	Model reveals reduced number and complexity of dopaminergic neurons. Upregulation of FOXA2 points at neurodevelopmental alterations in PD.	Invasive endpoint analysis	Wellplate/shaker	93
G2019S-LRRK2	Model recapitulates α -synuclein aggregation and identified role of TXNIP in development of PD phenotypes.	Invasive endpoint analysis	Wellplate/shaker	101
G2019S-LRRK2	Development of a machine learning classifier for optimized data processing and neurotoxicity prediction in a 6-ODHA hMO model.	Invasive endpoint analysis	Wellplate/shaker	102

1.3 FROM MICROFLUIDICS TO BRAIN-ON-A-CHIP TECHNOLOGY

One technology that provides an ideal basis for tackling the current limitations that restrict midbrain organoid technology from reaching its full potential, is organ-on-a-chip (OoC) technology or microfluidics respectively. Descending from the four parent technologies: molecular analysis, biodefence, molecular biology, and microelectronics, microfluidics encompasses systems and technologies capable of manipulating minute (10^{-9} to 10^{-18} liters) amounts of fluids, using micrometer-sized channels. Due to its beneficial properties including low sample and reagent volumes, increased sensitivities and resolution, small footprints, and reduced analysis times microfluidics quickly found high recognition, especially within the field of analytics.¹⁰³ In 1991, however, studies conducted by Andre Kleber reporting the construction of a ventricular myocardium through the patterned growth of cells *in vitro* pointed for the first time at the potential translatability of microfluidics into the field of biology.¹⁰⁴ With the introduction of the biocompatible and transparent elastomer poly(dimethylsiloxane) (PDMS) in the late 1990s, the field of biomicrofluidics swiftly started to emerge. In 2004 Michael Shuler proposed the concept of micro-cell culture analogs – miniaturized platforms that employ microfluidic technology for mimicking the organ-level function of human (patho)physiology.^{105–107} This concept was taken up by Donald Ingber, who coined it “OoC technology” in 2010, accompanied by a groundbreaking study using microfluidic engineering principles to develop a microphysiological system of the human lung. In their study, *Huh et al.* emulated organ-level responses to bacteria and inflammatory cytokines in a functional model of the alveolar capillary interface of the human lung, incorporating both fluid flow and mechanical actuation.¹⁰⁸ Since then, the field of OoC technology has rapidly expanded. interface of the human lung, incorporating both fluid flow and mechanical actuation.¹⁰⁸ Since then, the field of OoC technology has rapidly expanded.

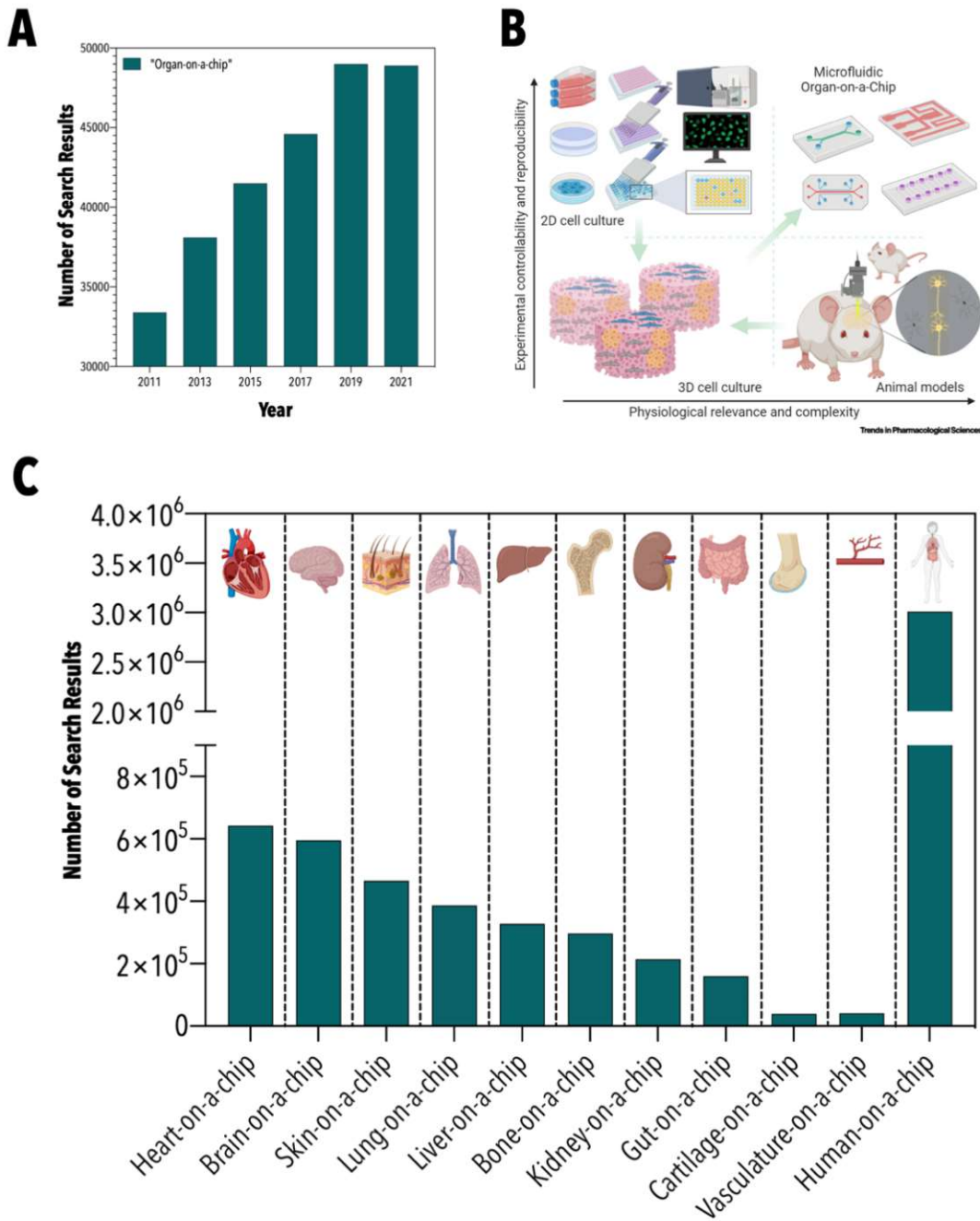


Figure 5: Graphical illustrations on OoC technology. Bar graph highlighting the increased interest in OoC technology over the last ten years (A). Graphical comparison of conventional *in vitro*, *in vivo*, and OoC technology (with copyright permission from the journal¹⁰⁹) (B). Distribution of the search results among the various organs of the human body. The graph was generated in Biorender (C). Note: The number of search results refers to the number of hits obtained in Google Scholar in response to the listed query keywords.

In 2016 OoC technology was listed among the top ten emerging technologies by the World Economic Forum. Overall, OoC technology can be defined as a highly transdisciplinary field encompassing elements of tissue engineering, cell biology, microtechnology, and, most

importantly, microfluidics. An essential driving force behind its development has been the strong need for reliable and low-cost alternatives to conventional *in vivo* and *in vitro* models. While animal models provide a highly complex testing system, accounting for, e.g., biophysiological stimuli, multi-tissue crosstalk, and the immune system, its intricacy impedes data interpretation and thus translatability, which in addition is hampered by interspecies differences. These limitations are further aggravated by high costs and ethical concerns, which restrict sample sizes and, therefore statistical significance. While conventional *in vitro* models provide high throughput and low costs, their substantial deviation from human physiology renders them unsuitable for clinical studies.¹⁰⁹ As depicted in Figure 6B, OoC technology sets out to bridge this gap by taking advantage of the underlying principles of microfluidics. The ability to provide precise spatial and temporal control over cellular microenvironments allows for the emulation of (patho-)physiological tissue niches at the microscale that account for organotypic cellular arrangements and biophysical stimuli, including compression, stretch as well as shear stress. At the same time, experimental costs can be kept low by reducing reagent volumes and allowing for high throughput compatibility. The high flexibility in design, material, and function coupled with the capability of non-invasive monitoring (e.g., embedded microsensors) allows for the generation of custom-made platforms applicable to emulate and study any tissue of the human body.¹¹⁰ OoC technology has already led to the successful recreation of various tissue analogs *in vitro*, ranging from models of the heart, the vasculature, the gut, and the lung up to models of the human brain.^{111–115} *Kasendra et al.*, for example, could emulate intestine-like microtissues *in vitro* by fusing organoid- with OoC technology.¹¹⁶ The model presents characteristic villi-like projections lined by polarized epithelial cells that undergo multi-lineage differentiation and, in contrast to its organoid parent tissue, exposes its apical surfaces to an open lumen. Underlining the importance of biophysical stimulation in tissue engineering, transcriptomic analysis confirmed a closer resemblance to the human

duodenum in dynamically differentiated microtissues compared to their organoid counterparts. *Homan et al.* utilized the ability to control fluid dynamics to promote the endogenous pool of endothelial progenitor cells and subsequently trigger *in vitro* vascularization of iPSC-derived kidney organoids *in vitro*.¹¹⁷ While this approach did not result in readily perfusable vascular networks; it highlights the importance of fluid shear stress on both vessel formation and tissue maturation. An alternative approach to the generation of vascular models *in vitro* was presented by *Campisi et al.*, who, by co-culturing primary human astrocytes, pericytes, and microvascular endothelial cells under interstitial fluid flow regimes, were able to bioengineer a 3D capillary network of the human blood-brain barrier (BBB).¹¹⁸ This self-assembled microphysiological model provides perfusable capillaries with significantly lowered barrier permeabilities, a critical functional characteristic of the BBB. *Maoz et al.* employed a modular microfluidic set-up to demonstrate the functional connectivity within the cellular constituents of the neurovascular unit.¹¹⁹ Using this interconnected platform, the authors were able to show for the first time that the cells of the BBB and neurons are metabolically coupled. Moreover, OoC technology was already successfully employed to emulate pathophysiological alterations *in vitro*. *Benam et al.*, for example, were able to recapitulate characteristic hallmarks of chronic obstructive pulmonary disease, including selective cytokine hypersecretion, increased neutrophil recruitment, and clinical exacerbation by exposure to viral and bacterial infections, upon introducing patient-derived epithelial cells into their small airway-on-a-chip.¹¹³ By modulating the compression forces in a microfluidic model of human cartilage, *Occhetta et al.* could initiate both a physiological chondrogenic phenotype and an osteoarthritic response when increasing biomechanical stimulation to hyperphysiological levels.¹²⁰ Over the last few years, efforts have been made to incorporate multi-tissue crosstalk into microfluidic platforms in the form of so-called humans-on-a-chip.

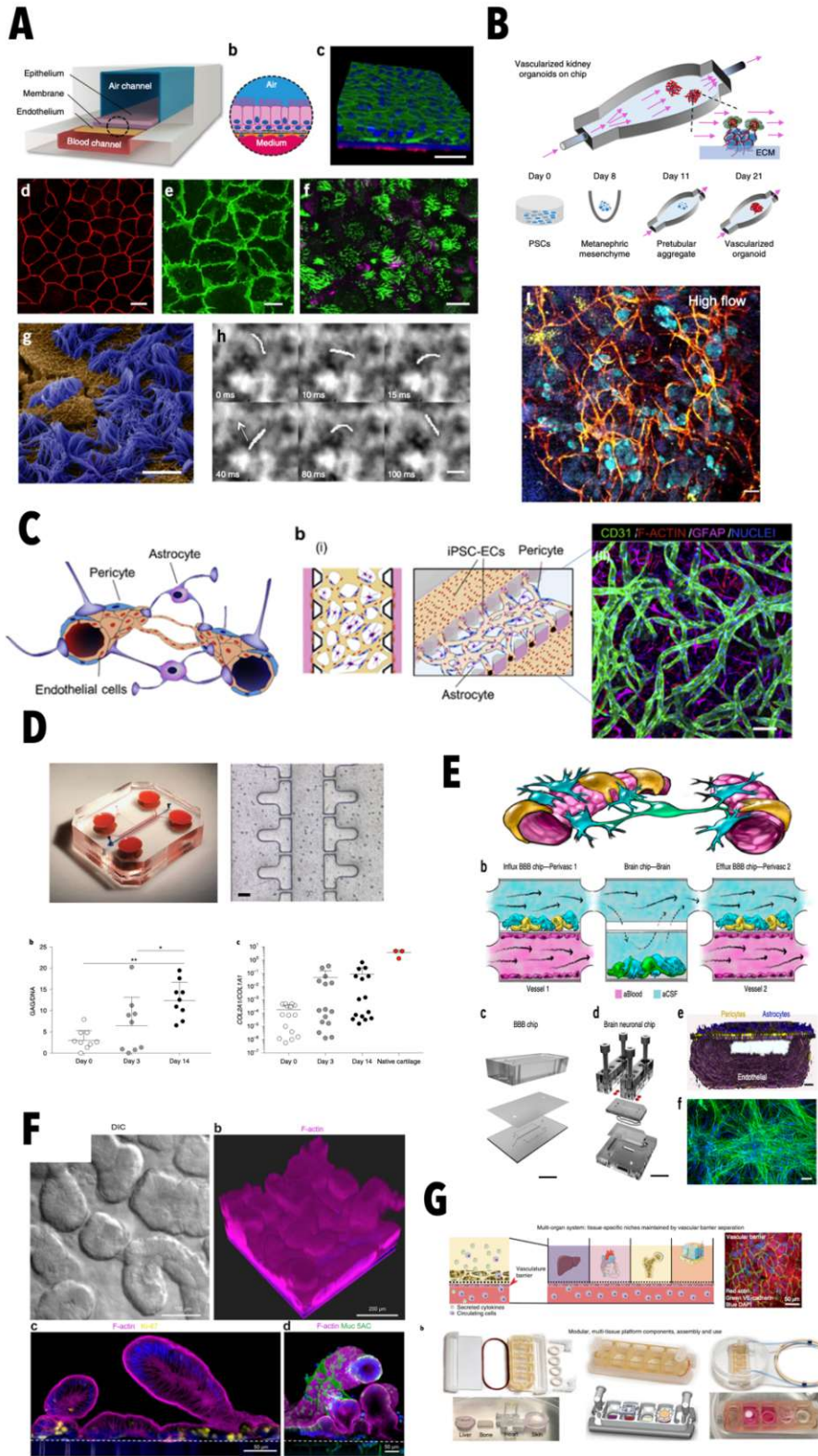


Figure 6: Representative overview of tissue-specific OoC platforms. Representative image of the tissue differentiation obtained in the small-airway-on-a-chip.¹¹³ (A) OoC platform for vascularization of iPSC-derived kidney organoids.¹¹⁷ (B) Bioengineered model of the human BBB.¹¹⁸ (C) OoC platform for mechanically actuating and cultivating chondrogenic microtissues.¹²⁰ (D) Interconnected modular set-up for the emulation of the neurovascular unit on-chip.¹¹⁹ (E) Intestinal microtissues generated in a mechanically actuated OoC platform.¹¹⁶ (F) Multi-chamber device for the emulation of tissue-tissue crosstalk on-chip.¹²¹ (G) All images are published with copyright permission from the respective journals.

A recent study by *Ronaldson-Bouchard et al.* reported the development of a human-on-a-chip platform capable of co-culturing and interconnecting four separate tissue analogs, including microtissues of the heart, the liver, the bone, and the skin, by an endothelial-lined vascular channel.¹²¹ The interlinked tissues not only maintained their molecular, structural, and functional phenotypes over a period of four weeks but, more importantly, were able to recapitulate the pharmacokinetic and pharmacodynamic profiles of doxorubicin in humans, highlighting the applicability of OoC technology for pharmaceutical applications. Although OoC technology has expanded massively over the last decade (see Figure 6), only a handful of studies have set out to combine brain organoids with OoC technology (see Figure 7). Among those studies, most have focused on assessing the effects of neuroteratogens such as nicotine or cannabis on neurogenesis. *Wang et al.*, for example, showed that prenatal nicotine exposure results in aberrant cortical differentiation and disrupted neuronal outgrowth, a prerequisite for forming mature neuronal networks.¹²² Similar observations were reported by *Ao et al.*, who assessed prenatal exposure to the neuroteratogen Δ -9-tetrahydrocannabinol in a microfluidic device featuring an air-liquid interface.¹²³ By increasing oxygen availability over the course of organoid differentiation, the authors were able to drastically reduce the formation of hypoxic cores in the neuronal microtissues. Impaired neurogenesis, characterized by increased cell death, altered regionalization, and reduced neuronal differentiation, was also reported upon exposure to cadmium, a common component of electrical batteries.¹²⁴ *Park et al.* employed a microfluidic cultivation set-up to investigate the interrelationship between interstitial fluid flow and β -amyloid mediated neurotoxicity.¹²⁵ Using their Alzheimer's disease model, the authors could demonstrate enhanced neurotoxic effects elicited by β -amyloid upon exposure to dynamic cultivation conditions, underlining the importance of interstitial fluid flow in neurobiological studies. It must be noted that while this study employed primary rat neurospheres, it could easily be expanded by human brain organoids. In an elegant study by

Karzbrun et al., a microfluidic device was employed to study the physical underpinnings of human brain wrinkling.¹²⁶ Using *in situ* imaging, cytoskeletal contraction at the organoid core and nuclear expansion at the organoid's perimeter were identified as the two opposing forces contributing to brain organoids' differential growth. Moreover, the authors observed reduced convolutions, modified scaling, and a lowered elastic modulus when monitoring the folding of organoids carrying a mutation in lissencephaly-1 (LIS1 +/-), a genetic predisposition giving rise to a lissencephalic phenotype characterized by a lack of cortical gyrations. *Rifes et al.* utilized the ability of microfluidics to provide a high degree of spatiotemporal control to emulate neural tube formation *in vitro*.¹²⁷ To that end, the authors integrated a gradient generator into their microfluidic device, exposing human embryonic stem cells to a linear gradient of the glycogen synthase kinase three inhibitor, an activator of the canonical wntless-related integration site (WNT) pathway, an essential signaling cascade in embryonic development. Using this approach, *Rifes et al.* induced rostrocaudal organization already 24 hours into on-chip cultivation, which resulted in a neuron-specific transcription profile in rostral cells 24 hours thereafter.¹²⁷ While this study technically does not include brain organoids; it illustrates the vast potential that OoC technology offers in the context of *in vitro* brain modeling. Lastly, a recent study by *Cho et al.* demonstrated significant improvements in the functional maturation of human brain organoids embedded within a brain extracellular matrix enriched hydrogel using gravity-driven flow.¹¹⁵ Next to improved cellular viabilities and reduced necrotic cores, dynamic cultivation could markedly reduce organoid size variation from a coefficient of variance of 43.4 % to 17.4%. It must be noted, however, that while the above-referenced studies have provided valuable insights into fundamental aspects of neurogenesis, none have exploited the potential of microfluidic technology to integrate in-line sensing strategies needed to increase analytical accessibility, a prerequisite of any high-quality *in vitro* tissue model and a significant limitation

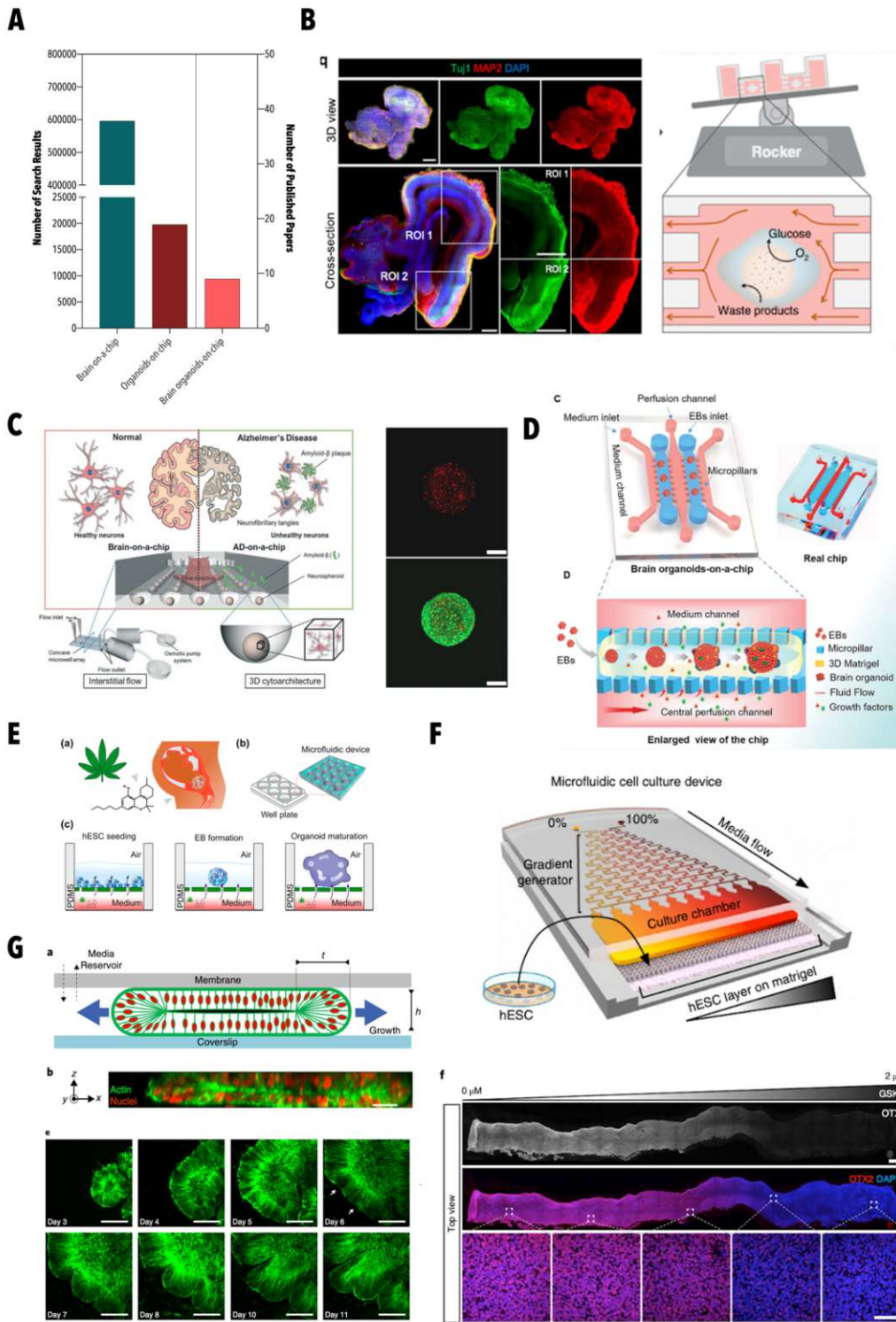


Figure 7: Representation of brain organoid-on-a-chip platforms. Graphical representation of neurological and organoid-based studies in OoC, highlighting the low number of OoC studies on brain organoids. (A) OoC platform for the dynamic cultivation and maturation of human cerebral organoids.¹¹⁵ (B) Neurosphere-based microfluidic model for assessing the effects of interstitial fluid flow in Alzheimer's.¹²⁵ (C) Microfluidic set-up for improving insufficient oxygenation by cultivating brain organoids at air-liquid interfaces¹²³ (E). Microfluidic model for studying brain folding events in vitro¹²⁶ (G). Gradient generator-based OoC platform for recapitulating the neural tube formation in vitro.¹²⁷ (F). All images are published with copyright permission from the respective journals.

in organoid technology. Furthermore, except for two studies, one employing primary rat neurons and the other omitting dynamic culture conditions, none of the presented studies focused on neurological diseases, despite increasing knowledge on the role of interstitial fluid flow in neuropathology.

1.4 TACKLING THE ISSUE OF LOW ANALYTICAL ACCESSIBILITY – SENSING STRATEGIES IN ORGAN-ON-A-CHIP TECHNOLOGY

While OoC technology provides a range of advantageous properties, one essential benefit, namely the ability of non-invasive monitoring through the integration of sensors, often remains overlooked. Overall, sensors in OoC technology can be classified into three categories: electrical, electrochemical, and optical.¹²⁸ In each case, the sensor is separated into three individual parts: a sensing or recognition element, a transducer that converts the sensing event into a signal, and lastly, a detector for signal processing (see Figure 8).

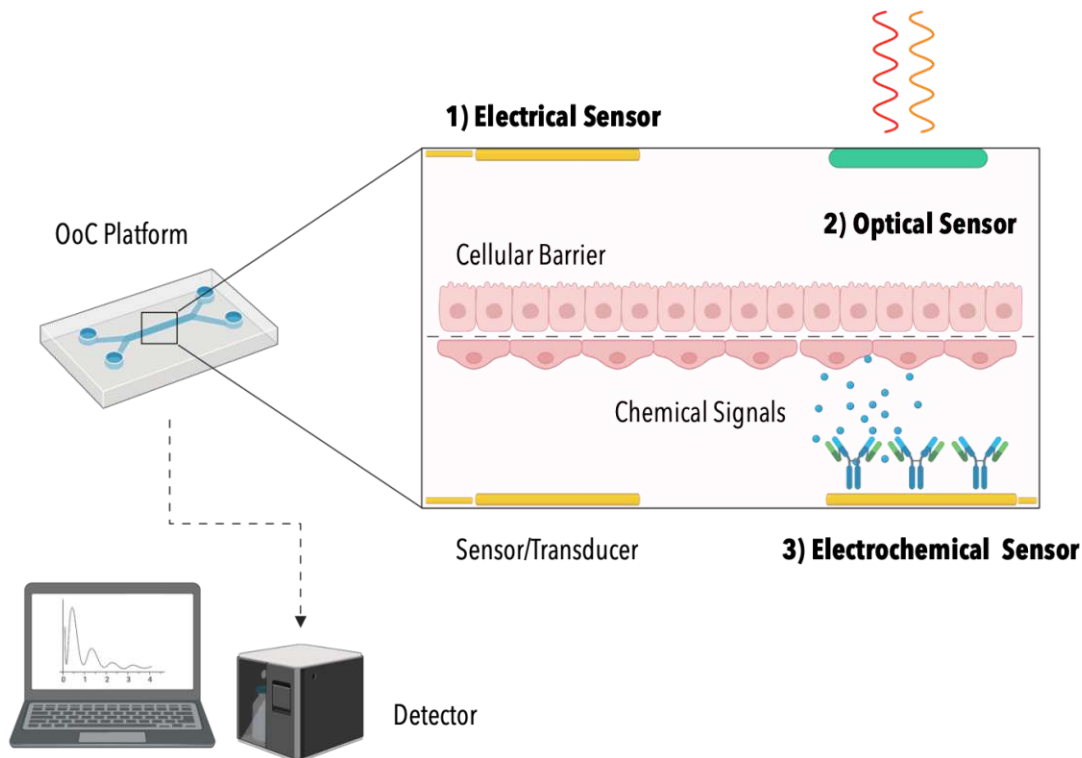


Figure 8: Schematic overview of the three different sensing principles found in OoC platforms. Modular configuration of 1) electrical sensors, 2) optical sensors, and 3) electrochemical sensors.

1.4.1 Electrical Sensors

Electrical sensors constitute the most common type of sensor within OoC platforms, owing to their ease of integration and extensive knowledge within the field of microelectronics. They can be employed to assess parameters such as strain, cellular impedance, and extracellular field potentials, providing valuable information about a range of cellular properties, including barrier integrity, cell growth, morphology, and electrophysiological activity.¹²⁸ As depicted in Table 3, trans-epithelial/endothelial electrical resistance (TEER) measurements present the predominant sensing strategy among any sensors in OoC platforms (> 1/3 of all studies). By assessing the resistance between two electrodes placed on either side of a semipermeable membrane - that acts as a culturing substrate for barrier-forming cells - conclusions on barrier integrity, a vital property of any physiological barrier, can be drawn. It must be noted, however, that the placement of the electrodes can significantly affect TEER results, as such measurement set-ups must be assessed prior to comparing different data sets.¹²⁹ *Zoio et al.* developed a TEER-integrated microfluidic platform for monitoring the barrier integrity of a full-thickness human skin model.¹³⁰ The study confirmed the strong correlation between sensitivity distribution, electrode placement, and electrode size by employing finite element analysis. Based on this data, the authors were able to improve the sensitivity of the on-chip TEER measurement in comparison to conventional chopstick set-ups by placing electrodes of a defined size directly opposite each other. *Odijk et al.* tried to account for the discrepancies between traditional and microfluidic TEER set-ups by developing and validating a mathematical model.¹³¹ Using the proposed model, the authors could extrapolate comparable TEER data from their microfluidic device as long as the tissue analog remained in a monolayer regime (first ~70 h). In their study, *Odijk et al.* further showed that a slight reduction in cell coverage (0.4%) could cause a significant drop (80%) in TEER, underlining the methods' intrinsic sensitivity and thus low comparability.¹³¹

In addition to conventional TEER measurements, studies in OoC have set out to expand the method's applicability and set-up. For example, *Van der Helm et al.* utilized impedance spectroscopy to non-invasively monitor colon tissue differentiation in a TEER-integrated gut-on-a-chip platform.¹³² Using a four-terminal sensing approach, the authors were able to show that capacitance can be used as a predictor of the state of villi formation. *Yeste et al.*, on the other hand, employed a planar measurement set-up using microgrooves to determine barrier integrity in a parallelly aligned model of the blood-retinal barrier.¹³³ Several small and independent platinum TEER electrodes were distributed throughout the platform to allow for optical access to the OoC model.

In contrast to TEER, electrical cell-substrate impedance sensing (ECIS) employs an array of small electrodes and a large common counter electrode embedded on a planar surface. By monitoring changes in impedance at a selected frequency, ECIS can provide information on cell attachment and growth, morphology, and cellular motility.¹²⁸ For example, *Wu et al.*¹³⁴ utilized ECIS for the time-resolved monitoring of cytotoxic effects mediated by three established antineoplastic drugs against lung cancer. To allow for the attachment of cancer spheroids on the electrodes and thus the measurement of the 3D microtissues on-chip, electrodes were coated with laminin prior to the seeding of the device. A novel ECIS sensing strategy was published by *Schuller et al.*, who integrated interdigitated electrodes on polyester membranes in a multi-step protocol.¹³⁵ The authors demonstrated comparable results between ECIS measurements using membrane electrodes and TEER, providing an alternative approach to monitoring barrier integrity in OoC platforms.¹³⁶ Multi electrode arrays (MEAs) comprise arrangements of hundreds of microelectrodes that enable the spatiotemporal mapping of electrophysiological events. As such, MEAs provide a valuable tool in the characterization and functional assessment of electrically active cells and microtissues such as neurons and cardiomyocytes.¹³⁷ By using platinum black electrodes and a field-programmable gate array,

Perrier et al. expanded the applicability of MEAs to pancreatic islet microtissues and their electrophysiological activities, characterized by slow potentials.¹³⁸ Using their measurement set-up, the authors could (i) record islet activation and (ii) discriminate between responses to varying glucose concentrations. Lastly, by measuring resistance changes in a conductive meander formed electrode, electrical sensors can further be employed to monitor and control mechanical deformation.¹³⁹ As of yet, however, strain sensors have not been integrated into OoC platforms.

1.4.2 Electrochemical Sensors

Electrochemical sensors utilize an analyte's electrochemical interaction with an electrode for its subsequent measurement. Read-out is achieved either by (i) the formation of a potential difference (potentiometric sensors) or (ii) a flow of current (amperometric sensors) between two electrodes. Electrochemical sensors are referred to as biosensors if biological molecules are employed as recognition elements. Potentiometric sensors encompass metal oxide-based (MOx) and ion-sensitive field-effect transistors (ISFET). While MOx sensors measure the potential difference between a MOx working electrode and an Ag/AgCl reference electrode, ISFET sensors employ ion-sensitive membranes to generate an electrochemical interaction between an electric field and a charged analyte of interest. In amperometric set-ups, on the other hand, a potential is applied between a chemically stable working electrode and a reference electrode, usually with the aid of a third auxiliary electrode. In the presence of electrochemically active species, the current measured between the two electrodes will be altered by the analyte's interaction with the working electrode. This interaction directly translates into an electrical signal measured by the amperometric sensor.¹²⁸ One successful application of an amperometric sensor in an OoC platform was published by *Jin et al.* in 2019.¹⁴⁰ By integrating a flexible electrochemical sensor into their vascular OoC platform, *Jin*

et al. were able to exert cyclic circumferential stretch within their platform and subsequently monitor mechanically induced biochemical signals of primary endothelial cells (nitric oxide (NO), ROS) in real-time.¹⁴⁰ To expand the application of amperometric sensors to non-electrochemically active species, electrodes can be functionalized with biological recognition elements, e.g., enzymes. For example, *Ortega et al.* functionalized screen-printed gold electrodes with capture antibodies against IL-6 and TNF- α to monitor myokine release in-line of their muscle chip.¹⁴¹ On-chip myoblasts were stimulated either electrically through an indium tin oxide array or biologically using bacterial lipopolysaccharides to induce muscle contraction.

1.4.3 Optical Sensors

To deduce information on the status of a system, optical sensors rely on the detection of changes in optical properties, including absorption, scattering, and luminescence.¹²⁸ *Rothbauer et al.* utilized light scattering to predict pathological changes in matrix remodeling observed during rheumatoid arthritis.¹⁴² Using this optical and label-free approach, the authors demonstrated significant differences in light scattering between control and TNF- α treated synovial microtissues, three days into biological stimulation. The study provides an elegant proof-of-principle highlighting the applicability of light scattering for the detection of subtle morphological variations on-chip. Photoluminescent sensors are composed of luminescent indicator dyes embedded within a polymer matrix. The sensor's properties and specificities can be modulated by the choice of the indicator dye, matrix, and further additives (e.g., enzymes). Read-out is accomplished by the combination of an external light source and detector mounted on top of the microfluidic platform. Optical detection in luminescent sensors can be based either on fluorescent lifetime or intensity.

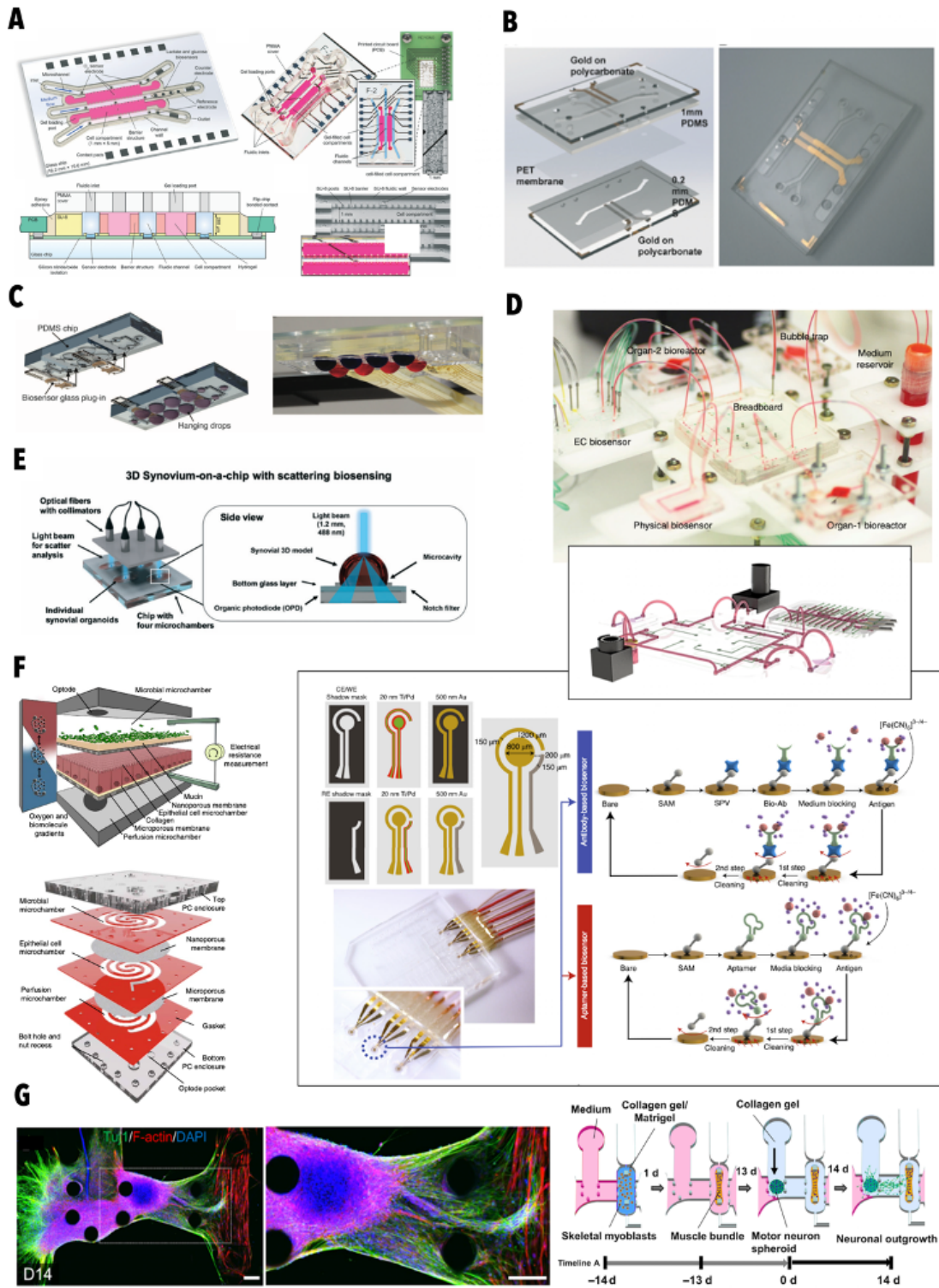


Figure 9: Representative examples of sensor integrated OoC platforms. Multi-electrochemical sensor integrated OoC platform for monitoring oxygen, lactate, and glucose of embedded tumor organoids.¹⁴³ (A) Example of a TEER-integrated OoC device¹⁵⁵ (B). Biosensor interface for real-time monitoring of 3D microtissue spheroids in microfluidic hanging-drop networks¹⁴⁴ (C). Measurement set-up for light-scattering measurements on-chip¹⁴² (E). Regeneratable breadboard set-up for in-line measurement of various biomarkers.¹⁴⁵ (D). HuMiX-platform for emulating the human-microbe interface on-chip¹¹⁴ (F). OoC platform for optical assessment of muscle contraction based on pillar deflection¹⁴⁶ (G). All images are published with copyright permission from the respective journals.

Fluorescent lifetime describes the time that passes between the excitation of the fluorescent indicator dye via an external light source and the subsequent emission of a photon. While intensity-based measurements are prone to errors associated with inhomogeneous illumination and bleaching, lifetime-based measurements provide a reliable alternative. In both cases, the interaction of an analyte of interest with the fluorescent indicator dye can modulate the resulting signal, either through amplification or quenching.¹²⁸ Due to their ease of integration, several OoC studies have employed luminescent-based sensors to monitor and control oxygen levels within microfluidic platforms.^{147–150} *Matsumoto et al.*, for example, utilized the cell's respiratory activity to generate a defined oxygen gradient on-chip by modulating media perfusion rates and monitoring via oxygen imaging.¹⁴⁸ As oxygen is a critical regulator in liver zonation; the authors could emulate both perivenous and periportal phenotypes in their OoC device. Absorption-based sensors make use of a shift in the absorption spectrum upon the interaction of an indicator dye with an analyte of interest. However, the small light paths within microfluidic devices restrict their applicability in OoC platforms. In addition to the abovementioned optical sensing strategies, a few studies in OoC have made use of the device's optical accessibility to monitor the functional parameter of myoblasts: cell contractibility by employing conventional microscopy.^{146,151,152} While this approach does not in itself constitute a sensor, it was included in Table 3, as it provides valuable information on the tissue's functionality in a label-free and non-invasive manner. *Osaki et al.*, for instance, employed this strategy in their intricate study on amyotrophy lateral sclerosis (ALS).¹⁴⁶ Using this method, the authors demonstrated pathological phenotypes of ALS, including impaired muscle function, which could be rescued after the co-administration of rapamycin and bosutinib in their neuromuscular junction on-a-chip platform.

1.4.4 Multiple-Sensor Integrated OoC Platforms

Over the last years, efforts have been made to combine multiple sensing strategies into single OoC platforms to enhance statistical power and provide comprehensive data. While most of these studies merely provide proof of principles, these attempts, nonetheless, have demonstrated a clear added value created by integrating complementary sensing strategies. For example, *Shah et al.* combined an optical oxygen sensor with TEER measurements to monitor barrier integrity and control oxygen availability in a model of the gastrointestinal human–microbe interface.¹¹⁴ *Qian et al.* provided a proof-of-principle study showing the beneficial aspects of incorporating MEAs with IDE to record the two critical functionalities of iPSC-derived cardiomyocytes on-chip, electrophysiological activity and cell contraction.¹⁵³ *Dornhof et al.* presented a multi-electrochemical sensor integrated polymethyl methacrylate- (PMMA-) platform capable of non-invasively monitoring the three analytes, oxygen, lactate, and glucose, on-chip.¹⁴³ When culturing patient-derived tumor microtissues generated from triple-negative breast cancer stem cells in hydrogels within the platform, the authors were able to quantitatively assess metabolite consumption and production rates and record responses to the anti-cancer drug doxorubicin. Despite the restricted stability of enzyme-based sensors, *Dornhof et al.* demonstrated sensor functionalities for more than one week.¹⁴³ To circumvent the issue of limited sensor stability, the group of Ali Khademhosseini developed an alternative, in-line microfluidic electrochemical biosensing approach, which provides built-in on-chip regeneration capability for continual measurement of cell-secreted soluble biomarkers in a fully automated manner.^{145,154–157} Using this approach, the group was able to detect a range of biomarkers, including albumin, glutathione transferase alpha (GST- α), and creatine kinase MB (CK-MB), by functionalizing the electrodes with aptamers or antibodies, respectively. A minimum of 25 regeneration cycles were reported by *Shin et al.*, underlining the sensing strategy's applicability for medium to long-term experiments.¹⁴⁵

Overall, sensor integrated OoC platforms provide a powerful strategy to address the issue of low analytical accessibility. It must be noted, however, that this part of OoC technology is still in its infancy, with more than 50% of all studies merely providing proof of principles that lack any follow-up studies or practical applications. In addition, many studies focus on developing novel sensing strategies instead of reusing available protocols or commercially available sensors. While every sensing strategy has intrinsic limitations and can be continuously optimized, it must be considered that any further information on the on-chip model's state already provides added value. Studies such as the work published by Khademhosseini's group, for example, offer an essential groundwork for establishing this goal, as by exchanging the recognition elements, the in-line platform can be readily adapted to a broad range of analytes. In summary, to address the limitation of low analytical accessibility that goes hand in hand with models of increased complexity, the next steps in OoC technology will need to focus on the development of multi-sensor integrated platforms. These steps include (i) the combination of orthogonal sensing strategies and (ii) the utilization of previously published off/on-chip protocols.

Table 3: Comprehensive overview of sensor integrated OoC platforms.

Sensing Strategy	Tissue Type and Dimensionality	Analyte/Parameter	Read-out	Application	Note	Ref.	
Electrical Sensor	Impedance Tomography	Human bronchial barrier - Bronchial cell line (16HBE14o) - Two-dimensional (2D)	Cell growth and membrane deflection	Real-time On-chip	Applicability assessment of microimpedance tomography for monitoring membrane deflection and cell growth	- Proof-of-principle	158
	TEER	Human skin barrier - Primary foreskin-derived dermal fibroblasts (HDF) - Primary epidermal keratinocytes (HEK) - 3D	Barrier integrity	Real-time On-chip	Assessment of barrier integrity	- Proof-of-principle - Impaired visualization but improved sensitivity distribution - Electrode wire	130
	TEER	Human skin barrier - Immortalized keratinocyte cell line (HaCaT) - Leukemic monocyte lymphoma cell line (U937) - 2D	Barrier integrity	Real-time On-chip	Assessment of barrier integrity upon chemical and physical stimulation	- Proof-of-principle - Integration of dendritic cells - Electrode wire	159
	TEER	Human BBB - iPSC derived blood endothelial cells, astrocytes, and neurons - 3D	Barrier integrity	Real-time On-chip	Assessment of barrier integrity	- Emulation of physiologically relevant TEER values for up to 5 days.	160
	TEER	Human and canine glomerular filtration barrier - Primary renal mixed epithelial cells (HREC) - Renal epithelial cell line (MDCK) - 2D	Barrier integrity	Real-time On-chip	Assessment of barrier integrity prior and after the initiation of a Ca ²⁺ switch	- Proof-of-principle - Electrode wire	161

TEER	Human colon tissue - Epithelial cell line (CaCo-2) - 2D	Barrier integrity	Real-time On-chip	Validation of a mathematical model to account for geometric differences in Transwell systems and microfluidic devices	- Proof-of-principle	131
TEER	Human blood-retinal-barrier - Retinal pigment epithelial cell line (ARPE-19) - Primary endothelial cells (HREC) - Neural cell line (SH- SY5Y) - 2D-3D	Barrier integrity	Real-time On-chip	Assessment of barrier integrity	- Proof-of-principle - Parallel multi-chamber set-up employing electrodes embedded on one common substrate	133
TEER	Human lung/gut barrier - Epithelial cell line (CaCo-2) - Primary airway epithelial cells - 3D	Barrier integrity	Real-time On-chip	Assessment of impedance spectroscopy for monitoring TEER	- Proof-of-principle - Changes in impedance spectra allow for the monitoring of tissue differentiation (villi formation)	132,162
TEER	Human corneal barrier - Corneal epithelial cell line (HCE-T) - Corneal keratocyte cell line (HCK) - 3D	Barrier integrity	Real-time On-chip	Assessment of barrier integrity	- Proof-of-principle - Dynamic cultivation conditions improve <i>in vivo</i> comparability	163,164
ECIS	Human placental barrier - Trophoblast cell line (BeWo) - 2D	Barrier integrity	Real-time On-chip	Comparison of TEER and ECIS. Assessment of barrier integrity upon exposure to nanoparticles (ZnO ₂ and SiO ₂)	- Proof-of-principle - Membrane-based electrodes	136
ECIS	Human lung cancer tissue - Epithelial cell lines (A549, H1299, H460) - 3D Multi organ set-up (murine/human): - Liver epithelial cell line (HepG2) - Cardiac muscle cell line (HL-1) - Lung epithelial cell line (A549)	Cell index	Real-time On-chip	Drug screening	- Proof-of-principle	134

		- 3D					
	MEA	Murine pancreatic islets - Isolated from adult male C57BL/6 mice (15–20 weeks old) - 3D	Islet ion flux	Real-time On-chip	Assessment of islet activity after stimulation with glucose	- Proof-of-principle	138
Electro-chemical Sensors	Amperometry	Murine muscle tissue - Skeletal myoblast cell line (C2C12) - 3D	Cytokine release: IL-6, TNF- α	In-line	Cytokine release upon electrical and biological stimulation	- Proof-of-principle	141
	Amperometry	Human vasculature - Primary endothelial cells (HUVECs) - 2D	Circumferential strain	Real-time On-chip	Assessment of biochemical signals released upon vascular mechanotransduction (NO)	- Proof-of-principle	140
Optical Sensors	Light-scattering	Human synovial tissue - Fibroblast like synoviocytes - 3D	Tissue remodeling	Real-time Off-chip	Identification of pathological alterations in extracellular matrix (ECM) remodeling in rheumatoid arthritis	- Proof-of-principle	142
	Luminescence	Human breast cancer tissue - Breast cancer cell line (MCF-7) - 2D	Oxygen	Real-time On-chip	Establishment of a hypoxic tumor microenvironment	- Use of laser-capture microdissection for region-specific analysis	147
	Luminescence	Rat liver tissue - Primary hepatocytes (isolated from an 8-weeks-old male Wistar rat) - 2D	Oxygen	Real-time On-chip	Establishment of a cell-mediated oxygen gradient results in partial liver-like zonation	- Oxygen imaging	148
	Luminescence	Murine BBB - Immortalized brain endothelial cell line (cerebEND) - 2D	Oxygen	Real-time On-chip	Modulation of oxygen in microfluidic devices and establishment of an ischemic stroke model	- Focus on oxygen scavenging properties of microfluidic device	149

	Luminescence	Human liver tissue - Bipotent progenitor cell line (HepaRG) - Peripheral blood mononuclear cells (PBMCs) - Primary endothelial cells (HUVECs) - 3D	Oxygen	Real-time On-chip	Monitoring of OCR in static and dynamic cultivation set-ups	- Enhanced differentiation of liver tissue under dynamic culture conditions.	150
Other Sensing Strategies in OoC	Microscopy	Murine and human neuromuscular junction - Embryonic muscle stem cell line HBG3 (Hb9-GFP) - Myoblast cell line (C2C12) - 3D	Contractile force (micropillar deflection)	Real-time Off-chip	Development of a microfluidic model for studying amyotrophic lateral sclerosis	- Development of optically excitable motor units	146,151
	Microscopy	Human muscle tissue - iPSCs - 3D	Contractile force (micropillar deflection)	Real-time Off-chip	Assessing the effect that cellular maturation has on drug responsiveness	- In-depth study	165,166
	Microscopy	Human muscle tissue - Pluripotent stem cell line (BJ1D)	Contractile force (micropillar deflection)	Real-time Off-chip	Development of a microfluidic perusable multi-well plate design for various applications	- Proof-of-principle	167
	Capillary-based pressure sensor	Human vasculature - Primary endothelial cells (HUVECs) - 2D	Pressure	Real-time On-chip	Development and characterization of a pressure sensor integrated microfluidic circulatory system	- Proof-of-principle - Emulation of physiological blood pressure	168
	Electrical and optical sensor	Human liver, cardiac, muscle and neuronal tissue - Primary hepatocytes / hepatocellular carcinoma cell line (HepG2/C3A) - iPSC-derived cortical neurons - iPSC-derived cardiomyocytes - Skeletal muscle progenitor cells - Primary motoneurons - 2D/3D	Contractile force (cantilever deflection) and electrical conductivity (MEA)	Real-time On-chip	Pharmacokinetics	- Multi-OoC set-up	169-171
		Human gut tissue - Epithelial colorectal cell line (Caco-2)	Oxygen (luminescent), barrier integrity (TEER),	Real-time On-chip	Development of a microfluidic model for studying the gastrointestinal microbe interface	- 24 h co-cultivation of human intestinal epithelial	114

Combined Sensing Approaches

Electrochemical and optical sensor	- 3D				cells with two commensal bacteria	
Electrochemical and optical sensor	Human liver tissue - Hepatocellular carcinoma cell line (HepG2/C3A) - Primary hepatocytes - 3D	Oxygen (phosphorescence), lactate and glucose (amperometry)	Real-time Oxygen (on-chip) Glucose and lactate (off-chip)	Assessment of the mitotoxic effects elicited by the pesticide rotenone and the anti-inflammatory drug troglitazone and assessment of drug induced steatosis	- PDMS and PMMA-based microwell bioreactor set-up	172-174
Electrical and optical sensor	Human liver, kidney and lung cancer tissue - Hepatocellular carcinoma cell line (HepG2) - Lung adenocarcinoma cell line (NCI-H1437) - Immortalized proximal tubule epithelial cell line (HK-2) - 2D	Monolayer integrity and metabolic activity	Real-time TEER In-line pH	Identification of drug-mediated cytotoxic effects	- Proof-of-concepts - Assessment of dynamic cultivation condition on cell growth and differentiation	175-177
Electrochemical sensors	Human breast cancer tissue - Breast cancer stem cell line 1 (BCSC1 eGFP) - 3D	Oxygen, glucose, and lactate (amperometry)	Real-time On-chip	Identification of drug-mediated cytotoxic effects	- Computer numerical control (CNC)-milled PMMA chip	143
Electrochemical sensors	Human colon tissue - Colon carcinoma cell line HCT116 eGFP - 3D	Glucose and lactate (amperometry)	Real-time On-chip	Development and characterization of a sensing interface for a microfluidic hanging drop culture set-up	- Proof-of-principle	144
Electrochemical sensors and optical sensors	Human liver, cardiac and lung tissue - Primary hepatocytes - iPSC derived cardiomyocytes - Hepatocellular carcinoma cell line (HepG2/C3A) - Lung microvascular cells (HMVEC-L) - Primary airway stromal mesenchymal cells - Bronchial epithelial cells	Oxygen (luminescence), pH (absorption), albumin, GST- α , CK-MB, transferrin (EIS)	In-line Off-chip	Identification of drug-mediated cytotoxic effects	- Includes protocol for sensor regeneration	145,154-157

	- 3D					
Electrical sensor and optical sensor	Human gut and kidney tissue - Primary colon epithelial cells - Primary proximal tubule epithelial cells (hRPTEC) - 2D	Barrier integrity (TEER), oxygen (luminescence)	Real-time On-chip	Development of a sensor integrated high-throughput microfluidic platform for drug-screening purposes	- Proof-of-principle - Various cell types and assays tested on platform	178
Electrical sensors	Human heart tissue - Primary endothelial cells (HUVECs) - iPSC derived cardiomyocytes - 3D	Barrier integrity (TEER), electrophysiological activity (MEA)	Real-time On-chip	Integration of a dual sensing approach in previously established OoC platform	- Proof-of-principle	179
Electrical sensors	Human heart tissue - iPSC derived cardiomyocytes - 2D	Electrophysiological activity (MEA), cell morphology and growth (ECIS)	Real-time On-chip	Assessment of tissue functionality	- Proof-of-principle	180

2. AIMS, RESULTS, AND CONCLUSION

2.1 AIMS OF THE THESIS

Organoid technology encompasses strategies and techniques that focus on the emulation of intricate organotypic characteristics *ex vivo*; as such, it has become an imperative tool in *in vitro* modeling. This scientific advancement has been of particular importance in the context of PD, a disorder that, due to a persistent lack of neuroprotective and disease-modifying treatment strategies, to this date, remains restricted to symptomatic control. Despite the significant progress that has been made in modeling PD employing midbrain organoids over the last years, a few fundamental limitations have restrained the technology from reaching its full potential. These drawbacks include (i) the omittance of biophysical cues such as interstitial fluid flow, an essential player in tissue homeostasis, (ii) nutrient-deficiency-based growth restrictions resulting from the organoids' intrinsic structure and the concomitant lack of vasculature, as well as (iii) low analytical accessibility restricting time-resolved monitoring. To address these limitations, the primary focus of this dissertation has been directed toward developing a multi-sensor integrated OoC platform for the long-term cultivation and non-invasive monitoring of hMOs. The key aspects of the dissertation include 1) the design, development, and fabrication of a microfluidic platform for the dynamic cultivation of midbrain organoids, 2) the development and characterization of non-invasive sensing strategies for monitoring essential cellular parameters including oxygen consumption, metabolic activity, DA release, and electrophysiological activity and 3) the study of interstitial fluid flow-mediated effects on hMO differentiation, PD phenotypes as well as therapeutic outcomes.

The dissertation is of cumulative origin. It consists of four first-author publications, thereof three original research articles and one preprint.

2.2 OVERVIEW OF RESEARCH ARTICLES

2.2.1 MANUSCRIPT #1

Title: Every Breath You Take: Non-invasive Real-Time Oxygen Biosensing in Two- and Three-Dimensional Microfluidic Cell Models.

Authors: Helene Zirath*, Mario Rothbauer*, Sarah Spitz*, Barbara Bachmann*, Christian Jordan, Bernhard Müller, Josef Ehgartner, Eleni Priglinger, Severin Mühleder, Heinz Redl, Wolfgang Holnthoner, Michael Harasek, Torsten Mayr and Peter Ertl.

**...These authors contributed equally to the work.*

Published: Front. Physiol. 9:815. doi: 10.3389/fphys.2018.00815

Summary: The oxygen tension a cell is exposed to *in vivo* strongly varies based on the cell's respective residential tissue. Control of this crucial physiological parameter *in vitro* requires precise information on the dissolved oxygen levels individual cell populations sense. While several oxygen sensing strategies have been reported for conventional *in vitro* cell culture set-ups, little is known about spatio-temporal variations of dissolved oxygen concentrations in microfluidic devices. To better understand the distribution of oxygen levels within these platforms, two oxygen sensor integrated microfluidic chips have been designed and were subsequently employed to investigate (I) oxygen consumption rates in 2D and 3D cell cultures set-ups, (II) the establishment of oxygen gradients along microfluidic culture chambers and (III) the influence of microfabrication materials (e.g., gas-tight vs. gas permeable), surface coatings, cell densities, and medium flow rates on the respiratory activities of four different cell types. Furthermore, the study shows how cyclic alternating normoxic-hypoxic microenvironments can be accomplished using programmable flow profiles.

Author Contribution:

Helene Zirath, Mario Rothbauer, Sarah Spitz, Barbara Bachmann, and Peter Ertl conceived the study and designed the experimental outline. Helene Zirath, Sarah Spitz, Barbara Bachmann, and Mario Rothbauer performed the microfluidic experiments, analyzed the data, and wrote the manuscript. Christian Jordan and Michael Harasek performed and analyzed the computational fluid dynamics (CFD) simulations. Bernhard Müller, Josef Ehrgartner and Torsten Müller manufactured the optical oxygen sensors. Eleni Priglinger, Severin Mühleder, Wolfgang Holnthoner, and Heinz Redl isolated and transfected the primary cells used within the study and provided knowledge on the development of the 3D vasculature model. All authors approved the final manuscript.

2.2.2 MANUSCRIPT #2

Title: Bridging the academic-industrial gap: Application of an oxygen and pH sensor integrated lab-on-a-chip in nanotoxicology.

Authors: Helene Zirath*, Sarah Spitz*, Doris Roth, Tobias Schellhorn, Mario Rothbauer, Bernhard Müller, Manuel Walch, Jatinder Kaur, Alexander Wörle, Yvonne Kohl, Torsten Mayr and Peter Ertl.

**...These authors contributed equally to the work.*

Published: Lab Chip, 2021, 21, 4237. doi: 10.1039/d1lc00528f

Summary: The ability to provide dynamic microenvironments, the use of small reagent volumes, and thus lowered experimental costs, coupled with a high degree of scalability, has rendered microfluidics a powerful asset in the field of nanotoxicology. However, a broader application of advanced microfluidic-based assays is greatly limited by the lack of industry-relevant prototypes. A dual-sensor integrated microfluidic platform using industrial specifications, materials, and fabrication methods was developed to address this academic-

industrial gap. Non-invasive and time-resolved monitoring of cellular oxygen uptake and metabolic activity (pH) in the absence and presence of nanoparticles was accomplished by integrating optical sensor spots into a cyclic olefin copolymer (COC)-based microfluidic platform. To assess the platform's applicability in the context of nanotoxicological screening, representative cells of two physiological barriers, essential in the protection from exogenous factors, the intestine (CaCo-2) and the vascular network (HUVECs), were integrated into the microfluidic platform for subsequent analysis under dynamic conditions. The results of the nanotoxicological study were contrasted using state-of-the-art dye exclusion assays, demonstrating a high degree of comparability. Overall, the study highlights the benefits of employing a compact and cost-efficient microfluidic dual-sensor platform as a pre-screening tool in nanomaterial risk assessment and as a rapid quality control measure in medium to high-throughput settings.

Author Contribution: Sarah Spitz, Helene Zirath, and Peter Ertl conceived the project, designed the experimental outline, and wrote the manuscript. Sarah Spitz, Helene Zirath, Tobias Schellhorn, and Mario Rothbauer performed the microfluidic experiments and analyzed the data. Sarah Spitz and Doris Roth performed the CFD simulations. Bernhard Müller and Torsten Mayr manufactured the optical oxygen and pH sensors. Jatinder Kaur, Alexander Wörle, and Manuel Walch fabricated and characterized the microfluidic device. Yvonne Kohl provided the A549 and the Caco-2 cell line and shared her expertise in cell culture. All authors contributed to and revised the final manuscript.

2.2.3 MANUSCRIPT #3

Title: Monitoring the neurotransmitter release of human midbrain organoids using a redox cycling microsensor as a novel tool for personalized Parkinson's disease modeling and drug screening.

Authors: Cristian Zanetti*, Sarah Spitz*, Emanuel Berger, Silvia Bolognin, Lisa M. Smits, Philipp Crepaz, Mario Rothbauer, Julie M. Rosser, Martina Marchetti-Deschmann, Jens C. Schwamborn and Peter Ertl.

**...These authors contributed equally to the work.*

Published: Analyst, 2021, 146, 2358. doi: 10.1039/d0an02206c.

Summary: With its ability to generate organotypic structures *in vitro*, iPSC technology has provided the basis for developing advanced patient-derived disease models. These include models of the human midbrain, the affected region in the neurodegenerative disorder Parkinson's disease. However, the analysis of so-called hMOs has relied on time-consuming and invasive strategies, incapable of monitoring organoid development. This study developed a novel electrochemical sensing approach capable of detecting DA, the primary biomarker in Parkinson's disease, within the highly complex cell culture matrix of hMOs. Using a non-invasive and label-free redox-cycling approach combined with a 3-mercaptopropionic acid self-assembled monolayer modification increased sensor selectivity and DA sensitivity while simultaneously reducing matrix-mediated interferences. The work demonstrates the ability to detect and monitor even slight differences in DA release between healthy and Parkinson's disease-specific hMOs over prolonged cultivation periods, which was additionally verified using liquid chromatography–multiple reaction monitoring mass spectrometry. Furthermore, the detection of a phenotypic rescue in hMOs carrying a pathogenic mutation in LRRK2 upon treatment with the LRRK2 inhibitor II underlines the applicability of the presented sensing approach for drug screening purposes.

Author Contribution: Sarah Spitz, Cristian Zanetti, Silvia Bolognin, Jens Schwamborn, and Peter Ertl designed and conceptualized the study with input from Julie Rosser and Mario Rothbauer. Sarah Spitz, Cristian Zanetti, and Peter Ertl wrote the manuscript. Sarah Spitz and Cristian Zanetti conducted the experiments and performed data analysis. Silvia Bolognin,

Emanuel Berger, and Lisa Smits provided the hMOs and performed immunohistochemical analyses. Philipp Crepaz and Martina Marchetti-Deschmann conducted high performance liquid chromatography (HPLC) multiple reaction monitoring-mass spectrometry (MRM-MS) measurements and performed data analysis. All authors have approved the final version of the manuscript.

2.2.4 MANUSCRIPT #4

Title: Development of a multi-sensor integrated midbrain organoid-on-a-chip platform for studying Parkinson's disease.

Authors: Sarah Spitz, Silvia Bolognin, Konstanze Brandauer, Julia Füßl, Patrick Schuller, Silvia Schobesberger, Christian Jordan, Barbara Schädl, Johannes Grillari, Heinz Wanzenböck, Torsten Mayr, Michael Harasek, Jens C. Schwamborn, Peter Ertl

Published: *Submitted to bioRxiv*

Summary: By emulating intricate cytoarchitectural features and physiological functions of the human midbrain, the afflicted region in Parkinson's disease, midbrain organoids have shown to provide a powerful alternative to conventional disease models, which remain unable to reflect the disease's complex pathology adequately. However, the technology's full potential is still hampered by a handful of key limitations, including tissue immaturity, insufficient nutrient supply, and low analytical accessibility. Employing a novel multi-sensor integrated OoC platform, a marked reduction in necrotic core formation, enhanced tissue differentiation, and the recapitulation of the main pathological hallmarks of PD were demonstrated. Non-invasive monitoring using a combination of optical, electrical, and electrochemical sensors revealed Parkinson's disease-associated phenotypes. Furthermore, drug-mediated rescue effects were observed after treatment with a repurposed compound, highlighting the platform's potential in the context of drug screening applications as well as personalized medicine.

Author Contribution: Sarah Spitz, Peter Ertl, Silvia Bolognin, and Jens C. Schwamborn conceived and designed the study. Sarah Spitz and Konstanze Brandauer conducted microfluidic experiments. Sarah Spitz, Julia Füßl, and Silvia Schobesberger performed DA measurements. Sarah Spitz, Patrick Schuller, Heinz Wanzenböck performed electrophysiological studies and provided expertise on microfabrication. Torsten Mayr provided expertise in oxygen sensing. Sarah Spitz, Silvia Bolognin, Barbara Schädler, and Johannes Grillari performed immunohistochemical analysis. Christian Jordan and Michael Harasek performed CFD simulations. Sarah Spitz and Silvia Bolognin conducted data analysis. All authors revised and approved the final manuscript.

2.3 SCIENTIFIC CONTRIBUTION OF THE DISSERTATION, CONCLUSION, AND OUTLOOK

This doctoral thesis set out to develop a multi-sensor integrated microfluidic platform for the long-term cultivation and monitoring of hMOs to a) increase the analytical accessibility of OoC platforms and b) establish an advanced PD model based on the combination of microfluidic technology with midbrain organoid technology. Analytical accessibility not only constitutes a key limitation in any *in vitro* 3D biological system such as organoids but is still considered an untapped potential within OoC technology. Consequently, specific focus of this doctoral thesis has been directed toward expanding the sensing portfolio of OoC technology.

As changes in dissolved oxygen levels (DO) can provide valuable information about key parameters - common among any tissue type - such as cellular viability, tissue growth and maturation, pathophysiological alterations, as well as toxicological effects, DO constitutes an ideal candidate for non-invasive monitoring in OoC platforms. To that end, **MANUSCRIPT #1**, titled: *“Every Breath You Take: Non-invasive Real-Time Oxygen Biosensing in Two- and Three-Dimensional Microfluidic Cell Models,”* set out to study the broad applicability of oxygen sensing within microfluidic platforms. Next to the development of an optimized protocol for determining respiratory activities on-chip, the applicability of oxygen monitoring in 3D hydrogel cultivation setups and gas permeable PDMS devices, a key requirement for on-chip monitoring, was demonstrated for the first time. Furthermore, alterations in respiratory activity were recorded as a function of surface coating, cell seeding density as well as cell type and origin, underlining the method’s sensitivity and versatility in the context of OoC technology. In **MANUSCRIPT #2**, entitled: *“Bridging the academic-industrial gap: Application of an oxygen and pH sensor integrated lab-on-a-chip in nanotoxicology.”*, the industrial applicability of luminescent sensor spots was tested, an essential prerequisite for

large-scale production and broad applicability of OoC platforms. Within this study, the oxygen sensing approach was expanded by a luminescent pH sensor in an industrially scalable platform. The method's usability was assessed by monitoring the effects of dynamic exposure scenarios on nanotoxicity. Using this non-invasive sensing approach, cellular viabilities could be calculated as quickly as 20 seconds into the on-chip assay while displaying a high degree of comparability to state-of-the-art live/dead assays. Overall, performance data demonstrated a 90-720 times faster analysis time over conventional techniques, highlighting the potential of sensor integrated microfluidic platforms for large-scale detection and monitoring of dynamic changes in cellular metabolism, a key indicator of cell health. To expand the sensing portfolio in OoC by a PD-specific sensing strategy, **MANUSCRIPT #3**: "*Monitoring the neurotransmitter release of human midbrain organoids using a redox cycling microsensor as a novel tool for personalized Parkinson's disease modeling and drug screening.*" focused on the establishment of a DA sensor, capable of monitoring the PD biomarker in the supernatant of hMOs. Using this approach, for the first time, phenotypical differences between healthy and PD patient-specific hMOs, carrying a mutation in LRRK2 could be observed and monitored over time using an electrochemical redox-cycling technique. In addition, rescue effects were observed in patient-specific hMOs, after treatment with the LRRK2 inhibitor II, highlighting the sensor's potential for drug screening purposes.

Finally, **MANUSCRIPT #4** titled: "*Development of a multi-sensor integrated midbrain organoid-on-a-chip platform for studying Parkinson's disease.*" builds upon the knowledge and protocols gained throughout **MANUSCRIPT #1-3** to demonstrate the advantages of OoC technology for PD research. The study set out to address the key limitations of midbrain organoid technology by developing a multi-sensor integrated OoC platform for the long-term cultivation and monitoring of healthy and PD patient-specific hMOs. Exposing midbrain microtissues to the biophysical stimuli interstitial fluid flow, a key regulator of tissue

homeostasis, not only markedly enhanced tissue differentiation as indicated by a 2.1-fold increase in TH/MAP2 signal as well as a 1.35-fold increase in GFAP-positive astrocytes but significantly improved insufficient nutrient supply, another essential limitation of organoid technology, resulting in a 2-fold reduction in the necrotic core size. Next to a significantly reduced number of dopaminergic neurons and astrocytes, dynamically cultivated patient-specific hMOs displayed Lewy-body-like inclusions, the second key hallmark of PD, highlighting the importance of biophysical cues in the emulation of (patho-) physiological tissue niches *in vitro*. To address the issue of analytical accessibility in organoid technology, an optical oxygen sensor, an electrical MEA, and an electrochemical DA sensor were integrated into the microfluidic platform. Next to the long-term stability of luminescent oxygen sensor spots, the study demonstrated the versatile applicability of oxygen sensing in PD modeling, encompassing the monitoring of tissue vitality, tissue differentiation, pathological phenotypes, as well as drug-mediated rescue effects after treatment with the repurposed excipient HP- β -CD. As the recording of electrophysiological activity within 3D tissues still constitutes a big challenge in the field of microelectronics, a novel measuring approach was explored as part of the study. By exposing mesencephalic microtissues to interstitial fluid flows, neuronal processes extending from the hMOs were directed onto a 2D planar MEA, positioned within the medium channels of the microfluidic platform. Using this approach, spontaneous electrophysiological activity and characteristic firing patterns of dopaminergic neurons could readily be recorded within the platform. To account for reduced levels of DA release within microfluidic platforms, an optimized tyrosinase-based DA sensor was developed and characterized for on-chip applications. Using this approach, significant differences between statically and dynamically cultivated hMOs were verified, and for the first time in an OoC model, a time-dependent onset of a pathological hallmark was recorded in patient-specific hMOs. Overall, the combination of optical, electrical, and electrochemical sensing strategies

into the microfluidic platform allowed for (i) the non-invasive monitoring of hMOs, (ii) the identification of phenotypical differences between healthy and patient-specific hMOs, and (iii) the discovery of drug-mediated rescue effects, highlighting the clear added value gained by sensor integration.

To conclude, as described in Chapter 1.1.2, next to a progressive onset of pathophysiological phenotypes, an ideal experimental PD model should exhibit the two key pathological hallmarks (i) the neurodegeneration of dopaminergic neurons and (ii) Lewy body formation. Unfortunately, a large proportion of current experimental models do not meet these requirements, which is reflected by the high failure rates in clinical trials and the persistent lack of neuroprotective and disease-altering treatment strategies. Patient-specific midbrain organoids have become a promising alternative as they can emulate essential features of the degenerative disorder *in vitro* while accounting for the disease's highly heterogeneous nature. However, the following limitations (a) insufficient nutrient supply, (b) lack of biophysical stimuli, (c) low analytical accessibility, and (d) lack of specific cell types such as endothelial cells - the building block of the blood-brain barrier - have restricted the technology from reaching its full potential. The combination of midbrain organoid technology with OoC technology, conducted as part of this dissertation, resulted in an *in vitro* platform (Manuscript #4) that fulfills the aforementioned critical requirements of an ideal experimental PD model while simultaneously addressing key limitations of hMOs. As such, the platform has the potential to provide a valuable tool in PD research. However, it must be noted that due to the lack of the BBB, the presented platform is restricted to the screening of drugs that are known for their ability to penetrate the BBB, such as HP- β -CD. To address this limitation, first attempts have been made to connect hMOs with bioengineered networks of the blood-brain barrier, employing bioengineering principles (data not shown).

Overall, five different sensing strategies, encompassing optical, electrical, and electrochemical sensors, have been validated and optimized throughout this dissertation. All presented sensing strategies can easily be integrated into or combined with existing OoC platforms, increasing the models' predictive values. In addition, two of the presented sensors (optical oxygen and pH sensor) were shown to adhere to industrial manufacturability standards, highlighting their potential for large-scale production. Throughout the dissertation, two DA sensors were developed and validated for the monitoring of the catecholamine in the highly complex cell culture matrix of midbrain organoids. While the redox-cycling-based DA-sensor provides long-term stabilities validated up to 20 months after the initial point of fabrication, rendering it ideal for long-term monitoring studies, the carbon-electrode-based DA-sensor produces significantly improved LODs in cell culture media, highlighting its applicability for chip-based screening purposes. Lastly, an alternative approach for measuring electrophysiological activity has been presented. While this sensing strategy does not allow for the measurement of neuronal firing in the center of the 3D construct, it enables a non-invasive readout that provides information on spontaneous activity and tissue differentiation and that further can easily be integrated into any existing platform.

In conclusion, this doctoral thesis has provided an in-depth assessment and characterization of various non-invasive optical, electrical, and electrochemical sensing strategies that can readily be integrated into existing OoC platforms and thus have the potential to expand the sensing portfolio of OoC technology. Furthermore, the dissertation put forth a multi-sensor integrated microfluidic platform for the optimized long-term cultivation and monitoring of hMOs *in vitro* that provides an ideal basis for patient-specific PD modeling and drug screening. To address all listed limitations of midbrain organoid technology and to provide a real alternative to current *in vivo* approaches, future studies will specifically focus on the extension of the OoC model by a three-dimensional network of the human BBB.

3. ORIGINAL RESEARCH ARTICLES

3.1 MANUSCRIPT #1 – ARTICLE

EVERY BREATH YOU TAKE: NON-INVASIVE REAL-TIME OXYGEN BIOSENSING IN TWO- AND THREE-DIMENSIONAL MICROFLUIDIC CELL MODELS



Every Breath You Take: Non-invasive Real-Time Oxygen Biosensing in Two- and Three-Dimensional Microfluidic Cell Models

Helene Zirath^{1,2*†}, Mario Rothbauer^{1,2*†}, Sarah Spitz^{1,2†}, Barbara Bachmann^{1,2,3†}, Christian Jordan¹, Bernhard Müller⁴, Josef Ehgartner⁴, Eleni Priglinger^{2,3}, Severin Mühleder^{2,3}, Heinz Redl^{2,3}, Wolfgang Holthoner^{2,3}, Michael Harasek¹, Torsten Mayr⁴ and Peter Ertl^{1,2}

¹ Institute of Applied Synthetic Chemistry, Institute of Chemical Technologies and Analytics, Institute of Chemical, Environmental and Bioscience Engineering, Vienna University of Technology, Vienna, Austria, ² Austrian Cluster for Tissue Regeneration, Vienna, Austria, ³ Ludwig Boltzmann Institute for Experimental and Clinical Traumatology, Allgemeine Unfallversicherungsanstalt (AUVA) Research Centre, Vienna, Austria, ⁴ Institute of Analytical Chemistry and Food Chemistry, Graz University of Technology, NAWI Graz, Graz, Austria

OPEN ACCESS

Edited by:

Alberto Rainer,
Università Campus Bio-Medico, Italy

Reviewed by:

Christoffer Laustsen,
Aarhus University, Denmark
Giovann Vozzi,
Università degli Studi di Pisa, Italy

*Correspondence:

Helene Zirath
helene.zirath@tuwien.ac.at
Mario Rothbauer
mario.rothbauer@tuwien.ac.at

† These authors have contributed
equally to this work.

Specialty section:

This article was submitted to
Integrative Physiology,
a section of the journal
Frontiers in Physiology

Received: 12 April 2018

Accepted: 11 June 2018

Published: 03 July 2018

Citation:

Zirath H, Rothbauer M, Spitz S,
Bachmann B, Jordan C, Müller B,
Ehgartner J, Priglinger E, Mühleder S,
Redl H, Holthoner W, Harasek M,
Mayr T and Ertl P (2018) Every Breath
You Take: Non-invasive Real-Time
Oxygen Biosensing in Two-
and Three-Dimensional Microfluidic
Cell Models. *Front. Physiol.* 9:815.
doi: 10.3389/fphys.2018.00815

Knowledge on the availability of dissolved oxygen inside microfluidic cell culture systems is vital for recreating physiological-relevant microenvironments and for providing reliable and reproducible measurement conditions. It is important to highlight that *in vivo* cells experience a diverse range of oxygen tensions depending on the resident tissue type, which can also be recreated *in vitro* using specialized cell culture instruments that regulate external oxygen concentrations. While cell-culture conditions can be readily adjusted using state-of-the-art incubators, the control of physiological-relevant microenvironments within the microfluidic chip, however, requires the integration of oxygen sensors. Although several sensing approaches have been reported to monitor oxygen levels in the presence of cell monolayers, oxygen demands of microfluidic three-dimensional (3D)-cell cultures and spatio-temporal variations of oxygen concentrations inside two-dimensional (2D) and 3D cell culture systems are still largely unknown. To gain a better understanding on available oxygen levels inside organ-on-a-chip systems, we have therefore developed two different microfluidic devices containing embedded sensor arrays to monitor local oxygen levels to investigate (i) oxygen consumption rates of 2D and 3D hydrogel-based cell cultures, (ii) the establishment of oxygen gradients within cell culture chambers, and (iii) influence of microfluidic material (e.g., gas tight vs. gas permeable), surface coatings, cell densities, and medium flow rate on the respiratory activities of four different cell types. We demonstrate how dynamic control of cyclic normoxic-hypoxic cell microenvironments can be readily accomplished using programmable flow profiles employing both gas-impermeable and gas-permeable microfluidic biochips.

Keywords: microfluidics, 3D culture, biosensor, oxygen, oxygen gradient, organ-on-a-chip, lab-on-a-chip, hydrogel

INTRODUCTION

With the emergence of advanced cell-based *in vitro* models, which resemble the architecture and physiology of actual native tissue, the ability to control and manipulate cellular microenvironment has become an important aspect in microfluidic cell culture systems. Spatio-temporal control over the cellular microenvironment includes (i) physical forces such as shear stress, (ii) biological cues such as direct and indirect cell–cell interactions, and (iii) chemical signals such as pH, oxygenation, and nutrient supply. Among biochemical signals, oxygen plays a key role in regulating mammalian cell functions in human health and disease. It is also important to note that oxygen concentration varies tremendously throughout the human body ranging from 14% in lungs and vasculature down to 0.5% in less irrigated organs such as cartilage and bone marrow (Jagannathan et al., 2016). Despite the different demand of oxygen in different tissues, routine cell culture is predominantly conducted under atmospheric oxygen tension of 21%. This elevated levels of oxygen exposure of cells is referred to as hyperoxia and can lead to altered cell behavior (Gille and Joenje, 1992). For instance, studies have shown that physiologic oxygen tension modulates stem cell differentiation (Mohyeldin et al., 2010), neurogenesis (Zhang et al., 2011), and is involved in a number of cellular mechanisms needed to maintain tissue function (Pugh and Ratcliffe, 2003; Volkmer et al., 2008). In turn, prolonged oxygen deprivation in a hypoxic oxygen milieu can result in a variety of human pathologies including cancer (Pouysségur et al., 2006), tumor development (Harris, 2002), necrosis (Harrison et al., 2007), infection (Zinkernagel et al., 2007), and stroke (Hossmann, 2006). The importance of monitoring and control of oxygen levels in mammalian cell cultures has therefore led to the implementation of a wide variety of sensing strategies ranging from standard electrochemical electrodes (Nichols and Foster, 1994) and enzymatic sensors (Weltin et al., 2014) to fluorescent and luminescent optical biosensors (Wolfbeis Otto, 2015; Ehgartner et al., 2016b). Of these methods, optical detection based on oxygen-sensitive dyes that are embedded in a polymer matrix are ideally suited for the integration in lab-on-a-chip systems due to the facile integration of sensor spots in microfluidic channels, their long-term stability, reliability, and cost-effectiveness of the sensing probes (Wang and Wolfbeis, 2014; Lasave et al., 2015; Sun et al., 2015). Luminescent intensity as well as decay time of the phosphorescent indicator dye is affected by the amount of the surrounding molecular oxygen, thus providing information on the local oxygen concentration (Gruber et al., 2017). Especially porphyrin-based sensor dyes are well suited for oxygen monitoring in cell-based microfluidic devices due to their high sensitivity, biocompatibility, and reversible quenching behavior (Ungerbock et al., 2013; Ehgartner et al., 2014). Typically, time-resolved optical oxygen monitoring of microfluidic cell culture systems is performed using a measurement set-up consisting of the biochip, optical fibers, a read-out system, and a data acquisition device (Oomen et al., 2016; Gruber et al., 2017). As an example, a polydimethylsiloxane (PDMS) microfluidic chip with oxygen flow-through sensors at the inlet and outlet and an optical oxygen sensor in the cell

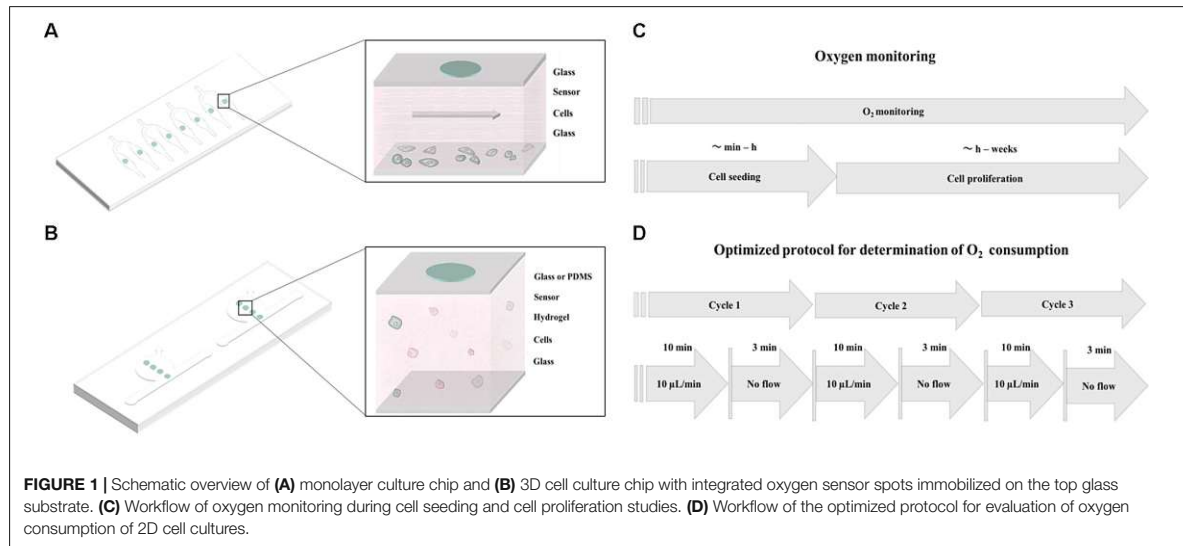
culture chamber has been realized for a real-time monitoring of respiratory rates of mouse embryonic stem cell cultures and for Chinese hamster ovary cells in monolayers for several days of culture (Super et al., 2016). Oxygen sensor spots were also integrated into microfluidic reaction chambers made of glass and silicon for monitoring of biocatalytic transformations (Ehgartner et al., 2016b). To create a more accessible read-out strategy for a broader research audience, a color CCD-camera mounted to a fluorescent microscope was used for 2D sensing of oxygen distribution inside microfluidic microchannels (Ungerbock et al., 2013). An additional multi-parametric analysis setup was established for simultaneous detection of oxygen and pH using core-shell nanoparticles incorporating oxygen- and pH-sensitive dyes (Ehgartner et al., 2016a). Despite these recent advances, little is still known on spatio-temporal variations of oxygen concentrations inside microfluidic 2D and 3D cell culture systems.

In this method paper, we investigate the influence of cell numbers, extra-cellular matrix (ECM) surface coatings, different cell types, as well as oxygen permeability of chip materials to determine the key microfluidic parameters needed to reliably monitor and precisely control oxygen levels during 2D and 3D cell cultivation. To gain deeper insight into oxygen supply to and demand of 2D and 3D cell cultures, we have developed two different microfluidic devices containing embedded sensor arrays as shown in **Figures 1A,B**. Material selection in particular influences gas exchange through the bulk chip material, which therefore directly influences the ability to control oxygen within the microfluidic environment. Initially, we have established two protocols for oxygen monitoring; **Figure 1C** shows the general methodology that can be used for oxygen monitoring of cell cultures during seeding, adhesion, and long-term cultivation. Additionally, another protocol, referred to hereafter as “optimized protocol,” is established for precise determination of oxygen consumption rates in 2D microfluidic cultures as shown in **Figure 1D**. Further, we have compared oxygen consumption of cells from epithelial, endothelial, and mesenchymal origin including cancer cells (A549 lung epithelial cells) and primary cells [e.g., normal human dermal fibroblasts (NHDF), adipose-derived stem cells (ASC), and human umbilical vein endothelial cells (HUVEC)]. The effect of a controlled oxygen gradient throughout fibrin hydrogels during vascular network formation over a 7-day culture period is demonstrated using a 3D vascular co-culture model based on HUVEC endothelial cells and ASC stem cells. A final practical application of the oxygen monitoring method involves the early identification of cell necrosis within hydrogel constructs, thus providing quality control information on 3D-cell-laden hydrogel and microtissue cultures.

RESULTS AND DISCUSSION

Non-invasive Oxygen Monitoring in 2D Microfluidic Cell Cultures

Prior to oxygen monitoring of 2D cell cultures, the influence of chip material permeability was evaluated based on the response



of the oxygen-sensitive microparticle-based sensors. Therefore, gaseous oxygen content within sealed microchannels was monitored for microfluidic chips fabricated either from oxygen-permeable PDMS or impermeable glass (see **Supplementary Figure S1**). Both devices were simultaneously exposed to an oxygen environment of 2.5% for 20 min before re-oxygenation. As shown in **Figure 2A**, no sensor response was observable for gas-impermeable glass chips with no detectable decrease in partial oxygen pressure. Microfluidic chips made of gas-permeable PDMS showed a decrease in partial oxygen pressure from 176.4 to 15.4 hPa with a t_{90} -value of 15 min and a delay in full recovery to atmospheric oxygen after 87 min. These results demonstrate the importance of material selection during microfluidic chip fabrication. Differences in demand and re-oxygenation linked to material permeability offer the opportunity to either inhibit or allow external oxygen supply to the cell cultures. In turn, sensor-to-sensor variation was evaluated using oxygen concentrations ranging from 20 to 0.5% via small gas feeding by a CO₂/O₂ controller equipped with zirconium-based oxygen sensor, which was connected to the inlet ports of the microfluidic chips. As shown in **Figure 2B**, sensor-to-sensor variation among the individual sensor spots was 221.2 ± 1.3 hPa for 20%, 122.4 ± 0.3 for 10%, 61.9 ± 0.2 hPa for 5%, and 0.2 ± 0.1 hPa for 0.5% oxygen, respectively. These results show excellent reproducibility despite the manual dispensing of the sensor spots into the microfluidic devices.

In the next set of experiments, the impact of cell density on oxygen consumption was evaluated during cell seeding and for fully attached cell cultures. A549 lung epithelial cells were seeded in gas-impermeable microfluidic chips at initial cell seeding densities ranging from 1×10^4 to 1×10^5 cells/cm². **Figure 3A** shows a partial oxygen pressure around 200 hPa right after seeding, which accurately represents ambient oxygen levels in cell culture media at 37°C. Difference in partial oxygen pressure for increasing cell numbers was observable already

10 min after cell seeding, thus pointing at higher oxygen demand in the presence of larger cell numbers. Interestingly, while similar oxygen depletion values were observed in the first 40 min, rapid increase in oxygen consumption was found already after 50 min for 1.0×10^5 cells/cm² (see **Supplementary Figure S2**), which can be linked to completed cell adhesion and start of exponential cell growth (Rehberg et al., 2013). Cell densities of 1×10^4 and 2.5×10^4 cells/cm² resulted in moderate total oxygen depletion values of 13.4 ± 6.7 hPa and 31.1 ± 1.5 hPa, respectively. A more pronounced oxygen depletion was found for the highest cell density of 1×10^5 cells/cm² of 153.8 ± 16.7 hPa. Results of this study show that in the presence of high cell densities oxygen depletion occurs 3 h after cell seeding when using gas-impermeable glass microfluidic chips. Next, an optimized protocol was established for precise measurements of oxygen consumption rates (see **Figure 1D** for details). To ensure oxygen consumption measurements, a flow rate of 10 µL/min over period of 10 min prior to the measurements was introduced to maintain oxygenated conditions of around 200 hPa. Flow rates below this threshold did not show full oxygenation (data not shown). For the actual determination of oxygen consumption rates, flow was halted and the decrease in oxygen partial pressure was immediately recorded for 3 min in all chambers. **Figure 3B** shows decreasing oxygen levels over a period of 3 min ($n = 3$) in the presence of increasing numbers of fully attached A549 lung cells after 4 h of post-seeding, indicating that sufficient re-oxygenation prior to measurement markedly improves data quality. Calculated total oxygen consumption rates of 0.8 hPa/min for 1×10^4 cells/cm², 2.6 hPa/min for 2.5×10^4 cells/cm², and 4.6 hPa/min for 1×10^5 cells/cm². Overall, integration of sensor spots above the cell monolayer culture are sensitive enough to estimate oxygen availability and cell population oxygen demands in microfluidic cell cultivation chambers.

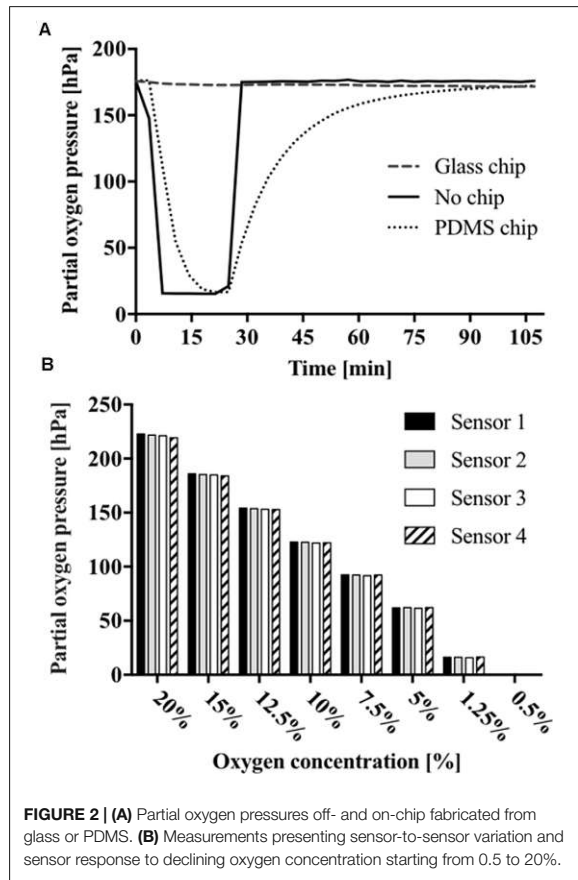


FIGURE 2 | (A) Partial oxygen pressures off- and on-chip fabricated from glass or PDMS. **(B)** Measurements presenting sensor-to-sensor variation and sensor response to declining oxygen concentration starting from 0.5 to 20%.

Impact of Cell Type on Oxygen Consumption Rates

Differences in oxygen consumption rates between well-established primary cell types (Manning et al., 2015; Haase and Kamm, 2017; Zhang et al., 2017) and cancer cell lines (Cooper et al., 2016) were investigated to further evaluate the presented non-invasive microfluidic oxygen monitoring method. Partial oxygen pressure was monitored during cell seeding for cells from epithelial (A549), endothelial (HUVEC), and mesenchymal origin (NHDF and ASC) at the same initial seeding density of 2.5×10^4 cells/cm² corresponding to 5.5×10^3 cells per microchannel. As shown in **Figure 4A** the different cell types can be readily distinguished by cell type-specific variations in oxygen depletion during adhesion to the surface of the microfluidic channels. NHDF fibroblast cells showed highest oxygen depletion values leveling off at a partial oxygen pressure of 17 hPa, which corresponds to a total oxygen consumption of 183 ± 0.4 hPa oxygen in 3 h during cell adhesion. The oxygen consumption for the other cell types were lower with 104.2 hPa ($n = 1$) for A549 lung cells, 28.4 ± 0.4 hPa for HUVEC endothelial cells, and 59.4 ± 15.4 hPa for ASC stem cells, respectively. Next, oxygen consumption rates were determined using the optimized

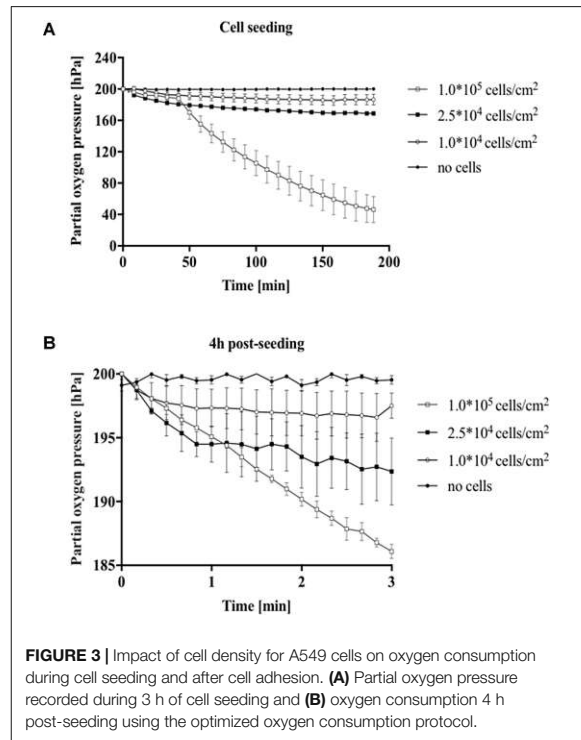


FIGURE 3 | Impact of cell density for A549 cells on oxygen consumption during cell seeding and after cell adhesion. (A) Partial oxygen pressure recorded during 3 h of cell seeding and **(B)** oxygen consumption 4 h post-seeding using the optimized oxygen consumption protocol.

protocol as shown in **Figure 4B**. Oxygen consumption varied heavily between the different cell types exhibiting low cellular respiratory activity of 3.7 ± 1.2 hPa (1.2 ± 0.4 hPa/min) for A549 lung cells and 6.8 ± 2.1 hPa (2.3 ± 0.7 hPa/min) for HUVEC, 13.9 ± 1.6 hPa (4.7 ± 0.5 hPa/min) for ASC, and highest rates observable of 35.4 ± 2.5 hPa (11.8 ± 0.8 hPa/min) for fibroblast cells. Overall, these results correspond well with literature values of the specific cell types demonstrating the good performance of the presented microfluidic oxygen sensing method (Heidemann et al., 1998; Powers et al., 2008; Abaci et al., 2010; Zhang et al., 2014). In addition, **Figure 4C** shows differences in both cell morphology and cell size with a cell size of $72.4 \mu\text{m}^2$ for HUVEC endothelial cells, $71.6 \mu\text{m}^2$ for A549, $232.9 \mu\text{m}^2$ for NHDF fibroblast cells, and $125.3 \mu\text{m}^2$ for ASC stem cells. Cell size directly correlates with oxygen consumption, (Wagner et al., 2011) which explains the high respiratory activity of fibroblast cells displaying the biggest cell size.

Impact of Cell Adhesion Promoters on Oxygen Consumption Rates

Since mammalian cells strongly interact and respond to surface properties such as the biocompatibility and functionalization of the interface, the influence of ECM surface promoters including 1% gelatin and collagen I was investigated on the respiratory activity of HUVEC endothelial cells during cell seeding and 3 h after attachment. As shown in **Figure 5A** already 3 min following the introduction of endothelial cells

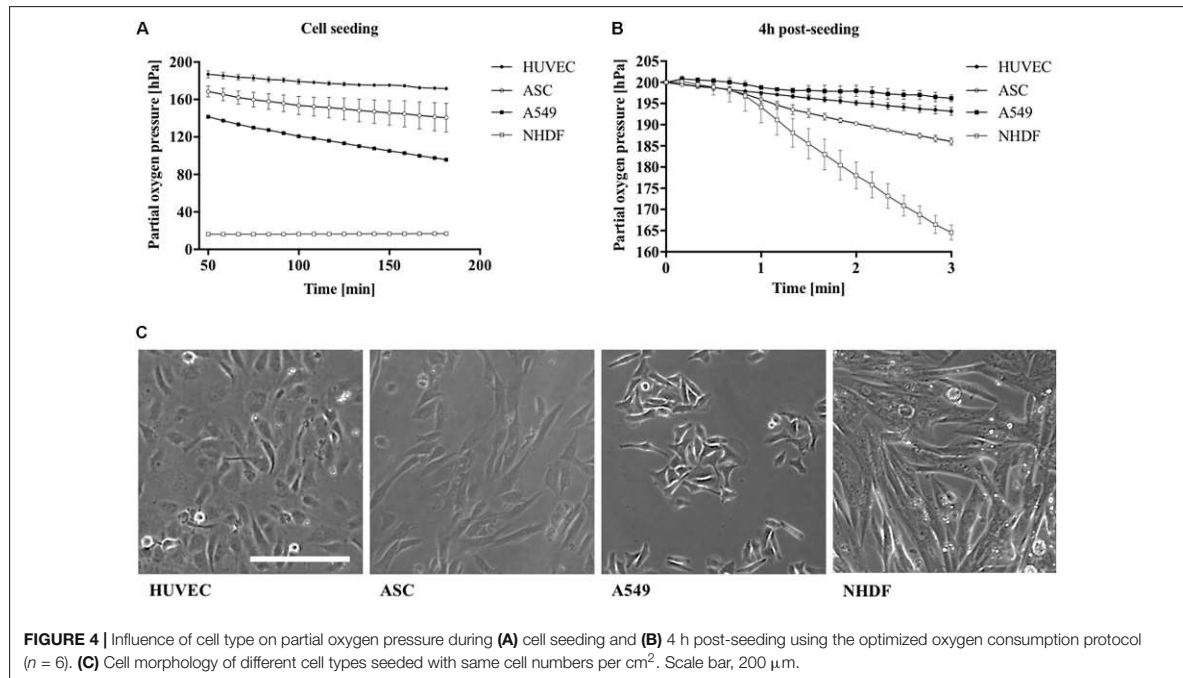


FIGURE 4 | Influence of cell type on partial oxygen pressure during (A) cell seeding and (B) 4 h post-seeding using the optimized oxygen consumption protocol ($n = 6$). (C) Cell morphology of different cell types seeded with same cell numbers per cm^2 . Scale bar, 200 μm .

seeded on gelatin and collagen I-coated microchannels, a drop in partial oxygen pressure by 1 hPa was recorded. In contrast, partial oxygen pressure of 200 hPa remained in the absence of cells. In turn, after completion of cell attachment and establishment of endothelial cell monolayers, both adhesion promoters initiated elevated respiratory activities in the range of 130–150 hPa compared to untreated glass with partial oxygen pressure around 165.7 ± 5 hPa. **Figure 5B** shows that respiration of HUVEC endothelial cells further increased from 4 to 24 h post-seeding by 140% for collagen I coating and 170% for gelatin-coated microchannels. Even though respiratory activity of HUVEC endothelial cells cultured on untreated glass displayed highest relative increase of 250% after 24 h, however, absolute respiration rates were 20–40% lower than cells cultivated on ECM-like adhesion promoters. These findings can be explained by incomplete adhesion of cells on untreated surfaces, where 10% of the cells were only partially attached as shown in **Figure 5C**. In other words, our results demonstrate that our non-invasive on-chip oxygen detection method can also be applied for adhesion and biocompatibility studies, where metabolic assays as well as microscopic inspection of cell phenotype alone can result in overestimation of cellular activity.

Non-invasive Oxygen Monitoring in Three-Dimensional Microfluidic Cell Cultures

Since state-of-the-art *in vitro* models frequently employ 3D-hydrogel-based cell cultures, the integrated oxygen sensor array

was evaluated using a well-established co-culture model of ASC stem cells with HUVEC endothelial cells (Muhleder et al., 2018). Here, an oxygen-permeable PDMS-based microfluidic biochip containing four spatially resolved sensor spots (see also **Figure 1B**) was seeded with a HUVEC/ASC cell co-culture. Oxygen monitoring was performed for medium supply channels (sensor #1) as well as at 2 to 7 mm within the fibrin hydrogel (sensors #2–4). On the first day of culture, cell co-cultures settled and established direct cell-cell contacts and reciprocal exchange of pro-angiogenic factors using a static stop-flow cultivation period over 24 h. **Figure 6A** (left panel) shows that after 45 min of hydrogel polymerization, partial oxygen pressure of the feeding channel stayed constant around 169.0 ± 1.1 hPa for the first day of culture. In contrast, within the hydrogel construct oxygen levels slowly decreased over time to around 132.4 ± 5.4 hPa independent of diffusion distance through the hydrogel with an average oxygen decrease of 2.5 hPa/h. After the first day of culture, continuous medium supply was initiated at a flow rate of 2 $\mu\text{L}/\text{min}$ for the next 5 days of culture. **Figure 6A** (right panel) shows that at day 6 of vascular network formation, an oxygen gradient was established starting at steady atmospheric partial oxygen pressure of around 198.4 hPa for sensor #1 at the medium feeding channel, and linear decreasing values of 176.3 hPa for sensor #2 at 2 mm, 152.1 hPa for sensor #3 at 4.5 mm, and 140.9 hPa for sensor #4 at 7 mm distance from the feeding channel. Overall, average decrease of partial oxygen pressure of 10 hPa per day was observed for the deepest regions of the hydrogel construct. **Figure 6B** shows that even though a linear oxygen gradient was established, vascular network formation with interconnecting endothelial tubes started at a

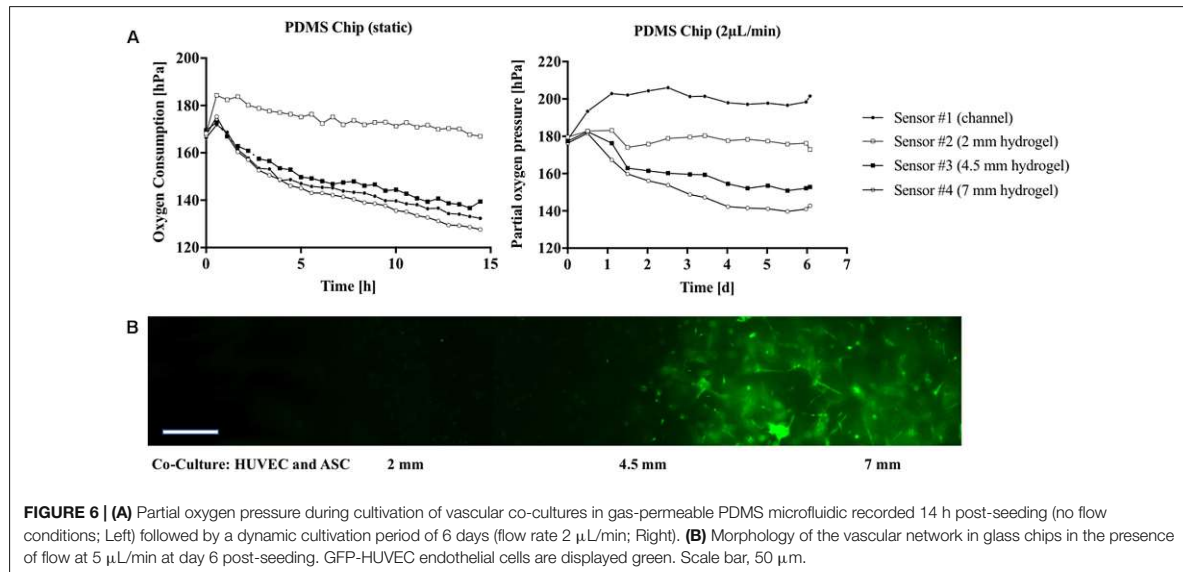


FIGURE 6 | (A) Partial oxygen pressure during cultivation of vascular co-cultures in gas-permeable PDMS microfluidic recorded 14 h post-seeding (no flow conditions; Left) followed by a dynamic cultivation period of 6 days (flow rate 2 μL/min; Right). **(B)** Morphology of the vascular network in glass chips in the presence of flow at 5 μL/min at day 6 post-seeding. GFP-HUVEC endothelial cells are displayed green. Scale bar, 50 μm.

in the range of 0–2 μL/min was used to expose cells to alternating cycles of normoxic and hypoxic culture conditions with peak-to-peak values for partial oxygen pressure of max. 200 hPa down to min. 17 hPa and an average cycle time around 2.5 h over several days for 3D cell culture. **Figure 7A** (bottom panel) shows that due to the cycling of normoxic and hypoxic conditions, formation of a vascular network with decreased length and thickness of vascular sprouts was observable; however, more even distribution of the network was observable starting already at 2 mm distance from the medium feeding channel. In a final set of experiments, we demonstrated how the presented non-invasive microfluidic oxygen monitoring method can be applied not only for oxygen control, but also for evaluation of cell health status during oxygen- and nutrient-dependent limitation of three-dimensional cultures in the absence of medium perfusion. As shown in **Figure 7B** (top panel) an oxygen gradient was established in the absence of medium perfusion due to the respiratory activity of intact cell co-cultures until day 3 post-seeding corresponding to vascular network formation (see **Figure 7B** bottom left image). Over the course of 36 h of nutrient and oxygen limitation, partial oxygen pressure gradually recovered to fully oxygenated conditions around 200 hPa, which is the result of cell death by nutrient and oxygen depletion over 6 days. **Figure 7B** shows a residual pattern of GFP-containing cell remnants (visible in the bottom center image) that resembles the vascular network morphology from day 3. These patterns were not observable for cell co-cultures closest to the medium feeding channel, which did not form vascular networks (bottom right image).

CONCLUSION

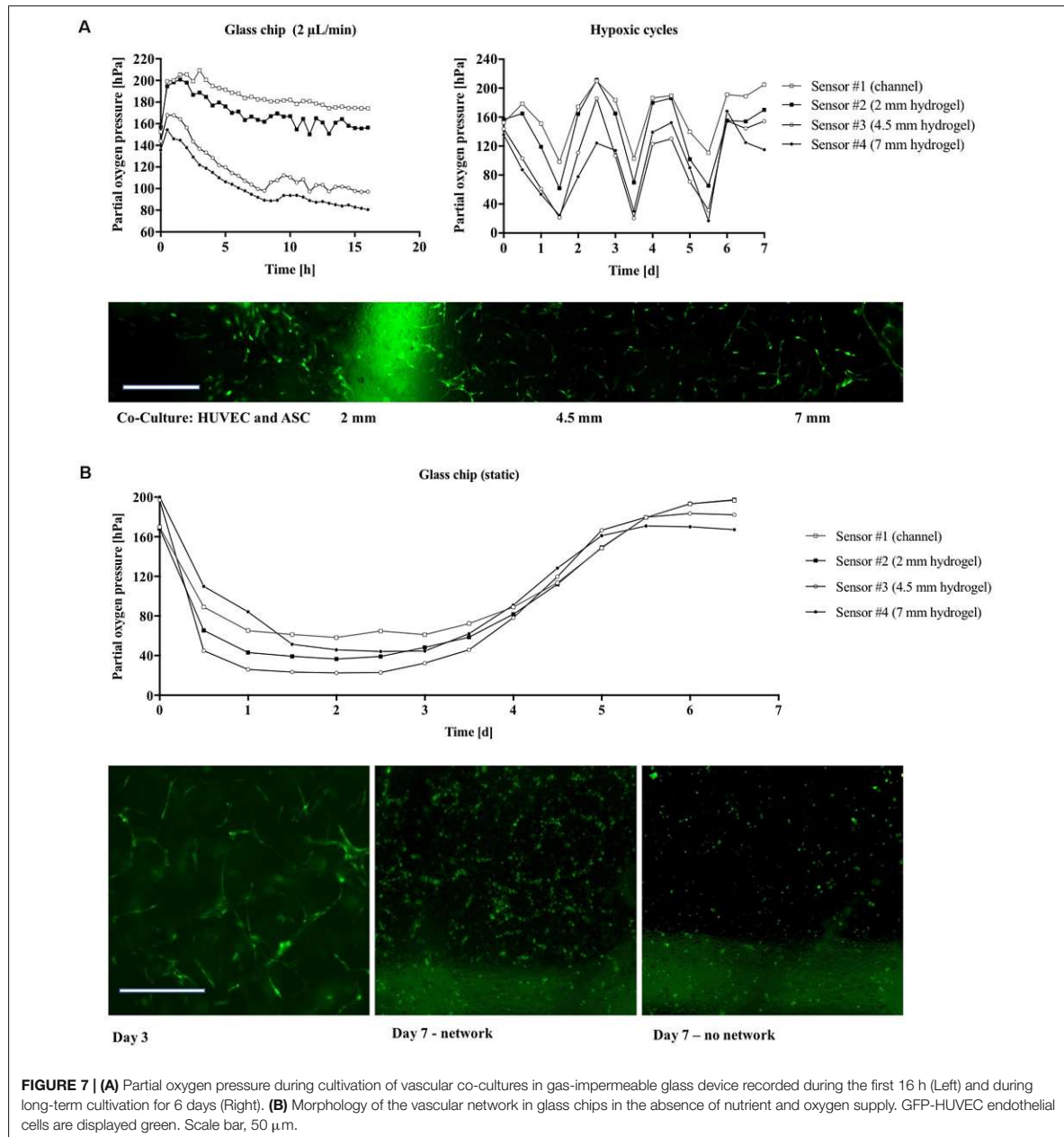
In this method paper, we demonstrate the ability to reliably and reproducibly detect dissolved oxygen levels and cellular oxygen

demands in 2D and 3D microfluidic cell culture systems. The integration of oxygen-sensitive microparticle-based sensor spots enables time-resolved monitoring of partial oxygen pressures, thus allowing the estimation of cellular oxygen consumption rates of cell monolayers in the presence of increasing flow rates, varying cell numbers, cell types, and ECM-coatings. The total oxygen consumption observed for the different cell densities increased linearly. This means that the presented measurement method has the potential to be used for indirect monitoring of cell viability in toxicological screening studies. Additionally, we show that metabolic evaluation of complex 3D tissue-engineered constructs can be accomplished using biologically relevant co-cultures. The ability to monitor complex 3D physiological cellular microenvironments further highlights the benefits of sensor integration in microfluidic systems to control, mitigate, and accurately predict cell behavior (Charwat et al., 2013, 2014; Ertl et al., 2014; Mahto et al., 2015; Rothbauer et al., 2015a,b). The presented on-chip-integrated oxygen-sensing method is well suited for applications in advanced organ-on-a-chip systems, because it enables non-invasive, real-time, label-free, *in situ* monitoring of oxygen demands, metabolic activity, oxygen uptake rates, and cell viability. We believe that the integration of cost-efficient and reliable sensor technology in microfluidic devices holds great promise for the reliable establishment of physiologic or pathologic tissue conditions, thus opening new avenues in biomedical research and pharmaceutical development.

MATERIALS AND METHODS

Preparation of the Oxygen Sensor

Amine-functionalized polystyrene beads (500 μL of a 50 mg/mL stock solution, micromer® product code 01-01-303, micromod,



Germany) were diluted with water (2 mL) and THF (200 μL). This dispersion was stirred for 30 min at room temperature. Afterward, an oxygen indicator solution [188 μL of a THF solution containing 2 mg/mL platinum (II) meso-tetra (4-fluorophenyl) tetrabenzoporphyrin (PtTPTBPF)] was added dropwise, the dispersion was sonicated for 30 min, centrifuged at a relative centrifugation force of 6200, and the supernatant was decanted. The particles were purified using multiple

washing, centrifugation, and decantation steps. The purification process was repeated with water (1–2 times) at the beginning, followed by ethanol (3–5 times) and finished with water (1–2 times). After the final decantation step the particles were diluted with water to a particle concentration of approx. 50 mg/mL. Characterization and calibration of oxygen sensor was performed as described previously (Ehgartner et al., 2016b).

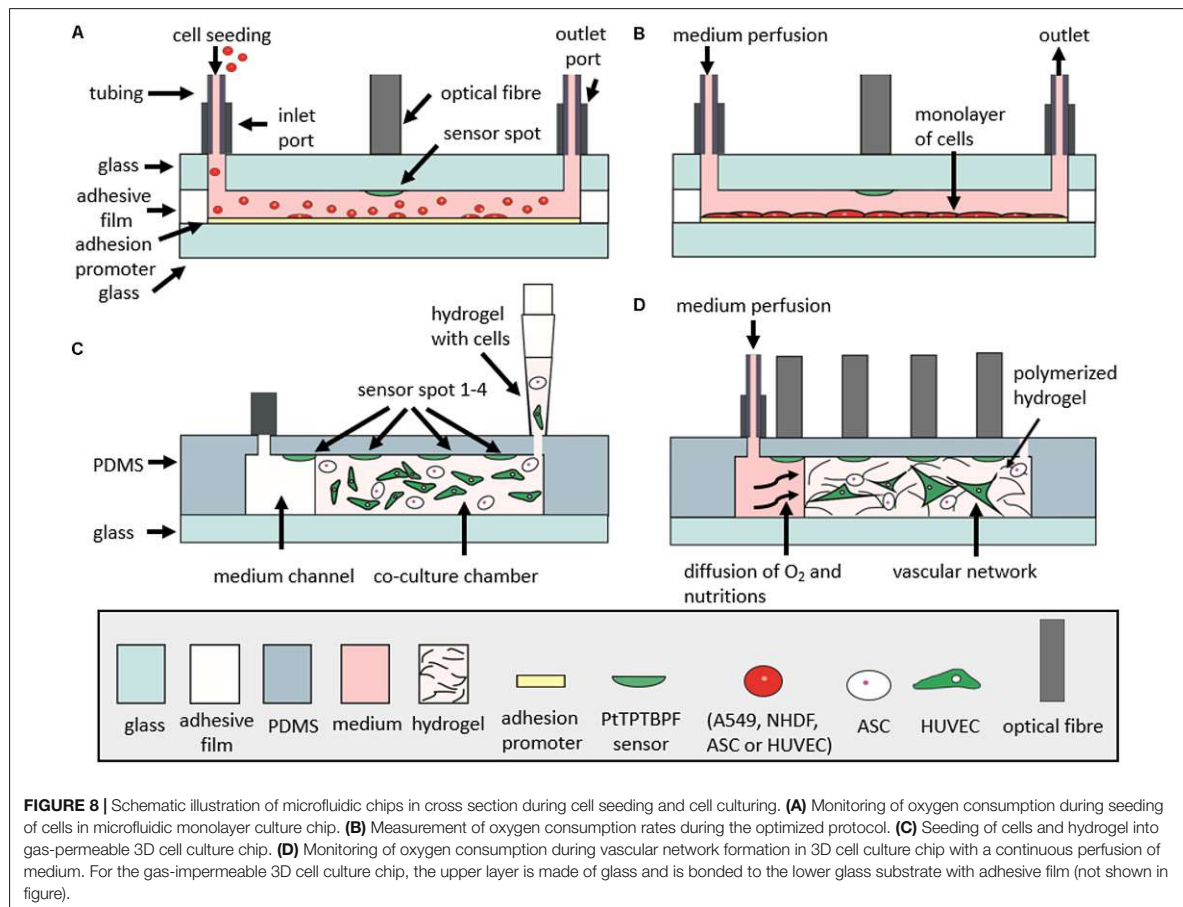


FIGURE 8 | Schematic illustration of microfluidic chips in cross section during cell seeding and cell culturing. **(A)** Monitoring of oxygen consumption during seeding of cells in microfluidic monolayer culture chip. **(B)** Measurement of oxygen consumption rates during the optimized protocol. **(C)** Seeding of cells and hydrogel into gas-permeable 3D cell culture chip. **(D)** Monitoring of oxygen consumption during vascular network formation in 3D cell culture chip with a continuous perfusion of medium. For the gas-impermeable 3D cell culture chip, the upper layer is made of glass and is bonded to the lower glass substrate with adhesive film (not shown in figure).

Microfluidic Chips and Sensor Integration

The microdevices for monolayer cultures were comprised of two glass substrates (VWR) bonded together with adhesive film containing the fluidic structure. Microfluidic chambers and channels were designed with CAD (AutoCAD 2017) and cut into the adhesive film (ARcare 8259 and ARseal 90880, Adhesive Research, Ireland) with a desktop vinyl cutter (GS-24 Desktop Cutter, Roland DGA Corporation, Germany). Three layers of adhesive film were used to obtain a chamber height of 460 μm . The chip contained 8 cell-culture chambers of 0.22 cm^2 (10 μL volume) with one inlet connected to two chambers with a 400 μm wide channel (Figure 1A). Holes for inlets and outlets were drilled into the upper glass substrate before integration of sensor particles. Oxygen sensor microparticles were applied by pipetting directly to the glass substrate. After drying for 2 h at room temperature, the microparticles were immobilized to the glass substrate and the fluidic structures were sealed with adhesive film via pressure activation. Devices for three-dimensional (3D) hydrogel cultures had a circular hydrogel chamber (65 μL volume) adjacent to a medium channel (see Figure 1B).

Microstructures were either fabricated by soft lithography using PDMS (Sylgard® 184 Silicone Elastomer Kit, Dow Corning, Germany) from 3D-printed molds (immateralize, Denmark) or sandblasted into glass slides. Oxygen-sensitive conjugated microparticles were again applied via pipetting directly to the glass substrate and immobilized after 2 h of drying. PDMS devices were sealed by plasma bonding to glass slides using air plasma (Harrick Plasma, High Power, 2 min) and glass devices were sealed using adhesive film (ARseal 90880, Adhesive Research, Ireland).

Cell Culture

A549 human lung carcinoma epithelial-like cell line (ATCC) were cultured in RPMI 1640 Medium (Gibco) supplemented with 10% fetal bovine serum, L-glutamine, and 1% antibiotic/antimycotic solution. NHDF (Lonza) were cultured in high glucose Dulbecco's modified Eagle's medium (DMEM, Sigma Aldrich) supplemented with 10% fetal bovine serum, 2 mM glutamine, and 1% antibiotic-antimycotic solution. Primary human ASC and HUVEC were isolated as previously described (Petzelbauer et al., 1993; Wolbank et al., 2007; Priglinger et al., 2017)

and maintained in fully supplemented endothelial cell growth medium 2 (EGM-2, PromoCell) with 5% fetal calf serum until passage 5–9. GFP-labeled endothelial cells were prepared as previously described (Knezevic et al., 2017; Muhleder et al., 2018) All cell cultures were maintained in a humidified atmosphere at 37°C and 5% CO₂. Cell culture media used during perfusion of the microfluidic monolayer chambers was supplemented with 0.5% HEPES (Sigma Aldrich). Prior to cell seeding, microfluidic tubing and valves were sterilized with 70% ethanol and rinsed thoroughly with PBS (Sigma Aldrich) and cell culture medium. The assembled microfluidic biochips were disinfected using 70% ethanol and rinsed with sterile PBS prior to coating with 5% collagen I solution (Sigma Aldrich, Austria).

On-Chip Oxygen Monitoring

Oxygen monitoring was carried out at a sampling frequency of 1 Hz using a FireStingO2 optical oxygen meter (Pyroscience, Germany¹) connected to optical fibers (length 1 m, outer diameter 2.2 mm, fiber diameter 1 mm). Integrated sensors were calibrated using a CO₂/O₂ oxygen controller (CO₂-O₂-Controller 2000, Pecon GmbH, Germany) equipped with integrated zirconium oxide oxygen sensors. Oxygen measurements were initiated directly after injection of cell solutions and partial oxygen pressure was monitored up to a maximum duration of 7 days. To evaluate the influence of cell number on oxygen consumption, A549 lung cells were seeded at concentrations of 1×10^4 cells/cm² (2.2×10^3 cells/chamber), 2.5×10^4 cells/cm² (5.5×10^3 cells/chamber), and 1.0×10^5 cells/cm² (22×10^3 cells/chamber). For oxygen monitoring of different cell types, A549 lung epithelial cells, NHDF fibroblast cells, HUVEC endothelial cells, and ASC stem cells were seeded at a concentration of 2.5×10^4 cells/cm² (5.5×10^3 cells/chamber) To investigate the influence of adhesion promoters on oxygen consumption, HUVEC endothelial cells were seeded at a concentration of 2.5×10^4 HUVEC/cm² (5.5×10^3 cells/chamber) on different surfaces including untreated glass 5% collagen I and 1% gelatin. For oxygen monitoring of 3D fibrin hydrogels, ASC stem cells and HUVEC endothelial cells were mixed at a cell density of 5×10^5 cells/mL (32.5×10^3 cells/chamber, 65 μ L chamber volume) per cell type in fibrinogen and thrombin (TISSEEL®, Baxter, Austria) to obtain a final concentration of 2.5 mg/mL fibrinogen and 1 U/mL thrombin. The hydrogel was loaded into the hydrogel chambers of the microfluidic chip and allowed to polymerize for 45 min before the addition of fully supplemented EGM-2 culture medium. Thereafter, vascular 3D cell cultures were maintained at a flow rate of 2 μ L/min. In **Figures 8A–D**, schematic illustrations depict the cell seeding and measurement setup of monolayer culture chips (A–B) and 3D culture chips (C–D).

Optimized Protocol for On-Chip Oxygen Consumption Measurements

For determination of oxygen consumption, an optimized protocol was established recording three consecutive measuring

¹www.pyro-science.com

cycles. Each cycle comprised of an oxygen saturation phase of 10 μ L/min for 10 min followed by a recording phase under stop-flow conditions for 3 min.

CFD Simulation of Oxygen

Oxygen saturation was simulated using a multipurpose finite volume CFD simulation (Ansys FLUENT®, v6.3.26). The hydrogel region was approximated as a porous zone with a porosity of $\epsilon = 0.99$ and isotropic viscous resistances of $R = 6.67 \cdot 10^{-12}$ 1/m². Simulations were performed using an oxygen diffusion coefficient of 2×10^{-9} m²/s.

AUTHOR CONTRIBUTIONS

HZ, MR, SS, BB, and PE conceived the project and designed the experimental outline. HZ, MR, SS, and BB performed the microfluidic experiments and analyzed the data. CJ and MH conceived and performed finite volume CFD simulations. BM, JE, and TM prepared the optical sensors for oxygen biosensing. EP, SM, WH, and HR isolated and transfected the primary endothelial and adipose-derived stem cell cultures and shared their expertise in vascular tissue engineering. HZ, MR, SS, and BB drafted the manuscript. All authors contributed to and revised the final manuscript.

FUNDING

This work was funded by the European Union's Horizon 2020 research and innovation programme (685817) and the Austrian Research Promotion Agency (FFG; 849791). The authors acknowledge the TU Wien University Library for financial support through its Open Access Funding Program.

ACKNOWLEDGMENTS

The authors acknowledge the band “The Police” for their fundamental contribution to the title and Christoph Eilenberger for image analysis and fruitful discussions.

SUPPLEMENTARY MATERIAL

The Supplementary Material for this article can be found online at: <https://www.frontiersin.org/articles/10.3389/fphys.2018.00815/full#supplementary-material>

FIGURE S1 | Images of microfluidic devices. **(A)** Microfluidic glass chip (76 mm × 26 mm × 2.3 mm) for monolayer culture containing eight chambers with a sensor spot centralized in each chamber. **(B)** Microfluidic glass chip (76 mm × 26 mm × 4.4 mm) for three-dimensional (3D) hydrogel cultures with four sensor spots in each chamber. Scale bar represent 10 mm.

FIGURE S2 | Partial oxygen pressure recorded during 3 h of cell seeding zoomed in to the first 50 min of oxygen monitoring.

FIGURE S3 | Finite volume simulation of oxygen distribution in 3D hydrogel after **(A)** 1 h, **(B)** 6 h, and **(C)** 12 h of medium perfusion without cells showing complete saturation of hydrogel with oxygen within 12 h.

REFERENCES

- Abaci, H. E., Truitt, R., Luong, E., Drazer, G., and Gerecht, S. (2010). Adaptation to oxygen deprivation in cultures of human pluripotent stem cells, endothelial progenitor cells, and umbilical vein endothelial cells. *Am. J. Physiol. Cell Physiol.* 298, C1527–C1537. doi: 10.1152/ajpcell.00484.2009
- Charwat, V., Joksich, M., Sticker, D., Purtscher, M., Rothbauer, M., and Ertl, P. (2014). Monitoring cellular stress responses using integrated high-frequency impedance spectroscopy and time-resolved ELISA. *Analyst* 139, 5271–5282. doi: 10.1039/c4an00824c
- Charwat, V., Rothbauer, M., Tedde, S. F., Hayden, O., Bosch, J. J., Muellner, P., et al. (2013). Monitoring dynamic interactions of tumor cells with tissue and immune cells in a lab-on-a-chip. *Anal. Chem.* 85, 11471–11478. doi: 10.1021/ac4033406
- Cooper, J. R., Abdullatif, M. B., Burnett, E. C., Kempell, K. E., Conforti, F., Tolley, H., et al. (2016). Long term culture of the A549 cancer cell line promotes multilamellar body formation and differentiation towards an alveolar type II pneumocyte phenotype. *PLoS One* 11:e0164438. doi: 10.1371/journal.pone.0164438
- Ehgartner, J., Strobl, M., Bolivar, J. M., Rabl, D., Rothbauer, M., Ertl, P., et al. (2016a). Simultaneous determination of oxygen and pH inside microfluidic devices using core-shell nanosensors. *Anal. Chem.* 88, 9796–9804.
- Ehgartner, J., Sulzer, P., Burger, T., Kasjanow, A., Bouwes, D., Krühne, U., et al. (2016b). Online analysis of oxygen inside silicon-glass microreactors with integrated optical sensors. *Sens. Actuators B Chem.* 228, 748–757. doi: 10.1016/j.snb.2016.01.050
- Ehgartner, J., Wiltische, H., Borisov, S. M., and Mayr, T. (2014). Low cost referenced luminescent imaging of oxygen and pH with a 2-CCD colour near infrared camera. *Analyst* 139, 4924–4933. doi: 10.1039/c4an00783b
- Ertl, P., Sticker, D., Charwat, V., Kasper, C., and Lepperdinger, G. (2014). Lab-on-a-chip technologies for stem cell analysis. *Trends Biotechnol.* 32, 245–253. doi: 10.1016/j.tibtech.2014.03.004
- Gille, J. J., and Joenje, H. (1992). Cell culture models for oxidative stress: superoxide and hydrogen peroxide versus normobaric hyperoxia. *Mutat. Res.* 275, 405–414. doi: 10.1016/0921-8734(92)90043-O
- Gruber, P., Marques, M. P. C., Szita, N., and Mayr, T. (2017). Integration and application of optical chemical sensors in microreactors. *Lab Chip* 17, 2693–2712. doi: 10.1039/c7lc00538e
- Haase, K., and Kamm, R. D. (2017). Advances in on-chip vascularization. *Regen. Med.* 12, 285–302. doi: 10.2217/rme-2016-0152
- Harris, A. L. (2002). Hypoxia — a key regulatory factor in tumour growth. *Nat. Rev. Cancer* 2, 38–47. doi: 10.1038/nrc704
- Harrison, B. S., Eberli, D., Lee, S. J., Atala, A., and Yoo, J. J. (2007). Oxygen producing biomaterials for tissue regeneration. *Biomaterials* 28, 4628–4634. doi: 10.1016/j.biomaterials.2007.07.003
- Heidemann, R., Lütkemeyer, D., Büntemeyer, H., and Lehmann, J. (1998). Effects of dissolved oxygen levels and the role of extra- and intracellular amino acid concentrations upon the metabolism of mammalian cell lines during batch and continuous cultures. *Cytotechnology* 26, 185–197. doi: 10.1023/A:1007917409455
- Hossmann, K.-A. (2006). Pathophysiology and therapy of experimental stroke. *Cell. Mol. Neurobiol.* 26, 1055–1081. doi: 10.1007/s10571-006-9008-1
- Jagannathan, L., Cuddapah, S., and Costa, M. (2016). Oxidative stress under ambient and physiological oxygen tension in tissue culture. *Curr. Pharmacol. Rep.* 2, 64–72. doi: 10.1007/s40495-016-0050-5
- Knezevic, L., Schapper, M., Muhleder, S., Schimek, K., Hasenberg, T., Marx, U., et al. (2017). Engineering blood and lymphatic microvascular networks in fibrin matrices. *Front. Bioeng. Biotechnol.* 5:25. doi: 10.3389/fbioe.2017.00025
- Lasave, L. C., Borisov, S. M., Ehgartner, J., and Mayr, T. (2015). Quick and simple integration of optical oxygen sensors into glass-based microfluidic devices. *RSC Adv.* 5, 70808–70816. doi: 10.1039/C5RA15591F
- Mahto, S. K., Charwat, V., Ertl, P., Rothen-Rutishauser, B., Rhee, S. W., and Sznitman, J. (2015). Microfluidic platforms for advanced risk assessments of nanomaterials. *Nanotoxicology* 9, 381–395. doi: 10.3109/17435390.2014.940402
- Manning, C. N., Martel, C., Sakiyama-Elbert, S. E., Silva, M. J., Shah, S., Gelberman, R. H., et al. (2015). Adipose-derived mesenchymal stromal cells modulate tendon fibroblast responses to macrophage-induced inflammation in vitro. *Stem Cell Res. Ther.* 6:74. doi: 10.1186/s13287-015-0059-4
- Mohyeldin, A., Garzón-Muñdi, T., and Quiñones-Hinojosa, A. (2010). Oxygen in stem cell biology: a critical component of the stem cell niche. *Cell Stem Cell* 7, 150–161. doi: 10.1016/j.stem.2010.07.007
- Muhleder, S., Pill, K., Schapper, M., Labuda, K., Priglinger, E., Hofbauer, P., et al. (2018). The role of fibrinolysis inhibition in engineered vascular networks derived from endothelial cells and adipose-derived stem cells. *Stem Cell Res. Ther.* 9:35. doi: 10.1186/s13287-017-0764-2
- Nichols, M. G., and Foster, T. H. (1994). Oxygen diffusion and reaction kinetics in the photodynamic therapy of multicell tumour spheroids. *Phys. Med. Biol.* 39, 2161–2181. doi: 10.1088/0031-9155/39/12/003
- Oomen, P. E., Skolimowski, M. D., and Verpoorte, E. (2016). Implementing oxygen control in chip-based cell and tissue culture systems. *Lab Chip* 16, 3394–3414. doi: 10.1039/c6lc00772d
- Petzeltbauer, P., Bender, J. R., Wilson, J., and Pober, J. S. (1993). Heterogeneity of dermal microvascular endothelial cell antigen expression and cytokine responsiveness in situ and in cell culture. *J. Immunol.* 151, 5062–5072.
- Pouyssegur, J., Dayan, F., and Mazure, N. M. (2006). Hypoxia signalling in cancer and approaches to enforce tumour regression. *Nature* 441, 437–443. doi: 10.1038/nature04871
- Powers, D. E., Millman, J. R., Huang, R. B., and Colton, C. K. (2008). Effects of oxygen on mouse embryonic stem cell growth, phenotype retention, and cellular energetics. *Biotechnol. Bioeng.* 101, 241–254. doi: 10.1002/bit.21986
- Priglinger, E., Schuh, C., Steffenhagen, C., Wurzer, C., Maier, J., Nuernberger, S., et al. (2017). Improvement of adipose tissue-derived cells by low-energy extracorporeal shock wave therapy. *Cytotherapy* 19, 1079–1095. doi: 10.1016/j.jcyt.2017.05.010
- Pugh, C. W., and Ratcliffe, P. J. (2003). Regulation of angiogenesis by hypoxia: role of the HIF system. *Nat. Med.* 9, 677–684. doi: 10.1038/nm0603-677
- Rehberg, M., Ritter, J. B., Genzel, Y., Flockerzi, D., and Reichl, U. (2013). The relation between growth phases, cell volume changes and metabolism of abiotic cells during cultivation. *J. Biotechnol.* 164, 489–499. doi: 10.1016/j.jbiotec.2013.01.018
- Rothbauer, M., Praisler, I., Docter, D., Stauber, R. H., and Ertl, P. (2015a). Microfluidic impedimetric cell regeneration assay to monitor the enhanced cytotoxic effect of nanomaterial perfusion. *Biosensors* 5, 736–749. doi: 10.3390/bios5040736
- Rothbauer, M., Wartmann, D., Charwat, V., and Ertl, P. (2015b). Recent advances and future applications of microfluidic live-cell microarrays. *Biotechnol. Adv.* 33, 948–961. doi: 10.1016/j.biotechadv.2015.06.006
- Sun, S., Ungerbock, B., and Mayr, T. (2015). Imaging of oxygen in microreactors and microfluidic systems. *Methods Appl. Fluoresc.* 3:034002. doi: 10.1088/2050-6120/3/3/034002
- Super, A., Jaccard, N., Cardoso Marques, M. P., Macown, R. J., Griffin, L. D., Veraitch, F. S., et al. (2016). Real-time monitoring of specific oxygen uptake rates of embryonic stem cells in a microfluidic cell culture device. *Biotechnol. J.* 11, 1179–1189. doi: 10.1002/biot.201500479
- Ungerbock, B., Charwat, V., Ertl, P., and Mayr, T. (2013). Microfluidic oxygen imaging using integrated optical sensor layers and a color camera. *Lab Chip* 13, 1593–1601. doi: 10.1039/c3lc41315b
- Volkmer, E., Drosse, I., Otto, S., Stangelmayer, A., Stengele, M., Kallukalam, B. C., et al. (2008). Hypoxia in static and dynamic 3D culture systems for tissue engineering of bone. *Tissue Eng. Part A* 14, 1331–1340. doi: 10.1089/ten.tea.2007.0231
- Wagner, B. A., Venkataraman, S., and Buettner, G. R. (2011). The rate of oxygen utilization by cells. *Free Radic. Biol. Med.* 51, 700–712. doi: 10.1016/j.freeradbiomed.2011.05.024
- Wang, X. D., and Wolfbeis, O. S. (2014). Optical methods for sensing and imaging oxygen: materials, spectroscopies and applications. *Chem. Soc. Rev.* 43, 3666–3761. doi: 10.1039/c4cs00039k
- Weltin, A., Slotwinski, K., Kieninger, J., Moser, I., Jobst, G., Wego, M., et al. (2014). Cell culture monitoring for drug screening and cancer research: a transparent, microfluidic, multi-sensor microsystem. *Lab Chip* 14, 138–146. doi: 10.1039/c3lc50759a
- Wolbank, S., Peterbauer, A., Fahrner, M., Hennerbichler, S., van Griensven, M., Stadler, G., et al. (2007). Dose-dependent immunomodulatory effect of human

- stem cells from amniotic membrane: a comparison with human mesenchymal stem cells from adipose tissue. *Tissue Eng.* 13, 1173–1183. doi: 10.1089/ten.2006.0313
- Wolfbeis Otto, S. (2015). Luminescent sensing and imaging of oxygen: fierce competition to the Clark electrode. *Bioessays* 37, 921–928. doi: 10.1002/bies.201500002
- Zhang, J., Wei, X., Zeng, R., Xu, F., and Li, X. (2017). Stem cell culture and differentiation in microfluidic devices toward organ-on-a-chip. *Future Sci. OA* 3:FSO187. doi: 10.4155/fsoa-2016-0091
- Zhang, K., Zhu, L., and Fan, M. (2011). Oxygen, a key factor regulating cell behavior during neurogenesis and cerebral diseases. *Front. Mol. Neurosci.* 4:5. doi: 10.3389/fnmol.2011.00005
- Zhang, L., Marsboom, G., Glick, D., Zhang, Y., Toth, P. T., Jones, N., et al. (2014). Bioenergetic Shifts during transitions between stem cell states (2013 Grover Conference series). *Pulm. Circ.* 4, 387–394. doi: 10.1086/677353
- Zinkernagel, A. S., Johnson, R. S., and Nizet, V. (2007). Hypoxia inducible factor (HIF) function in innate immunity and infection. *J. Mol. Med.* 85, 1339–1346. doi: 10.1007/s00109-007-0282-2
- Conflict of Interest Statement:** The authors declare that the research was conducted in the absence of any commercial or financial relationships that could be construed as a potential conflict of interest.
- Copyright © 2018 Zirath, Rothbauer, Spitz, Bachmann, Jordan, Müller, Ehartner, Priglinger, Mühleder, Redl, Holnthoner, Harasek, Mayr and Ertl. This is an open-access article distributed under the terms of the Creative Commons Attribution License (CC BY). The use, distribution or reproduction in other forums is permitted, provided the original author(s) and the copyright owner(s) are credited and that the original publication in this journal is cited, in accordance with accepted academic practice. No use, distribution or reproduction is permitted which does not comply with these terms.

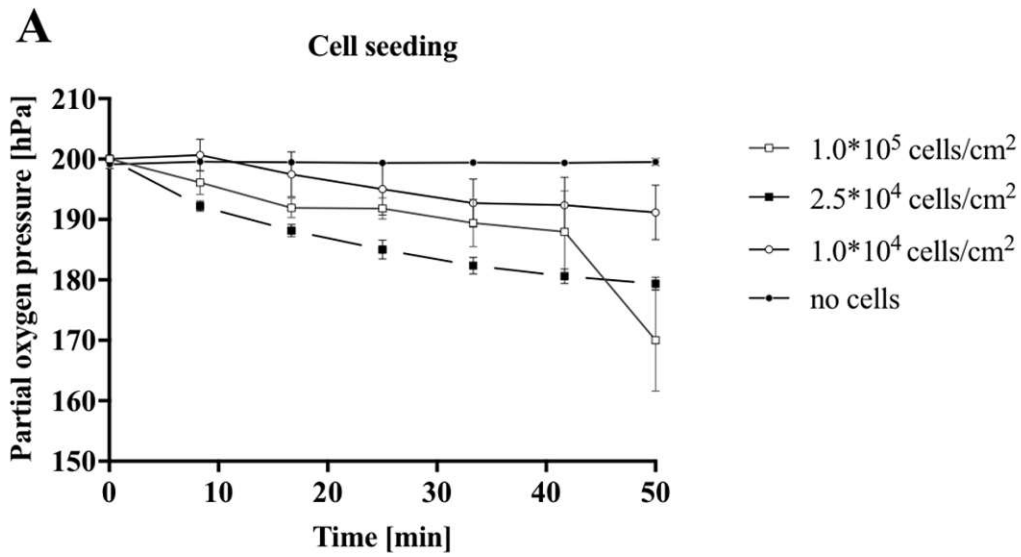
3.2 MANUSCRIPT #1 – SUPPLEMENTARY INFORMATION

Supplementary Information

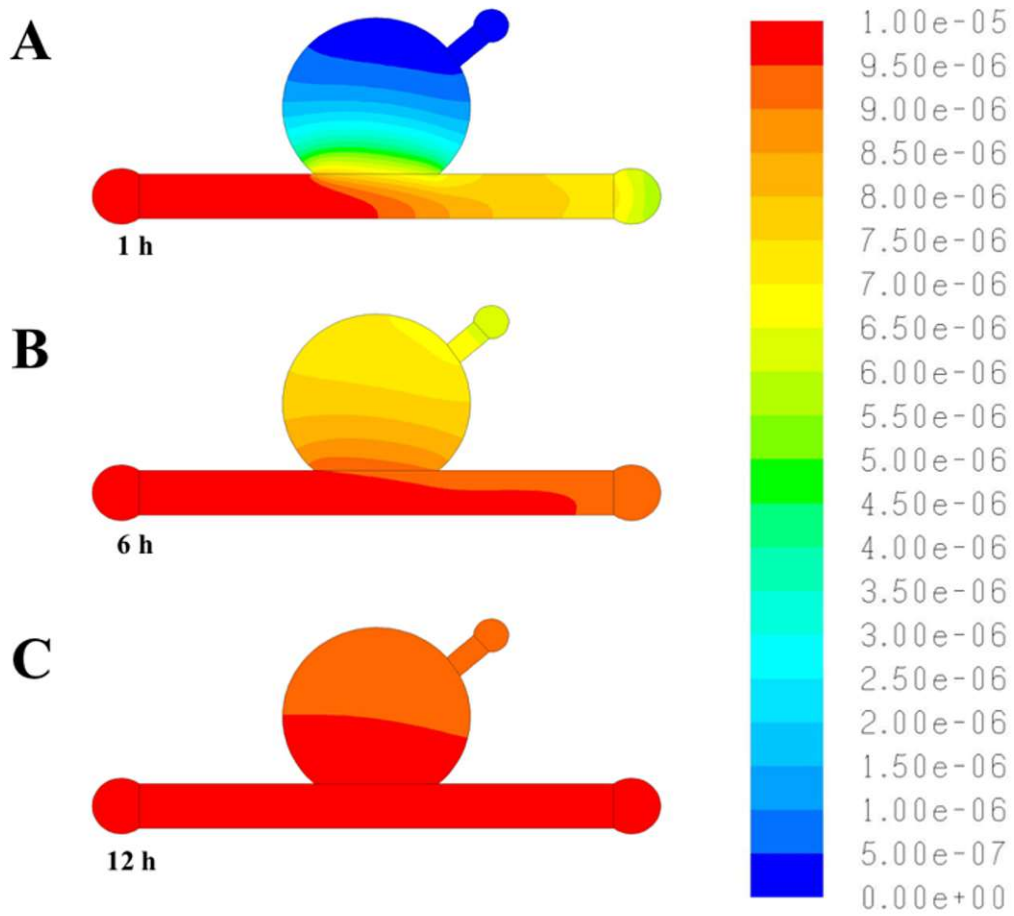
Every Breath You Take: Non-Invasive Real-Time Oxygen Biosensing in Two- and Three-Dimensional Microfluidic Cell Models



SI Figure 1: Images of microfluidic devices. (A) Microfluidic glass chip (76 x 76 x 2.3 mm) for monolayer culture containing 8 chambers with a sensor spot centralized in each chamber. (B) Microfluidic glass chip (76 x 26 x 4.4 mm) for three-dimensional (3D) hydrogel cultures with 4 sensor spots in each chamber. Scale bar represents 10 mm.



SI Figure 2: Partial oxygen pressure recorded during 3 hours of cell seeding zoomed into the first 50 min of oxygen monitoring.



SI Figure 3: Finite volume simulation of oxygen distribution in 3D hydrogel after (A) 1 hour, (B) 6 hours and (C) 12 hours of medium perfusion without cells showing complete saturation of the hydrogel with oxygen within 12 hours.

3.1 MANUSCRIPT #2 - ARTICLE

BRIDING THE ACADEMIC-INDUSTRIAL GAP: APPLICATION OF AN OXYGEN AND PH SENSOR INTEGRATED LAB-ON-A-CHIP IN NANOTOXICOLOGY



Cite this: *Lab Chip*, 2021, 21, 4237

Bridging the academic–industrial gap: application of an oxygen and pH sensor-integrated lab-on-a-chip in nanotoxicology†

Helene Zirath,^{id} ‡*^{ab} Sarah Spitz,[‡] ^{ab} Doris Roth,^{id} ^{ab} Tobias Schellhorn,^a Mario Rothbauer,^{bc} Bernhard Müller,^d Manuel Walch,^e Jatinder Kaur,^e Alexander Wörle,^e Yvonne Kohl,^f Torsten Mayr,^{id} ^d and Peter Ertl,^{id} ^{*ab}

Translation of advanced cell-based assays exhibiting a higher degree of automation, miniaturization, and integration of complementary sensing functions is mainly limited by the development of industrial-relevant prototypes that can be readily produced in larger volumes. Despite the increasing number of academic publications in recent years, the manufacturability of these microfluidic cell cultures systems is largely ignored, thus severely restricting their implementation in routine toxicological applications. We have developed a dual-sensor integrated microfluidic cell analysis platform using industrial specifications, materials, and fabrication methods to conduct risk assessment studies of engineered nanoparticles to overcome this academic–industrial gap. Non-invasive and time-resolved monitoring of cellular oxygen uptake and metabolic activity (pH) in the absence and presence of nanoparticle exposure is accomplished by integrating optical sensor spots into a cyclic olefin copolymer (COC)-based microfluidic platform. Results of our nanotoxicological study, including two physiological cell barriers that are essential in the protection from exogenous factors, the intestine (Caco-2) and the vasculature (HUVECs) showed that the assessment of the cells' total energy metabolism is ideally suited to rapidly detect cytotoxicities. Additional viability assay verification using state-of-the-art dye exclusion assays for nanotoxicology demonstrated the similarity and comparability of our results, thus highlighting the benefits of employing a compact and cost-efficient microfluidic dual-sensor platform as a pre-screening tool in nanomaterial risk assessment and as a rapid quality control measure in medium to high-throughput settings.

Received 15th June 2021,
Accepted 20th September 2021

DOI: 10.1039/d1lc00528f

rsc.li/loc

Introduction

Nanoparticles present a growing field within the industrial and medicinal sectors because of their wide spectra of advantageous properties. Due to their small nanometer dimensions, nanomaterials display a high surface-to-volume ratio, causing the properties of the surface layer to dominate over those of the bulk material, altering the material's intrinsic properties.¹ The

resulting unique mechanical, magnetic, and electric properties, as well as the strong surface reactivity, make nanomaterials highly valuable in various fields, including electronics, cosmetics, diagnostics, drug delivery, and the food industry.^{2–5} Unfortunately, the often-unknown effects of nanoparticles on human health are still restricting their broader application, especially within the food industry and cosmetics, where their usage is still highly debated.⁵ One of the main problems is that collateral toxic health effects associated with nanoparticle exposure are impossible to predict based on their physicochemical properties alone. Consequently, toxicological testing has therefore been highly recommended for all nanomaterials^{6–8} to better understand the interrelationship between nanoparticle exposure and human health.⁹ Conventional methods for testing the safety of nanomaterials include *in vivo* animal models, which, apart from pressing ethical concerns, present a labor-, time-, and cost-intensive endeavor. Additionally, pre-existing genotypic and phenotypic differences between humans and animals, *e.g.*, rodents, decrease the tests' validity and translatability.¹⁰ Alternatively, *in vitro*, cell-based assays, *e.g.*, MTT, calcein-AM/PI, or WST-1

^a Institute of Applied Synthetic Chemistry and Institute of Chemical Technologies and Analytics, Faculty of Technical Chemistry, Vienna University of Technology, Getreidemarkt 9/163-164, 1060 Vienna, Austria.

E-mail: helene.zirath@tuwien.ac.at, peter.ertl@tuwien.ac.at

^b Austrian Cluster for Tissue Regeneration, Vienna, Austria

^c Karl Chiari Lab for Orthopaedic Biology, Department of Orthopedics and Trauma Surgery, Medical University of Vienna, Währinger Gürtel 18-20, 1090 Vienna, Austria

^d Institute of Analytical Chemistry and Food Chemistry, Graz University of Technology, Stremayrgasse 9, 8010 Graz, Austria

^e kdg opticom GmbH, Am kdg Campus, Dorf 91, 6652 Elbigenalp, Austria

^f Fraunhofer Institute for Biomedical Engineering IBMT, 66280 Sulzbach, Germany

† Electronic supplementary information (ESI) available. See DOI: 10.1039/d1lc00528f

‡ These authors contributed equally.

assays, are performed to assess the impact of nanoparticle exposure on cell viability, which in addition can be supported by morphological analysis.¹¹ Since standard *in vitro* cell-based assays are performed in microtiter plates, they are limited to static cultivation conditions and time-consuming (45 min–4 h), invasive endpoint analysis. The absence of fluid flow, moreover, can result in the gravitational settling of nanoparticles, ultimately favoring nanoparticle aggregation, which has been linked to the creation of physiochemical stress as well as cell death.^{12,13} In other words, reported cytotoxicities using static cell culture conditions may not represent the actual toxicity levels of the investigated nanomaterials. This methodological limitation impacts the predictability of nanotoxicological evaluations, as uptake, accumulation, and biopersistence of nanoparticles *in vivo* are primarily governed by dynamic microenvironments.

We have recently demonstrated that nanoparticle uptake and thus toxicity is strongly modulated by fluid flow, resulting in a strong increase in endocytosis mediated nanoparticle uptake with increasing flow rates up to a critical maximum flow rate above which nanoparticle uptake is severely restricted.¹⁴

Its inherent ability to provide precise spatial and temporal control over fluid dynamics, coupled with low sample volumes and a high degree of flexibility, has rendered microfluidics a promising tool in nanotoxicology, as it allows for the recapitulation of physiological scenarios such as the dynamic nanoparticle exposure of cells within the human body in custom-made platforms.^{12,15} In addition, the option to integrate electrical or optical sensors further equips microfluidics with the ability to non-invasively monitor various critical parameters such as cell-to-cell, cell-to-substrate interactions as well as metabolic activity.^{16–18} Herein, the combinatorial monitoring of oxygen consumption rates (OCR) and acidification rates (ECAR) has proven to be a powerful strategy as it enables the assessment of metabolic shifts or, more specifically, of cytotoxicological effects exerted upon the cell by the uptake of nanoparticles.

While several commercial and academic platforms (see ESI† Table S1) that allow for the assessment of the two physiological parameters OCR and ECAR have been developed, including the Agilent's MitoXpress assay, the Agilent's Seahorse XF analyzer platform, the O2k-FluoRespirometer (Orobo), the SC 1000 Metabolic Chip (Bionas), and the Biochip D (Cellasys), these platforms often fail to account for essential aspects such as dynamic microenvironments, low-production costs, high throughput as well as manufacturing scalability. Among these commercially available platforms, only one technology allows for the integration of the biophysical stimuli fluid flow. Unfortunately, the broad applicability of this system is hampered by the use of an electrochemical sensing approach, low throughput ($n = 6$) coupled with a comparatively large footprint. The use of an electrochemically based read-out also constitutes one of the most significant disadvantages of current academic strategies,^{40–44} as these approaches have been associated with complex integration procedures, the dependency on reference electrodes as well as potential interferences through the consumption of the analyte of interest.

Optical sensing strategies, on the other hand, provide a great alternative as they combine easy miniaturization, integration, and external read-out with low manufacturing costs. Furthermore, optical sensor spots have already shown great promise in determining several essential cell functions, including cell cycle stage, viability, apoptosis, and necrosis, by detecting pericellular concentrations of dissolved oxygen.¹⁹ In addition to cellular respiration, the metabolic activity of cells defined by the accumulation of acidic products such as lactic acid and carbonic acid (*e.g.*, pH-shift) can be monitored using dye-impregnated sensor beads.²⁰ We have recently demonstrated that luminescent oxygen and pH sensor spots can readily be integrated into microfluidic devices and are capable of monitoring cellular responses to different drug exposure scenarios in a dynamic microenvironment.²¹ As such, optical sensing strategies provide the optimal basis for the assessment of crucial cellular parameters such as metabolic activity in the context of industrially relevant nanotoxicological screening platforms.

This study aims to determine whether the non-invasive monitoring of the two metabolic parameters cellular respiration and acidification can be suited to detect nanotoxicological effects in a dynamic microenvironment. Specific focus of the study is directed towards the applicability of non-invasive monitoring as a rapid tool for cellular viability assessments. To that end, a cost-efficient, automatable, dual-sensor integrated microfluidic cell analysis platform compatible with industrial mass manufacturing strategies has been developed adhering to industrial specifications (*e.g.*, aspect ratios, angles, *etc.*), materials (*e.g.*, thermoplastic such as COC) and fabrication methods (*e.g.*, injection molding). First, measurement protocols for non-invasive and real-time monitoring of the two metabolic markers were established and optimized using a highly metabolically active cell line (A549), originating from the alveoli of the lung. Practical application of our industrial-relevant prototype is demonstrated by investigating the two main entry routes of nanoparticles, including the gut barrier in the case of oral exposure as well as the circulatory system *via* the endothelial barrier.²² Established cell barrier models based on immortalized cell lines originating from the small intestine (Caco-2 intestinal epithelial cells) and primary endothelial cells (human umbilical vein endothelial cells, HUVEC) were used.^{11,23} Finally, SiO₂ nanoparticles were selected as reference nanomaterials due to their extensive usage in agriculture, cosmetics, health applications as well as targeted drug delivery.²⁴ Assay verification was performed using state-of-the-art dye exclusion assays as a benchmark to demonstrate the comparability and benefits of employing a microfluidic dual-sensor platform as a rapid nanotoxicological pre-screening tool in medium-throughput to high-content settings.

Materials and methods

Cell culture

A549 human lung carcinoma cells (ATCC® CCL-185™) were cultured in RPMI 1640 Medium (Gibco) supplemented with



10% fetal bovine serum (Sigma Aldrich), L-glutamine (Sigma Aldrich), and 1% antibiotic/antimycotic solution (Sigma Aldrich). Human umbilical vein endothelial cells (HUVECs, PromoCell) were cultured in fully supplemented endothelial cell growth medium 2 (EGM-2, PromoCell) with 5% fetal calf serum up to passages 5–9. Caco-2 (ATCC® HTB-37™) cells were cultured in Eagle's minimum essential medium supplemented with 20% fetal bovine serum (Sigma Aldrich) and 1% antibiotic/antimycotic solution (Sigma Aldrich). All cell cultures were incubated in a humidified atmosphere with 5% CO₂ at 37 °C.

Nanoparticles

Silica nanoparticles (SiO₂-NPs, NM200-JRCNM02000a) with a particle size of 14–23 nm (batch-to-batch variation) and a specific surface area of 189 m² g⁻¹ were kindly provided from the Nanomaterials Repository of the Joint Research Centre (JRC, Ispra, Italy). The silica nanoparticles were dispersed in ddH₂O at a concentration of 10 mg mL⁻¹ by sonication for 30 min. To mitigate errors associated with SiO₂ precipitation within the stock suspension, the nanoparticle solution was vortexed for 1 minute prior to dilution in cell culture medium in the presence or absence of 10% FCS depending on the conducted experiment. The stock solution (10 mg mL⁻¹) was stored at 4 °C.

Microfluidic platforms

1. Academic prototype. Due to its disadvantageous gas permeability properties that render PDMS undesirable for

precise oxygen measurement applications, a xurography based approach was selected for the fabrication of the prototype. Xurography is a rapid prototyping technique that allows for further reduction in iteration periods in chip fabrication compared to standard photolithography.^{25,26} Using this approach a microfluidic device (25 mm × 75 mm × 2.2 mm) consisting of a pre-structured adhesive tape (ARcare 8259 and ARseal 90880, Adhesive Research, Ireland) layered between two glass slides (VWR) was fabricated as previously described.²⁷ Glass was selected as bottom and top substrate to limit unwanted gas transfer during on-chip oxygen measurements. Each biochip layout (see Fig. 2A) features four inlets (drilled diameter 1 mm) that extend into 400 μm wide channels and split into two channels, resulting in 8 cell culture chambers of 0.22 cm² area and 300 μm height in total (total volume of 6.6 μL). Luminescent sensors (*r* = 0.5 mm) were spotted at different locations inside the cell culture chambers as previously described.^{27,28} Additionally, fixtures to house the microfluidic chip and optical fibers were designed using the CAD software (AutoCAD 2017), 3D printed (Original Prusa i3 MK2, Prusa Research), and assembled onto the microfluidic chip.

2. Industrial prototype. Two microfluidic layouts V1 and V2, were designed wherein version 1 (V1), in addition to the Mini Luer connectors at the four inlets and eight outlets, an integrated optical fiber holder (height 10 mm, width 5 mm, diameter 2 mm) was added to stabilize the fibers during luminescent lifetime measurements. The industrial COC-based microfluidic prototypes were manufactured using a high-precision injection molding machine (Engel V200 90 Tech, Arburg) and sealed by bonding a microscope slide with a 142

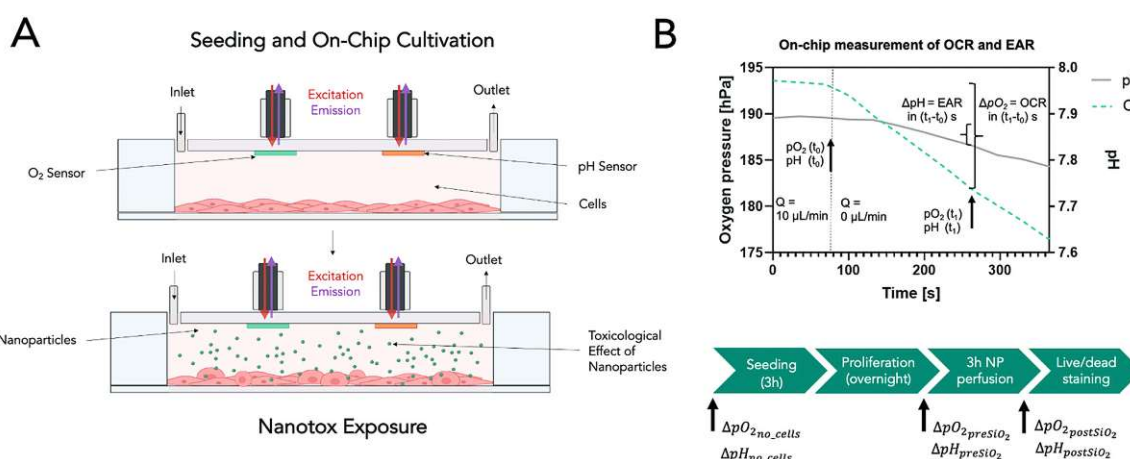


Fig. 1 Set-up and working principle of microfluidic nanotoxicological assessment and on-chip luminescence-based oxygen and pH sensing. A) Schematic representation of the main components during the microfluidic nanotoxicological assessment. Cells are seeded through the inlet of the microfluidic chamber to form a confluent monolayer. Light emitted from the FireSting oxygen/pH meter is guided through the optical fibers and excites the oxygen and pH sensors spots located on the upper part of the chamber. The sensor spots generate oxygen and pH concentration-dependent light signals (emission), which are guided back through the optical fibers and detected by the oxygen/pH meter. B) To measure OCR and ECAR, medium perfusion through the chip (*Q*, 10 μL min⁻¹) was stopped (*t*₀), and the decrease in oxygen pressure and pH within a specific time frame (*t*₁ – *t*₀) was measured, enabling the determination of metabolic rates within a few minutes. OCR (Δ*p*O₂) and ECAR (Δ*p*H) were measured before cell seeding, after overnight cell adhesion and proliferation, and after three h nanoparticle exposure. After the on-chip nanotoxicological assessment, cell viability was controlled with live/dead staining.

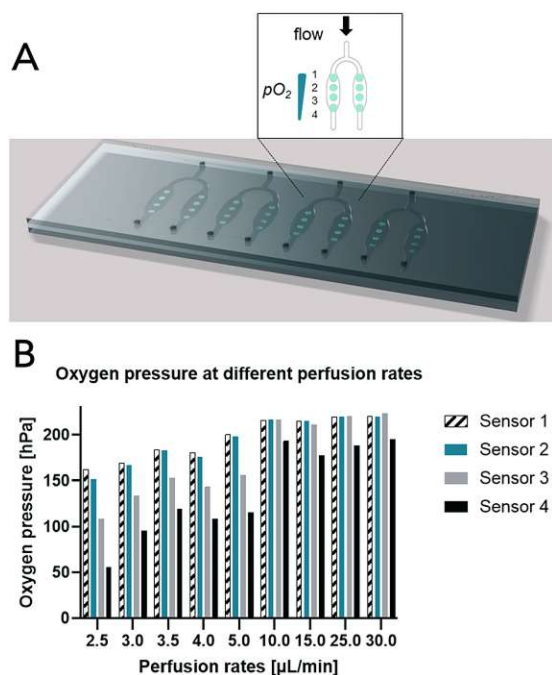


Fig. 2 Characterisation of the oxygen pressure in the microfluidic cell culture chambers. A) Characterisation of the oxygen pressure along microfluidic cell culture chambers in glass prototype. Four oxygen sensor spots were positioned in line along the flow direction to optimize the flow for a homogenous oxygen pressure. B) Measured oxygen gradients in cell culture chamber with a monolayer of A549 cells at different flow rates of medium with flow rates above $10 \mu\text{L min}^{-1}$, a homogenous oxygen pressure was obtained in the upper 3/4 part of the chambers (sensor 1–3) while the cells at the lower part never received fully oxygenized medium (sensor 4).

μm thick pre-cut (GS-24 Desktop Cutter, Roland DGA Corporation, Germany) adhesive film (ARseal 90880, Adhesive, Research, Ireland) to the microfluidic COC biochip layer. Before bonding, two $\sim 250 \mu\text{m}$ small pockets were drilled inside the cell chambers using a 0.8 mm drill mounted on a micro-milling-CNC machine (from BZT (PFK0603) equipped with a milling motor from Kress (1050FME)) to (a) reliably locate the two sensor spots and (b) to enhance the adhesion of the sensor material to the chip. Chemiluminescent oxygen and pH sensors were spotted into the separate $800 \mu\text{m}$ wide pockets using a microdispenser (MDS3200+, Vermes) equipped with a $70 \mu\text{m}$ nozzle and a tungsten tappet was used (tip diameter of 0.7 mm).

Luminescent oxygen and pH sensor integration

For the glass prototype, oxygen sensor microparticles (polystyrene–silicone rubber composite matrix with embedded palladium(II) or platinum(II) *meso*-tetra(4-fluorophenyl)-tetrabenzoporphyrin (PtTPTBPF and PtTPTBPF)) were integrated into the academic prototype by manually pipetting

$1 \mu\text{L}$ of the particle solution directly onto the glass substrate before bonding. Sensor spots were positioned directly above the cell culture chambers. Fabrication and characterization of the oxygen sensor microparticles are described in the work by Ehgartner *et al.*²⁸ For the industrial COC prototype fabrication, the oxygen sensor formulation consisted of 82.5 mg poly-*tert*-butylstyrene particles, stained with 2% PtTPTBPF, which were suspended in 1650 mg of a hydrogel Hydromed D4 solution (5%) in isopropanol/water (3 + 1), leading to a relative PtTPTBPF concentration of 1% after solvent evaporation. In turn, for the pH sensor formulation 0.33 mg of an aza-BODIPY pH indicator dye 4-(5,5-difluoro-7-(4-hydroxyphenyl)-1,9-diphenyl-5H-5 λ 4,6 λ 4-dipyrrolo[1,2-*c*:2',1'-*f*]-[1,3,5,2]triazaborin-3-yl)-*N*-dodecylbenzamide were combined with 54.8 mg of a microcrystalline silanized Egyptian Blue as reference.²¹ Both luminophores were suspended in 1380 mg of a solution of hydrogel Hydromed D4 (8% w/w) in THF/water (9 + 1), leading to an indicator dye concentration of 0.2% w/w and a reference compound concentration of 33.3% w/w after evaporation of the solvents. Homogenization of the sensor formulations was accomplished utilizing a sonifier (Branson) with ten pulses (1 s) and nine seconds cooldown intervals.

CFD modeling of microfluidic flow profiles

To ensure that the microfluidic platform allows for the establishment of uniform flow profiles and thus uniform cell seeding as well as nanoparticle distribution, computational fluid dynamic (CFD) simulations were performed. To that end, 3D models of the microfluidic channel network and cultivation chambers were established for the industrial COC-based prototype using the CAD software Fusion 360. Subsequently, the CFD software Autodesk CFD 2019 was used to simulate flow profiles, velocities, and pressures at the bifurcation points and along the cultivation chambers using a channel height of $342 \mu\text{m}$. The cell culture medium was approximated using the physical properties of water (dynamic viscosity $\mu = 10^{-3} \text{ Pa s}$, density $\rho = 1 \text{ g mL}^{-1}$, $37 \text{ }^\circ\text{C}$). The medium flow rate at the inlet was set to a volumetric flow rate of $10 \mu\text{L min}^{-1}$ to match the external pumping parameter during on-chip nanoparticle flow experiments. The mesh size was automatically generated by the software and optimized after each iteration step. To further support the results obtained by the CFD simulations, microfluidic studies employing fluorescently labeled particles ($\phi 4.8 \mu\text{m}$) were conducted. The analysis of particle speed was performed using the TrackMate Plugin²⁹ and the software ImageJ.

Nanotoxicological reference examination

Before the conduction of the microfluidic toxicology assays, nanotoxicological reference experiments were performed using a conventional Presto Blue (Invitrogen) viability assay in a 48-well plate format with a protocol adapted from Rothbauer *et al.*³⁰ Toxic effects of increasing concentrations of SiO_2 -nanoparticles were assessed using the two epithelial



cell lines A549 and Caco-2, as well as the endothelial cells line HUVECs. Cells were seeded at a density of 3×10^4 cells per well and cultivated under standard conditions (37°C , $5\% \text{CO}_2$) until an 80% confluency was reached. Since serum supplements in cell culture media can alter the bioactivity of nanoparticles, nanoparticle exposure was performed in both serum-free and serum-supplemented media (5–20% FCS).⁸ The medium was changed to serum-free cell media for 60 minutes prior to nanoparticle administration. SiO_2 nanoparticles were diluted/prepared in cell culture medium specific for each cell type, with and without serum, at 7 different concentrations ($0 \mu\text{g mL}^{-1}$, $15.6 \mu\text{g mL}^{-1}$, $31.3 \mu\text{g mL}^{-1}$, $62.5 \mu\text{g mL}^{-1}$, $125 \mu\text{g mL}^{-1}$, $250 \mu\text{g mL}^{-1}$, $500 \mu\text{g mL}^{-1}$).^{31–33} Cell culture medium was aspirated and replaced with medium containing SiO_2 nanoparticles and incubated for 4 hours to induce nanotoxicity. After incubation, the nanoparticles were aspirated, and the solution was replaced with medium containing serum to allow for cellular regeneration (18 h). Subsequently, medium containing 10% Presto Blue (Thermo Fischer Scientific) solution was added, and the plates were incubated for another 2 h at 37°C . The fluorescence of each well was measured (560 nm and 590 nm) on a microplate reader (PerkinElmer multimode EnSpire 2300). Viability was determined by comparing the fluorescence signal of exposed cells to that of the negative control (non-exposed).

Microfluidic set-up

The microfluidic set-up comprised the sensor-integrated microfluidic platforms mounted on top of a heated glass plate (ThermoPlate® Tokai-hit, Japan) within an inverted microscope (IX70, Olympus), connected (Marprene Manifold

Tubes 0.25 mm, Watson-Marlow and Tubing FEP Nat 1/16 \times 0.030, IDEX Health and Science) to a peristaltic pump (205S/CA manual control variable speed pump, Watson Marlow) as well as 16 optical fibers (length 1 m, outer diameter 2.2 mm, fiber diameter 1 mm, Pyrosience) via four FireSting optical oxygen meters (2x FireStingO2, 2x FSPRO-4, Pyrosience, Germany).

The cell culture medium and the nanoparticle solutions were preconditioned employing a desktop incubator, connected to the peristaltic pump using FEP tubing (Tubing FEP Nat 1/16 \times 0.030, IDEX Health and Science). Both the oxygen meters and the microscope were connected to a workstation enabling the interaction through the respective interfaces (Cellsens, Olympus and OxygenLogger, Pyrosience). Fig. 3 comprises a schematic representation of the microfluidic set-up.

Nanotoxicological assessment

Prior to nanotoxicological experiments, the COC microfluidic prototypes were sealed with micro plugs (Hard Tubing Connector, Micro Fluid Connector, and Micro Plug, ThinXXS) and sterilized for 30 minutes using UV light. Microfluidic ports and tubing were sterilized in 70% ethanol before connection to the chip, followed by extensive rinsing with PBS (Sigma Aldrich). Before cell seeding, the chip was coated with 5% collagen type I (Sigma-Aldrich) solution for 1 hour at 37°C and rinsed with sterile PBS (Sigma Aldrich). The heated microscope plate was set at 37°C , and the microfluidic chip was connected to either cell culture medium or nanoparticle solutions (15 mL and 50 mL, Falcon, Fisher-Scientific) located and preconditioned inside a desktop incubator (37°C). The cell culture medium that was used during on-chip cultivation (until nanotoxicological assessment) was

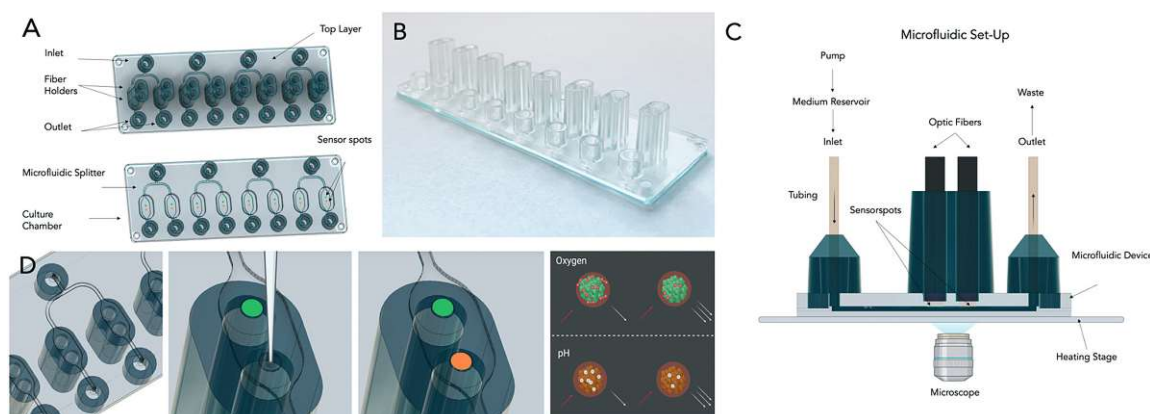


Fig. 3 Industrial prototype of the microfluidic chip with integrated sensors. A) 3D CAD designs (V1 and V2) of the top layers of the 8-chamber chip, including inlets, fluidic splitter, culture chambers, and outlets. V1 (upper panel) displays integrated holders for the optical fibers. B) Photograph of the manufactured chip, (V1), injection-molded in COC and bonded to a glass substrate. C) Overview of the microfluidic set-up comprised of the microfluidic platform mounted on top of a heated microscope stage. D) A sketch illustrating the integration process of the luminescent sensor spots into the top part of the microfluidic device, as well as a schematic illustrating the working principle of the individual sensor spots.





supplemented with 0.5% 2-[4-(2-hydroxyethyl)-1-piperazinyl]-ethanesulfonic acid (HEPES, Sigma Aldrich). Oxygen and pH monitoring was performed at a sampling frequency of 1 Hz and an LED intensity of 80×. For the calibration of the oxygen sensor spots a two-point calibration at anoxic conditions and air-saturated conditions was performed for one spot at 37 °C in cell culture medium to account for slight environmental changes. This calibration was used for all oxygen sensor spots. Anoxic conditions were established by adding NaSO₃, air saturated conditions by shaking the medium right before measurement. To calibrate the pH sensor spots, the signal of each spot was recorded after exposing each chamber with buffers of 8 different pH values ranging from pH 4–10. The cotangents of the measured signal were plotted against the pH values, and the calibration function was obtained by fitting with a Boltzmann sigmoidal equation (as previously described²¹) in a data analysis program (GraphPad Prism).

Following cell seeding (5.5×10^3 cells per chamber) and an attachment period of three hours, medium perfusion ($5 \mu\text{L min}^{-1}$) was initiated and maintained for at least 16 hours (e.g., overnight proliferation) before nanoparticle exposure. Time-resolved measurements of the oxygen consumption and acidification rates were conducted sequentially by halting the flow for 5–10 minutes once every hour. OCR (ΔO_2) and ECAR (ΔpH) were calculated by employing the following equations:

$$\text{Cell viability (\%)} = 100 \times \frac{\Delta p\text{O}_{2\text{postSiO}_2} - \Delta p\text{O}_{2\text{no_cells}}}{\Delta p\text{O}_{2\text{preSiO}_2} - \Delta p\text{O}_{2\text{no_cells}}}$$

$$\text{Cell viability (\%)} = 100 \times \frac{\Delta \text{pH}_{\text{postSiO}_2} - \Delta \text{pH}_{\text{no_cells}}}{\Delta \text{pH}_{\text{preSiO}_2} - \Delta \text{pH}_{\text{no_cells}}}$$

For $\Delta p\text{O}_{2\text{no_cells}}$ and $\Delta \text{pH}_{\text{no_cells}}$ the measured variation in oxygen pressure and pH in chambers without cells during the stop phase was used ($n = 3$). In total, three recordings were taken during each period to estimate the mean ($n = 3$) difference in oxygen pressures (referred to as ΔO_2 in the result section) before and after exposure to the nanoparticle suspensions. Increasing concentrations of SiO₂ nanoparticles in serum-free medium without HEPES at a flow rate of $10 \mu\text{L min}^{-1}$ were added for a period of 3 h, and oxygen consumption and acidification rates were monitored. For each cell type, the microfluidic nanotoxicity assessment has been repeated a minimum of 6 times using different passages of cells and batches of microfluidic chips. At the end of each experiment, cell viability was determined employing a LIVE/DEAD® Viability/Cytotoxicity Assay kit (Life Technologies, Vienna, Austria), Hoechst 33258 solution (94403, Sigma Aldrich) and a fluorescent microscope (IX83 Olympus LifeCell). Staining solutions were prepared according to the manufacturer's instructions and incubated for 15 min at 37 °C. Cells were analyzed and counted with the image analysis software Fiji or ImageJ, respectively. In addition, phase-contrast images were taken before and after

nanoparticle exposure to assess any impact on cell morphology.

Statistical analysis

Cell viability and extracellular acidification rate data were expressed as mean \pm SD or mean \pm SEM. The statistical comparisons of means were performed employing a one-way analysis of variance (ANOVA) test using the biostatistical analysis software GraphPad. Significances were depicted as follows: ≤ 0.0332 (*), ≤ 0.0021 (**), ≤ 0.0002 (***). Estimation of the inhibition concentration 50 and 90 (EC_{50} , EC_{90}) was performed using the SigmaPlot software.

Results and discussion

From the academic prototype and design optimization to industrial prototyping

As a starting point of our design optimization strategy, a previously published microfluidic chamber design²⁷ ($9 \times 3 \times 0.3$ mm per cell culture area 0.22 cm^2 , $6.6 \mu\text{L}$ volume) was used to evaluate on-chip luminescence-based oxygen and pH sensing (see Fig. 1) as a novel tool for rapid nanotoxicological assessments. Initial experiments determined the dissolved oxygen distribution within our microfluidic cell culture chambers to estimate dissolved oxygen levels along the 9 mm long confluent cell layers. To monitor oxygen gradients along the entire length of the culture chamber in the presence of increasing flow rates, four oxygen sensor spots were distributed evenly along the flow direction (see Fig. 2A) and alveolar lung cells (A549), known for their high metabolic activities, were used in this study. Results are shown in Fig. 2B, pointing at a clear flow velocity-dependent oxygen distribution along the cell cultivation chamber. In other words, in the presence of lower flow rates such as 2.5 to $5.0 \mu\text{L min}^{-1}$, a significant cell-induced oxygen level drop from 160 hPa to 50 hPa or 3.4 fold reduction and 190 hPa 110 hPa or 1.7 fold reduction are apparent between sensor 1 and 4. Continuous cellular oxygen uptake resulted in (a) linear dissolved oxygen gradient along the chamber at $2.5 \mu\text{L min}^{-1}$ flow rate, (b) a linear increase of oxygen levels from 160 hPa to 200 hPa at the upstream sensor 1 location in the presence 2.5, 3.0, 4.0, 5.0 and 10 mL min^{-1} and (c) oxygen saturation (200 hPa) at locations 1, 2 and 3 in the presence of $10 \mu\text{L min}^{-1}$. This means that volume flow rates above $10 \mu\text{L min}^{-1}$ are needed to ensure comparable ($\pm 1.5\%$ variation) oxygen tensions throughout our measurement chambers. As an 11% lower dissolved oxygen level between upstream sensor 1 and downstream sensor 4 was still present even at flow rates of $50 \mu\text{L min}^{-1}$ (data not showed), it was concluded that the chamber length needs to be reduced to ensure a homogenous oxygen pressure in the entire chamber.

To ensure that the design of the microfluidic device allows for an even distribution of volume flow, a prerequisite for uniform nanoparticle exposure and thus comparability and reproducibility, a CFD simulation was performed (ESI† Fig. S1). A flow velocity of $10 \mu\text{L min}^{-1}$ (at the T-junction and cell

culture chambers ($5 \mu\text{L min}^{-1}$), which was selected based on the initial oxygen distribution experiments, revealed a uniform volume flow suggesting even nanoparticle distribution throughout the chip covering the entire cell culture area. Microfluidic studies employing fluorescently labeled particles were conducted to further support the results obtained by the CFD simulation. As expected, particle distribution throughout the cell culture chamber revealed an even flow as well as particle distribution.

Based on the above results, two minor design optimizations were performed prior to the industrial-relevant prototyping, including the reduction of the cell culture chamber length by 20% (from 9 mm to 7.2 mm) to ensure similar and homogenous oxygen pressure distribution along the entire cell culture area under measurement conditions. In addition, the channel width of the inlets and outlets were narrowed from 1 mm to 0.5 mm to restrict unwanted cell growth in the inlet that may compromise optimal oxygen availability. Moreover, the spatial distance between individual cell culture chambers was adapted to a microtiter plate format (e.g., 9 mm center-to-center). Fig. S1† shows the industrial prototype's final design and dimensions that employ the oxygen impermeable material cycloolefin copolymer (COC). While the microfluidic top layer (total volume of $6 \mu\text{L}$), including Mini Luer connectors, sensor grooves, and optical fiber ports, was fabricated using hot embossing technology, a glass microscope slide was bonded to the microfluidic COC layer using an adhesive film ARseal 90880. Fig. 3 depicts the two configurations of the industrial-relevant prototypes where design V1 features additional guiding ports as a simple plug-in system for the optical cables needed for the chemiluminescent oxygen and pH measurements. Oxygen and pH sensors were spotted into the circular grooves before the device assembly. Microfluidic chips were stored in light-impermeable containers before usage up to 24 months without any stability loss, sensor drifts, and a decrease in signal (data not shown).

High sensitivity nanotoxicity assessment based on combined oxygen consumption and extracellular acidification rates

Before on-chip experiments, the cytotoxicity of silicon oxide nanoparticles (SiO_2 diameter $25.0 \pm 3.66 \text{ nm}$) was characterized using standard static culture plates to determine their suitability as a reference nanomaterial. Initial experiments (see Fig. S3†) show dose–response curves for

lung, gut, and endothelial cells using decreasing concentrations of nanosilica ($500\text{--}250\text{--}125\text{--}62.5\text{--}31.3\text{--}15.6 \mu\text{g mL}^{-1}$) in the presence and absence of serum protein. This study revealed that a 4-hour exposure in the absence of serum protein is sufficient to induce significant cytotoxic effects, thus confirming the mitigating effect of protein corona at the surface of nanoparticles.³⁴ Interestingly, a significant cell type-dependent shift in MIC values from $9 \mu\text{g mL}^{-1}$ to $23 \mu\text{g mL}^{-1}$ to $180 \mu\text{g mL}^{-1}$ was found for endothelial, lung, and gut cells, respectively. The observed differences in dose–response curves between the selected cell types highlight the importance of including various cell types in nanotoxicological evaluations. Table 1 lists the calculated EC_{50} values obtained from our nanotoxicology study and compares previously published values. As a result of our pre-screening study, subsequent microfluidic nanotoxicity assessments were conducted using $50 \mu\text{g mL}^{-1}$ nanosilica for A549 (used in initial prototype study), $100 \mu\text{g mL}^{-1}$ and $500 \mu\text{g mL}^{-1}$ for HUVECs as well as $50 \mu\text{g mL}^{-1}$ and $500 \mu\text{g mL}^{-1}$ for Caco-2 cells.

Next, the additive effect of nanoparticle perfusion, which has been linked to an increase in nanoparticle uptake and intracellular accumulation, on cytotoxicity was investigated in more detail. In a comparative study, differences in cellular viability among static and dynamic exposure scenarios were evaluated. Viability results using live/dead staining are shown in Fig. S6† and point at increased toxicities in the presence of fluid flow. For instance, a decrease of viability by 13% ($50 \mu\text{g mL}^{-1}$) and 25% ($500 \mu\text{g mL}^{-1}$) was observed in the dynamic model compared to the static model for Caco-2 monolayers. In the case of HUVECs, a decrease of 14% ($100 \mu\text{g mL}^{-1}$) and 25% ($500 \mu\text{g mL}^{-1}$) was observed for the dynamic exposure scenario compared to the static exposure scheme. Table 2 lists the calculated cell viabilities for each scenario and cell type, as well as a comparison thereof. The modulatory effects of fluid flow on nanotoxicity seen in the current work are in line with previous investigations of our group and other microfluidic studies on uptake and toxicity of nanoparticles for epithelial and endothelial models, where dynamic conditions increase cytotoxicity even for nanoparticle species with low toxicity (e.g., Au nanoparticles).^{14,37–39} This observation can be explained by a combination of i) increased endocytosis mediated uptake under physiological shear stress as well as ii) an overall higher dosage of nanoparticles at a dynamic exposure scenario compared to a static exposure scheme at the same concentrations.

Table 1 Calculated EC_{50} and EC_{90} values of $\text{SiO}_2\text{-NP}$ ($25.0 \pm 3.66 \text{ nm}$) after 4 h treatment with A549, Caco-2, and HUVEC

Cell type	EC_{50} ($\mu\text{g mL}^{-1}$)	EC_{90} ($\mu\text{g mL}^{-1}$)	EC_{50} values from literature ($\mu\text{g mL}^{-1}$, 0% serum)
A549	56 (0% serum) >500 (10% serum)	419 (0% serum) >500 (10% serum)	50 (60 nm) ³¹
Caco-2	>500 (0% serum) >500 (10% serum)	>500 (0% serum) >500 (10% serum)	>256 (55 nm) ³⁵
HUVEC	20 (0% serum) 97 (5% serum)	49 (0% serum) 176 (5% serum)	<50 (ref. 33) >200 (20 nm) ³⁶



Table 2 Calculated cell viabilities for Caco-2 cells and HUVECs after 3 h static and dynamic exposure scenarios with silica nanoparticles inside the microfluidic COC prototype. Cell viabilities are derived from live/dead assays and expressed as mean value \pm SD ($n = 3-9$). The difference in the viability of the dynamic scenario compared to the static is shown under “static vs. dynamic”

NP concentration (0% serum)	Caco-2		
	Viability static	Viability dynamic	Static vs. dynamic
0 $\mu\text{g mL}^{-1}$	96.8 \pm 1%	98.9 \pm 1%	2.19%
50 $\mu\text{g mL}^{-1}$	90.8 \pm 1%	79.5 \pm 9%	-12.45%
500 $\mu\text{g mL}^{-1}$	78.5 \pm 1%	58.8 \pm 2%	-25.07%

NP concentration (5% serum)	HUVECs		
	Viability static	Viability dynamic	Static vs. dynamic
0 $\mu\text{g mL}^{-1}$	98.7 \pm 0.5	95.5 \pm 3.0	-3.11%
100 $\mu\text{g mL}^{-1}$	97.5 \pm 0.5	84.0 \pm 6.6	-13.85%
500 $\mu\text{g mL}^{-1}$	82.9 \pm 6.2	41.1 \pm 14.9	-50.50%

The impact of cell type and number on cellular acidification rates was investigated in subsequent experiments using the industrial-relevant prototype to determine optimum assay conditions. In a series of experiments, Caco-2 cells and HUVECs were seeded with increasing seeding densities (1×10^5 , 5×10^5 , and 1×10^6 cells per mL), and pH shifts were monitored during cell adhesion and spreading processes. Extracellular acidifications rates, expressed as changes in pH, were measured every hour following a 20 min stop of flow. Results shown in Fig. 4A/B reveal a linear decrease in pH values in the presence of increasing Caco-2 and HUVEC cell seeding densities after a 3 h cultivation period. Additionally, luminescence-based pH measurements showed a significantly stronger (3-fold) metabolic activity of Caco-2 cells over HUVECS (see Fig. 4C) already during cell seeding, thus highlighting the ability of integrated microfluidic pH sensing to detect even minor metabolic differences. To

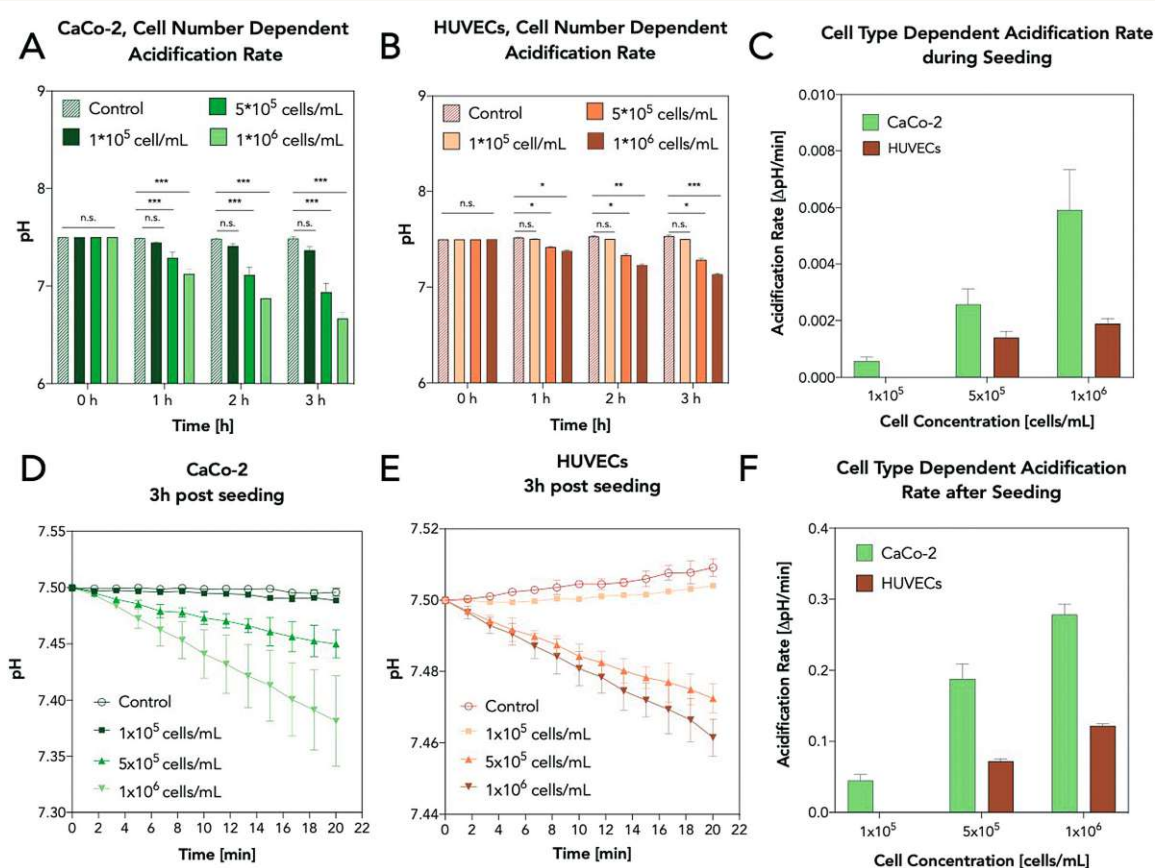


Fig. 4 Impact of cell density and cell type on ECAR. A) Cell number-specific acidification of Caco-2 cells during 3 hours of adhesion. B) Cell number-specific acidification of HUVECs during 3 hours of adhesion. C) Calculated ECAR during 3 hours of adhesion for Caco-2 cells and HUVECs. D) Cell number specific acidification of Caco-2 cells during stop flow phase 4 hours after cell seeding. E) Cell number specific acidification of HUVECs during stop flow phase 4 hours after cell seeding. F) Calculated ECAR during stop flow phase 4 hours after cell seeding for Caco-2 cells and HUVECs.



determine the minimum assay time needed to identify differences in cellular metabolism, acidification rates are recorded after 3 h post-seeding for every two minutes in the presence of increasing cell numbers. Fig. 4D shows pH shifts induced by the metabolic activity of Caco-2 cells over a period of 20 min resulting in a total ΔpH of 0.13 ± 0.04 , 0.56 ± 0.09 , 0.845 ± 0.06 after 3 hours of cell adhesion (for 1×10^5 , 5×10^5 , and 1×10^6 cells per mL, respectively). The above cell densities were selected to achieve either a confluent monolayer of cells (1×10^6 cells per mL), 50% surface coverage (5×10^5 cells per mL) and 10% confluency in the presence of 1×10^5 cells per mL. Similar results were obtained using HUVECs, where a total ΔpH of 0.22 ± 0.02 and 0.37 ± 0.01 was obtained for higher cell densities (see Fig. 4E). In other words, metabolic differences can be readily detected within 10 min during stop-flow conditions (see Fig. 4F). To further investigate whether pH changes can be identified during continuous flow conditions, cellular acidification rates were constantly monitored during nanoparticle exposure. Fig. 5 shows calculated pH values over a period of 1 hour in the absence and presence of increasing nanoparticle concentrations. While measured pH values in control chambers containing no cells but NPs remained stable, the chambers containing monolayers of Caco-2 cells all revealed a time-dependent pH change. While in the absence of nanoparticles, an almost linear pH decrease was evident, chambers perfused with nanoparticle concentrations of $50 \mu\text{g mL}^{-1}$ and $500 \mu\text{g mL}^{-1}$ revealed lower metabolic activities that decreased over nanoparticle exposure time. Similar results were observed in repeated experiments

Table 3 Change in extracellular pH for Caco-2 after 3 h perfusion with silica nanoparticle at different concentrations expressed as mean values \pm SD ($n = 3-6$)

Nanoparticle concentration	ΔpH
$0 \mu\text{g mL}^{-1}$	-0.063 ± 0.07
$50 \mu\text{g mL}^{-1}$	0.288 ± 0.04
$500 \mu\text{g mL}^{-1}$	1.282 ± 0.25
Medium	0.018 ± 0.01

displaying the same trend for each nanoparticle scenario. Table 3 shows ΔpH presented as the difference in pericellular pH between the start and after 3 h perfusion at a flowrate of $5 \mu\text{L min}^{-1}$. Overall, the ability to rapidly obtain information on dynamic cellular metabolic changes in a time-resolved manner further supports the application of acidification rates as a reliable and robust indicator of cell viability. However, to increase the sensitivity of the integrated pH sensor solely, stop-flow measurement conditions are used in all subsequent experiments.

To finally verify the ability to detect induced metabolic shifts in the presence of $50 \mu\text{g mL}^{-1}$ and $500 \mu\text{g mL}^{-1}$ nanosilica, in the case of Caco-2 cells as well as $100 \mu\text{g mL}^{-1}$ and $500 \mu\text{g mL}^{-1}$ nanosilica in the case of HUVECs, oxygen consumption rates, and extracellular acidification were monitored. Fig. 6 shows raw data before and after exposure to silicon oxide nanoparticle suspensions. Oxygen consumption and acidification were recorded in triplicates before cell seeding, after overnight adhesion before nanoparticle exposure, and again after 3 hours of nanoparticles exposure. During the stop-flow measurement period (pump off), an immediate decrease in pericellular oxygen pressure (see Fig. 6G) and extracellular pH (see Fig. 6H) was noticeable for both cell types. In fact, obtained metabolic changes correlated well with obtained cell viabilities using state-of-the-art dye exclusion assays and morphological evaluations using phase-contrast micrographs (see also Fig. S5†). While in the presence of $10 \mu\text{L min}^{-1}$ flow rates, oxygen and pH levels remained stable, reduced oxygen depletion rates and pH shifts (see insets) were already detected for Caco-2 cells in the presence of $50 \mu\text{g mL}^{-1}$ silica nanoparticles. To evaluate the comparability of on-chip metabolic sensing to standard cell-based nanotoxicological assays, cell viabilities obtained from oxygen, pH sensing, and live/dead staining in the presence of increasing silica oxide nanoparticle concentrations were compared between Caco-2 cells and HUVECs.

Results in Fig. 6G/H not only show a dose-dependent viability decrease in the presence of increasing nanosilica concentrations but also highlight the similarity of calculated %-viability values. For instance, viability of Caco-2 cells after exposure to a nanoparticle concentration of $50 \mu\text{g mL}^{-1}$ decreased to $79.5 \pm 8.9\%$ (live/dead), $79.4 \pm 6.1\%$ (oxygen consumption rates), and $77.1 \pm 9.2\%$ (extracellular acidification rates). In the presence of $500 \mu\text{g mL}^{-1}$ nanoparticles cell viability decreased to $58.8 \pm 2.4\%$ (live/dead), $52.3 \pm 5.2\%$ (oxygen consumption), and $58.9 \pm 2.7\%$

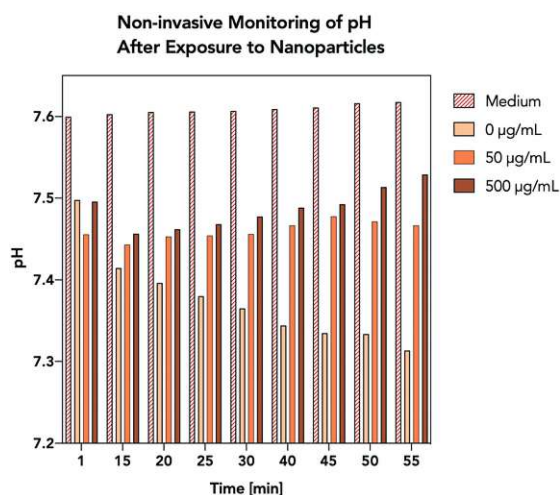


Fig. 5 Representative graph of extracellular pH in chambers with monolayers of Caco-2 cells during nanoparticle exposure. While in the control chamber ($0 \mu\text{g mL}^{-1}$), the ECAR of cells is higher than the exchange of new medium, for both chambers exposed to nanoparticles (50 and $500 \mu\text{g mL}^{-1}$), a decrease in metabolic rate (increasing pH) is observed, visualizing the toxicological effect of nanoparticles.



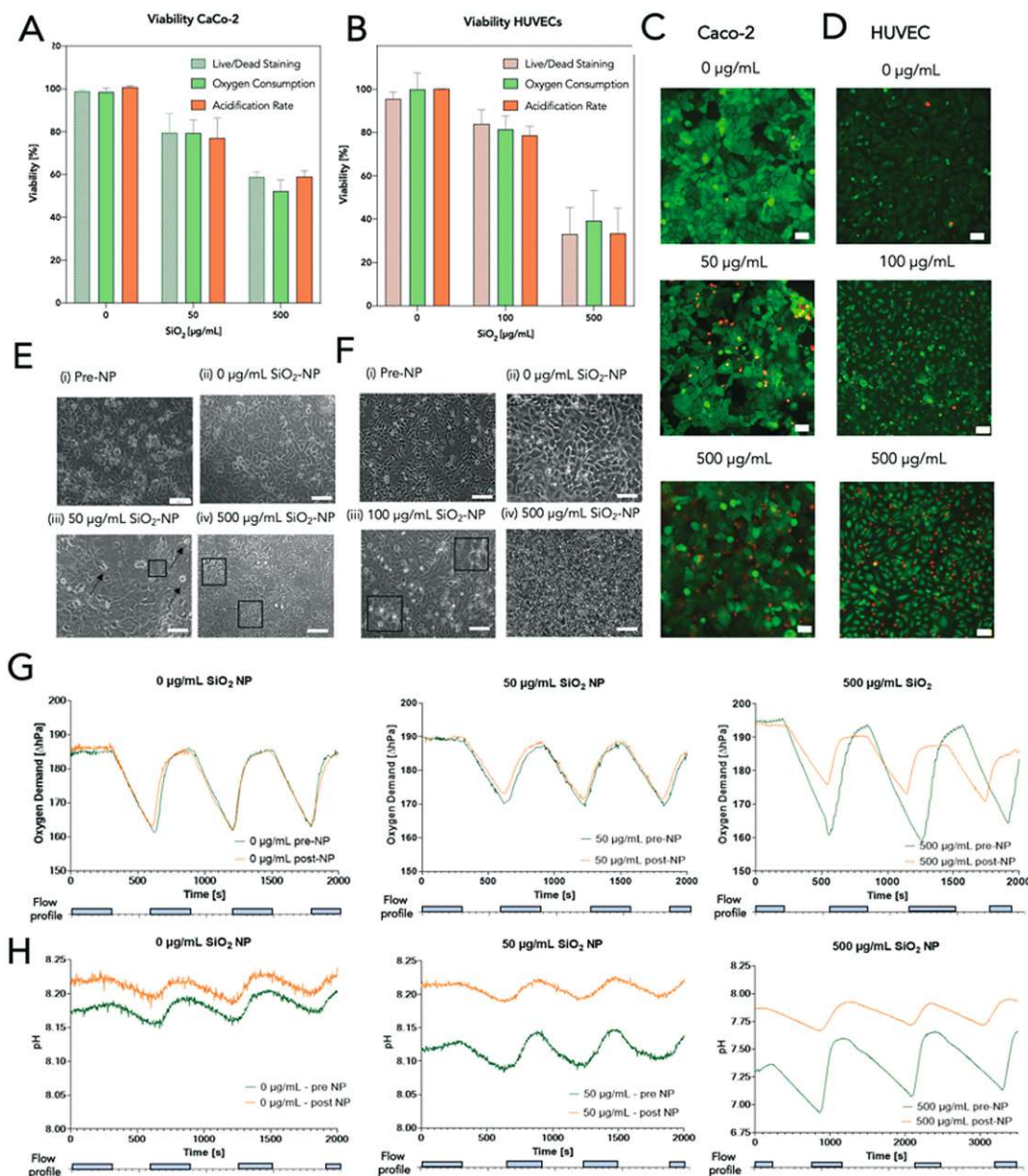


Fig. 6 Nanotoxicity assessment after three h perfusion in microfluidic cell culture chambers with different validation methods. A) Cell viability of CaCo-2 cells calculated with live/dead staining, oxygen consumption, and acidification rates. B) Cell viability of HUVECs calculated with live/dead staining, oxygen consumption, and acidification rates. C) Fluorescence images of a live/dead assay of CaCo-2 cells after 3 hours of nanoparticle exposure. Scale bar: 50 µm. 20× magnification. D) Fluorescence images of a live/dead assay of HUVECs after 3 hours of nanoparticle exposure. Scale bar: 50 µm. 20× magnification. E) Phase-contrast micrographs of CaCo-2 cells after (i) over-night proliferation in standard culture medium, (ii) after 3 h perfusion of medium (control), (iii) after 3 h perfusion with 50 µg ml⁻¹ SiO₂-NP (arrows depict detaching and disruptions in the cell monolayer) and (iv) and 500 µg ml⁻¹ SiO₂-NP (highlighted images present sections of detaching and fragmented cells). Scale bar: 100 µm. 10× magnification. F) Phase-contrast micrographs of HUVECs after (i) over-night proliferation in standard culture medium, (ii) after 3 h perfusion of medium (control), (iii) after 3 h perfusion with 100 µg ml⁻¹ SiO₂-NP (inlets display zoomed in picture sections of rounded/detaching cells and apoptotic bodies) (iv) and 500 µg ml⁻¹ SiO₂-NP. Scale bar: 100 µm. 10× magnification. Representative graphs of pH and oxygen measurements during stop phase (pump off) and return to the baseline during the flow phase (10 µl min⁻¹) in microfluidic cell culture chambers before and after nanoparticle exposure. The related flow profile is shown under each graph. G) Oxygen consumption of CaCo-2 cells measured in three different chambers with increasing nanoparticle concentration (green lines: before nanoparticle exposure, orange lines: after nanoparticle exposure). H) Extracellular acidification of CaCo-2 cells measured in three different chambers with increasing nanoparticle concentration (green lines: before nanoparticle exposure, orange lines: after nanoparticle exposure).



(acidification). Similar comparability was found using HUVECs where 3 h exposure to $100 \mu\text{g mL}^{-1}$ nanoparticles resulted in a cell viability decrease to $84.0 \pm 6.6\%$ (live/dead), $81.6 \pm 6.3\%$ (oxygen consumption), and $79.7 \pm 4.3\%$ (acidification), respectively, while $500 \mu\text{g mL}^{-1}$ concentration revealed a viability of $41.1 \pm 14.9\%$ (live/dead), $37.6 \pm 11.6\%$ (oxygen consumption), and $36.1 \pm 11.6\%$ (acidification).

In fact, data analysis (see Fig. S4†) has shown that by using this sensor-based microfluidic analysis approach, cellular viabilities can be readily detected after 20 seconds, resulting in a 90–720× reduction in assay time, compared to conventional viability assays. Examples from live/dead staining images after nanoparticle exposure are depicted in Fig. 6C (Caco-2) and D (HUVECs). It is also important to note that microfluidic culture conditions, including the assay protocol, did not have a significant adverse effect on cell viabilities since control measurements yielded viabilities around $100 \pm 5\%$. Since morphological evaluations are also routinely conducted to assess adverse effects of nanoparticles, phase-contrast images are also provided in Fig. 6E/F. As an example, before NP-perfusion, Caco-2 cells formed a confluent monolayer exhibiting a cobblestone morphology typical of epithelial cells (Fig. 6Ei), which changed following the exposure to 50 and $500 \mu\text{g mL}^{-1}$ nanoparticles, wherein Caco-2 cells displayed a disrupted monolayer, detaching as well as fragmented cells (Fig. 6Eiv). Similar morphological changes were observed in HUVECs, which initially showed elongated cells (Fig. 6Fi), leading to rounded cell morphology, characteristic for detaching cells, as well as indications of cellular fragmentation (Fig. 6Fiii). After exposure with the highest concentration ($500 \mu\text{g mL}^{-1}$), cell density reduction, irregular shape, and cellular shrinkage (apoptotic cells) were observed (Fig. 6Fiv).

Conclusions

In the current work, we have developed an industry-compatible microfluidic multi-sensor integrated prototype to accelerate the transition from academic prototyping to large-scale production of next-generation microfluidic systems containing integrated optical microsensors. It is essential to highlight that a wide range of academic prototypes can either not be fabricated by large-scale microfluidic producers or need significant re-engineering, thus resulting in long development times and accumulation of costs. This academic–industrial development gap can primarily be associated with the different materials and methods, including design specifications used for rapid prototyping in academic and industrial settings. While academic prototyping moves from soft lithography using PDMS to 3D printing technologies, industrial manufacturers are still limited to hot embossing and injection molding using thermoplastic polymers (e.g., COC, PMMA, PE). This means that material choice and properties, as well as manufacturable aspect ratios, wall angles, and other features, are predefined by industrial standards.

We have employed a two-step engineering strategy to reduce the overall microfluidic development time needed to go from academic prototyping to industrial prototypes to piloting to mass production. While in the first step, xurography is used to optimize geometries of the microfluidic network, two injection-molded substrates using COC are fabricated in a second step to produce industrial-relevant prototypes. Although device assembly, surface modification, and sensor integration are still performed manually, a medium number (above 100) of fully functional biochips can be readily built and tested prior to a final design freeze needed for large-volume production using automated assembly streets. In our study, we demonstrated the ability to non-invasively monitor cellular metabolic activities, including oxygen consumption and acidification rates, in real-time using our industrial-relevant prototypes. Our results show that oxygen consumption and extracellular acidification rates linearly depend on increasing cell densities but significantly differ between cell types featuring higher (e.g., cancer cells) or lower (e.g., primary cells) metabolic activities. In a final practical application, our dual-sensing microfluidic platform was used to reliably and reproducibly determine the cytotoxicity of SiO_2 nanoparticles on epithelial (Caco-2) and endothelial (HUVEC) cells. Results of our microfluidic nanotoxicological screening study further revealed that rapid, non-invasive monitoring of nanomaterial–biology interactions provides similar outcomes than recommended endpoint cell-based assays using dye-exclusion principles, while significantly reducing assay times by a factor of 90–720×. In summary, the developed chip system is ready to be directly translated into mass production due to the fast and time-efficient prototyping strategy, manufacturability of the industrial-relevant prototypes combined with the easy operation and integration of sensors spots.

Author contributions

HZ, SS, and PE conceived the project, designed the experimental outline, and wrote the manuscript. HZ, SS, TS, and MR performed the microfluidic experiments and analyzed the data. DR and SS conceived and performed finite volume CFD simulations. BM and TM prepared the optical sensors for oxygen and pH biosensing. JK, AW, and MW fabricated and characterized the microfluidic device. YK provided both A549 and Caco-2 cell lines and shared her expertise in cellular handling. All authors contributed to and revised the final manuscript.

Conflicts of interest

There are no conflicts to declare.

Acknowledgements

This work was funded by the Austrian Research Promotion Agency (FFG; 869173), by the European Union's Marie Skłodowska-Curie Action (823981) and by the Fonds National



de la Recherche (FNR) Luxembourg in the M-era Net project NanoPD (INTER/MERA/17/11760144). The authors acknowledge the TU Wien University Library for financial support through its Open Access Funding Program. Schematics were created using BioRender.com.

Notes and references

- C. A. Silvera Batista, R. G. Larson and N. A. Kotov, *Science*, 2015, **350**, 1242477.
- C. E. Carlton, L. Rabenberg and P. J. Ferreira, *Philos. Mag. Lett.*, 2008, **88**, 715–724.
- S. Moeinzadeh and E. Jabbari, in *Springer Handbook of Nanotechnology*, Springer, Berlin, Heidelberg, 2017, pp. 335–361.
- M. Orazzadeh, A. Khodadadi, V. Bayati, S. Saremy, M. Farasat and L. Khorsandi, *Cell J.*, 2015, **17**, 412–421.
- G. Pinget, J. Tan, B. Janac, N. O. Kaakoush, A. S. Angelatos, J. O'Sullivan, Y. C. Koay, F. Sierro, J. Davis, S. K. Divakarla, D. Khanal, R. J. Moore, D. Stanley, W. Chrzanowski and L. Macia, *Front. Nutr.*, 2019, **6**, DOI: 10.3389/fnut.2019.00057.
- M. S. Olson and P. L. Gurian, *J. Nanopart. Res.*, 2012, **14**, 786.
- J. S. Qianjun He, Z. Zhang, F. Gao and Y. Li, *Small*, 2011, **7**, 271–280.
- C. Pisani, E. Rascol, C. Dorandeu, J. Gaillard, C. Charnay, Y. Guari, J. Chopineau, J. Armengaud, J.-M. Devoisselle and O. Prat, *PLoS One*, 2017, **12**, e0182906.
- H. M. Braakhuis, S. K. Kloet, S. Kezic, F. Kuper, M. V. D. Z. Park, S. Bellmann, M. Van Der Zande and S. Le, *Arch. Toxicol.*, 2015, **89**, 1469–1495.
- S. K. Kloet, *PhD*, Wageningen University, 2016.
- F. Sambale, F. Stahl, F. Rüdinger, D. Seliktar, C. Kasper, D. Bahnemann and T. Scheper, *J. Nanomater.*, 2015, **2015**, 1–16.
- S. K. Mahto, T. H. Yoon, H. Shin and S. W. Rhee, *Biomed. Microdevices*, 2009, **11**, 401–411.
- S. K. Mahto, T. H. Yoon and S. W. Rhee, *Biomicrofluidics*, 2010, **4**, 034111.
- V. Charwat, I. Olmos Calvo, M. Rothbauer, S. R. A. Kratz, C. Jungreuthmayer, J. Zanghellini, J. Grillari and P. Ertl, *Anal. Chem.*, 2018, **90**, 3651–3655.
- S. K. Mahto, V. Charwat, P. Ertl, B. Rothen-Rutishauser, S. W. Rhee and J. Sznitman, *Nanotoxicology*, 2015, **9**, 381–395.
- L. Richter, V. Charwat, C. Jungreuthmayer, F. Bellutti, H. Brueckl and P. Ertl, *Lab Chip*, 2011, **11**, 2551–2560.
- V. Charwat, M. Purtscher, S. F. Tedde, O. Hayden and P. Ertl, *Lab Chip*, 2013, **13**, 785–797.
- V. Charwat, M. Rothbauer, S. F. Tedde, O. Hayden, J. J. Bosch, P. Mueller, R. Hainberger and P. Ertl, *Anal. Chem.*, 2013, **85**, 11471–11478.
- P. Ebbesen, K. U. Eckardt, F. Ciampor and E. O. Pettersen, *Acta Oncol.*, 2004, **43**, 598–600.
- J. C. Owicki and J. Wallace Parce, *Biosens. Bioelectron.*, 1992, **7**, 255–272.
- M. Müller, P. Sulzer, M. Walch, H. Zirath, T. Buryška, M. Rothbauer, P. Ertl and T. Mayr, *Sens. Actuators, B*, 2021, **334**, 129664.
- W. W. Robert Landsiedel, L. Ma-Hock, A. Kroll, D. Hahn, J. Schnekenburger and K. Wiench, *Adv. Mater.*, 2010, **22**, 2601–2627.
- B. Ekwall, V. Silano and F. Zucco, *Short-Term Toxic. Tests Non-Genotoxic Eff.*, 1990, vol. 7, pp. 75–98.
- P. G. Jeelani, P. Mulay, R. Venkat and C. Ramalingam, *Silicon*, 2020, **12**, 1337–1354.
- S. R. A. Kratz, C. Eilenberger, P. Schuller, B. Bachmann, S. Spitz, P. Ertl and M. Rothbauer, *Sci. Rep.*, 2019, **9**, 1–12.
- D. A. Ferreira, M. Rothbauer, J. P. Conde, P. Ertl, C. Oliveira and P. L. Granja, *Adv. Sci.*, 2021, **8**(8), 2003273.
- H. Zirath, M. Rothbauer, S. Spitz, B. Bachmann, C. Jordan, B. Müller, J. Ehgartner, E. Priglinger, S. Mühleder, H. Redl, W. Holthöner, M. Harasek, T. Mayr and P. Ertl, *Front. Physiol.*, 2018, **9**, 1–12.
- J. Ehgartner, P. Sulzer, T. Burger, A. Kasjanow, D. Bouwes, U. Krühne, I. Klimant and T. Mayr, *Sens. Actuators, B*, 2016, **228**, 748–757.
- J. Y. Tinevez, N. Perry, J. Schindelin, G. M. Hoopes, G. D. Reynolds, E. Laplantine, S. Y. Bednarek, S. L. Shorte and K. W. Eliceiri, *Methods*, 2017, **115**, 80–90.
- S. Peter, D. Sticker, M. Rothbauer, S. Lechner, M. Hehenberger and P. Ertl, *Lab Chip*, 2015, **15**, 4542–4554.
- I.-L. H. Annika Mareike Gramatke, *J. Nanomed. Nanotechnol.*, 2014, **05**(06), 1000248.
- L. Armand, A. Tarantini, D. Beal, M. Biola-Clier, L. Bobyk, S. Sorieul, K. Pernet-Gallay, C. Marie-Desvergne, I. Lynch, N. Herlin-Boime and M. Carriere, *Nanotoxicology*, 2016, **10**, 913–923.
- J. Duan, Y. Yu, Y. Li, Y. Yu, Y. Li, X. Zhou, P. Huang and Z. Sun, *PLoS One*, 2013, **8**, e62087.
- A. Lesniak, F. Fenaroli, M. P. Monopoli, C. Åberg, K. A. Dawson and A. Salvati, *ACS Nano*, 2012, **6**, 5845–5857.
- A. Tarantini, R. Lancelot, A. Mourot, M. T. Lavault, G. Casterou, G. Jarry, K. Hogeveen and V. Fessard, *Toxicol. In Vitro*, 2015, **29**, 398–407.
- X. Liu and J. Sun, *Biomaterials*, 2010, **31**, 8198–8209.
- M. Rothbauer, I. Praisler, D. Docter, R. H. Stauber and P. Ertl, *Biosensors*, 2015, **5**, 736–749.
- A. Oddo, M. Morozesk, E. Lombi, T. B. Schmidt, Z. Tong and N. H. Voelcker, *Nanoscale Adv.*, 2021, **3**, 682–691.
- V. Raghavan, Y. Rbaibi, N. M. Pastor-Soler, M. D. Carattino and O. A. Weisz, *Proc. Natl. Acad. Sci. U. S. A.*, 2016, **113**, E1587.
- E. Tanumihardja, R. H. Slaats, A. D. Van Der Meer, R. Passier, W. Olthuis and A. Van Den Berg, *ACS Sens.*, 2021, **6**, 267–274.
- S. A. M. Shaegh, F. De Ferrari, Y. S. Zhang, M. Nabavinia, N. B. Mohammad, J. Ryan, A. Pourmand, E. Laukaitis, R. B. Sadeghian, A. Nadhman, S. R. Shin, A. S. Nezhad, A. Khademhosseini and M. R. Dokmeci, *Biomicrofluidics*, 2016, **10**(4), 044111.
- K. S. Lee, P. Boccazzi, A. J. Sinskey and R. J. Ram, *Lab Chip*, 2011, **11**, 1730–1739.
- A. Weltin, K. Slotwinski, J. Kieninger, I. Moser, G. Jobst, M. Wego, R. Ehret and G. A. Urban, *Lab Chip*, 2014, **14**, 138–146.
- S. H. Huang, K. S. Huang and Y. M. Liou, *Microfluid. Nanofluid.*, 2017, **21**(1), DOI: 10.1007/s10404-016-1841-z.



3.4 MANUSCRIPT #2 – SUPPLEMENTARY INFORMATION

Supplemental Information

Table S1: Comparative overview of state-of-the-art oxygen and pH sensing platforms

		MICROENVIRONMENT	THROUGHPUT	SENSORS AND SENSING PRINCIPLE	ADDITIONAL COMMENTS
COMMERCIALIZED	<i>MitoXpress assay (Agilent)</i>	Static	High	Dispersed Oxygen and pH Probes	Requires mineral oil → potential extraction of lipophilic substances; Assay time: 60-90 min
	<i>Seahorse XF analyzer platform (Agilent)</i>	Static	High	Optical O ₂ and pH measurement	Up to 4 compounds can be added; Assay time: 60-90 min
	<i>O2k-FluoRespirometer (Orbos)</i>	Static	Low	Electrochemical O ₂ and pH measurement	Invasive Requires Permeabilized Tissues or Cells, Individual Cells
	<i>SC 1000 Metabolic Chip (Bionas)</i>	Dynamic	Low N=6 Big Footprint	Electrochemical O ₂ and pH measurement	Non-invasive monitoring; Limited Optical Access; Discontinued
	<i>Biochip D (Cellasys) IMOLA-IVD</i>	Dynamic	Low N=6 Big Footprint	Electrochemical O ₂ and pH measurement	Non-invasive monitoring; Optical Access
ACADEMIC	<i>Tanumihardja et al.⁴⁰</i>	Static	Low N=1	Electrochemical O ₂ and pH measurement	Sensor integrated Transwell system; Oxygen sensing cannot be performed more than once per hour; ECAR
	<i>Shaegh et al.⁴¹</i>	Dynamic	Low N=1	Optical O ₂ and pH (absorption) measurement	Non-invasive monitoring; Design limitation due to absorption-based detection approach
	<i>Lee et al.⁴²</i>	Dynamic	Low N=1	Optical O ₂ and pH measurement	Microfluidic continuous culture reactors with high working volumes of 1 mL for bacterial cultures; Non-invasive monitoring
	<i>Weltin et al.⁴³</i>	Dynamic	Low N=1	Electrochemical O ₂ and pH measurement	Proof of Principle; Non-invasive monitoring of T98G human brain cancer cells
	<i>Huang et al.⁴⁴</i>	Dynamic	Low N=1	Optical O ₂ and pH measurement	Monitoring of OCR and ECAR of a developing zebrafish; Non-invasive monitoring; No optical access in sensor integrated setup
	<i>Dual sensor-integrated prototype</i>	Dynamic	Moderate N=8 (36x76 cm)	Optical O ₂ and pH measurement	Low Footprint; Non-invasive monitoring; Cellular Viability < 60 s

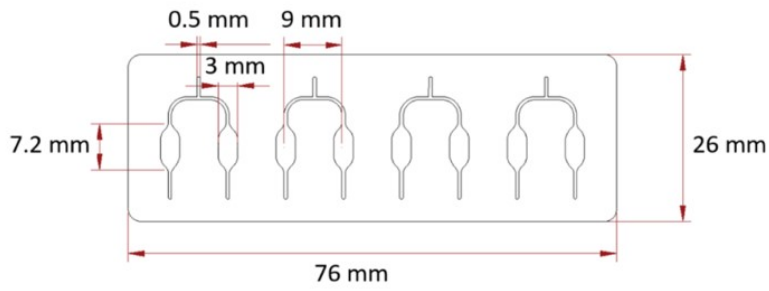


Figure S11: Schematic illustration of the COC microfluidic prototype with the individual dimensions of the chip, the chambers, and the microfluidic channels.

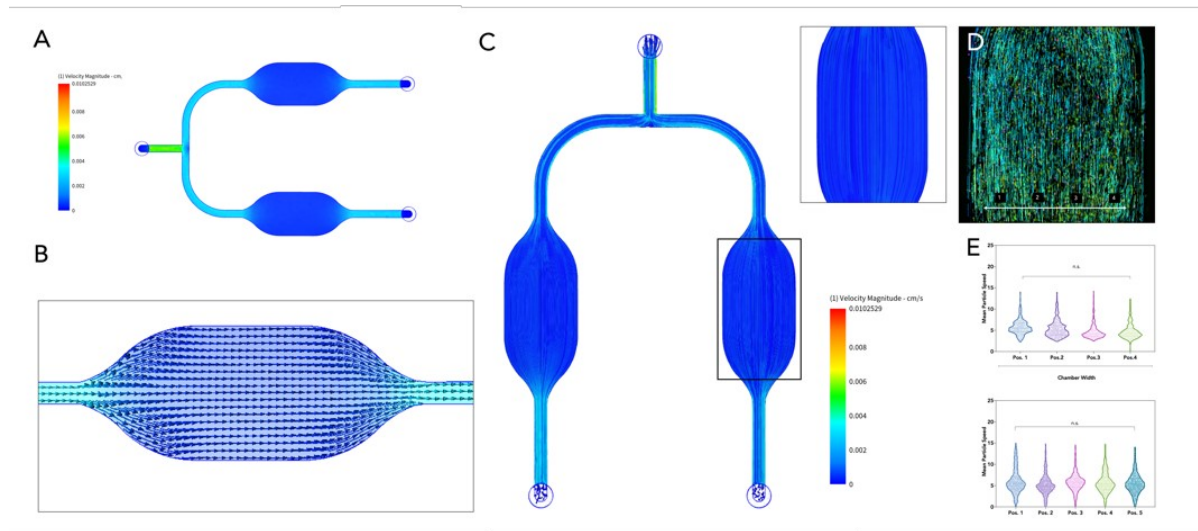


Figure S12: CFD analysis of the microfluidic prototype. a) Simulated flow behavior through the cell culture chambers (h:280 μm) at a flow rate of 10 $\mu\text{L}/\text{min}$, depicting a uniform flow profile with parallel streamlines. b) Simulated particle distribution within the microfluidic chamber at a flow rate of 10 $\mu\text{L}/\text{min}$. c) Representative image of the tracked particles within the microfluidic chamber. d) Comparative analysis of the mean particle speed along the width of the microfluidic chamber and at five randomly located positions within the device, revealing no significant difference and thus a uniform particle distribution through the chamber.

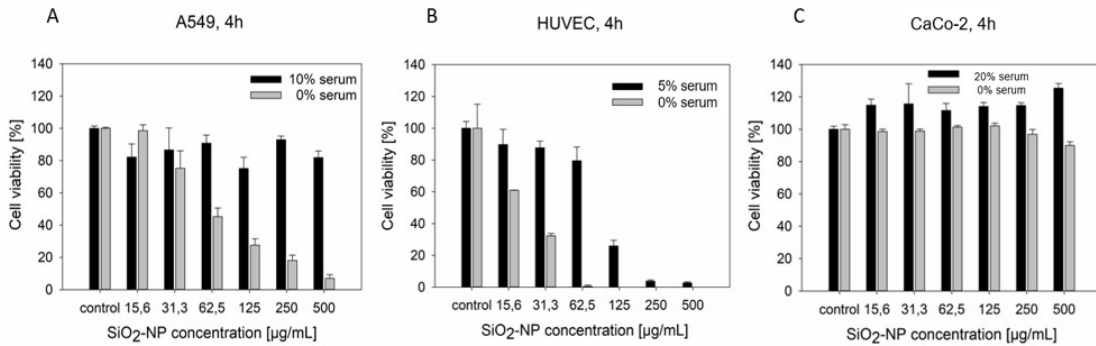


Figure S13: Cell viability of (a) A549 cells, (b) HUVECs, and (c) Caco-2 cells in standard 48-well plates after 4h SiO₂-NP exposure of increasing concentrations in medium with and without serum determined with a Presto Blue assay. The signals of untreated cells were set as 100%. The plotted data represent the mean ± standard deviation (CV: %), n = 3.

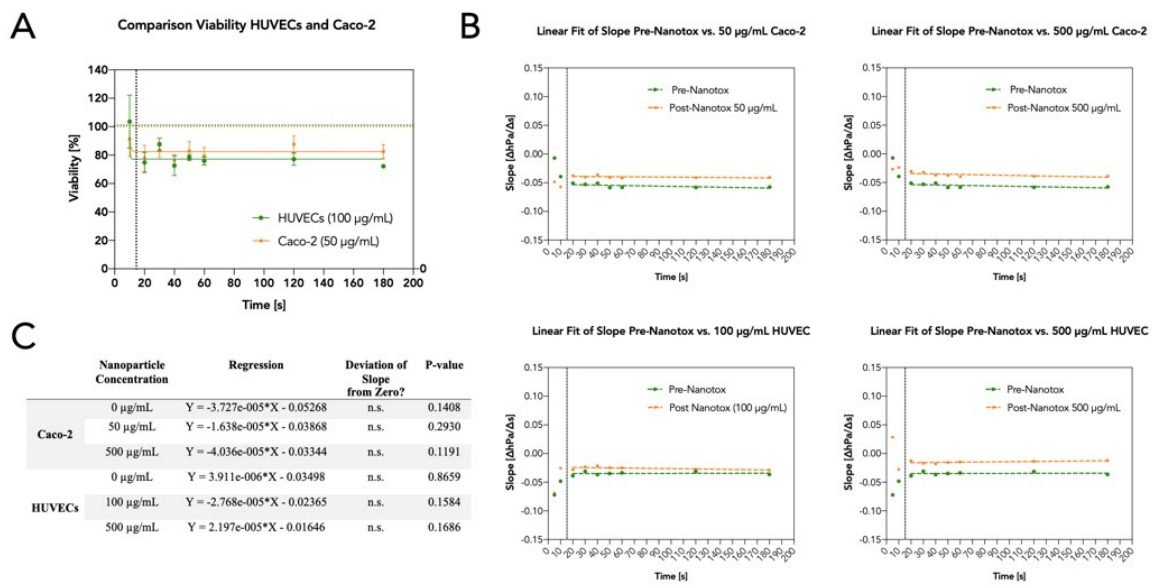


Figure S14: Assay time validation. a) Viability calculations for HUVECs (green (CoV < 5%)) and Caco-2 (orange (CoV < 7%)) for three individual experiments at different measurement time points (10s-180s) revealing comparable viability results after 20 seconds of measurement. b) Comparative analysis of the acquired slopes ($\Delta hPa/\Delta s$) for HUVECs and Caco-2 cells prior (green) and after (orange) different nanoparticle exposure scenarios revealing stable slopes after 20 seconds of measurement. Slopes were fitted with a linear regression. c) Table listing the linear regression equations and the deviation of the respective slopes from 0.

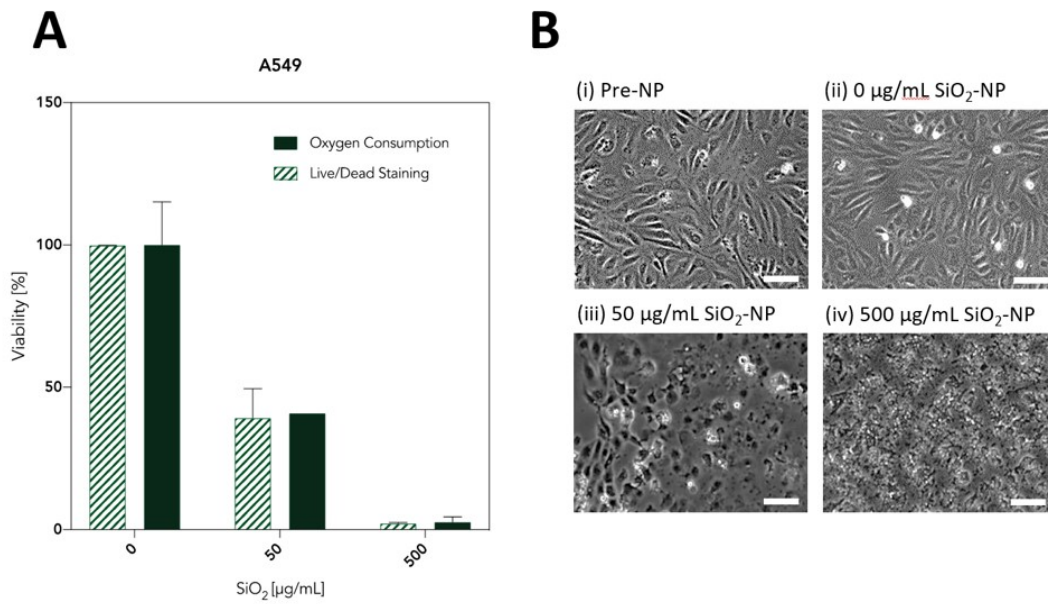


Figure S15: Effect of SiO₂-NP on cell viability and cell morphology in A549 cells after 3h perfusion in microfluidic cell culture chambers with the glass prototype. (A) Cell viability calculated from oxygen consumption and from Live/Dead staining both showed dose-dependent decreases at comparable rates. The plotted data represent the mean \pm standard deviation (CV: 1.5-15.6 %), $n = 3$. (B) Morphology studies of A549 cells (i) after over-night proliferation in standard culture medium showed a typical cobblestone morphology with triangular shapes. (ii) After 3 h perfusion of serum-free medium (control) about 50% of the cells have contained their triangular shape while the rest transformed into rounded shapes. (iii) After exposure with 50 µg/mL SiO₂-NP the majority (>90%) of cells had lost cell-cell contacts and changed the morphology into rounded shapes, probably caused by a combination of nanoparticle exposure and the serum-free medium. Despite this, the cells did not detach from the substrate during flow conditions. (iv) After exposure with 500 µg/mL, the cells showed both rounded shapes as well as fragmented morphology typical of dead cells. Scale bar: 100 µm. 10x magnification.

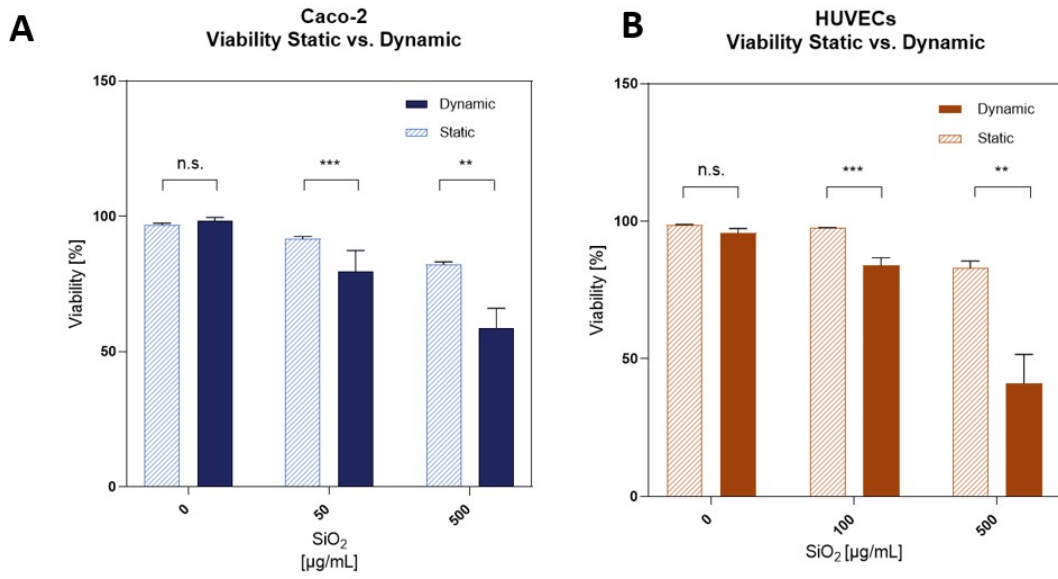


Figure S16: Impact of static and dynamic silica nanoparticles exposure scenarios on (a) Caco-2 cells (20% FCS) and (b) HUVECs (serum free). The plotted are derived from the live/dead assays and expressed as mean value \pm SD (n= 3-9).

3.5 MANUSCRIPT #3 - ARTICLE

MONITORING THE NEUROTRANSMITTER RELEASE OF HUMAN MIDBRAIN ORGANOIDS USING A REDOX CYCLING MICROSENSOR AS A NOVEL TOOL FOR PERSONALIZED PARKINSON'S DISEASE MODELLING AND DRUG SCREENING

Cite this: *Analyst*, 2021, **146**, 2358

Monitoring the neurotransmitter release of human midbrain organoids using a redox cycling microsensor as a novel tool for personalized Parkinson's disease modelling and drug screening†

Cristian Zanetti,^{ib} ‡^a Sarah Spitz,[‡]^a Emanuel Berger,^b Silvia Bolognin,^b Lisa M. Smits,^{ib} †^b Philipp Crepaz,^a Mario Rothbauer,^{ib} §^a Julie M. Rosser,[¶]^a Martina Marchetti-Deschmann,^{ib} †^a Jens C. Schwamborn,^{ib} †^b and Peter Ertl^{ib} *^a

In this study, we have aimed at developing a novel electrochemical sensing approach capable of detecting dopamine, the main biomarker in Parkinson's disease, within the highly complex cell culture matrix of human midbrain organoids in a non-invasive and label-free manner. With its ability to generate organotypic structures *in vitro*, induced pluripotent stem cell technology has provided the basis for the development of advanced patient-derived disease models. These include models of the human midbrain, the affected region in the neurodegenerative disorder Parkinson's disease. Up to now, however, the analysis of so-called human midbrain organoids has relied on time-consuming and invasive strategies, incapable of monitoring organoid development. Using a redox-cycling approach in combination with a 3-mercaptopropionic acid self-assembled monolayer modification enabled the increase of sensor selectivity and sensitivity towards dopamine, while simultaneously reducing matrix-mediated interferences. In this work, we demonstrate the ability to detect and monitor even small differences in dopamine release between healthy and Parkinson's disease-specific midbrain organoids over prolonged cultivation periods, which was additionally verified using liquid chromatography–multiple reaction monitoring mass spectrometry. Furthermore, the detection of a phenotypic rescue in midbrain organoids carrying a pathogenic mutation in leucine-rich repeat kinase 2, upon treatment with the leucine-rich repeat kinase 2 inhibitor II underlines the practical implementability of our sensing approach for drug screening applications as well as personalized disease modelling.

Received 10th November 2020,

Accepted 10th February 2021

DOI: 10.1039/d0an02206c

rsc.li/analyst

With yet unresolved etiology, Parkinson's disease is the second most common neurodegenerative disease worldwide.¹ The heterogeneous disease is characterized by the accumulation of the protein α -synuclein and the loss of dopaminergic neurons within the *substantia nigra* of the human midbrain. As a consequence of dopamine (DA) depletion within the striatum, Parkinson's disease ultimately leads to a variety of debilitating motor and non-motor symptoms.² Significant progress has

been made to unravel the underlying causes of the disease, most notably through the identification of key risk factors of genetic (*e.g.* SNCS, GBA, and LRRK2 genes) and environmental origin (*e.g.* pesticide exposure).^{3,4} Among the genetic risk factors one of the most common pathogenic modification is the G2019S mutation of the leucine-rich repeat kinase 2 (LRRK2). This mutation has been associated with many hereditary cases as well as sporadic cases of Parkinson's disease, rendering LRRK2 a potential target for novel drug candidates.⁵ Despite these advancements little is known about the complex and time-dependent interplay of these predisposing risk factors ultimately leading up to the onset of the disease. This gap in knowledge is further reflected by the clinical need for disease-modifying or neuroprotective strategies, which until today remains unmet. The high failure rates of putative drug candidates in clinical trials can be explained at least in part by the inability of current disease models to adequately replicate the hallmarks of the pathology.^{6,7} While existing animal models have provided valuable information on partial aspects

^aFaculty of Technical Chemistry, Vienna University of Technology (TUW), Getreidemarkt 9/164, 1060 Vienna, Austria. E-mail: peter.ertl@tuwien.ac.at

^bDevelopmental and Cellular Biology, Luxembourg Centre for Systems Biomedicine (LCSB), University of Luxembourg, 7 avenue des Hauts-Fourneaux, 4362 Esch-sur-Alzette, Luxembourg

† Electronic supplementary information (ESI) available: Details on experimental methods and results for: electrochemistry, LC-MRM-MS, cell culture and immunohistochemistry (PDF). See DOI: 10.1039/d0an02206c

‡ These authors contributed equally.

§ Current address: Medical University Vienna, Austria

¶ Current address: Pregenerate GmbH, Vienna, Austria



of the disease, they remain mere approximations, incapable of recapitulating the degenerative nature of Parkinson's disease.⁸ With the emergence of induced pluripotent stem cell (iPSC) technology, however, opportunities to generate more physiologically relevant patient-derived *in vitro* models, including that of the human midbrain, have opened up.⁹ Human mid-brain organoids (hMOs) represent a promising tool for modeling not only developmental but also degenerative processes of the human midbrain *in vitro*.^{10,11} The analysis of hMOs is limited to time-consuming and invasive strategies including immunohistochemistry and PCR. In order to monitor crucial aspects in organoid development such as differentiation, disease onset, and progression, however, the development and establishment of novel non-invasive sensing strategies are imperative.^{10–13} Due to its involvement in the neurodegenerative disease the catecholamine DA has been considered an ideal biomarker.^{2,14} Therefore, DA has been investigated with several analytical approaches including chromatography,^{15,16} spectrometry,^{17–19} and electrochemistry.^{20,21} The latter constitutes the most straightforward, rapid, and multiplexable among DA detection strategies.^{22–28} Electrochemical quantification of DA encompasses several techniques including chronoamperometry, differential pulse voltammetry, as well as fast-scan cyclic voltammetry.²⁰ All these techniques were used to detect the biogenic amine neurotransmitter DA *in vivo* (e.g. rat brain),^{27,29} in the human blood, as well as *in vitro* using two-dimensional cell cultures.²⁵ Although electrochemical analysis techniques are powerful tools for the detection of electroactive molecules such as DA, they have remained severely limited in their applicability for biologically relevant implementations, due to low neurotransmitter concentrations, rapid polymerization of oxidation products, protein fouling as well as the presence of physiological interferences such as ascorbic acid (AA). Due to its high concentrations within the matrix of interest (e.g. cell culture medium, CSF), the negatively charged interferent AA (pH = 7.4) has been of particular interest in the development of DA sensors. To that end several strategies have been developed including the modification of sensor surfaces with negatively charged functional groups (Nafion,³⁰ self-assembled monolayers^{26,27}), providing sterical hindrance by introducing molecularly imprinted polymers²⁸ as well as providing increased specificity through the immobilization of enzymes.²⁹ Among these, electrode modification using self-assembled monolayers of 3-mercaptopropionic acid (MPA) has emerged as an auspicious strategy for DA detection. This approach combines the advantages of self-assembled monolayers namely the ability to functionalize electrode surfaces in a simple, convenient and flexible manner with the ability of MPA to reduce AA interferences and albumin adhesion *via* the electrostatic force exerted by the negatively charged groups located at the MPA's tail.²⁷ While these approaches have shown to improve sensor selectivity, parallelization, throughput, and automation, required to increase reproducibility, however, remain challenging. Besides surface modifications, different electrode geometries and setups have been considered to increase sensor performance. One of which is redox cycling, a technique wherein

diffusive mass transfer is improved by placing two working microelectrodes in close proximity.^{31,32} In other words, by keeping one microelectrode at an oxidizing potential (generator) and poisoning the other at a reducing potential (collector), a reversible redox species such as DA, will undergo continuous oxidation to the DA quinone at a generator electrode, followed by diffusion as well as reduction to DA at a nearby collector electrode. Due to the geometrical arrangement of the interdigitated electrodes the diffusion layers of the collector and generator overlap, resulting in an optimized diffusive mass transfer (DA and DA quinone) that will continuously replenish DA at the generator electrode and DA quinone at the collector electrode, ultimately resulting in signal amplification (see Fig. 1).³³ Interestingly, so far, published redox cycling-based DA sensors are predominantly operated in simplistic matrices (e.g. TRIS buffer) that do not account for protein fouling and interferences typically encountered in biological applications.

In this study, we have combined the advantages of a redox cycling approach with a sensor surface modification strategy using self-assembled monolayers of 3-mercaptopropionic acid (MPA) to detect DA in complex cell culture matrices. It is important to note that DA, under physiological measurement conditions, is a reactive and unstable molecule. In other words, studying cellular dynamics in a time-resolved manner requires the implementation of rapid *in situ* detection methods. To demonstrate a broader applicability of our sensing strategy, advanced iPSC-derived three-dimensional hMOs were used to determine distinct differences in DA release between isogenic pairs over prolonged cultivation periods of up to 5 weeks. The results from our electrochemical sensor subsequently were verified by liquid chromatography–multiple reaction monitoring mass spectrometry (LC-MRM-MS). The practical applicability of our sensor was demonstrated by the assessment of personalized treatment options, wherein hMOs were treated with the LRRK2 inhibitor II. We demonstrate that the LRRK2 inhibitor II can elicit phenotypic rescue within hMOs carrying a pathogenic mutation in LRRK2-G2019S.

Methods

Chemicals

3-Mercaptopropionic acid (MPA), DA hydrochloride (DA-HCl), L-DOPA, L-DOPA-(phenyl-d₃), DOPAC, γ -aminobutyric acid (GABA), (–)-epinephrine, (–)-norepinephrine, L-ascorbic acid (AA), KNO₃, Na₂S₂O₅, EDTA and H₂O₂ were bought from Sigma-Aldrich (Austria). Potassium hexacyanoferrate(II) trihydrate was bought from Fluka, potassium hexacyanoferrate(III) was bought from Alfa Aesar. KOH was bought from Lachema, absolute ethanol was bought from CL Chemlab. Formic acid LC-MS grade and acetonitrile LC-MS grade were bought from Merck. DI water (18.2 M Ω cm⁻¹) was obtained with a Simplicity UV water purification system (Merck). Phosphate Buffer Saline (PBS) 10X was bought from VWR.



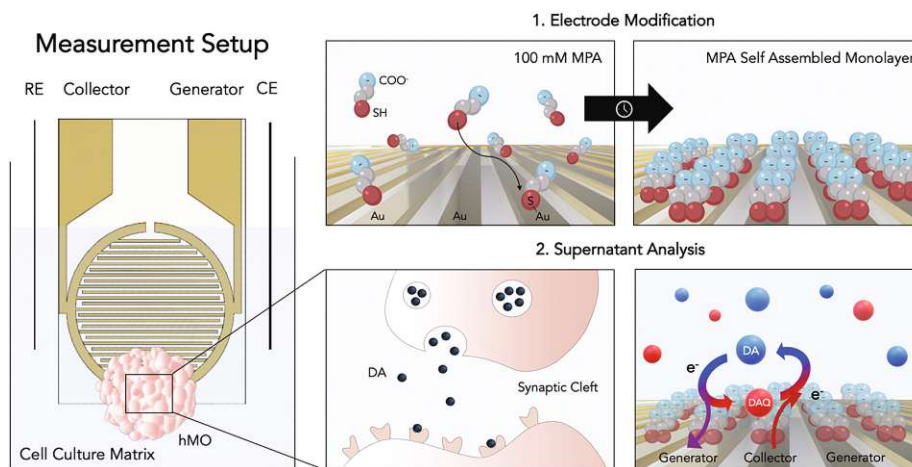


Fig. 1 Schematic of the improved electrochemical dopamine (DA) detection method. On the left panel: the electrochemical set-up consisting of two interdigitated electrodes (generator and collector) with a counter (CE) and a reference electrode (RE). On the right panels: the modification process and its application. By employing thiol-modification a self-assembled monolayer of MPA is created on the gold sensor surface in order to reduce negative interferences (top left and top right panels). Dopaminergic neurons within the hMO secrete DA within the synaptic cleft (bottom left panel). Using redox-cycling on interdigitated and MPA modified gold thin-film electrodes DA can enter a cycle of oxidation (generator electrode) to dopamine quinone (DAQ) and reduction to DA (collector electrode, bottom right panel), enabling its electrochemical detection. The image was generated using Biorender.com.

Electrochemical methods

Prior to thiol modification, the interdigitated gold microsensors (Micrux, ED-IDE3-Au, 5 μm gaps and width, 180 pairs of fingers, 3.5 mm \varnothing sensing area) were cleaned following a published cleaning protocol by Heiskanen *et al.*³⁴ Preceding the cleaning process the electrodes were pre-treated by sonication in isopropanol and water for 10 minutes each. Electrodes were then submerged in a mixture of H_2O_2 (25% v/v) and KOH (50 mM) for 10 minutes, followed by a potential sweep from -200 mV to -1200 mV (vs. Ag/AgCl) in 50 mM KOH. Before electrode modification, the sensors were rinsed in DI water, followed by absolute ethanol. The cleaned sensors were modified with MPA following the published protocol by Spégel *et al.*²⁶ To that end the microelectrodes were modified by a 2 h incubation process in a 100 mM MPA solution in ethanol and subsequently rinsed with ethanol and water to remove any non-binding thiols. Modified electrodes were stored in perforated centrifuge tubes at room temperature.

MPA electrode modification was confirmed with electrochemical impedance spectroscopy, using a sinusoidal perturbation of 10 mV amplitude, with a 100 mHz–100 kHz scan in a solution of 5 mM potassium hexacyanoferrate(II) and 5 mM potassium hexacyanoferrate(III) in 0.1 M KNO_3 .

The electrochemical setup was composed of the MPA modified interdigitated sensor containing two comb-like gold working electrodes, with both gaps and band widths of 5 μm . A Pt wire was used as a counter electrode and a chlorinated Ag wire as a pseudo-reference. The 4-electrode electrochemical cell was placed in a homemade Faraday cage and controlled by a potentiostat (VMP3, Bio-Logic) connected in bipotentiostat

mode using low current modules (Low current module, Bio-Logic). 20 μL of each sample were applied on the interdigitated circular sensing area. The potential program consisted in applying an oxidizing potential of +0.25 V at one electrode (generator), and a reducing potential of -0.1 V to the other one (collector) for 60 seconds (for potential optimization data see ESI Fig. S2 and 3†). For both electrodes averaged intensities were recorded with an acquisition rate of 0.1 s and the readout was the charge flown in the last 30 seconds. The signals were background subtracted (either PBS for characterization studies or cultivated cell culture medium for hMO analyses). Stock solutions were prepared freshly each day in nitrogen purged solvents (DI water for stocks, PBS or medium for final dilution).

To ensure comparability and reproducibility of the sensitivity within the experimental application of our sensor, we have performed a DA calibration curve in cultivated medium prior to each hMO supernatant analysis (accepted coefficient of variance < 10%). For each measurement the supernatants of three organoids were pooled. Measurements were performed in technical triplicates.

LC-MRM-MS analysis

The supernatant was mixed 1 : 1 with a preservation solution (8 mM $\text{Na}_2\text{S}_2\text{O}_5$, 2 mM EDTA) and frozen at -80 $^\circ\text{C}$ for storage. The frozen samples were thawed on the day of analysis and triplicates of 50 μL were centrifuged at 12 000 rpm for 20 minutes using 3 kDa MWCO centrifuge filters (VWR). The filtrate and the standard dilutions used for calibration were spiked with $\text{L-DOPA-(phenyl-}d_3\text{)}$ as internal standard to reach a constant concentration in the injected samples. Samples were kept in



an autosampler at 15 °C and 1 to 5 µl were injected in the UHPLC-MS/MS system (Shimadzu, LCMS-8060), equipped with a C18 column (Waters, Acquity C18 SB, 150 mm length, 1.8 µm particles, 2.1 mm ID, 100 Å pore size), a precolumn cartridge (Waters, Acquity UPLC HSS C18 VanGuard Precolumn, 5 mm length) at 40 °C, using acetonitrile and 0.1% aqueous formic acid as eluents (details see ESI Table S6†). L-DOPA, GABA, epinephrine, norepinephrine, DA and DOPAC were detected and quantified by Multiple Reaction Monitoring (MRM, details for MRM transitions and LODs and LOQs see ESI Tables S7 and 8†). Analyte identification was guaranteed by the presence of at least two analyte-specific MRM transitions. The loss of sample during filter centrifugation was carefully validated and monitored periodically. Based on this validation a correction factor was introduced to take into account sample loss within the final quantitation. The correction factor was calculated by comparing the DA signal of a freshly cultivated cell culture medium with a fresh standard solution in water.

hNESc maintenance, hMO generation and cultivation

Human neuroepithelial stem cell (hNESc, provided by the University of Luxembourg) lines (see Table 1) were derived from human iPSCs as previously described.³⁵

For the generation of hMOs 3000 cells were seeded into each well of an ultra-low attachment round bottom 96-well plate (Greiner). Cells were incubated at 37 °C, 5% CO₂. Seeded cells were kept under maintenance conditions (1 : 1 mixture of DMEM-F12 (Sigma Aldrich) and Neurobasal medium (Gibco) supplemented with 1 : 200 N2 supplement (Invitrogen), 1 : 100 B27 supplement lacking vitamin A (Invitrogen), 1% L-glutamine, 1% penicillin/streptomycin (Invitrogen), 3 µM CHIR-99021 (Axon Medchem), 0.5 µM SAG (Merck), 10 µM SB-431542 (Ascent Scientific), 250 nM LDN (Sigma), 5 µM ROCK-inhibitor (Sigma Aldrich) and 200 µM AA (Sigma)) for 7 days. Subsequently, pre-patterning was started by the withdrawal of LDN, ROCK-inhibitor and SB-431542. After 3 days the concentration of CHIR was reduced to 0.7 µM. On day 9 of differentiation, the medium was changed to neuronal maturation medium including 10 µM DAPT, 500 µM dbcAMP, 10 ng mL⁻¹ hBDNF and hGDNF (Peprotech), 1 ng mL⁻¹ TGF-β3 (Peprotech) as well as 2.5 ng mL⁻¹ Activin A (Thermo Fisher Scientific). The organoids were kept under static culture conditions with media changes every other to third day for up to

70 days. Subsequently, hMOs were fixed with 4% PFA at room temperature overnight before being washed with PBS three times. The drug screening experiment was performed by adding the LRRK2 inhibitor II (Sigma-Aldrich) to the cell culture medium (0.5 µM) from differentiation day 7, while the control hMOs were cultured in cell culture medium containing the vehicle (DMSO).

Immunofluorescence

Cultured and fixed hMOs were embedded in a 3% low-melting-point agarose (Biozym) in PBS. Subsequently, 50 µm thick sections were cut using a vibratome (Leica VT1000s) and center-sections were used for assessing TH/FOXA2/TUJ1 expression. Prior to the immunostaining, sections were permeabilized using 0.5% Triton X-100 in PBS. Depending on the antibody, permeabilization times varied between 30 min and 2 h. Unspecific antigen blocking was achieved by incubating cut sections for 2 h in 2.5% donkey serum (Sigma-Aldrich, D9663), 2.5% BSA, 0.1% Triton X-100 and 0.1% sodium azide, followed by primary antibody incubation at 4 °C for 48 h on a shaker. Antibodies were diluted in blocking buffer as follows: rabbit anti-TH (1 : 1000, Abcam), chicken anti-TUJ1 (1 : 600, Millipore). This was followed by the incubation with secondary antibodies diluted in PBS containing 0.01% Triton X-100 and Hoechst-33342 nuclear dye (1 : 1000, Sigma-Aldrich). All secondary antibodies (Invitrogen) were conjugated to Alexa Fluor fluorochromes. Sections were mounted in Fluoromount-G mounting medium (Southern Biotech) and analyzed employing a confocal laser scanning microscope (Zeiss LSM 710).

Results and discussion

Electrochemical characterization of the sensor

To verify successful electrode modification employing the organosulfur compound MPA, electrochemical impedance spectroscopy was employed. Impedance analysis of the MPA-modified interdigitated electrodes resulted in a significant increase of the semicircle radius in the Nyquist plot, with an increase of the charge transfer resistance from 0.9 ± 0.1 kΩ (mean \pm SD, $n = 3$) for the control electrodes up to 3.5 ± 0.3 kΩ for the MPA modified electrodes (see Fig. 2a). This increase in resistance to charge transfer can be attributed to the successful immobilization of the sensor surface with self-assembled monolayers of MPA. In a subsequent experiment the effect of MPA modification on sensor sensitivity and signal stability was assessed. While results depicted in Fig. 2b show that MPA modification has resulted in a lowered DA signal, as previously reported by Tsai *et al.*,²⁷ a significant reduction in signal drift was observed (ESI Fig. S1 and Table S1†). This improved signal stability points at the elimination of sensor surface fouling events. To evaluate the effects of common interferents, sensor responses to AA, norepinephrine, epinephrine, DOPAC, L-DOPA, and GABA were evaluated.²⁹ To match the concentrations of the respective cell culture medium, AA was set at a concentration of 200 µM. The catecholamines norepinephrine,

Table 1 hMO lines^{36,37}

hMO line	CRISPR/Cas9	LRRK2 gene
Healthy	No	WT
Healthy-Mut	Yes	G2019S
PD2	No	G2019S
PD2-GC	Yes	WT
PD1	No	G2019S

Description of the used hMO lines with information on whether they were gene edited (CRISPR/Cas9) and what sequence is found in the LRRK2 gene (healthy (WT) or with the PD related mutation G2019S). For further information, see ESI Table S10.†



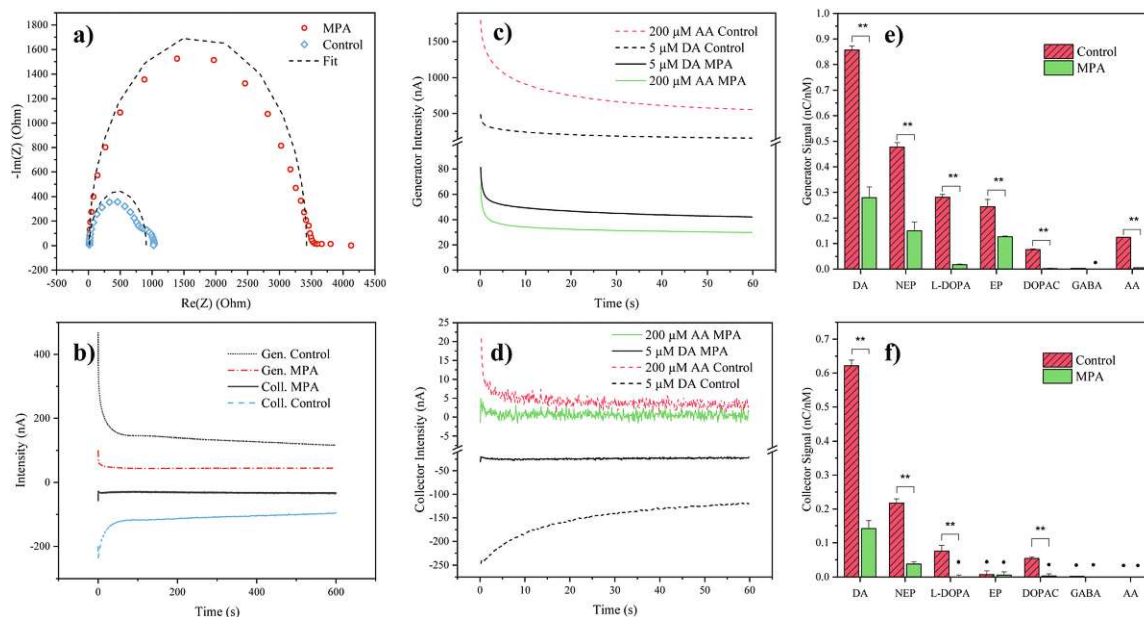


Fig. 2 (a) Nyquist plot of MPA modified and pristine electrodes. Dashed curves represent the fitting done using the Randles circuit; (b) Analysis of 5 μM DA in PBS over time (10 minutes) for MPA modified and control electrodes, including generator (Gen.) and collector (Coll.) signals; (c) and (d) Generator and collector intensity signals (background subtracted, PBS) of AA and DA, of modified (MPA) and control electrodes, respectively.; (e) and (f) Generator and collector signals for different biomolecules. (Last 30 seconds charge, background subtracted (PBS) and divided by the concentration of the analyzed solution) DA (DA), norepinephrine (NEP), L-DOPA, epinephrine (EP), DOPAC, GABA and L-ascorbic acid (AA). Error bars represent the propagated standard deviation ($n = 3$), signals marked with the symbol (*) are not significantly different from the PBS background ($\alpha = 0.05$, two tailed t-test).

epinephrine, DA, DOPAC and L-DOPA were analyzed at a concentration of 5 μM , based on the levels of the most abundant catecholamine in the medium: L-DOPA, which was assessed during preliminary LC-MRM-MS studies (data not shown). Similarly, GABA concentration was set at a concentration of 40 μM based on preliminary LC-MRM-MS studies (data not shown). Due to its high concentration within the analyte and its similar redox potential to the catecholamine DA, a particular interest of our interference study was concerned with AA mediated signal contributions. While both DA and AA signals decreased at the generator (see Fig. 2c) after MPA modification, the AA signal was suppressed 5-fold stronger, thus drastically reducing its interference potential. In turn, at the collector electrodes the AA signal contribution was completely eliminated (see Fig. 2d) supporting previous findings which demonstrate rapid hydrolysis of the oxidation product dehydroascorbic acid.³¹

While AA enhanced the DA signal at the generator electrode, the presence of AA decreased the DA signal at the collector electrode. This observation can be explained by a previously introduced hypothesis claiming that AA reduces DA-quinone back to DA.³¹ This means that the DA-quinone reduction, which results in an increase in DA concentration gradient at the generator, enhances signal at the generator, while the depletion of DA-quinone diminishes the signal at the collector

(see ESI Fig. S4†). Overall, these results demonstrate improved DA detection at the generator in the presence of MPA-modified electrodes. To further assess the influence and/or interference of other neurotransmitters, background subtracted signals of both generator (see Fig. 2e) and collector electrodes (see Fig. 2f) with and without MPA modification were compared. Similar to the effect seen for AA, MPA modification resulted in significantly ($p < 0.01$) reduced sensitivities towards the interferents: L-DOPA, DOPAC, norepinephrine and epinephrine.

Notably, a particularly strong signal reduction was observed in the case of negatively charged interferents such as L-DOPA, DOPAC, and AA. This can be explained by the preferential repulsion of anions by MPA, which at physiological pH is negatively charged itself (see Fig. 2e and f).²⁷ While the two catecholamines epinephrine and norepinephrine displayed a similar signal reduction to DA, which can be explained by their similarity in molecular structure and redox potentials, DA nonetheless resulted in the signal with the highest intensity. This observation can be explained by the different intracyclization rates of DA-quinone ($k_{\text{DA}} = 0.13 \pm 0.05 \text{ s}^{-1}$), norepinephrine-quinone ($k_{\text{NEP}} = 0.98 \pm 0.52 \text{ s}^{-1}$), and epinephrine-quinone ($k_{\text{EP}} = 87 \pm 10 \text{ s}^{-1}$).³⁸ In other words, DA displays the highest redox cycling signal while norepinephrine and epinephrine display reduced or silent signals (epinephrine at the collector).



While the MPA modification did not result in the elimination of the signals from both epinephrine and norepinephrine, it has to be noted that these potentially interfering neurotransmitters were undetectable ($S/N < 3$) in the hMO supernatants, when assessed using LC-MRM-MS. Therefore, the influence of epinephrine and norepinephrine on the overall signal can be considered negligible. While L-DOPA showed a higher selectivity (see Table 2) at the generator electrode, LC-MRM-MS studies of the hMO supernatant detected its presence in the micromolar range. This necessitates considering a potential signal contribution caused by L-DOPA. However, it is important to note that L-DOPA, being the precursor of DA, might reinforce a phenotypic difference when the generator electrode is employed in the comparative assessment of healthy and diseased hMOs. More importantly, selectivity over AA at the generator improved by 702% (see Table 2), which is crucial given its high concentration in the cell culture medium.

Next, the reproducibility of the sensor and its time stability was assessed. Intra- and inter-batch variability were calculated by analyzing DA sensitivities across three batches prepared on different days, showing acceptable coefficients of variance ($CV < 10\%$, see ESI Table S2†). Time stability was monitored over a period of 12 days showing no significant change ($\alpha = 0.05$, see ESI Fig. S5†) in DA sensitivity over time. Finally, the effect of long-term storage was evaluated by comparing DA responses of electrodes ($n = 3$) directly after manufacture and after 20 months of storage, revealing an average loss of 33% sensitivity, while maintaining comparable DA selectivity against AA (mean \pm SD, 58 ± 9 , see ESI Table S3†). Overall, these results show that the combination of redox cycling and MPA self-assembled monolayers represent a promising strategy for the noninvasive monitoring of hMOs in Parkinson's disease models.

Next, to evaluate sensor performance calibration curves of the catecholamine DA were obtained for MPA-modified electrodes in both PBS as well as cultivated cell culture medium (see ESI Fig. S6†). In both matrices the generator provided higher

sensitivity, while the collector electrode allowed for higher selectivity (only DA and norepinephrine could be detected). Calibration in cultured medium resulted in decreased sensitivities (slopes) at both the generator (-80%) and the collector (-89%), as well as reduced linear ranges (see ESI Table S5†), highlighting the significant impact of complex matrices in DA electroanalysis. As previously mentioned, by contributing to the generator's signal, L-DOPA will strengthen a phenotypic difference between healthy and diseased hMOs. Taking this, a higher noise and persistent negative interferences of AA at the collector into consideration, only the generator signal was used for the subsequent application of the sensor in hMO supernatant analysis.

Neurotransmitter profiling using LC-MRM-MS

In order to verify our electrochemical sensor results, an LC-MRM-MS method specific for hMO supernatants was established. In particular, profiles of the neurotransmitters epinephrine, norepinephrine, DA, GABA as well as the DA precursor L-DOPA and the DA metabolite DOPAC were investigated in this study. The method was optimized for analyte detection in cell culture medium with minimum sample preparation to detect and quantify the analytes of interest (chromatographic details see ESI Fig. S7, Tables S6 and S7†). LOQs ranged between 8 nM (epinephrine) and 45 nM (L-DOPA) (details see ESI Table S8†). Intra-day repeatability for hMO supernatant analysis showed acceptable results revealing an averaged coefficient of variation $< 10\%$, see ESI Table S9.† LC-MRM-MS results verified not only the presence of the neurotransmitters GABA, L-DOPA, DA and DOPAC in the supernatant of the analyzed hMOs, but also confirmed the ability of our electrochemical method to detect the presence of the catecholamine DA within the matrix of the tested hMOs (see Table 3).

Electrochemical analysis of healthy and diseased hMOs

As practical application of our novel sensing strategy in complex biological matrices, supernatants from hMOs derived from five individual iPSC lines (see Table 1) were investigated. In total, iPSC lines from one healthy (Healthy) and two diseased individuals (PD1, PD2) carrying the pathogenic LRRK2-

Table 2 Biomolecule selectivity to DA

	Selectivity to DA of MPA sensor (SD), % change compared to unmodified sensor	
	Generator	Collector
Norepinephrine	1.9 (0.05), +4%	3.7 (0.02), +30%
L-DOPA	15.8 (0.04), +419%	Not detected
Epinephrine	2.2 (0.04), -37%	Not detected
AA	55 (0.04), +702%	Not detected
DOPAC	115.2 (0.04), +934%	Not detected
GABA	Not detected	Not detected

Selectivity was calculated as the ratio of the DA signal (nC/nM) and the signal of each compound listed. Not detected: the compound's signal after electrode modification was not significantly different from background ($\alpha = 0.05$, $n = 3$, two-tailed t-test). The percentages indicate the gain or loss in selectivity after the electrode modification. A detailed version of this table is presented in the ESI Table S4.†

Table 3 Biomolecule concentrations in the supernatants of hMOs derived from four individual iPSC lines at day 60 of differentiation as measured by LC-MRM-MS

hMO line	Concentration (nM) (SD)			
	L-DOPA	DA	DOPAC	GABA
Healthy	1912.9 (81.5)	252.3 (6.8)	1066.5 (58.4)	55 120 (2826)
Healthy-Mut	1661.5 (49.3)	78.4 (0.3)	271.1 (1.7)	45 641 (580)
PD2	1199.5 (93.8)	40.2 (1.6)	201 (9.4)	10 696 (515)
PD2-GC	1422.2 (107.5)	45.3 (3.7)	259.8 (25.9)	13 840 (2068)

Norepinephrine and epinephrine signals were below the respective LODs (35 nM and 320 nM respectively). Standard deviations (SD) were calculated from a technical triplicate ($n = 3$) of a pooled hMO supernatant ($n = 3$). For a description of the hMOs lines see Table 1.



G2019S mutation were used in this study. To provide adequate control lines, the iPSC line from the healthy patient was genetically modified to carry the G2019S mutation in LRRK2 (Healthy-Mut), while the iPSC cell line from patient PD2 was corrected for said mutation (PD2-Mut). To confirm successful hMO maturation immunohistochemical analysis was performed. Characteristic for differentiated hMOs, immunohistochemistry revealed both TUJ1-positive neurons as well as tyrosine hydroxylase (TH) positive neurons in all of the analyzed hMOs (see ESI Fig. S8†).

Moreover, significant differences ($p < 0.05$, one tail t-tests) in electrochemical sensor signals were obtained for the supernatants of mature hMOs at day 60 of differentiation (see Fig. 3a). Interestingly, differences in the DA levels were observed not only between healthy and diseased organoids but also within the individual isogenic pairs. In other words, the introduction of a single mutation in the LRRK2 gene of healthy organoids resulted in a significant reduction of DA (Fig. 3a Healthy-Mut, -26% signal, $p < 0.05$), indicating that the pathogenic G2019S mutation alone already causes a reduction in DA biosynthesis, a hallmark of Parkinson's disease. Similarly, the correction for the pathogenic mutation

in the diseased organoid (PD2-GC) resulted in a significant ($p < 0.05$) increase in DA production. Notably, while the gene correction in the diseased organoid increased the sensor signal by 65%, it is still significantly lower compared to the healthy organoid (-34% , $p < 0.01$), highlighting the multifactorial nature of Parkinson's disease.

Since our redox-cycling sensor also detects the presence of norepinephrine and epinephrine as well as the DA precursor ι -DOPA, albeit to a lesser extent, LC-MRM-MS was employed to verify the obtained electrochemical results in more detail. In a series of experiments, the supernatants of mature hMOs (day 60 of differentiation) were analyzed and listed in Table 3. Similar to the electrochemical sensor, the LC-MRM-MS method showed distinct differences between the individual organoid lines regarding the neurotransmitter DA (e.g. Healthy-Mut, -69%). In addition, LC-MRM-MS analysis revealed a decrease in both ι -DOPA (e.g. Healthy-Mut, -13%) and DOPAC (e.g. Healthy-Mut, -75%) levels, while the two catecholamines norepinephrine and epinephrine were undetectable. As such both ι -DOPA and DOPAC variations could potentially contribute to the recorded signal at the electrochemical sensor. However, sensor characterization has shown that MPA

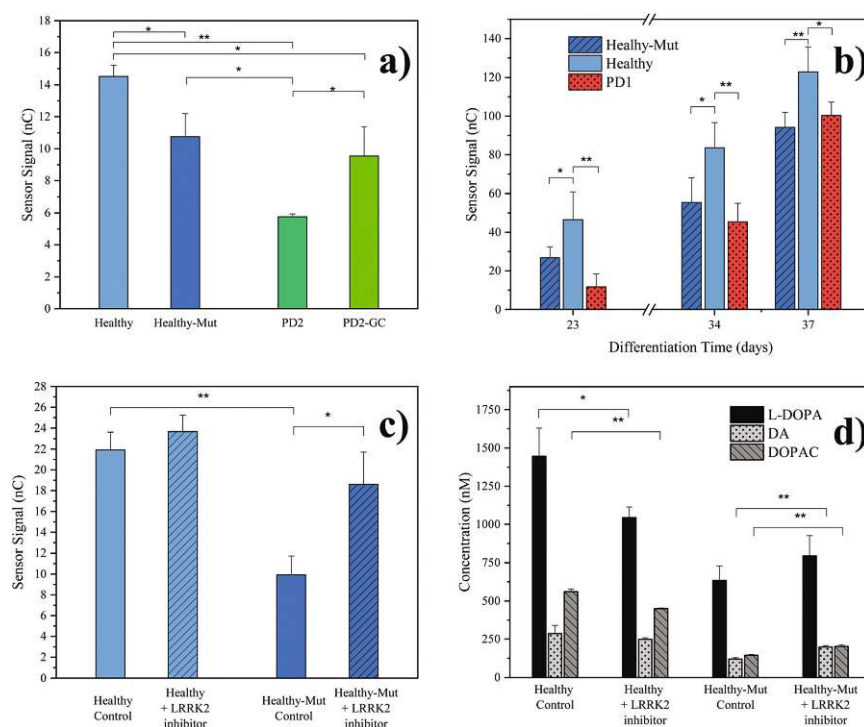


Fig. 3 hMOs supernatant analyses. (a) Comparison of electrochemical results at differentiation day 60 with different hMO lines. Error bars: standard error of the mean (SEM), $n = 3$, background subtracted signals (cultivated cell culture medium); (b) time resolved monitoring of organoid supernatant. Error bars: SEM, $n = 3$, background subtracted signals; (c) evaluation of the effect of LRRK2 inhibitor II drug ($0.5 \mu\text{M}$) on healthy and LRRK2 mutated hMOs (control, DMSO), differentiation day 46. Error bars: SEM, $n = 2$, background subtracted signals; (d) LC-MRM-MS results of the LRRK2 inhibitor II experiment, differentiation day 46. Error Bars: standard deviation, $n = 3$. p values for one tailed t-test: * $p < 0.05$, ** $p < 0.01$. Presented results were obtained from a pooled hMO supernatant ($n = 3$). For a description of hMO lines see Table 1.



modification provides good DA selectivity in the presence of the two biomolecules.

In a subsequent experiment, the supernatant of growing organoids was tested over a period of 37 days using our electrochemical sensor (see Fig. 3b). The first neurotransmitter release signal ($S/N > 3$) was detected as early as day 23 of differentiation, at which point already distinct differences in sensor signals between healthy hMOs (Healthy) and healthy hMOs carrying the mutation in LRRK2 (Healthy-Mut) could be identified. Interestingly, these early individual phenotypic differences were detected over the entire maturation period of 37 days, underlining the ability of the developed sensor for time-resolved monitoring of hMOs.

In a final set of experiments, the potential of our redox-cycling sensing approach for personalized drug screening applications was assessed, by treating healthy (Healthy) and CRISPR/Cas9 mutated (Healthy-Mut) hMOs with the LRRK2 inhibitor II. While no distinctive influence was detected for healthy hMOs, a significant signal increase (+87%) was obtained following the treatment of hMOs carrying the mutation in the LRRK2 (Healthy-Mut) gene (see Fig. 3c), thus indicating a phenotypic rescue in the presence of the LRRK2 inhibitor II. This observation was further confirmed using LC-MRM-MS measurements (Fig. 3d), where significant increases ($p < 0.01$) in DA (+67%) and DOPAC (+40%) levels were detected when treated with the kinase inhibitor LRRK2 inhibitor II.

In summary, the herein presented redox-cycling approach not only reliably detected differences in the release of the catecholamine DA in between individual hMOs in their complex matrix in a time-resolved manner, but furthermore demonstrated phenotypic rescue upon treatment with the kinase inhibitor LRRK2 inhibitor II. As such it presents a powerful tool for both *in vitro* disease modelling as well as personalized drug screening applications.

Conclusions

Overall, the presented sensing approach combines the advantages of selective electrode modification with a redox cycling-based signal amplification strategy to detect DA release of hMOs in a complex biological matrix. While the application of a self-assembled 3-mercaptopropionic acid monolayer efficiently repelled negatively charged molecules such as AA, L-DOPA and DOPAC, redox cycling of DA provided stable, reliable and robust current signals. Using this novel combination, for the first time, time-resolved, non-invasive and label-free detection of DA release was conducted in supernatants of healthy and diseased hMOs. It is important to note that no artificial exocytosis trigger was needed for signal detection, thus making our redox cycling sensing approach an ideal and non-invasive screening tool in neurobiology.

While the negatively charged biomolecules such as AA, L-DOPA and DOPAC could successfully be repelled by the negative charge of the MPA modified sensor surface, interference from the two catecholamines epinephrine and norepinephrine was reduced by addressing their difference in intracyclization

rate through employing a redox cycling strategy. Although the interference could not be eliminated, it has to be noted that both biomolecules were not detectable in the supernatant of the hMOs and as such can be considered negligible.

Using our sensing method even small differences between isogenic pairs of hMOs were detected, highlighting the influence of individual genetic backgrounds in neurodegenerative diseases. These differences across individual midbrain organoid lines were monitored over a prolonged period of time (*e.g.* weeks and months), making this approach a potential candidate for the non-invasive monitoring of Parkinson's onset and disease progression in patient-derived samples. Practical application of our technology for personalized drug testing was demonstrated using both healthy and LRRK2-G2019S mutated hMOs. Following treatment with the LRRK2 inhibitor II, phenotypic rescue, expressed by an increase of DA release, was detected only in hMOs carrying the pathogenic mutation in the LRRK2-G2019S gene. In future, we plan to expand our drug screening study to include a larger number of patient-derived hMOs to evaluate different drug-candidates, combinations thereof and dose-response relationships for personalized therapy options in Parkinson's disease.

Associated content

Ethical statement

All experiments were performed in accordance with the national and international ethics guidelines, and approved by the ethics committee at the University of Luxembourg and the national ethics committee (CNER, Comité National d'Ethique de Recherche). Informed consents were obtained from human participants of this study.

Author contributions

CZ, SS, PE, SB, JCS, MR, and JR designed the experiments. CZ, SS, and PE drafted the manuscript. CZ and SS conducted all the experiments and performed data analysis. SB, EB, LS, and JCS provided the hMOs and performed immunohistochemical analyses. PC and MMD established the HPLC-MRM-MS method, performed analyses and analyzed the data.

The manuscript was written through contributions of all authors. All authors have given approval to the final version of the manuscript.

Conflicts of interest

There are no conflicts of interest to declare.

Acknowledgements

CZ wishes to thank Prof. Camilla Ferrante (University of Padova, Italy) for her support. We thank Edis Saini for his



support in the acquisition of part of the electrochemical data during his internship at TU Wien.

The JCS's lab is supported by the Fonds National de la Recherche (FNR) Luxembourg in the M-era. Net project NanoPD (INTER/MERA/17/11760144). Further work from the JCS lab was supported by a Proof-of-Concept grant from the Fonds National de la Recherche (FNR) Luxembourg (FNR/PoC16/11559169). Further, this is an EU Joint Program – Neurodegenerative Disease Research (JPND) project (INTER/JPND/15/11092422) receiving funding from the FNR.

References

- D. B. Ramsden, R. B. Parsons, S. L. Ho and R. H. Waring, The aetiology of idiopathic Parkinson's disease, *Mol. Pathol.*, 2001, **54**(6), 369–380.
- J. A. Obeso, M. Stamelou, C. G. Goetz, W. Poewe, A. E. Lang, D. Weintraub, D. Burn, G. M. Halliday, E. Bezard, S. Przedborski, S. Lehericy, D. J. Brooks, J. C. Rothwell, M. Hallett, M. R. DeLong, C. Marras, C. M. Tanner, G. W. Ross, J. W. Langston, C. Klein, V. Bonifati, J. Jankovic, A. M. Lozano, G. Deuschl, H. Bergman, E. Tolosa, M. Rodriguez-Violante, S. Fahn, R. B. Postuma, D. Berg, K. Marek, D. G. Standaert, D. J. Surmeier, C. W. Olanow, J. H. Kordower, P. Calabresi, A. H. V. Schapira and A. J. Stoessl, Past, present, and future of Parkinson's disease: A special essay on the 200th Anniversary of the Shaking Palsy: The Shaking Palsy: Past, Present and Future, *Mov. Disord.*, 2017, **32**(9), 1264–1310.
- W. Satake, Y. Nakabayashi, I. Mizuta, Y. Hirota, C. Ito, M. Kubo, T. Kawaguchi, T. Tsunoda, M. Watanabe, A. Takeda, H. Tomiyama, K. Nakashima, K. Hasegawa, F. Obata, T. Yoshikawa, H. Kawakami, S. Sakoda, M. Yamamoto, N. Hattori, M. Murata, Y. Nakamura and T. Toda, Genome-wide association study identifies common variants at four loci as genetic risk factors for Parkinson's disease, *Nat. Genet.*, 2009, **41**(12), 1303–1307.
- A. Verstraeten, J. Theuns and C. Van Broeckhoven, Progress in unraveling the genetic etiology of Parkinson disease in a genomic era, *Trends Genet.*, 2015, **31**(3), 140–149.
- B. D. Lee, V. L. Dawson and T. M. Dawson, Leucine rich repeat kinase 2 (LRRK2) as a potential therapeutic target for Parkinson's disease, *Trends Pharmacol. Sci.*, 2012, **33**(7), 365–373.
- W. Poewe, K. Seppi, C. M. Tanner, G. M. Halliday, P. Brundin, J. Volkman, A.-E. Schrag and A. E. Lang, Parkinson disease, *Nat. Rev. Dis. Primers*, 2017, **3**, 17013.
- W. G. Meissner, M. Frasier, T. Gasser, C. G. Goetz, A. Lozano, P. Piccini, J. A. Obeso, O. Rascol, A. Schapira, V. Voon, D. M. Weiner, F. Tison and E. Bezard, Priorities in Parkinson's disease research, *Nat. Rev. Drug Discovery*, 2011, **10**(5), 377–393.
- M. Jucker, The benefits and limitations of animal models for translational research in neurodegenerative diseases, *Nat. Med.*, 2010, **16**(11), 1210–1214.
- K. Takahashi and S. Yamanaka, Induction of Pluripotent Stem Cells from Mouse Embryonic and Adult Fibroblast Cultures by Defined Factors, *Cell*, 2006, **126**(4), 663–676.
- H. Kim, H. J. Park, H. Choi, Y. Chang, H. Park, J. Shin, J. Kim, C. J. Lengner, Y. K. Lee and J. Kim, Modeling G2019S-LRRK2 Sporadic Parkinson's Disease in 3D Midbrain Organoids, *Stem Cell Rep.*, 2019, **12**(3), 518–531.
- L. M. Smits, L. Reinhardt, P. Reinhardt, M. Glatza, A. S. Monzel, N. Stanslowsky, M. D. Rosato-Siri, A. Zanon, P. M. Antony, J. Bellmann, S. M. Nicklas, K. Hemmer, X. Qing, E. Berger, N. Kalmbach, M. Ehrlich, S. Bolognin, A. A. Hicks, F. Wegner, J. L. Sternecker and J. C. Schwamborn, Modeling Parkinson's disease in mid-brain-like organoids, *npj Parkinson's Dis.*, 2019, **5**(1), 5.
- J. Jo, Y. Xiao, A. X. Sun, E. Cukuroglu, H.-D. Tran, J. Göke, Z. Y. Tan, T. Y. Saw, C.-P. Tan, H. Lokman, Y. Lee, D. Kim, H. S. Ko, S.-O. Kim, J. H. Park, N.-J. Cho, T. M. Hyde, J. E. Kleinman, J. H. Shin, D. R. Weinberger, E. K. Tan, H. S. Je and H.-H. Ng, Midbrain-like Organoids from Human Pluripotent Stem Cells Contain Functional Dopaminergic and Neuromelanin-Producing Neurons, *Cell Stem Cell*, 2016, **19**(2), 248–257.
- A. S. Monzel, L. M. Smits, K. Hemmer, S. Hachi, E. L. Moreno, T. van Wuelen, J. Jarazo, J. Walter, I. Brüggemann, I. Boussaad, E. Berger, R. M. T. Fleming, S. Bolognin and J. C. Schwamborn, Derivation of Human Midbrain-Specific Organoids from Neuroepithelial Stem Cells, *Stem Cell Rep.*, 2017, **8**(5), 1144–1154.
- F. N. Emamzadeh and A. Surguchov, Parkinson's Disease: Biomarkers, Treatment, and Risk Factors, *Front. Neurosci.*, 2018, **12**, 612.
- G. Cannazza, M. M. Carrozzo, A. S. Cazzato, I. M. Bretis, L. Troisi, C. Parenti, D. Braghieri, S. Guiducci and M. Zoli, Simultaneous measurement of adenosine, dopamine, acetylcholine and 5-hydroxytryptamine in cerebral mice microdialysis samples by LC–ESI-MS/MS, *J. Pharm. Biomed. Anal.*, 2012, **71**, 183–186.
- G. M. Anderson and J. G. Young, Determination of neurochemically important compounds in physiological samples using HPLC, *Schizophr. Bull.*, 1982, **8**(2), 333–348.
- S. S. An, J. Kim and S. R. Ankireddy, Selective detection of dopamine in the presence of ascorbic acid via fluorescence quenching of InP/ZnS quantum dots, *Int. J. Nanomed.*, 2015, 113.
- A. a. Manaf, M. Ghadir, R. Soltanian, H. Ahmad and C. K. Lai, Picomole Dopamine Detection Using Optical Chips, *Plasmonics*, 2016, 1–6.
- M. I. Zibaii, H. Latifi, A. Asadollahi, A. H. Bayat, L. Dargahi and A. Haghparast, Label Free Fiber Optic Apta-Biosensor for *In vitro* Detection of Dopamine, *J. Lightwave Technol.*, 2016, **34**(19), 4516–4524.
- K. Jackowska and P. Krysinski, New trends in the electrochemical sensing of dopamine, *Anal. Bioanal. Chem.*, 2013, **405**(11), 3753–3771.
- E. S. Bucher and R. M. Wightman, Electrochemical Analysis of Neurotransmitters, *Annu. Rev. Anal. Chem.*, 2015, **8**(1), 239–261.





- 22 H. Ghadimi, M. R. Mahmoudian and W. J. Basirun, A sensitive dopamine biosensor based on ultra-thin polypyrrole nanosheets decorated with Pt nanoparticles, *RSC Adv.*, 2015, **5**(49), 39366–39374.
- 23 J. Njagi and S. Andreescu, Response to Enzyme-Linked Biosensors: Michaelis–Menten Kinetics Need Not Apply, *J. Chem. Educ.*, 2010, **87**(9), 907–907.
- 24 S. J. Park, S. H. Lee, H. Yang, C. S. Park, C.-S. Lee, O. S. Kwon, T. H. Park and J. Jang, Human Dopamine Receptor-Conjugated Multidimensional Conducting Polymer Nanofiber Membrane for Dopamine Detection, *ACS Appl. Mater. Interfaces*, 2016, **8**(42), 28897–28903.
- 25 L. Sasso, A. Heiskanen, F. Diazzi, M. Dimaki, J. Castillo-León, M. Vergani, E. Landini, R. Raiteri, G. Ferrari, M. Carminati, M. Sampietro, W. E. Svendsen and J. Emnéus, Doped overoxidized polypyrrole microelectrodes as sensors for the detection of dopamine released from cell populations, *Analyst*, 2013, **138**(13), 3651.
- 26 C. Spégel, A. Heiskanen, J. Acklid, A. Wolff, R. Taboryski, J. Emnéus and T. Ruzgas, On-Chip Determination of Dopamine Exocytosis Using Mercaptopropionic Acid Modified Microelectrodes, *Electroanalysis*, 2007, **19**(2–3), 263–271.
- 27 T.-C. Tsai, C.-X. Guo, H.-Z. Han, Y.-T. Li, Y.-Z. Huang, C.-M. Li and J.-J. Jason Chen, Microelectrodes with gold nanoparticles and self-assembled monolayers for in vivo recording of striatal dopamine, *Analyst*, 2012, **137**(12), 2813–2820.
- 28 C. Xue, Q. Han, Y. Wang, J. Wu, T. Wen, R. Wang, J. Hong, X. Zhou and H. Jiang, Amperometric detection of dopamine in human serum by electrochemical sensor based on gold nanoparticles doped molecularly imprinted polymers, *Biosens. Bioelectron.*, 2013, **49**, 199–203.
- 29 J. Njagi, M. M. Chernov, J. C. Leiter and S. Andreescu, Amperometric Detection of Dopamine in Vivo with an Enzyme Based Carbon Fiber Microbiosensor, *Anal. Chem.*, 2010, **82**(3), 989–996.
- 30 P. Capella, B. Ghasemzadeh, K. Mitchell and R. N. Adams, Nafion-coated carbon fiber electrodes for neurochemical studies in brain tissue, *Electroanalysis*, 1990, **2**(3), 175–182.
- 31 A. Aggarwal, M. Hu and I. Fritsch, Detection of dopamine in the presence of excess ascorbic acid at physiological concentrations through redox cycling at an unmodified microelectrode array, *Anal. Bioanal. Chem.*, 2013, **405**(11), 3859–3869.
- 32 M. Hu and I. Fritsch, Application of Electrochemical Redox Cycling: Toward Differentiation of Dopamine and Norepinephrine, *Anal. Chem.*, 2016, **88**(11), 5574–5578.
- 33 P. Tomčík, Microelectrode Arrays with Overlapped Diffusion Layers as Electroanalytical Detectors: Theory and Basic Applications, *Sensors*, 2013, **13**(10), 13659–13684.
- 34 A. R. Heiskanen, C. F. Spégel, N. Kostasheva, T. Ruzgas and J. Emnéus, Monitoring of *Saccharomyces cerevisiae* Cell Proliferation on Thiol-Modified Planar Gold Microelectrodes Using Impedance Spectroscopy, *Langmuir*, 2008, **24**(16), 9066–9073.
- 35 L. M. Smits, L. Reinhardt, P. Reinhardt, M. Glatza, A. S. Monzel, N. Stanslowsky, M. D. Rosato-Siri, A. Zanon, P. M. Antony, J. Bellmann, S. M. Nicklas, K. Hemmer, X. Qing, E. Berger, N. Kalmbach, M. Ehrlich, S. Bolognin, A. A. Hicks, F. Wegner, J. L. Sternecker and J. C. Schwamborn, Modeling Parkinson's disease in mid-brain-like organoids, *npj Parkinson's Dis.*, 2019, **5**, 5.
- 36 X. Qing, J. Walter, J. Jarazo, J. Arias-Fuenzalida, A.-L. Hillje and J. C. Schwamborn, CRISPR/Cas9 and piggyBac-mediated footprint-free LRRK2-G2019S knock-in reveals neuronal complexity phenotypes and α -Synuclein modulation in dopaminergic neurons, *Stem Cell Res.*, 2017, **24**, 44–50.
- 37 P. Reinhardt, M. Glatza, K. Hemmer, Y. Tsytsyura, C. S. Thiel, S. Höing, S. Moritz, J. A. Parga, L. Wagner, J. M. Bruder, G. Wu, B. Schmid, A. Röpke, J. Klingauf, J. C. Schwamborn, T. Gasser, H. R. Schöler and J. Sternecker, Derivation and Expansion Using Only Small Molecules of Human Neural Progenitors for Neurodegenerative Disease Modeling, *PLOS ONE*, 2013, **8**(3), e59252.
- 38 M. Hu and I. Fritsch, Redox Cycling Behavior of Individual and Binary Mixtures of Catecholamines at Gold Microband Electrode Arrays, *Anal. Chem.*, 2015, **87**(4), 2029–2032.

3.5 MANUSCRIPT #3 – SUPPLEMENTARY INFORMATION

Supporting Information for

Monitoring the neurotransmitter release of human midbrain organoids using a redox cycling microsensor array as a novel tool for personalized Parkinson's disease modeling and drug testing

Cristian Zanetti[‡], Sarah Spitz^{‡,‡}, Emanuel Berger[†], Silvia Bolognin[†], Lisa Smits[†], Mario Rothbauer^{‡1}, Philipp Crepaz[‡], Julie Rosser^{‡2}, Martina Marchetti-Deschmann[‡], Jens C. Schwamborn[†] and Peter Ertl^{‡*}

[‡] Faculty of Technical Chemistry, Vienna University of Technology (TUW), Getreidemarkt 9/164, 1060 Vienna, Austria

[†] Developmental and Cellular Biology, Luxembourg Centre for Systems Biomedicine (LCSB), University of Luxembourg, 7 avenue des Hauts-Fourneaux, 4362 Esch-sur-Alzette, Luxembourg).

* corresponding author: Peter Ertl, peter.ertl@tuwien.ac.at

Keywords: Dopamine, Parkinson disease, redox-cycling, electrochemistry, iPSC, midbrain organoid, MPA, LC-MRM-MS

¹ Current address: Medical University Vienna, Austria

² Current address: Pregenerate Inc., Vienna, Austria

Table of Contents

Electrochemistry

Figure S1. 10-minutes redox cycling signals of 5 μ M DA in PBS, for both MPA and control sensors. The signal drift was calculated with a linear fit between 110 s and 600 s. The MPA effect on the signal drift was evaluated by comparing the slopes from the linear fits, see Table below for details.3

Table S1. Results of the signal drift calculation from the 10-minutes redox cycling experiment. The linear fit results were averaged ($n = 2$) and are displayed in the table with the correlated standard error and the slope in degrees. The effect of MPA at the generator removed the signal drift (the value marked with an asterisk was not significantly different from zero). The MPA effect on the collector (cathodic currents) significantly reduced drift of signal from a positive (decreasing signal) slope to a slightly negative value (increasing signal over time), overall this shows a positive impact of MPA on the signal stability.3

Figure S2. Optimization of the generator potential. On the top: Chronoamperometric responses of DA and AA at the sensor with increasing generator electrode potentials. The potential was stepped every 30 s from 0 to +0.30 V, the collector potential was set to -0.1 V. On the bottom: ratio of the recorded DA and AA signals. The experiment was performed in PBS (pH = 7.4).4

Figure S3. Optimization of the collector potential. On the top: chronoamperometric responses of DA and AA at the sensor with decreasing collector electrode potentials. The potential was stepped every 30 s from 0 to -0.20 V, the generator potential was set to +0.25 V. On the bottom: ratio of the recorded DA and AA signals. The experiment was performed in PBS (pH = 7.4).4

Figure S4. Generator and Collector signals of ascorbic acid (AA) and dopamine (DA) solutions in PBS at MPA modified sensor. a) At the generator the DA signal is higher than the AA signal, and when the two components are mixed in the same solution the resulting signal is higher than the sum of the separate ones, this synergic action is attributed to AA reducing DA-quinone, thus increasing diffusion gradients and leading to higher currents; b) at the collector the AA signal is silent, while the DA signal is visible (due to reduction of DA-quinone), the copresence of DA and AA in solution leads to a silent signal, this is also attributed to AA reducing DA-quinone.5

Table S2. Sensor intra-batch and inter-batch repeatability. Each sensitivity measurement was obtained from the slope of a 0-1000 nM DA calibration curve in PBS.6

Figure S5. Time resolved monitoring of DA sensitivity of the sensor ($n = 4$) to assess sensor stability. The slope of the linear regression was not significantly different from zero ($\alpha = 0.05$).6

Table S3. Long-term stability study. DA signal was measured on the month of manufacturing and also after 20 months ($n = 3$). Selectivity towards AA was also measured after 20 months.6

Table S4. Detailed Results of the analysis of selectivities to DA change after MPA modification. The selectivity was calculated as the ratio of the biomolecule signal (nC/nM) and the DA signal (nC/nM). The percent change represents the change in selectivity to DA after MPA modification. Not detected or n.a.: the signal of the compound was not significantly different from the background (PBS, $\alpha = 0.05$, two-tailed t test).7

Figure S6. Electrochemical sensor calibration of DA in both PBS and cell culture medium. Generator (Gen.) signals include PBS (open squares) and cell culture medium (open circles). Collector (Coll.) signals include PBS (up open triangles) and cell culture medium (down open triangles). Linear regressions equations are visible. Error bars: standard error of the mean.7

Table S5. Detailed results of the linear regression of DA calibration in PBS and cell culture medium. The LOD was calculated as the value of the blank (cultivated cell culture medium) plus three times the error of the blank (SEM). The lowest limit of the linear range is the adjusted to be \geq LOD.7

LC-MRM-MS

Table S6. Elution program of the LC-MRM-MS method using 0.1 % aqueous formic acid as eluent A and acetonitrile as eluent B.8

Figure S7. LC-MRM-MS chromatograms showing chromatographic performance for the most intense MRM transitions. A) Injection of an aqueous mixture of standards (on column: 19.3 pmol GABA, 2.5 pmol norepinephrine (NE), 3.1 pmol epinephrine (EP), 3.7 pmol L-DOPA, 4.0 pmol dopamine (DA), 9.1 pmol DOPAC); B) Chromatogram of the healthy organoid line sample at day 60. EP and NEP had a $S/N < 3$8

Table S8. Limits of Detection (LOD) and Limits of Quantitation (LOQ) obtained for 6 neurotransmitters measured from cell culture medium after minimal sample preparation by LC-MRM-MS. 5 μ l injections. LOD: $S/N > 3$, LOQ: $S/N > 10$9

Table S9. Summary of intraday reproducibility for the LC-MRM-MS analysis of neurotransmitters measured directly from cell culture medium after minimal sample preparation. On the left column averaged coefficient of variation (CV) values of four different human midbrain organoid supernatant (differentiation day 60), N/A: data not available ($S/N < 3$); On the right column averaged CV values of five different standard dilutions ($S/N > 10$, same data as Table 3 in the manuscript). Every injection was done thrice.9

Cell Culture and Immunohistochemistry

Table S10. hMO lines description with references.10

Figure S8. Immunohistochemical staining of an hMO at day 53 of differentiation. The staining reveals tyrosine hydroxylase (TH, red) positive dopaminergic neurons ((a) and (b)) as well as the neuronal marker TUJ1 (green) and DAPI stained nuclei (blue) (a).10

Electrochemistry

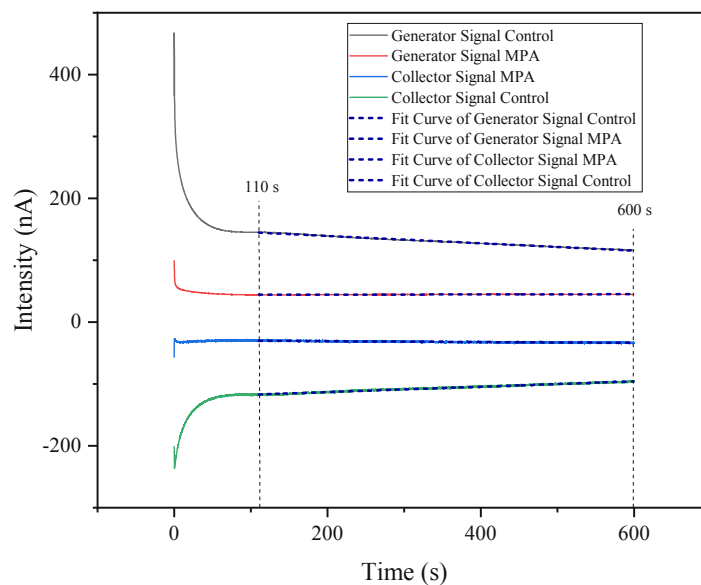


Figure S1. 10-minute redox cycling signals of 5 μM DA in PBS, for both MPA and control sensors. The signal drift was calculated with a linear fit between 110 s and 600 s. The MPA effect on the signal drift was evaluated by comparing the slopes from the linear fits, see Table below for details.

Table S1. Results of the signal drift calculation from the 10-minute redox cycling experiment. The linear fit results were averaged ($n = 2$) and are displayed in the table with the correlated standard error and the slope in degrees. The effect of MPA at the generator removed the signal drift (the value marked with an asterisk was not significantly different from zero). The MPA effect on the collector (cathodic currents) significantly reduced drift of signal from a positive (decreasing signal) slope to a slightly negative value (increasing signal over time), overall this shows a positive impact of MPA on the signal stability.

	Angular coefficient from linear fit Mean ($n = 2$) (nA/s)	Standard Error for angular coefficient (nA/s)	Slope (degrees)	t-test on slope values (one-tailed) Mean ($n = 2$)
Generator Control	-0.0678	8.23 E-05	-3.88	Generator Control vs Generator MPA: $p < 0.01$
Generator MPA	* -2 E-05	2.15 E-05	* -0.0011	
Collector MPA	-0.00903	1.02 E-04	-0.518	Collector Control vs Collector MPA $p < 0.01$
Collector Control	0.0497	1.11 E-04	2.85	

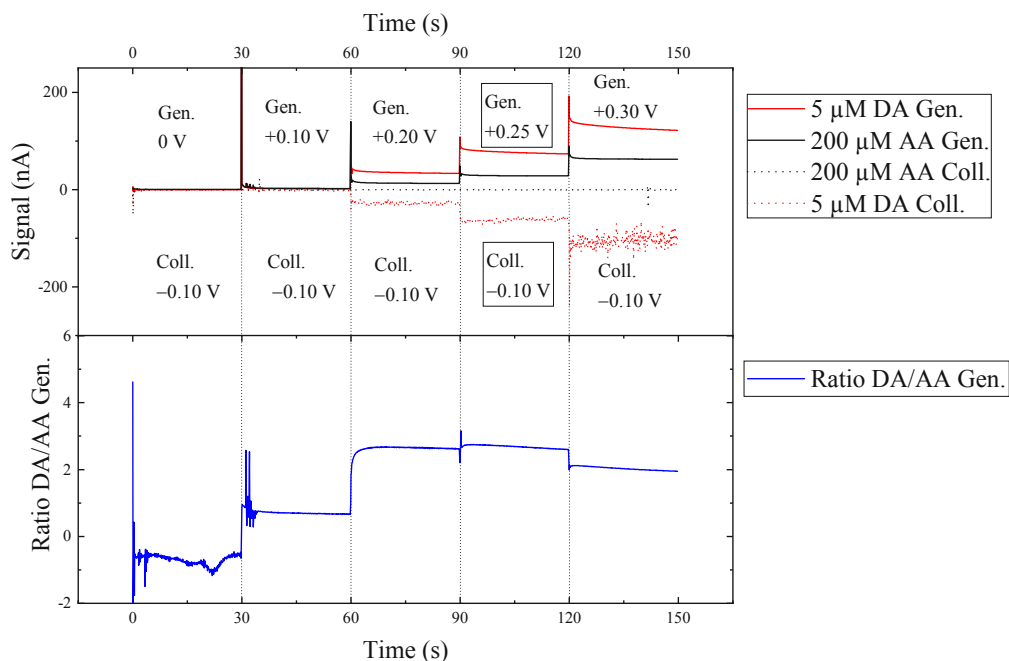


Figure S2. Optimization of the generator potential. On the top: Chronoamperometric responses of DA and AA at the sensor with increasing generator electrode potentials. The potential was stepped every 30 s from 0 to +0.30 V, the collector potential was set to -0.1 V. On the bottom: ratio of the recorded DA and AA signals. The experiment was performed in PBS (pH = 7.4)

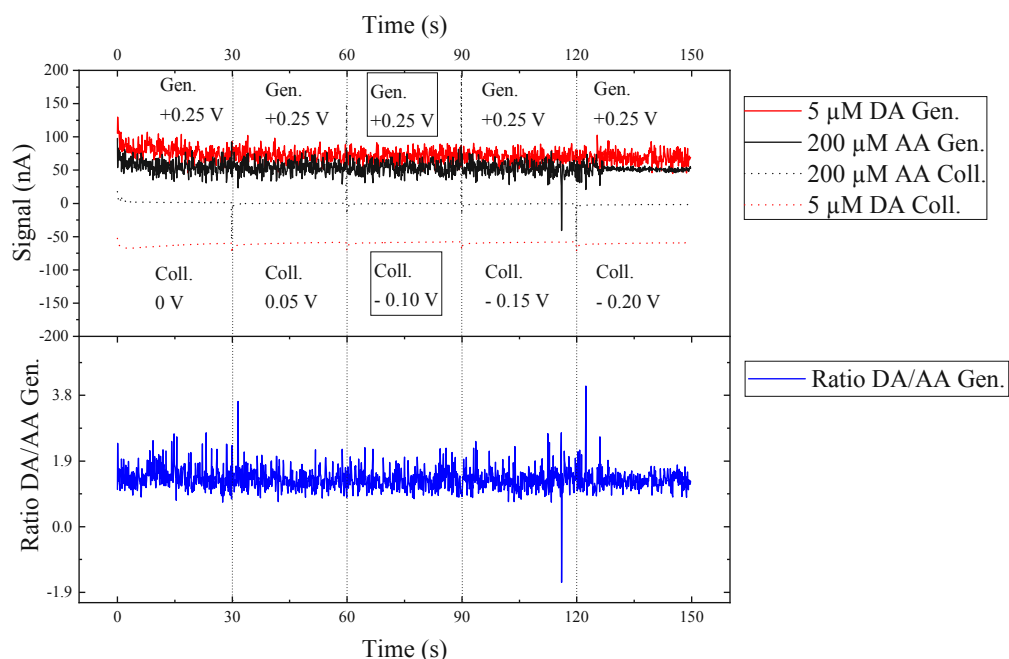


Figure S3. Optimization of the collector potential. On the top: chronoamperometric responses of DA and AA at the sensor with decreasing collector electrode potentials. The potential was stepped every 30 s from 0 to -0.20 V, the generator potential was set to +0.25 V. On the bottom: ratio of the recorded DA and AA signals. The experiment was performed in PBS (pH = 7.4).

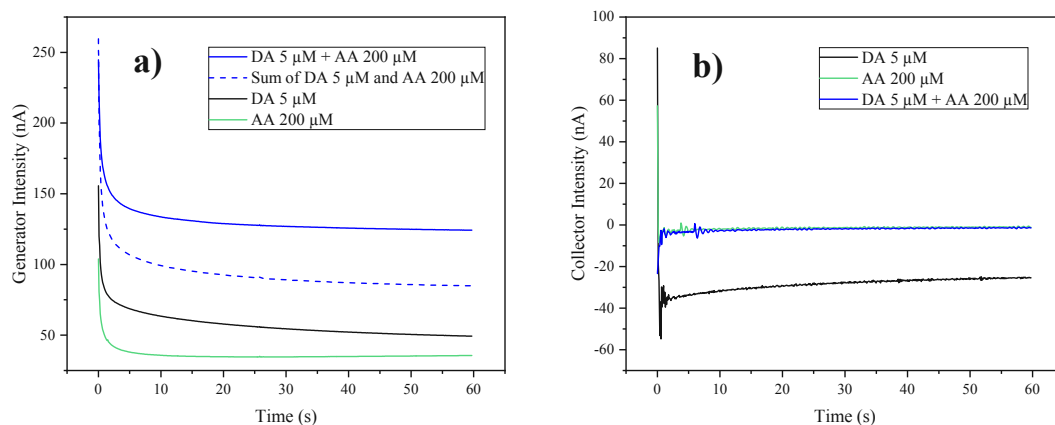


Figure S4. Generator and Collector signals of ascorbic acid (AA) and dopamine (DA) solutions in PBS at MPA modified sensor. a) At the generator the DA signal is higher than the AA signal, and when the two components are mixed in the same solution the resulting signal is higher than the sum of the separate ones, this synergic action is attributed to AA reducing DA-quinone, thus increasing diffusion gradients and leading to higher currents; b) at the collector the AA signal is silent, while the DA signal is visible (due to reduction of DA-quinone), the copresence of DA and AA in solution leads to a silent signal, this is also attributed to AA reducing DA-quinone.

Table S2. Sensor intra-batch and inter-batch repeatability. Each sensitivity measurement was obtained from the slope of a 0-1000 nM DA calibration curve in PBS.

Replicate Batch	DA sensitivity (nC/nM)				Intra-batch CV (<i>n</i> = 4)	Inter-batch CV (<i>n</i> = 3)
	1	2	3	4		
A	0.955	0.973	0.960	1.041	4.1 %	9.9 %
B	1.113	1.084	1.090	1.085	1.3 %	
C	1.240	1.171	1.259	1.242	3.2 %	

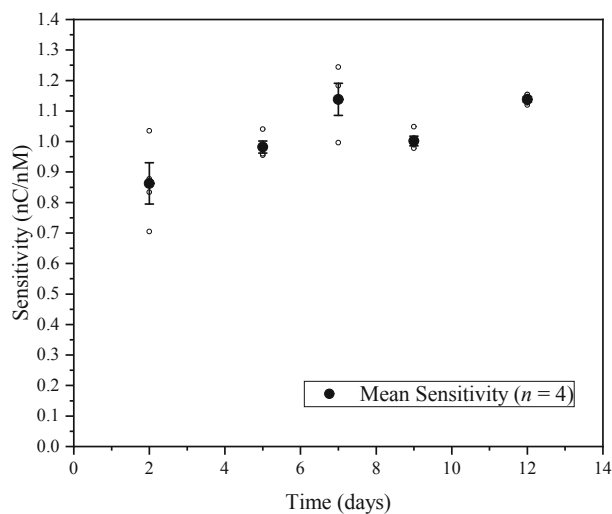


Figure S5. Time resolved monitoring of DA sensitivity of the sensor (*n* = 4) to assess sensor stability. The slope of the linear regression was not significantly different from zero ($\alpha = 0.05$).

Table S3. Long-term stability study. DA signal was measured on the month of manufacturing and also after 20 months (*n* = 3). Selectivity towards AA was also measured after 20 months.

replicate	DA signal (nC/nM) at month 0	DA signal (nC/nM) at month 20	% change	Selectivity towards AA after 20 months
A	0.86	0.41	-52 %	57
B	0.58	0.53	-8%	49
C	0.76	0.52	-31%	68
Average ± SD	0.73 ± 0.14	0.49 ± 0.07	-33 ± 22 %	58 ± 9.5

Table S4. Detailed Results of the analysis of selectivities to DA change after MPA modification. The selectivity was calculated as the ratio of the biomolecule signal (nC/nM) and the DA signal (nC/nM). The percent change represents the change in selectivity to DA after MPA modification. Not detected or n.a.: the signal of the compound was not significantly different from the background (PBS, $\alpha = 0.05$, two-tailed t test).

Selectivity to DA (standard deviation, $n = 3$) at the control sensor and at MPA modified sensor, percent change after MPA modification.						
Compound	Generator			Collector		
	Control	MPA	% Change	Control	MPA	% Change
Norepinephrine	1.8 (0.02)	1.9 (0.05)	+4%	2.9 (0.02)	3.7 (0.02)	+30%
L-DOPA	3 (0.02)	15.8 (0.04)	+419%	8.2 (0.02)	Not detected	n.a.
Epinephrine	3.5 (0.03)	2.2 (0.04)	-37%	83.7 (0.02)	Not detected	n.a.
AA	6.9 (0.02)	55 (0.04)	+702%	3714.6 (0.02)	Not detected	n.a.
DOPAC	11.1 (0.02)	115.2 (0.04)	+934%	11.4 (0.02)	Not detected	n.a.
GABA	288 (0.02)	Not detected	n.a.	Not detected	Not detected	n.a.

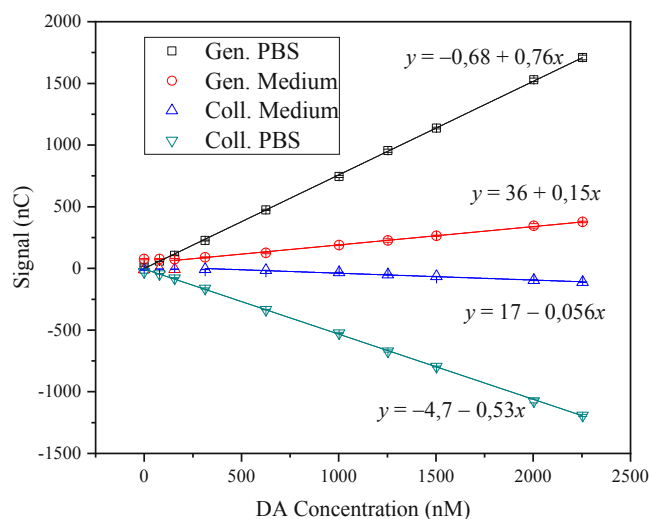


Figure S6. Electrochemical sensor calibration of DA in both PBS and cell culture medium. Generator (Gen.) signals include PBS (open squares) and cell culture medium (open circles). Collector (Coll.) signals include PBS (up open triangles) and cell culture medium (down open triangles). Linear regressions equations are visible. Error bars: standard error of the mean.

Table S5. Detailed results of the linear regression of DA calibration in PBS and cell culture medium. The LOD was calculated as the value of the blank (cultivated cell culture medium) plus three times the error of the blank (SEM). The lowest limit of the linear range is the adjusted to be \geq LOD.

Signal, Solvent	LOD	Linear Range	Intercept		Slope		Statistics
	Value \pm C.I. $\alpha = 0.05$ (nM)		Concentration (nM)	Value (nC)	Standard Error	Value (nC/nM)	
Generator, PBS	69 ± 25	157–2254	-0.68	6.37	0.759	0.005	0.99956
Generator, Medium	369 ± 44	369–2254	41.71	3.74	0.149	0.003	0.99755
Collector, Medium	476 ± 249	476–2254	16.75	3.82	-0.056	0.003	0.9864
Collector, PBS	108 ± 29	108–2254	-4.68	5.21	-0.528	0.004	0.99939

LC-MRM-MS

Table S6. Elution program of the LC-MRM-MS method using 0.1 % aqueous formic acid as eluent A and acetonitrile as eluent B.

Time (min)	B %	Flow rate (ml/min)
0	2	0.4
4	2	0.4
8	80	0.4
9	90	0.4
10	2	0.4
12	2	0.4

Table S7. Ion transitions relevant for the established LC-MRM-MS method to detect and quantify six biomolecules and the internal standard.

Analyte	Retention time (min)	MRM Transitions (precursor ion mass > product ion mass)		
		quantitation	confirmation	
GABA	1.2	104.30 > 87.15	104.30 > 45.10	104.30 > 69.05
Norepinephrine	1.4	170.10 > 135.10	170.10 > 107.10	170.10 > 152.20
Epinephrine	1.8	184.10 > 166.20	184.10 > 123.10	184.10 > 107.10
d3-L-DOPA	2.0	201.10 > 110.20	201.10 > 154.75	201.10 > 184.30
L-DOPA	2.0	198.20 > 152.15	198.20 > 107.10	198.20 > 181.15
Dopamine	2.1	154.10 > 137.00	154.10 > 119.10	154.10 > 91.00
DOPAC	6.2	166.80 > 123.05	166.80 > 122.85	166.80 > 105.00

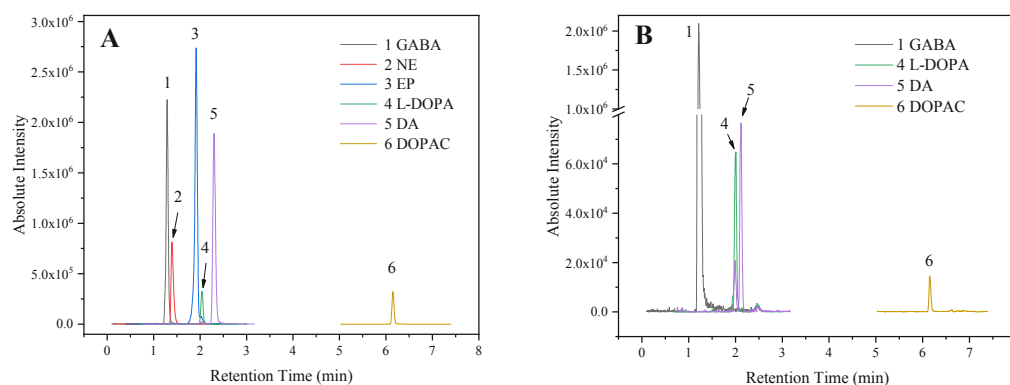


Figure S7. LC-MRM-MS chromatograms showing chromatographic performance for the most intense MRM transitions. A) Injection of an aqueous mixture of standards (on column: 19.3 pmol GABA, 2.5 pmol norepinephrine (NE), 3.1 pmol epinephrine (EP), 3.7 pmol L-DOPA, 4.0 pmol dopamine (DA), 9.1 pmol DOPAC); B) Chromatogram of the healthy organoid line sample at day 60. EP and NE had a S/N < 3.

Table S8. Limits of Detection (LOD) and Limits of Quantitation (LOQ) obtained for 6 neurotransmitters measured from cell culture medium after minimal sample preparation by LC-MRM-MS. 5 μ l injections. LOD: S/N > 3, LOQ: S/N > 10.

	LOD (nM)	LOQ (nM)
GABA	4.3	14.2
Norepinephrine	8.6	28.8
Epinephrine	2.5	8.3
L-DOPA	13.5	44.9
Dopamine	10.9	36.2
DOPAC	12.4	41.4

Table S9. Summary of intraday reproducibility for the LC-MRM-MS analysis of neurotransmitters measured directly from cell culture medium after minimal sample preparation. On the left column averaged coefficient of variation (CV) values of four different human midbrain organoid supernatant (differentiation day 60), N/A: data not available (S/N < 3); On the right column averaged CV values of five different standard dilutions (S/N > 10, same data as Table 3 in the manuscript). Every injection was done thrice.

	% Intraday CV samples (n = 4, triplicate inj.)	% Intraday CV standards (n = 5, triplicate inj.)
GABA	6.5	10.5
Norepinephrine	N/A	4.3
Epinephrine	N/A	8.7
L-DOPA	5.6	3.1
Dopamine	3.8	14.6
DOPAC	5.2	3.0

Cell Culture and Immunohistochemistry

Table S10. hMO lines description with references.

Line name in this work	CRISPR/Cas9	LRRK2 gene	Line name in ref.	Reference
Healthy	No	WT	Healthy2	Qing et al., 2017
Healthy-Mut	Yes	G2019S	Healthy2-Mut	Qing et al., 2017
PD1	No	G2019S	PD1	Reinhardt et al., 2013
PD2	No	G2019S	PD2	Reinhardt et al., 2013
PD2-GC	Yes	WT	PD2-GC	Reinhardt et al., 2013

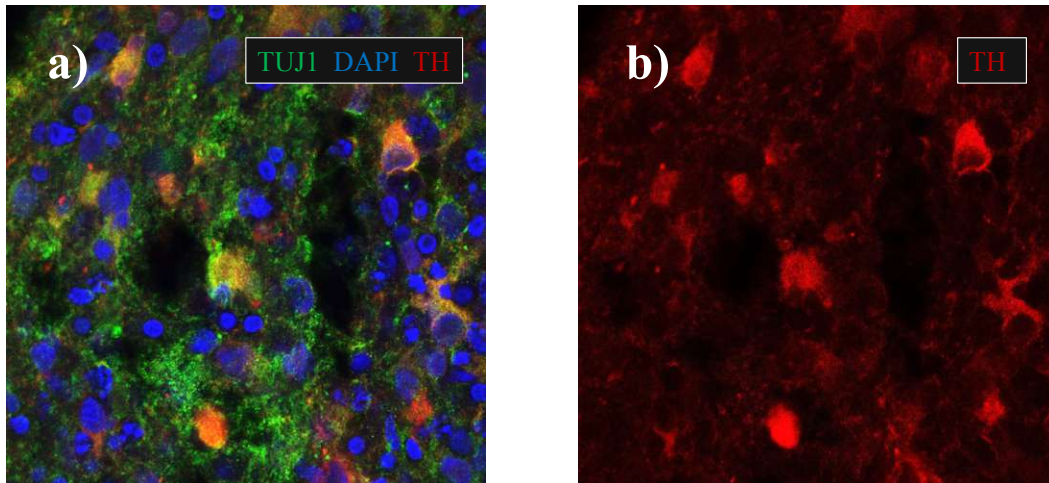


Figure S8. Immunohistochemical staining of an hMO at day 53 of differentiation. The staining reveals tyrosine hydroxylase (TH, red) positive dopaminergic neurons ((a) and (b)) as well as the neuronal marker TUJ1 (green) and DAPI stained nuclei (blue) (a).

3.6 MANUSCRIPT #4 - ARTICLE

DEVELOPMENT OF A MULTI-SENSOR INTEGRATED MIDBRAIN ORGANOID-ON-A- CHIP PLATFORM FOR STUDYING PARKINSON'S DISEASE

Development of a multi-sensor integrated midbrain organoid-on-a-chip platform for studying Parkinson's disease

Sarah Spitz^{a,h}, Silvia Bolognin^b, Konstanze Brandauer^a, Julia Füßl^a, Patrick Schuller^a, Silvia Schobesberger^a, Christian Jordan^d, Barbara Schädli^{c,g,h}, Johannes Grillari^{c,h,i}, Heinz Wanzenböck^e, Torsten Mayr^f, Michael Harasek^d, Jens C. Schwamborn^b, Peter Ertl^{a,h}

a. Faculty of Technical Chemistry, Vienna University of Technology, Getreidemarkt 9/163-164, 1060 Vienna, Austria

b. Developmental and Cellular Biology, Luxembourg Centre for Systems Biomedicine, University of Luxembourg, seven avenue des Hauts-Fourneaux, 4362 Esch-sur-Alzette, Luxembourg

c. Ludwig Boltzmann Institute for Traumatology in Cooperation with AUVA, 1200 Vienna, Austria

d. Institute of Chemical, Environmental and Bioscience Engineering, Thermal Process Engineering and Simulation, TU Wien, 1060 Vienna, Austria

e. Institute of Solid State Electronics, Vienna University of Technology, 1040 Vienna, Austria

f. Institute of Analytical Chemistry and Food Chemistry, Graz University of Technology, Stremayrgasse 9, 8010 Graz, Austria

g. Medical University of Vienna, University Clinic of Dentistry; Vienna, Austria

h. Austrian Cluster for Tissue Regeneration, Vienna, Austria

i. Institute for Molecular Biotechnology, University of Natural Resources and Life Sciences, Vienna, Austria

**Correspondence:*

Peter Ertl - peter.ertl@tuwien.ac.at

Keywords: Parkinson's disease, iPSCs, midbrain organoids, organ-on-a-chip, neurodegeneration, non-invasive monitoring

Abstract

Due to its ability to recapitulate key pathological processes *in vitro*, midbrain organoid technology has significantly advanced the modeling of Parkinson's disease over the last few years. However, some limitations such as insufficient tissue differentiation and maturation, deficient nutrient supply, and low analytical accessibility persist, altogether restricting the technology from reaching its full potential. To overcome these drawbacks, we have developed a multi-sensor integrated organ-on-a-chip platform capable of monitoring the electrophysiological, respiratory, and dopaminergic activity of human midbrain organoids. Our study showed that microfluidic cultivation resulted in a marked reduction in necrotic core formation, improved tissue differentiation as well as the recapitulation of key pathological hallmarks. Non-invasive monitoring employing an orthogonal sensing strategy revealed a clear time dependency in the onset of Parkinson's disease-related phenotypes, reflecting the complex progression of the neurodegenerative disorder. Furthermore, drug-mediated rescue effects were observed after treatment with the repurposed compound 2-hydroxypropyl β -cyclodextrin, highlighting the platform's potential in the context of drug screening applications as well as personalized medicine.

1. Introduction

With a prevalence of 9.4 million, Parkinson's disease (PD) constitutes the second most common neurodegenerative disorder worldwide.¹ Characterized by intracellular inclusions of α -synuclein and the loss of dopaminergic neurons within the *substantia nigra* of the human midbrain, this heterogeneous disease results in a variety of debilitating motor and non-motor symptoms.² Whereas the lack of disease-modifying and neuroprotective strategies has restricted the treatment of PD to symptomatic control, the development of new therapeutics remains hampered by the high failure rates observed in clinical trials. This ill success of putative drug candidates can be attributed, at least in part, to the inability of current disease models to replicate critical pathological hallmarks of the disease.³ With the emergence of induced pluripotent stem cell (iPSC)-technology, however, new possibilities toward physiologically relevant and patient-specific *in vitro* models have opened up in the form of so-called "organoids".^{4,5} Organoids denote *in vitro* derived microtissues that, by undergoing some level of self-organization, can recapitulate fundamental physiological facets of *in vivo* organs. Several organoid-based models of the human brain have been developed so far, including microtissues of the forebrain, the hindbrain, and of the midbrain, the afflicted region in PD.⁶⁻⁸ Midbrain organoid models not only exhibit essential features of the tissue's three-dimensional (3D) cytoarchitectural arrangement and function but also mirror pathological hallmarks of PD including dopaminergic neurodegeneration.⁹⁻¹² Despite these significant advancements, however, several challenges persist, including the lack of specific cell types (e.g., endothelial cells), the tissue's immaturity, organoid variability, and nutrient deficiency-based growth restrictions – a result of the organoid's inherent structure and the concomitant lack of vasculature. Moreover, organoid technology still strongly relies (a) on unphysiological cultivation conditions that omit critical biophysical cues and (b) on the use of invasive endpoint analysis that hinder the investigation of progressive developmental processes. One important biophysical cue that has been largely overlooked is the brain-specific interstitial fluid flow, which has been linked to a variety of essential functions, including the delivery of nutrients, the removal of metabolic and neurotoxic waste, non-synaptic cell-cell communication, tissue homeostasis as well as cell migration.^{13,14} Moreover, as part of the so-called "glymphatic system" – a glial-mediated clearance system of the human brain – interstitial fluid flow has been connected to exacerbated protein deposition in models of Alzheimer's disease and PD as well as to the delivery and clearance of drugs, making it of considerable importance in the context of pharmacological screening applications.^{13,15,16}

One technology capable of applying defined flow profiles, fluid velocities, and shear forces is microfluidics.¹⁷ Its ability to reproducibly control various parameters such as mechanical stimulation, laminar fluid dynamics (e.g., perfusion), temperature profiles, and gaseous permeability has already led to the successful recreation of various tissue models *in vitro* in the form of so-called organs-on-a-chip.¹⁸⁻²⁰ Although organ-on-a-chip technology has expanded massively over the last decade, only a handful of studies have set out to combine brain organoids with organ-on-a-chip technology.^{7,21-28} For example,

brain-on-a-chip platforms have already been successfully employed to assess the effects of prenatal exposure to various neuroteratogens such as cadmium, nicotine, and cannabis, to study the physical underpinnings of human brain folding as well as to model neural tube development *in vitro*.^{7,22,25–27} A more recent study by Cho *et al.*²⁴ demonstrated significant improvements in the functional maturation of human brain organoids embedded within a brain extracellular matrix enriched hydrogel using gravity-driven flow. Next to improved cellular viabilities and reduced necrotic cores, dynamic cultivation could markedly reduce organoid size variation from a coefficient of variance of 43.4 % to 17.4%. However, none of the above-referenced studies have investigated neurodegenerative processes or exploited the potential of microfluidic technology to integrate in-line sensing strategies needed to increase analytical accessibility, a prerequisite of any high-quality *in vitro* tissue model.

Here, we present, for the first time, a multi-sensor integrated microfluidic platform for the dynamic long-term cultivation and analysis of human iPSC-derived midbrain organoids. The main design feature of the organoid-on-a-chip platform consists of unidirectional medium flow through three interconnected chambers, each equipped with an optical, electrical or electrochemical microsensor (Fig. 1). Dynamic cultivation of the organoids is accomplished by combining a hydrogel-based flow restrictor with gravity-driven flow to simulate interstitial flow profiles.²⁹ To provide information on essential cellular parameters, including cell growth, metabolic activity, tissue viability, and differentiation, as well as cellular pathology, an optical, luminescent-based oxygen sensor spot is located in the organoid chamber.^{30–32} Additionally, a multi-electrode array is integrated to monitor the electrophysiological activity of neuronal processes, an essential prerequisite for functional cell coupling and tissue maturation. Furthermore, an enzyme-based amperometric sensor is introduced into the downstream compartment to monitor the release of the neurotransmitter dopamine, as it directly reflects the maturation progress and pathological status of midbrain tissues. As this study sets out to investigate pathophysiological alterations in PD, midbrain organoids derived from a PD patient carrying a triplication mutation of the α -synuclein gene (3xSNCA) have been selected. Under physiological conditions, α -synuclein modulates crucial cellular processes such as synaptic vesicle trafficking, neurotransmitter release, and neuronal differentiation.^{33,34} Due to its structural instability, however, α -synuclein can adopt several conformations that favor oligomerization and aggregation, which have been associated with neurotoxicity and neurodegeneration.³⁵ Elevated levels of α -synuclein (e.g., through multiplications of the gene) further reinforce the protein's propensity to aggregate and have been associated with full PD penetrance.^{36–38} We have previously shown that the compound 2-hydroxypropyl β -cyclodextrin (HP- β -CD) can rescue PD-related phenotypes in a personalized PD model carrying biallelic pathogenic variants in the PINK1 gene by elevating the neuronal autophagy and mitophagy capacity.³⁹ Autophagy dysregulation has been implicated in many genetic models of PD including that of α -synuclein, rendering HP- β -CD, an ideal candidate for the evaluation of the microfluidic platform.

Thus, in our final set of experiments, the multi-sensor integrated platform is employed to investigate the dynamic exposure of HP- β -CD on PD onset and progression.

2. Results and Discussion

2.1 Hydrostatic pressure-driven flow emulates cerebral interstitial fluid flow rates *in vitro*

To account for interstitial fluid flow in our sensor-integrated *in vitro* model, a combination of hydrostatic pressure-driven flow and hydrogel-based fluid restriction was explored.²⁹ As depicted in Figure 1A, each cultivation chamber of the PDMS-based organ-on-a-chip platform is comprised of three individual compartments interconnected by two micropillar arrays. While the two outer chambers form the medium channels, the middle chamber is designed to accommodate the differentiating human midbrain organoid (hMO) in a three-dimensional matrix, emulating *in vivo* elasticities (Matrigel®).^{40,41} To facilitate the reproducible positioning of the organoids in the microfluidic device, a 250 μm deep cylindrical well was integrated at the bottom of the central hydrogel chamber (Fig. 1B). Hydrostatic pressure-driven flow is generated by filling up both reservoirs of the supply channel (left medium channel), which subsequently directs medium flow through the hydrogel matrix and the embedded microtissue within towards the waste compartment (right medium channel) (Fig. 1B). Therefore, nutrient supply is no longer restricted to diffusion, but nutrients are actively transported to the embedded organoid via convective flow. It is important to note that the integrated hydrogel-restrictor keeps shear forces at a minimum, thus fulfilling an essential requirement in the cultivation of neuronal microtissues. To gain a deeper understanding of the applied flow behavior within the microfluidic platform, a computational fluid dynamic (CFD) simulation was performed. In-silico analysis demonstrated that the main pressure drop occurs at the hydrogel interface (Fig. 1C), resulting in a highly uniform volume flow with parallelly aligned streamlines (Fig. 1C) throughout the central part of the organoid cultivation compartment (SI Fig. 1B). At a level difference of 3 mm (equivalent to approx. 30 Pa pressure difference), an average flow velocity of 0.71 $\mu\text{m}/\text{s}$ was observed, indicative of an interstitial fluid flow regime (Fig. 1C). Based on the established CFD model, an initial reservoir pressure difference of 3 mm was selected to drive interstitial fluid flow through the hydrogel and thus provide optimal culture conditions for the embedded organoid. Over a period of 24 hours, hydrostatic pressure-driven flow profiles followed an exponential decay resulting in a 1.8-fold higher influx during the first 6.5 hours of dynamic exposure (SI Fig. 1D). This behavior correlates well with recent findings that the glymphatic system is under circadian control, featuring significantly higher glymphatic influx and thus clearance during resting compared to active phases.^{42,43}

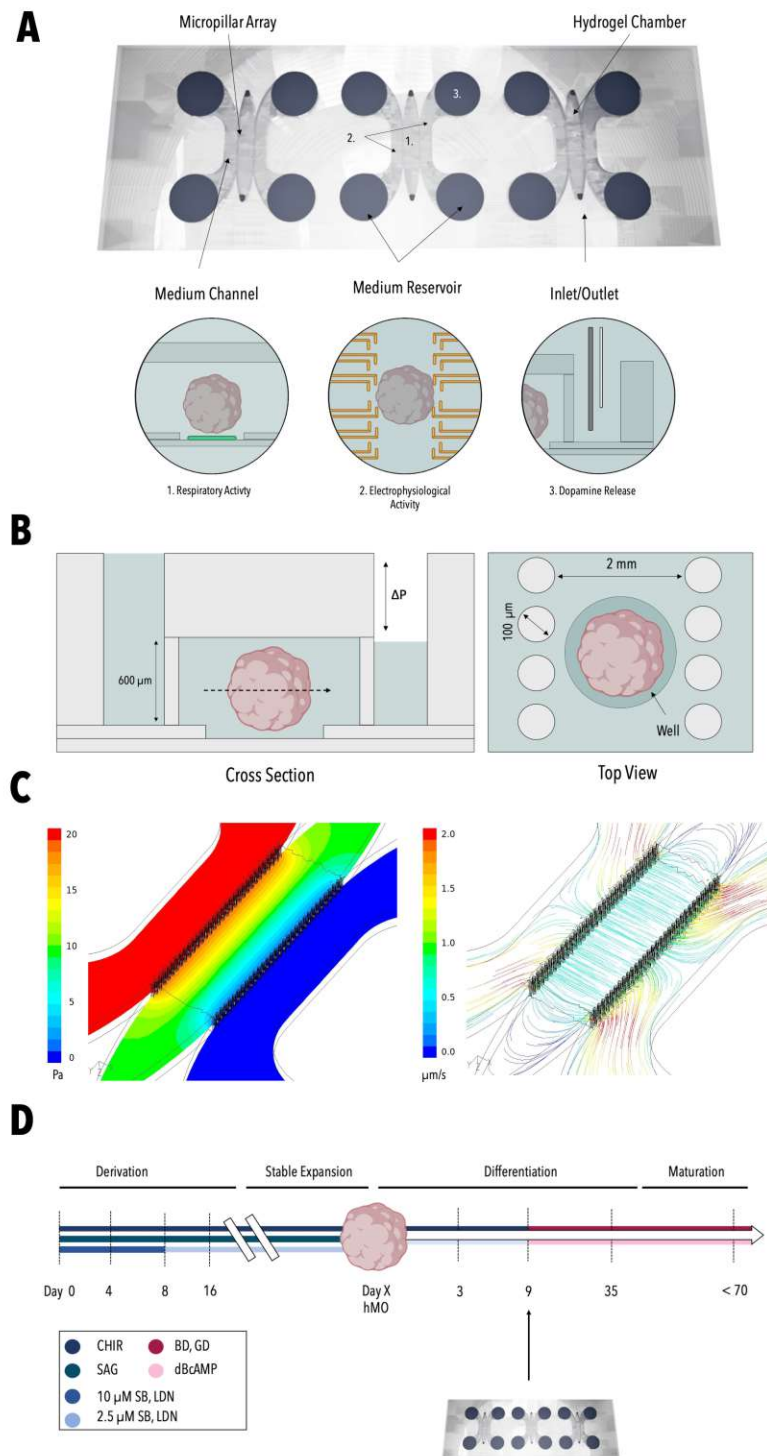


Figure 1: Render of the PDMS-based microfluidic device (Fusion 360) comprised of three individual culture chambers, including the positioning of 1. the optical oxygen sensor, 2. the multi-electrode array (MEA), and 3. the electrochemical dopamine sensor. (A). Cross view and top view of the microfluidic organ-on-a-chip platform (B). Results of the CFD simulation depicting the pressure profile on-chip (left panel) and the generated laminar flow profile (right panel) (C). Workflow of organoid maturation and microfluidic cultivation (D).

2.2 Dynamic cultivation significantly reduces the necrotic core formation and improves neuronal differentiation

Initial on-chip studies, employing healthy midbrain hMOs focused on assessing the effects of a dynamic cultivation milieu on both nutrient supply as well as tissue differentiation. To that end, WT hMOs were introduced either into the microfluidic device (see Fig.2A) based on the workflow depicted in Figure 1D or cultivated in a conventional static tissue culture plate set-up. Neurite outgrowth is essential for the formation of mature neuronal networks and can therefore be considered an important indicator of tissue differentiation. As depicted in Figure 2D, exposure to interstitial fluid flow rates significantly enhanced neurite outgrowth, with a 1.5-fold higher average neurite outgrowth rate in dynamically cultivated microtissues compared to static controls already 24 hours into the on-chip cultivation. Since insufficient nutrient supply in organoids is generally linked to the formation of so-called "dead cores," WT hMOs were analyzed for the apoptotic marker caspase 3 after 35 days of differentiation.

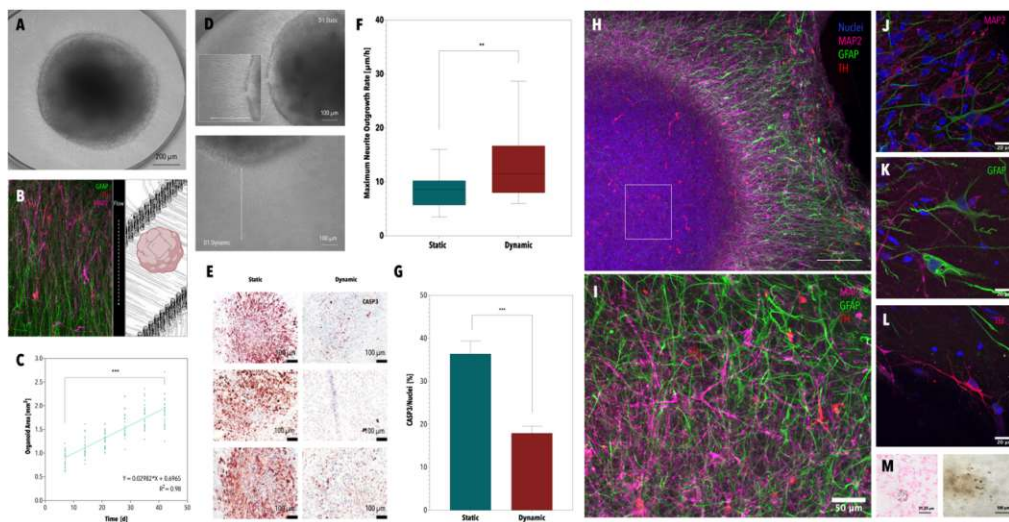


Figure 2: Brightfield image of an embedded hMO on-chip (A). Alignment of glial and neuronal processes in direction of the applied flow: TH (red), GFAP (green), MAP2 (magenta) (B). Growth curve of midbrain microtissues on-chip. Statistical significance by mixed-effects analysis and Tukey test $*p < 0.033$, $**p < 0.002$, $***p < 0.001$ ($n = 8-10$ from 3 independent organoid generations) (C). Brightfield images of statically (top panel) and dynamically (bottom panel) cultivated hMOs depicting differences in neurite outgrowth (left panel) (D). Boxplot of maximum neurite outgrowth rates of statically and dynamically cultivated hMOs. Statistical significance by Mann-Whitney test $*p < 0.033$, $**p < 0.002$, $***p < 0.001$. ($n \geq 3$, from 3 independent organoid generations) (F). Micrographs and the respective quantitative analysis of immunohistochemically stained sections of hMOs depicting significant differences in the apoptotic marker caspase 3 after 35 days of differentiation. Statistical significance by Welch t-test $*p < 0.033$, $**p < 0.002$, $***p < 0.001$. Column and error bars represent mean \pm SEM ($n \geq 3$, from 3 independent organoid generations) (E,G). Whole-mounted midbrain organoid after 60 days of differentiation: TH (red), GFAP (green), MAP2 (magenta), nuclei (blue) (H). Enlarged detail of the core of the whole-mounted hMO (H) at a magnification of 60x (I). Immunohistochemical staining of MAP2-positive neurons (J). Immunohistochemical staining of GFAP-positive astrocytes (K). Immunohistochemical staining of TH-positive dopaminergic neurons (L). Brightfield image (right panel) of neuromelanin aggregates in a midbrain organoid and the corresponding Fontana Masson staining revealing intra- and extracellular neuromelanin aggregation (left panel) (M).

Strikingly, a 2-fold reduction in the normalized caspase 3 signal was observed in the presence of interstitial flow conditions (Fig. 2E/G), strongly pointing at improved nutrient availabilities under convective mass transfer. Overall, morphological assessment of dynamically cultivated microtissues revealed a significant increase in hMO size over time, ranging from $0.87 \pm 0.17 \text{ mm}^2$ at day 7 to $1.87 \pm 0.3 \text{ mm}^2$ at day 42 (Fig. 2C). In addition, immunohistochemical analysis of WT hMOs after 50 days in dynamic culture revealed the presence of key midbrain-associated cell types including microtubule-associated protein 2 (MAP2)-positive neurons (Fig. 2J), tyrosine hydroxylase (TH)-positive dopaminergic neurons (Fig. 2L) as well as glial fibrillary acidic protein (GFAP)-positive astrocytes (Fig. 2K). Unexpectedly, a unidirectional interstitial fluid flow resulted in the alignment of both neuronal and glial cellular processes, clearly reflecting the parallel arrangement of the simulated streamlines as seen in Figures 1C and 2B. Occasionally, neuromelanin-like granules were detected within hMOs on-chip starting at about 30 days of differentiation (Fig. 2M/SI Fig.2A). Fontana-Masson staining confirmed the presence of both extra- and intra-cellular neuromelanin deposits, indicating that this physiological pigment, which is inherent to the *substantia nigra*, gets secreted within the hMOs on-chip. To further support the observation that interstitial fluid flow improves midbrain tissue differentiation a comparative whole-mount analysis of WT hMOs was conducted after 50 days of on/off-chip culture. In addition to robust neuronal differentiation, dynamically cultivated microtissues displayed substantial glial differentiation, characterized by the presence of highly ramified GFAP-positive astrocytes. Moreover, immunohistochemical analysis of whole-mounted hMOs revealed a 2.1-fold higher TH/MAP2 ratio, as well as a 1.4-fold higher GFAP signal for dynamically cultivated hMOs compared to static controls (SI Table 1), pointing towards improved microtissue differentiation on-chip. In summary, the introduction of hMOs into our microfluidic platform not only supported tissue differentiation but also resulted in a marked improvement of one of the key limitations in organoid technology: insufficient nutrient supply.

2.3 Patient-specific hMOs (3xSNCA)-on-chip recapitulate key pathological hallmarks of PD

Following the establishment of a healthy microphysiological midbrain model, organoids derived from a PD patient carrying a triplication mutation of the α -synuclein gene were added to the study. A combination of morphological and immunohistochemical analysis was performed to verify the presence of PD phenotypes. Figure 3A shows the organoid growth dynamics of healthy and PD hMOs featuring distinct differences over a seven-week on-chip cultivation period. While WT (healthy) hMOs followed a linear trend that plateaued at around day 42, 3xSNCA hMOs displayed a complex dynamic growth behavior that can be characterized by an initial steep incline (D7-14), followed by a steady increase that subsequently declined by day 42. Whereas the organoid growth rates of healthy hMOs did not markedly change during the first 35 days of cultivation ($0.033 \pm 0.01 \text{ mm}^2/\text{day}$), the growth rates of PD hMOs displayed a progressive decline over time ranging from $0.082 \text{ mm}^2/\text{day}$ on day 14 to $0.031 \text{ mm}^2/\text{day}$

at day 35 (SI Fig. 3A). Upon comparison to their healthy controls, PD hMOs exhibited a 1.3-fold bigger cross-sectional area, with an up to 2.3-fold higher growth rate in the first phase of cultivation.

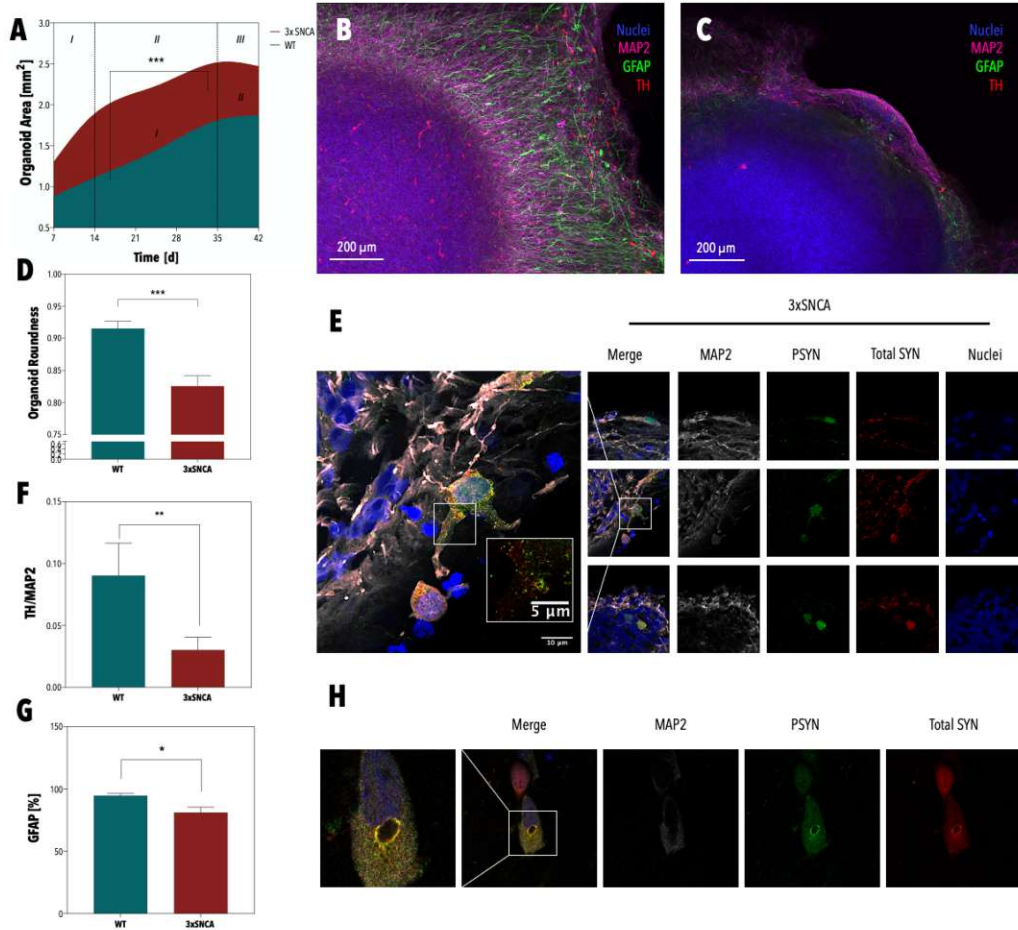


Figure 3: Growth curve of healthy and PD hMOs on-chip. Statistical significance by mixed-effect analysis and Tukey test $*p < 0.033$, $**p < 0.002$, $***p < 0.001$ ($n = 8-10$ from 3 independent organoid generations) (A). Image of an immunohistochemically stained healthy hMO after 60 days of differentiation on-chip: TH (red), GFAP (green), MAP2 (magenta), nuclei (blue) (B). Image of an immunohistochemically stained PD hMO carrying a triplication mutation of the α -synuclein gene after 60 days of differentiation on-chip: TH (red), GFAP (green), MAP2 (magenta), nuclei (blue) (C). Comparative analysis of organoid roundness of WT and 3xSNCA hMOs at D31 of differentiation. Statistical significance by Welch's t -test $*p < 0.033$, $**p < 0.002$, $***p < 0.001$. Column and error bars represent mean \pm SEM ($n = 8-10$ from 3 independent organoid generations) (D). Micrographs of 100 μ m-thick sections of PD hMOs depicting the colocalization of α -synuclein and p-S129- α -synuclein after 60 days of differentiation on-chip (E). Quantitative analysis of immunohistochemically stained WT and PD hMOs revealing significantly reduced levels of TH/MAP2 ratios. Statistical significance by Mann-Whitney test $*p < 0.033$, $**p < 0.002$, $***p < 0.001$. Column and error bars represent mean \pm SEM ($n = 6-8$ from 3 independent organoid generations) (F). Quantitative analysis of immunohistochemically stained WT and PD hMOs revealing significantly reduced levels of GFAP-positive astrocytes. Statistical significance by Mann-Whitney test $*p < 0.033$, $**p < 0.002$, $***p < 0.001$. Column and error bars represent mean \pm SEM ($n = 6-8$ from 3 independent organoid generations) (G). Lewy-body-like inclusions observed in 100 μ m-thick sections of 3xSNCA hMOs after 60 days of differentiation on chip (H).

The observation that 3xSNCA hMOs displayed a rapid size increase early on followed by a reduction in cell mass after 42 days correlates well with our previous findings that neurogenerative degeneration in 3xSNCA hMOs is preceded by an overproduction of the dopaminergic neuron population at early

stages of differentiation.⁴⁴ Figure 3D further shows that 3xSNCA hMOs displayed aspherical morphologies, as characterized by a significant reduction in organoid roundness from 0.92 for WT hMOs to 0.83 for 3xSNCA hMOs. Most importantly, immunohistochemical analysis of both healthy controls and 3xSNCA hMOs after 60 days of differentiation revealed a significant (3-fold) reduction in TH-positive dopaminergic neurons within patient-specific microtissues (Fig. 3F) – indicative of a neurodegenerative phenotype. Moreover, a significantly lower number of GFAP-positive astrocytes was detected in PD hMOs, in line with previously reported pathology-associated impairments in glial differentiation.⁴⁴ Further analysis of PD hMOs (Fig. 3E) revealed the presence of both α -synuclein as well as p-S129- α -synuclein – a post-translationally modified version, which was found to be enriched in newly formed aggregates *in vivo*.⁴⁵ Colocalization of p-S129- α -synuclein and α -synuclein was validated by calculating the Pearson's correlation coefficient (>0). Intriguingly, immunohistochemical analysis additionally pointed towards the presence of Lewy body-like inclusions (the second hallmark of PD), as characterized by a peripheral halo, enriched in both α -synuclein and p-S129- α -synuclein and an electron-dense core (Fig. 3H and SI Fig. 3C).⁴⁶ This means that two key pathological hallmarks of PD, namely neurodegeneration and synuclein aggregation in the form of so-called Lewy-bodies, were observed after 60 days of dynamic culture.

2.4 Orthogonal sensing enables the time-resolved monitoring of PD-related phenotypes

To demonstrate the analytical accessibility of our microfluidic midbrain organoid model, three non-invasive orthogonal sensing strategies (Fig. 1A) were evaluated in subsequent experiments to follow the onset and progression of (patho)physiological phenotypes. Figure 4A shows the position and working principle of the luminescence-based oxygen microsensors integrated into the microfluidic platform. Monitoring of healthy hMOs revealed a clear correlation between organoid growth and respiratory activity within the first 21 days of cultivation, resulting in an average normalized oxygen demand of 119.9 ± 4.4 hPa/mm² (Fig. 4B). Comparative analysis of both healthy and 3xSNCA hMOs, shown in Figure 4E, revealed a significantly higher respiratory activity in PD microtissues over a cultivation period of 7 weeks. Similar to the complex growth behavior seen above (Fig. 3A), the oxygen demand of PD hMOs displayed high initiating demands of 137.7 ± 30.4 hPa, plateauing around 164.7 ± 4.1 hPa at day 21, before eventually dropping to 155.1 ± 10.5 hPa around day 42. These results align well with our previous findings that neurodegenerative processes in 3xSNCA hMOs are preceded by an overproduction of the dopaminergic neuron population (e.g., high mitochondrial activity) early on.⁴⁴ In turn, healthy hMOs displayed a steady increase in oxygen demand from 112.6 ± 35.85 hPa at day 3 to a peak of 159.7 ± 17.8 hPa at day 21, followed by a subsequent decline in respiratory activity between day 21 and day 42. This dynamic respiratory profile of healthy hMOs might reflect the chronology of brain development where neurogenesis (e.g., high mitochondrial activity) precedes

astrogenesis (e.g., glycolytic metabolism).^{47,48} In an attempt to account for cell number variations between healthy and PD hMOs, organoid size-corrected data was calculated, revealing an inverted respiratory behavior. Results in Figure 4F point towards a significantly lower normalized oxygen demand in PD microtissues, indicative of impaired cellular respiration. To verify whether the reduction in normalized oxygen demand in PD hMOs can be linked to increased levels of aggregated α -synuclein, which has previously been shown to bind to and impair mitochondria,⁴⁹ a comparative immunohistochemical analysis was performed. Quantitative image analysis using an in-house-developed algorithm confirmed elevated levels of p-S129- α -synuclein in 3xSNCA hMOs in relation to healthy controls (Fig. 4C). To subsequently ensure that reduced normalized oxygen demands of 3xSNCA hMOs are caused by impaired mitochondrial physiology, fluorescence analysis employing a TOM20 antibody was performed. Indeed, distinct differences encompassing a significant reduction in the overall mitochondria count, reduced mitochondrial complexity, as well as lower mitochondria numbers within dopaminergic neurons were detected for PD hMOs (Fig. 4D).

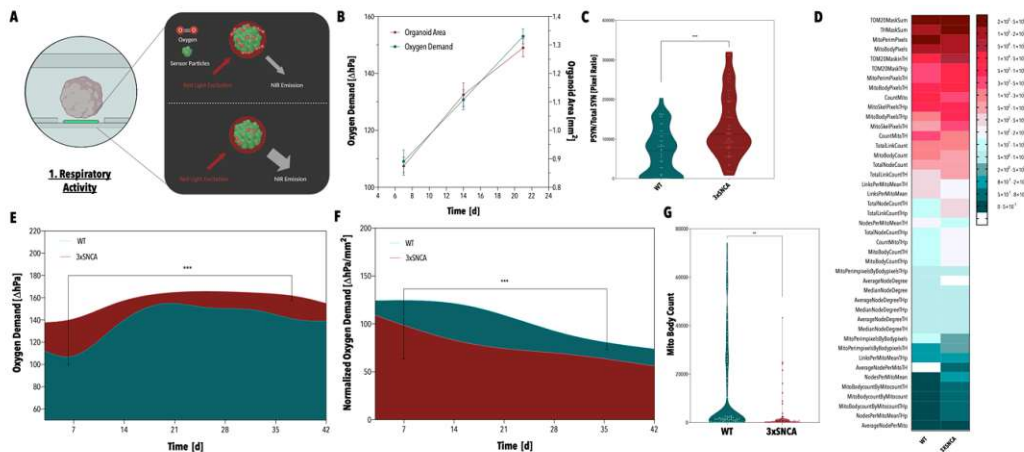


Figure 4: Schematic of the arrangement and working principle of the optical oxygen sensor (A). Correlation between healthy hMO growth and oxygen demand over 21 days of on-chip cultivation (B). Violin plot revealing elevated p-S129- α -synuclein to α -synuclein ratios in 3xSNCA hMOs (C). Heatmap providing an overview of altered mitochondria markers observed in 3xSNCA hMOs. 001 ($n \geq 3$ from 3 independent organoid generations) (D). Fitted oxygen demand profiles of healthy and PD hMOs over a cultivation period of 42 days (E). Fitted normalized oxygen demand profiles of healthy and PD hMOs over a cultivation period of 42 days (F). Violin plot revealing significantly reduced mitochondria body counts in 3xSNCA hMOs (G). (E,F) Statistical significance by mixed-effect analysis and Tukey test * $p < 0.033$, ** $p < 0.002$, *** $p < 0.001$ ($n = 8-10$ from 3 independent organoid generations). (C,G) Statistical significance by Mann-Whitney test * $p < 0.033$, ** $p < 0.002$, *** $p < 0.001$ ($n \geq 3$ (C) $n \geq 3$ from 3 independent organoid generations).

The neurotransmitter dopamine can be considered a crucial PD-specific biomarker, as its levels directly reflect the tissue's pathological status. By inserting a nanoparticle-based enzymatic biosensor into the waste reservoir of the microfluidic device, changes in dopamine concentrations in the organoid's supernatant were recorded over time. Figure 5A provides a schematic of the hydrogel-covered carbon electrode, comprising the enzyme tyrosinase, the hydrogel chitosan, and the two oxygen donors, cerium oxide and titanium oxide. Results in Figure 5B show a steady increase in dopamine levels for both healthy and 3xSNCA hMOs over a period of 7 weeks, with the first detectable signals retrieved after 35 days of microfluidic cultivation. By week 7 (59 days of differentiation), significant differences in dopamine secretion between healthy and PD hMOs started to emerge, correlating well with our previous findings that showed first discernable variations in TH expression around day 60 of differentiation.⁴⁴ In addition, the electrochemical analysis supported our earlier observation that dynamic cultivation improves tissue differentiation, or the TH-positive neuronal population, respectively, with a 3.9-fold higher dopamine signal obtained for hMOs exposed to interstitial fluid flows compared to static controls (Fig. 5C). Since electrophysiological activity constitutes an important (patho)physiological parameter, assessing neuronal firing activity is essential for any *in vitro* brain model. Consequently, a multi-electrode array (MEA) was integrated into the supply and waste channels of the organ-on-a-chip platform, enabling electrophysiological recordings of the neuronal microtissues (Fig. 5H/D/E). Flow-directed outgrowth was utilized to direct neuronal processes extending from the three-dimensional microtissue onto the two-dimensional electrode array. (Fig. 5E/H). By using this approach, spontaneous electrophysiological activity was recorded starting at 24 days of differentiation (Fig. 5G). Next to monophasic and biphasic spikes (Fig. 5Ib/c), various firing patterns were observed, including tonic spiking, phasic bursting as well as tonic bursting (Fig. 5F). Overall, 66 ± 14 % of all active electrodes displayed bursting activity, a characteristic of dopaminergic neurons.⁵⁰ Dopaminergic identity was further supported by clusters of spikes that displayed breaks in the initial spike segments (Fig. 5Ia).⁵¹ Electrophysiological activity was validated by silencing with the neurotoxin tetrodotoxin (Fig. 5F) as well as by performing Fluo-4 acetoxymethyl ester (AM)-based calcium imaging (data not shown).

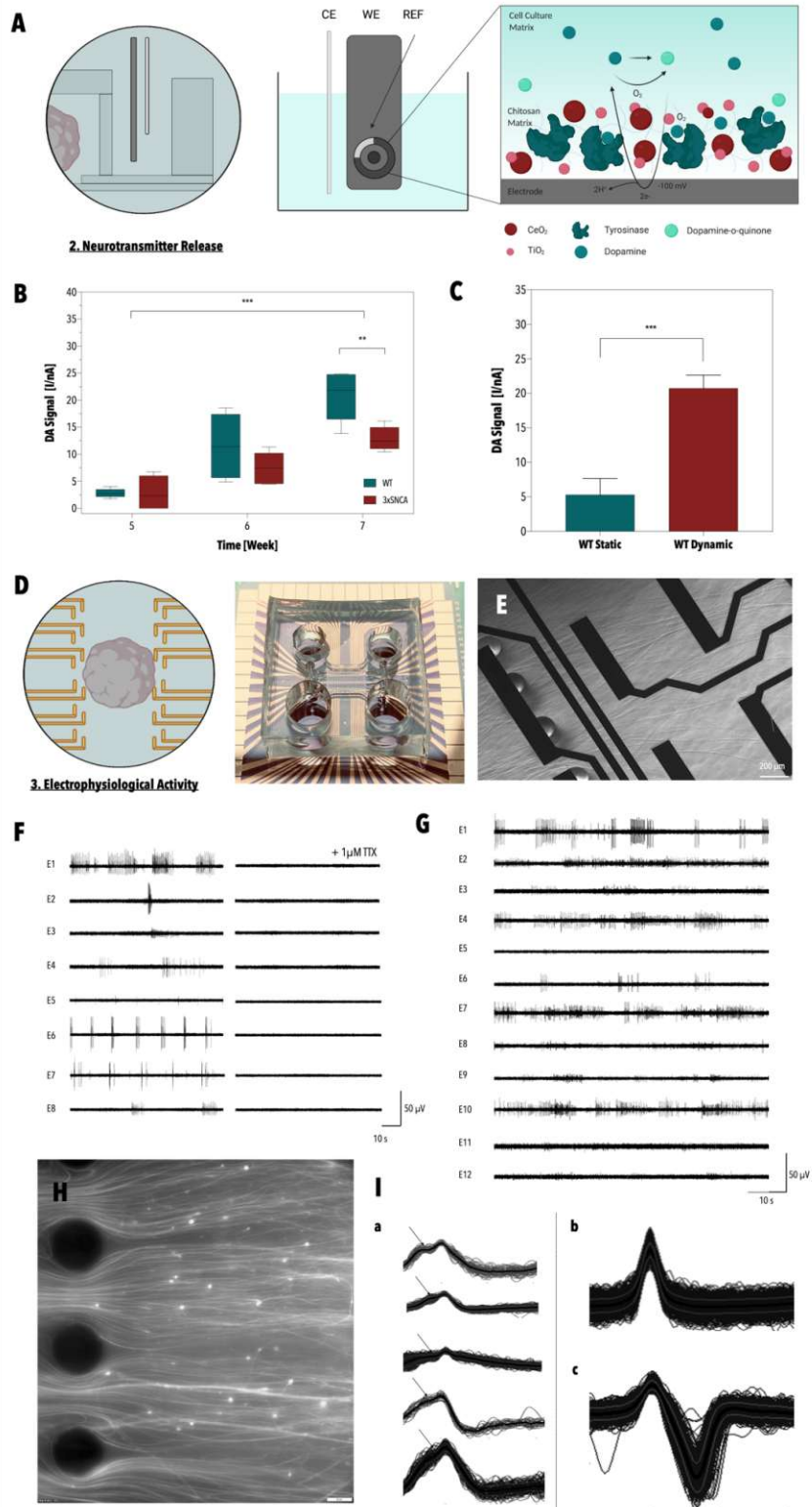


Figure 5: Schematic of the working principle of the electrochemical dopamine biosensing approach and the three-electrode set-up (A). Increase in dopamine signal in the supernatant of healthy and PD midbrain organoids over time. Statistical significance by two-way ANOVA and Tukey test * $p < 0.033$, ** $p < 0.002$, *** $p < 0.001$ ($n = 10$ (pooled) from 2 independent organoid generations (technical triplicates)) Comparative analysis between WT and 3xSNCA at week 7 was conducted by Welch' t-test * $p < 0.033$, ** $p < 0.002$, *** $p < 0.001$ ($n = 10$ (pooled) from 2 independent organoid generations) (B). Comparative analysis of the dopamine signal of statically and dynamically cultivated WT hMOs. Statistical significance by Welch' t-test * $p < 0.033$, ** $p < 0.002$, *** $p < 0.001$ Column and error bars represent mean \pm SEM ($n = 10$ (pooled) from 2 independent organoid generations (technical triplicates)) (C). Schematic and image of the MEA integrated microfluidic device (D). Micrograph of neurites extending over the microelectrodes on-chip (E). Electrophysiological recordings of human midbrain organoids on-chip prior to and after the exposure to the neurotoxin TTX (F). Representative read-out of the electrophysiological activity of a healthy hMO in a microfluidic device (G). Flow-directed outgrowth of neurites on-chip (H). Examples of dopaminergic clusters, characterized by the break in the initial segment (I/arrow) as well as mono- and bi-phasic spikes recorded on-chip (I_{bc}).

2.7. On-chip monitoring reveals HP- β -CD-mediated phenotypic rescue in 3xSNCA organoids

While HP- β -CD has been established as a promising excipient in pharmacology, its repurposed application for enhancing autophagic capacity in PD organoids has only been reported recently.³⁹ In an attempt to demonstrate the ability of our multi-sensor integrated midbrain organoid-on-a-chip platform to detect phenotypic rescue, exposure of 3xSNCA hMOs to 5 μ M of HP- β -CD was assessed. To that end, dopamine release and respiratory activity of healthy, 3xSNCA, as well as HP- β -CD-treated 3xSNCA hMOs were investigated in a final time-resolved comparative study. As autophagy is directly involved in the removal of both aggregated protein species as well as impaired organelles, specific focus has been directed towards assessing mitochondrial parameters and p-S129- α -synuclein to α -synuclein ratios. While no significant differences in dopamine release were found between 3xSNCA hMOs and HP- β -CD treated 3xSNCA hMOs (Fig. 6E), markedly altered growth behaviors were observed. Figure 6G shows a significantly lower mean organoid growth rate of 0.02 μ m²/day for treated hMOs compared to 0.03 μ m²/day for untreated controls (D14-D35), resulting in overall smaller microtissues upon treatment with HP- β -CD. As improved autophagy has been linked to limited cell growth, we speculate that the average size reduction of 12% in HP- β -CD treated hMOs after 42 days of on-chip cultivation is indicative of enhanced cellular degradation.⁵² Furthermore, when taking into account reduced hMO sizes into the DA measurements, by normalizing the amperometric signal to microtissue size, CD treated hMOs give rise to an average 1.73-fold higher DA signal compared to their untreated controls. While the highest overall oxygen demand of 102.8 \pm 31 hPa/mm² ($n = 410$) was detected in healthy hMOs, HP- β -CD treatment significantly raised the average normalized oxygen demand of PD hMOs from 78.21 \pm 23.2 hPa/mm² ($n = 587$) to 88.54 \pm 21.8 hPa/mm² ($n = 541$), pointing at improved mitochondrial physiology. To confirm that the observed phenotypic improvements originate from rescue effects of PD-associated phenotypes, such as α -synuclein aggregation, additional immunohistochemical analysis was performed after 60 days of differentiation. As shown in Figure 6C, quantitative analysis of hMO-sections revealed a significant reduction in the amount of pathological p-S129- α -synuclein, with comparable p-S129- α -synuclein to α -synuclein ratios in healthy and HP- β -CD treated hMOs. These observations support previous findings that impaired autophagic clearance

promotes the exocytosis of α -synuclein, ultimately linking autophagic dysfunction to a progressive spread of Lewy pathology.⁵³ To assess whether reduced levels of aggregated p-S129- α -synuclein consequently resulted in improved mitochondrial morphology, fluorescence analysis was performed. In agreement with the p-S129- α -synuclein data, we observed marked rescue effects in mitochondrial physiology for HP- β -CD treated hMOs, as indicated by the clustering of the WT and the CD-treated group in a hierarchical cluster analysis (Fig. 6D). In a final attempt to prove, the beneficial effects of HP- β -CD, a whole-mount analysis (Fig. 6H) was performed. Image analysis revealed a significant increase in dopaminergic neurons (TH/MAP2 ratio), the afflicted cell type in PD, following treatment with the repurposed excipient HP- β -CD. This finding supports our previous assumption that elevated DA levels, were masked by reduced microtissue sizes observed in HP- β -CD treated organoids.

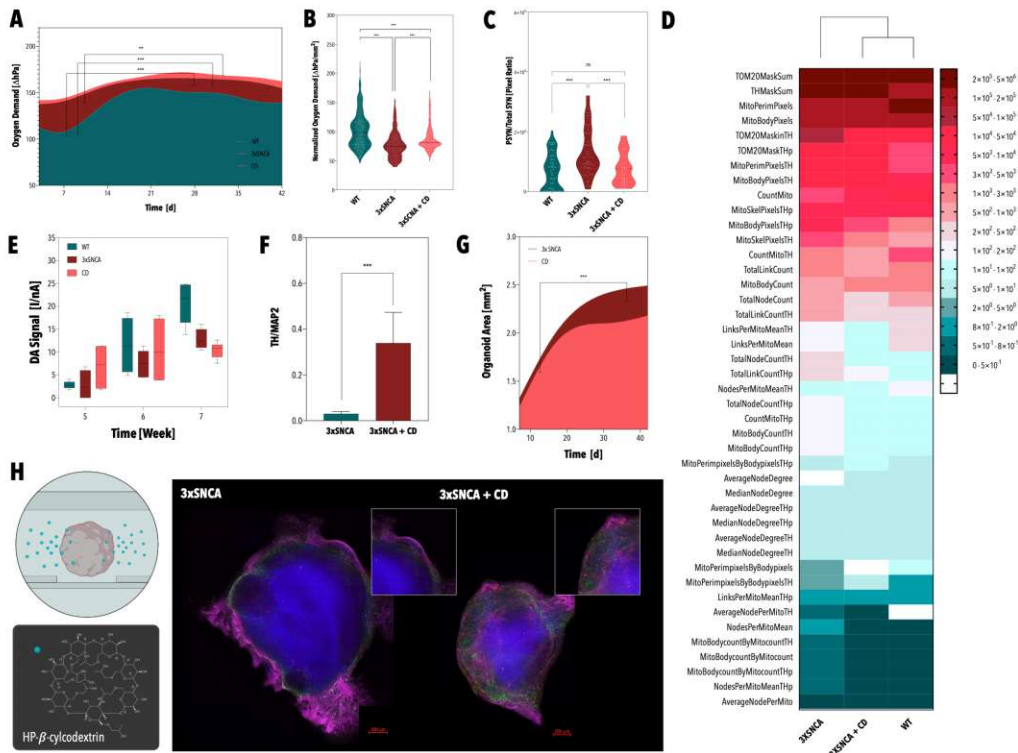


Figure 6: Oxygen demand profiles of healthy, 3xSNCA, and HP- β -CD-treated hMOs over a cultivation period of 42 days (A). Normalized oxygen demands of healthy, 3xSNCA, and HP- β -CD-treated hMOs. Statistical significance by Kruskal-Wallis test and Dunn's multiple comparison test $*p < 0.033$, $**p < 0.002$, $***p < 0.001$ ($n = 8-10$, from 3 independent organoid generations and 12 timepoints) (B). Violin plot of p-S129- α -synuclein to α -synuclein ratios calculated for healthy, 3xSNCA, and HP- β -CD-treated hMOs. Statistical significance by Kruskal-Wallis test and Dunn's multiple comparison test $*p < 0.033$, $**p < 0.002$, $***p < 0.001$ ($n \geq 3$) (C). Heatmap-based overview of improved mitochondrial markers in HP- β -CD-treated 3xSNCA hMOs. Hierarchical clustering was performed using MATLAB. (D) Time-resolved dopamine data of healthy, 3xSNCA, as well as HP- β -CD-treated hMOs, cultivated in microfluidic devices. Statistical significance by two-way ANOVA and Tukey test $*p < 0.033$, $**p < 0.002$, $***p < 0.001$ ($n = 10$ (pooled) from 2 independent organoid generations (technical triplicates) (E). Comparative image analysis of immunohistochemically stained 3xSNCA and HP- β -CD-treated 3xSNCA organoids revealing a significant rescue in the TH/MAP2 ratio. Statistical significance by Mann-Whitney test $*p < 0.033$, $**p < 0.002$, $***p < 0.001$. Column and error bars represent mean \pm SEM ($n \geq 5$ from 3 independent organoid generations) (F). Growth curves of 3xSNCA hMOs and HP- β -CD-treated hMOs over a cultivation period of 42 days ($n = 8-10$ from 3 independent organoid generations) (G). Graphical illustration of HP- β -CD-treatment and representative fluorescence images of a 3xSNCA hMO (left panel) and a HP- β -CD-treated hMO (right panel): TH (red), GFAP (green), MAP2 (magenta), nuclei (blue) (H). (A,G) Statistical significance by mixed-effect analysis and Tukey test $*p < 0.033$, $**p < 0.002$, $***p < 0.001$ ($n = 8-10$ from 3 independent organoid generations).

3. Discussion and Conclusion

In this study, we have developed a patient-specific multi-sensor integrated midbrain organoid-on-a-chip model capable of monitoring the onset, progression, and rescue of PD-related phenotypes, while simultaneously providing for shorter organoid handling times, reduced contamination risks as well as high content analysis compatibility.^{54,8} It is important to note that the quality of any *in vitro* disease/tissue model can be defined by two parameters 1) the (patho)physiological similarity to the organ of interest and 2) its accessibility to biochemical analysis methods. Both aspects are essential to foster clinical translation in precision medicine and routine application in pharmaceutical development. In this work, we have taken advantage of the synergistic effects created by combining organoid technology and its capability to emulate intricate organotypic structures *in vitro* with organ-on-a-chip systems that allocate analytical accessibility, scalability, and physiological fluid dynamics. A key biophysical aspect of our multi-sensor integrated midbrain organoid-on-a-chip platform is the application of flow profiles that mimic brain-specific circadian flow regimes, resulting in a drastic reduction of necrotic core formation - a key limitation of organoid technology - and improved midbrain tissue differentiation.⁵⁵ In other words, cultivating hMOs under interstitial fluid flow clearly promotes brain organogenesis by increasing oxygen availabilities, improving nutrient supply, and promoting the removal of locally accumulated toxic compounds such as acids or reactive oxygen species.⁵⁶ Analytical accessibility through non-invasive multi-parametric sensing strategies is particularly important when studying time-dependent processes, such as tissue differentiation or disease progression, in an otherwise contained *in vitro* system. Time-resolved oxygen sensing of healthy hMOs, for example, reflected the sequential nature of brain development, characterized by high initial neuronal differentiation (correlating with increasing respiratory activities) that is succeeded by astrogenesis (marked by lower respiratory activities) initiated at about day 21 of hMO differentiation.^{44,57} In accordance with the degree of tissue differentiation, electrochemical dopamine measurements revealed a time-dependent increase in dopamine signals with significantly higher catecholamine levels observed under dynamic cultivation conditions compared to static controls. Electrophysiological recordings further supported functional network maturity and the presence of dopaminergic populations. A comparative analysis between healthy and PD hMOs (3xSNCA) within our multi-sensor-integrated microfluidic platform revealed a clear time dependency in the onset of Parkinson's disease-related phenotypes, reflecting the complex progression of the neurodegenerative disorder. While initial high numbers in TH-positive neurons can be attributed to differentiation upregulating effects elicited by elevated levels of α -synuclein,³³ heightened dopamine metabolism, in turn, was shown to promote oxidative stress that together with the accumulation of toxic forms of α -synuclein subsequently can contribute to increased neurotoxicity and -degeneration.⁵⁸ Importantly, elevated levels of p-S129- α -synuclein, impaired mitochondrial physiology, diminished TH-positive neuronal populations, as well as the presence of Lewy-body-like

inclusions, were detected in 3xSNCA organoids, demonstrating the validity of our microfluidic *in vitro* model for studying PD.⁴⁶ Since the observed pathological phenotypes can be linked, at least in part, to impaired autophagy, the repurposed excipient HP- β -CD, which has previously been shown to induce rescue effects in a PD organoid model with mutations in PINK1, was used to challenge the ability of our multi-sensor integrated midbrain organoid-on-a-chip platform.³⁹ Intriguingly, integrated oxygen sensing alone pointed towards significant rescue effects expressed by a marked increase in normalized oxygen demands for HP- β -CD-treated hMOs compared to PD controls. These effects were further verified by immunohistochemical analysis, revealing significant reductions in aggregated α -synuclein, distinct improvements of several mitochondrial characteristics as well as significantly enlarged populations of TH-positive dopaminergic neurons.

Overall, the presented multi-sensor integrated platform significantly improved the differentiation of midbrain microtissues by exposing them to physiological flow profiles and enabled for the first time in an on-chip brain organoid model the ability of non-invasive and multi-parametric monitoring. As such, it surpasses existing in-vitro models of the human midbrain, opening the way to precision medicine employing personalized PD models.

Materials and Methods

Microfabrication

The microfluidic chip was designed using the CAD program Autocad. Pre-molds were fabricated by casting polydimethylsiloxane (PDMS/ 1:10 ratio) (Sylgard[®] 184 Silicone Elastomer Kit, Down Corning) from a computer numerical control (CNC) milled polycarbonate master mold using standard soft lithography techniques (SI Fig. 1C). After 2 h of polymerization at 80 °C, the pre-mold was removed from the polycarbonate master mold and cured for another 24 h at 120°C. Afterward, the pre-mold was silanized with 2 µL of trichloro (1H, 1H, 2H,2H-perfluorooctyl) silane (Sigma Aldrich) and incubated for 1 h at 80°C. The same procedure was repeated for the generation of the PDMS mold, starting from the silanized pre-mold (SI Fig. 1C). PDMS molds were used for the fabrication of the microstructured top layers. To facilitate the removal of the microstructured layer from the mold, ethanol (absolute, ChemPur) was applied between the two layers prior. After 2h of polymerization at 80 °C, microfluidic reservoirs and inlets were introduced employing biopsy punches (Ø 6mm, Ø 8mm, Ø 2mm, Kai Medical). Cleaned microstructured PDMS top layers (adhesive tape (Scotch)) were subsequently bonded to blotted 250 µm PDMS foils as well as cleaned glass substrates using air plasma (Harrick Plasma, High Power, 2 min). PDMS foils (MVQ Silicones GmbH) were processed using xurography (CMM-1 GS-24, Roland). Microfluidic devices equipped with oxygen sensors were generated by the deposition of 2 µL of a microparticle solution into PDMS cavities within glass substrates by the use of a pipette as previously described by *Zirath et al.*^{30,31} After drying for 2 h at room temperature, the microparticles were immobilized to the glass substrate, and the fluidic structures were sealed, employing air plasma. Prior to their use, microfluidic devices were sterilized, utilizing a combination of 70 % ethanol as well as UV treatment.

CFD Simulation

A multipurpose finite volume CFD code (Ansys Fluent 6.3.26, www.ansys.com / OpenFoam www.openfoam.org) was used for calculating the flow profile on-chip. The geometry consisting of the hydrogel cavity, the two feed channels, and the two collection units was split into 136.000 hexahedral control volumes (SI Fig. 1A). The grid pillars at the gel inflow and outflow boundary were fully resolved. For adequate numerical accuracy, second or higher-order discretization schemes have been selected for all flow variables (Navier-Stokes equation – momentum conservation, Continuity equation – mass conservation) and the species equations. All wall boundaries were treated as ideally smooth; no-slip boundary conditions (zero flow velocity at the wall) were selected for all surfaces. The outlet was set to a pressure outlet at a standard pressure of $p = 1 \text{ atm}$ (101325 Pa). The hydrogel region was

approximated as a homogeneous and isotropic porous zone (Darcy-Forchheimer equation) with a constant porosity of $\varepsilon = 0.99$ and viscous resistance of $R = 1.89 \cdot 10^{13} \text{ 1/m}^2$ having been assumed for all directions.^{59–64} Isothermal flow was assumed, no temperature or energy field was solved. For simplicity, Newtonian fluid behavior was applied for the simulation using a constant dynamic viscosity and constant density (incompressible) for all mixture components. As the concentrations of the dissolved species in the fluid are low, the properties of the solvent, water, have been used for the simulation ($\rho = 993 \text{ kg/m}^3$, $\eta = 0.001003 \text{ Pa}\cdot\text{s}$ at $37 \text{ }^\circ\text{C}$). The diffusion coefficients for the tracer components have been estimated according to literature values (glucose: $0.18 \text{ kDa} - 4 \cdot 10^{-10} \text{ m}^2/\text{s}$, oxygen: $32 \text{ Da} - 2 \cdot 10^{-9} \text{ m}^2/\text{s}$, water: $18 \text{ Da} - 2 \cdot 10^{-9} \text{ m}^2/\text{s}$) assuming a dilute solution.⁶⁰ Different water species have been used for both inlets to investigate the cross mixing of the two inlet channel fluids. Simulations were carried out on the cluster server `cae.zserv.tuwien.ac.at` (operated by the IT department of TU Wien, `www.zid.tuwien.ac.at`). As the major flow resistances are inside the hydrogel and in the flow channels, but not in the feed and collection cavities, a simplification was used: To reduce the computational effort, steady-state simulations for different selected feed cavity filling levels have been carried out. The simulated filling level was translated into a corresponding relative pressure difference between the feed inlet zone and the pressure outlet.

hMO Generation and On-Chip Cultivation Protocol

iPSCs from a healthy individual (identifier: 2.0.0.51.0.0) and a PD patient (triplication mutation of 3xSNCA, identifier: 2.1.3.138.0.0) were used in this study. The maintenance of iPSCs was performed as previously described.⁶⁵ From the iPSC line, human ventralized neural epithelial stem cells (hvNESCs) were generated, which were subsequently used to generate midbrain organoids.¹² For on-chip hMO cultivation, organoids suspended in Matrigel[®] (Corning) were transferred into the microfluidic chip on day 0 of the maturation phase and cultivated for up to 60 days of differentiation. Dynamic cultivation was achieved by filling the feed medium reservoirs up to a 3.4 mm feeding level, while the medium at the collector side was kept at 0.4 mm height. The medium was exchanged every 48 - 72 h. To prevent any drying out of the microfluidic chips, (i) devices were kept in a compartmentalized cultivation platform (Quadriperm[®], Greiner) with 10 mL of PBS on both sides, and (ii) inlets of the hydrogel chamber were sealed using PCR tape (Sigma Aldrich). Depending on the type of analysis, static controls were either cultivated in microfluidic devices under static conditions or were embedded in a droplet of Matrigel[®] (Corning[®]) and cultivated in a 24-well plate (Greiner). Equal amounts of cell culture medium and Matrigel[®] (Corning[®]) were used, and the medium change procedure was kept identical under static conditions.

HP- β -CD-Treatment

For HP- β -CD-treatment 3xSNCA hMOs were exposed to 5 μ M HP- β -CD (Sigma Aldrich) in cell culture media starting from D10 of differentiation.

Immunohistochemistry

Chromogenic Immunohistochemistry

Caspase 3 Staining

HMOs were fixed with 4 % paraformaldehyde overnight at room temperature, washed three times with phosphate-buffered saline (PBS) (Gibco) for 15 minutes, before being dehydrated, embedded in paraffin, and sectioned using a microtome (Thermo Scientific HM355 S). Prior to heat-induced antigen retrieval using Tris-EDTA buffer at pH 9, sectioned hMOs were deparaffinized and rehydrated. After rinsing the sections in TBS, endogen peroxidase and alkaline phosphatase activity were blocked by treating the sectioned hMOs with BLOXALL (VectorLaboratories) for 10 min. The primary antibody (ASP175, #9661, CellSignaling) was incubated for one hour at room temperature before the sections were rinsed again in TBS and the secondary antibody, an anti-rabbit HRP conjugated antibody (BrightVision), was applied for 30 min at room temperature. Color development was achieved by a 6-minute-long exposure to ImmPACTTMNova RedTM (VectorLaboratories). Subsequently, the sections were stained with Haematoxylin (Roth) and mounted with EprediaTM Consul-MountTM (Fisher Scientific).

Fontana Masson Staining

HMOs were fixed with 4 % paraformaldehyde overnight at room temperature, washed three times with phosphate-buffered saline (PBS) (Gibco) for 15 minutes, before being dehydrated and embedded in paraffin, and sectioned using a microtome (Thermo Scientific HM355 S). After deparaffinization and rehydration, sectioned hMOs were stained for 10 minutes in a Lugol's solution (2 g Potassium iodide (Roth), 1g Iodine (Roth)) before being transferred into a 5% sodium thiosulfate solution (Morphisto) for two minutes. Rinsed slides (3x, aqua dest.) were transferred in an ammoniacal silver solution (5% silver nitrate (Roth); ammonium hydroxide, 18% NH₃ (Alfa Aesar)) and incubated at 60°C for two hours. After rinsing (3x, aqua dest.), slides were exposed to a 0,2% gold chloride solution (Fluka) for three minutes. Slides were rinsed in aqua dest. before being treated with 5% sodium thiosulfate solution for two minutes and subsequently rinsed in tap water for two minutes. Cell nuclei were stained using

0,1% nuclear fast red (Merck). After finishing the staining procedure, the slides were dehydrated in ethanol and mounted with Eprepia™ Consul-Mount™ (Fisher Scientific).

Immunofluorescence

Sectioned hMOs

HMOs were fixed with 4 % paraformaldehyde overnight at room temperature and washed 3x with PBS for 15 min. For sectioned analysis, hMOs were embedded in 3-4 % low-melting-point agarose in PBS. The solid agarose block was sectioned with a vibratome (Leica VT1000s) into 100 µm sections. The sections were blocked for 90 min at room temperature on a shaker using 0.5 % Triton X-100, 0.1% sodium azide, 0.1% sodium citrate, 5 % normal goat serum, and 2% bovine serum albumin in tris-buffered saline (TBS). Primary antibodies were diluted in the same solution and incubated for 48 h at 4 °C. Antibodies were diluted according to the supplementary table SI Table 2. After incubation with the primary antibodies, sections were washed 3x with TBS for 15 minutes and incubated for 30 minutes in TBS supplemented with 0.5 % Triton X-100, 0.1% sodium azide, 0.1% sodium citrate, 5 % normal goat serum, and 2% bovine serum albumin. Subsequently, sections were incubated with the respective secondary antibodies (SI Table 2) and the nuclear dye Hoechst 33342 (Invitrogen) in TBS with 0.5 % Triton X-100, 0.1% sodium azide, 0.1% sodium citrate, 5 % normal goat serum, and 2% bovine serum albumin for 2 h at room temperature. Afterward, samples were washed 3x with TBS, 1x with Milli-Q water before being mounted in Fluoromount-G mounting medium (Southern Biotech). Sections were imaged using confocal microscopes (Yokogawa, Zeiss).

Whole-mounted hMOs

Paraformaldehyde fixed (4%) hMOs were washed 3x with PBS for 15 minutes on a shaker. Subsequently, hMOs were blocked and permeabilized using 1% Triton X-100 and 10% normal goat serum in 1x PBS for 24h on a shaker at room temperature. Primary antibodies were diluted in PBS supplemented with 0.5 % Triton X-100 and 3% normal goat serum and incubated for 4 days at 4°C on a shaker (SI Table 2). Samples were washed 3x with PBS for 1 hour at room temperature before incubating with the diluted secondary antibody solution at 4°C, including the nuclear dye Hoechst 33342 (Invitrogen). After 2 days, samples were washed 3x with 0.05% Tween-20 in PBS and 1x with Milli-Q water for 5 minutes at room temperature, prior to mounting with Fluoromount-G mounting medium (Southern Biotech). Images were acquired using a high content analysis system (Operetta®, PerkinElmer).

Oxygen Monitoring

On-chip oxygen monitoring was carried out at a sampling frequency of 1 Hz using a FireStingO₂ optical oxygen meter (Pyroscience) connected to optical fibers (length 1 m, outer diameter 2.2 mm, fiber diameter 1 mm). Integrated sensors were calibrated using a CO₂/O₂ oxygen controller (CO₂-O₂-Controller 2000, Pecon GmbH) equipped with integrated zirconium oxide oxygen sensors (SI Fig. 4A/B). Oxygen measurements were performed every 3 to 4 days. For this purpose, chips were sealed with PCR foil and transferred into an external incubation chamber set-up (5% CO₂/37°C). Each sample was measured for a minimum of 3 minutes to guarantee proper equilibration. To ensure that fluid flow does not interfere with the oxygen measurement, oxygen demand was measured prior to the re-establishment of flow (under static conditions). Oxygen demand was subsequently calculated according to the following formula: hMO oxygen demand (ΔP_{O_2}) = P_{O₂} blank – P_{O₂} hMO.

Dopamine Sensing

The fabrication and subsequent characterization of the dopamine sensor were based on a protocol previously published by Niagi *et al.*⁶⁶ Carbon electrodes of a thick-film electrode set-up with an integrated silver reference electrode (S1PE, MicruX Technologies) were coated with 15 μ L of a tyrosinase (Sigma Aldrich), chitosan (1%, Sigma Aldrich), CeO₂ (10 mg/mL, Sigma Aldrich) and TiO₂ (10 mg/mL, chemPUR) mixture at the following ratio (4:4:1:1) and incubated for a duration of 1 hour. Amperometric measurements were conducted at a potential of -0.15 V using a three-electrode set-up with a platinum wire as a counter electrode and a potentiostat (VMP3, Bio-Logic) equipped with a low current module (Bio-Logic). Dopamine (Sigma Aldrich) calibration curves were recorded in both PBS and N2B27 medium (SI Figure 4C/D). Concentrations of tested interferents were based on previous studies, media composition, and HPLC-derived neurotransmitter profiles of hMOs⁶⁷. Next to 5 μ M dopamine (dopamine hydrochloride), interference studies encompassed the measurement of 5 μ M L-DOPA (Sigma Aldrich), 5 μ M DOPAC (Sigma Aldrich), 5 μ M norepinephrine (Sigma Aldrich), 5 μ M epinephrine (Sigma Aldrich), 5 μ M serotonin (Sigma Aldrich), 40 μ M γ -aminobutyric acid (GABA) (Sigma Aldrich) and 200 μ M ascorbic acid (Sigma Aldrich) in PBS (SI Figure 4F). To assess potential interference effects of phenol red on the DA measurement, a comparative analysis between phenol red basal media (Neurobasal Medium, Gibco) and phenol red-free basal media (Neurobasal Medium, minus phenol red, Gibco) employing 5 μ M DA was conducted (SI Figure 4G). Stability measurements were performed at a DA concentration of 5 μ M DA in PBS (SI Figure 4E). Measurements were conducted by dipping the three-electrode set-up into the respective analyte. For each measurement, the supernatants of 10 hMOs were pooled and three technical triplicates were recorded.

MEA Fabrication and Analysis of Electrophysiological Activity

The fabrication of the MEAs followed a previously published protocol by Mika *et al.*⁶⁸ In detail, cleaned (sonication in acetone for 1 minute) glass substrates (49mm x 49mm glass substrates (D263 T ECO, Schott GmbH)) were sputtered with chrome using an RF power of 100W, 30s sputter time, a working pressure of 2-5 mbar and a base pressure of 8-3 mbar (Von Ardenne LS320 Sputtersystem). Photoresist AZ5214E was spun onto the chrome sputtered substrates using a spin speed of 3000 rpm, a spin time of 30 s, and ramp set to 4. The soft bake was performed at 100°C for 60 s. Using a Karl Suss MJB3 UV400 mask aligner, the mask and substrate were aligned and exposed to a dose of 40 mJ/cm². Next, the reversal bake was performed at 120°C for 70 s and immediately flood-exposed with a dose of 240 mJ/cm². After flood exposure, substrates were developed using AZ726 MIF for 60 s. Development was stopped by rinsing with water. After the substrates were dried with N₂, the chrome layer was etched using CHROME ETCH 18 (Micro Resist Technology). After inhibiting the etching process by rinsing with water, substrates were dried. Titanium was sputtered with an RF power of 100 W, a 50 s sputter time, a working pressure of 2-5 mbar, and a base pressure of 8-3 mbar. Next, two layers of gold were sputtered with an RF power of 50 W, a sputtering time of 50 s, a working pressure of 2-5 mbar, and a base pressure of 8-3 mbar. Lift-off was performed by sonication in acetone, before rinsing the substrates with acetone and isopropanol. The remaining chrome was removed using CHROME ETCH 18 (Micro Resist Technology). The insulation layer of Si₃N₄ was deposited using plasma-enhanced chemical vapor deposition with an RF power of 12 W, a processing time of 30 minutes, 1 torr working pressure, 0.06 torr base pressure, a SiH₄ flow of 700 sccm, an NH₃ flow of 18 sccm and a substrate holder temperature of 300°C (Oxford Plasmalab 80 Plus). To etch the insulation layer, a sacrificial layer of AZ5214E was spun onto the substrates using a spin speed of 3000 rpm, a spin time of 30 s, and ramp set to 4. The soft bake was performed at 100°C for 60 s. The exposure dose was 40 mJ/cm² (equals ~4s in the case of MJB3 Mask Aligner). Next, the reversal bake was performed at 120°C for 70 s and immediately flood-exposed with a dose of 240 mJ/cm². After flood exposure, substrates were developed using AZ726 MIF for 60 s. Development was stopped by rinsing with water. Exposed areas were etched using reactive ion etching with an RF power of 50 W, an inductively coupled plasma power of 100W, an SF₆ flow rate of 20 sccm, an Ar flow rate of 10 sccm, and a processing time of 10 minutes (Oxford Plasmalab System 100). The sacrificial photoresist layer was removed by sonication in acetone and rinsing with isopropanol. The analysis of the electrophysiological data retrieved from the Multichannel System Software was performed employing a previously published algorithm for spike detection and sorting (wave_clus 3)⁶⁹ using the programming and numeric computing platform MATLAB (R2021a).

Calcium Fluo-4 Assay

To verify the electrophysiological activity of hMOs on-chip, the intracellular calcium flux within the hMOs was analyzed employing a Fluo-4 Calcium Imaging Kit (Thermo Fisher) according to the manufacturer's instructions (n=4). Videos were recorded using live-cell imaging (IX83, Olympus).

FITC Diffusion Study

5 kDa FITC-dextran (Thermo Fisher) was used for the assessment of dextran diffusion into hMOs on-chip (SI Figure 5A/B). To that end, a 100 μM solution of 5 kDa FITC-dextran in N2B27 medium was introduced into the media reservoirs of the microfluidic device. hMOs were exposed to the dextran solution for a period of 24 hours under both static and dynamic cultivation conditions, while transport into the microtissues was recorded simultaneously using live-cell imaging (IX83, Olympus). Influx and efflux into the organoids were analyzed by assessing the fluorescence intensity over time using the open-source image processing program FIJI.

Image Analysis

Neurite Outgrowth Rate and Organoid Growth

Both maximum neurite outgrowth rate [$\mu\text{m}/\text{h}$] and organoid growth [μm^2] were determined using the open-source image processing program FIJI. To determine the organoid growth, brightfield images of the hMOs were used to calculate the area of the individual organoids. To that end, images were transferred to 8-bit images; thresholds were adjusted to separate the hMOs from the background before converting the images to a mask and measuring the area using the measure function of the program. For the determination of the maximum neurite outgrowth rate, neurites extending from the hMOs were traced and measured using the freehand lines tool or the measure function, respectively.

Caspase 3

To analyze the apoptotic marker caspase 3 in the hMOs, images of the sectioned organoids were retrieved using a standard brightfield microscope (IX71, Olympus). The data analysis pipeline includes the adjustment of the contrast, color deconvolution, transfer to a binary image, generation of a mask, and measurement. The ratio of caspase 3 to total nuclei was subsequently calculated as follows:

$$\frac{\text{Caspase 3}}{\text{Nuclei}} = \frac{\text{red area}}{\text{total area (red + blue)}}$$

Immunohistochemistry

The image analysis algorithms used in the study were applied as previously described.⁷⁰

Statistical Analysis

Statistical analysis and data visualization was conducted using the biostatistics program GraphPad Prism 8. For the assessment of statistical significance, Welch's t-tests, Mann-Whitney tests, Kruskal-Wallis tests with Dunn's multiple comparison tests, one-way, two-way ANOVAs or mixed-effect analysis with Geisser-Greenhouse correction and Tukey's multiple comparison tests were performed. Normality was tested using a combination of the Shapiro-Wilk test and the Kolmogorov-Smirnov test. For the detection of outliers in normally distributed data sets, either a Grubb's test for single outliers or a ROUST outlier test for multiple outliers was employed. Significances were assigned as follows: 0.12 (ns.), 0.033 (*), 0.002 (**), < 0.001 (***)

Acknowledgments

Graphical illustrations were generated using the online software Biorender. The study was supported by the Fonds National de la Recherche (FNR) Luxembourg (INTER/MERA/17/11760144, BRIDGES18/BM/12719664_MOTASYN). This work was supported by the U.S. Army Medical Research Materiel Command endorsed by the U.S. Army through the Parkinson's Research Program Investigator-Initiated Research Award under Award No. W81XWH-17-PRP-IIRA. Opinions, interpretations, conclusions and recommendations are those of the author and are not necessarily endorsed by the U.S. Army.

Author Contributions

SSp, PE, SB, and JCS conceived and designed the study. SSp and KB conducted microfluidic experiments. SSp, JF, and SS performed dopamine measurements. SSp, PS, HW performed electrophysiological studies and provided expertise on microfabrication. TM provided expertise on oxygen sensing and costume-made microparticles for sensor integration. SSp, SB, BS, and JG performed immunohistochemical analysis. CJ and MH performed CFD simulations. SSp and SB conducted data analysis. All authors revised and approved the final manuscript.

References

1. Maserejian, N., Vinikoor-Imler, L. , Dilley, A. Estimation of the 2020 Global Population of Parkinson’s Disease (PD). in (MDS Virtual Congress 2020, 2020).
2. Poewe, W. *et al.* Parkinson disease. *Nat. Rev. Dis. Prim.* **3**, 1–21 (2017).
3. Obeso, J. A. *et al.* Past, present, and future of Parkinson’s disease: A special essay on the 200th Anniversary of the Shaking Palsy. *Mov. Disord.* **32**, 1264–1310 (2017).
4. Takahashi, K. & Yamanaka, S. Induction of Pluripotent Stem Cells from Mouse Embryonic and Adult Fibroblast Cultures by Defined Factors. *Cell* **126**, 663–676 (2006).
5. Di Lullo, E. & Kriegstein, A. R. The use of brain organoids to investigate neural development and disease. *Nat. Rev. Neurosci.* **18**, 573–584 (2017).
6. Cederquist, G. Y. *et al.* Specification of positional identity in forebrain organoids. *Nat. Biotechnol.* **37**, 436–444 (2019).
7. Wang, Y., Wang, L., Zhu, Y. & Qin, J. Human brain organoid-on-a-chip to model prenatal nicotine exposure. *Lab Chip* **18**, 851–860 (2018).
8. Monzel, A. S. *et al.* Machine learning-assisted neurotoxicity prediction in human midbrain organoids. *Park. Relat. Disord.* **75**, 105–109 (2020).
9. Jo, J. *et al.* Midbrain-like Organoids from Human Pluripotent Stem Cells Contain Functional Dopaminergic and Neuromelanin-Producing Neurons. *Cell Stem Cell* **19**, 248–257 (2016).
10. Tripathi, P. *et al.* Stem Cell Reports. *Stem Cell Reports* **9**, 667–680 (2017).
11. Smits, L. M. *et al.* Modeling Parkinson ’ s disease in midbrain-like organoids. 1–8 (2019).
12. Nickels, S. L. *et al.* Reproducible generation of human midbrain organoids for in vitro modeling of Parkinson’s disease. *Stem Cell Res.* **46**, (2020).
13. Abbott, N. J. Evidence for bulk flow of brain interstitial fluid: Significance for physiology and pathology. *Neurochem. Int.* **45**, 545–552 (2004).
14. Mestre, H., Mori, Y. & Nedergaard, M. The Brain’s Glymphatic System: Current Controversies. *Trends Neurosci.* **43**, 458–466 (2020).
15. Iliff, J. J. *et al.* A Paravascular Pathway Facilitates CSF Flow Through the Brain Parenchyma and the Clearance of Interstitial Solutes, Including Amyloid beta. **4**, (2012).

16. Zou, W. *et al.* Blocking meningeal lymphatic drainage aggravates Parkinson's disease-like pathology in mice overexpressing mutated α -synuclein. *Transl. Neurodegener.* **8**, 1–17 (2019).
17. Whitesides, G. M. The origins and the future of microfluidics. *Nature* **442**, 368–373 (2006).
18. Huh, D. A human breathing lung-on-a-chip. *Ann. Am. Thorac. Soc.* **12**, S42–S44 (2015).
19. Campisi, M. *et al.* 3D self-organized microvascular model of the human blood-brain barrier with endothelial cells, pericytes and astrocytes. *Biomaterials* **180**, 117–129 (2018).
20. Osaki, T., Uzel, S. G. M. & Kamm, R. D. Microphysiological 3D model of amyotrophic lateral sclerosis (ALS) from human iPS-derived muscle cells and optogenetic motor neurons. *Sci. Adv.* **4**, 1–16 (2018).
21. Park, J. *et al.* Three-dimensional brain-on-a-chip with an interstitial level of flow and its application as an in vitro model of Alzheimer's disease. *Lab Chip* **15**, 141–150 (2015).
22. Rifès, P. *et al.* Publisher Correction: Modeling neural tube development by differentiation of human embryonic stem cells in a microfluidic WNT gradient (Nature Biotechnology, (2020), 38, 11, (1265-1273), 10.1038/s41587-020-0525-0). *Nat. Biotechnol.* **38**, 1357 (2020).
23. Wang, Y., Wang, L., Guo, Y., Zhu, Y. & Qin, J. Engineering stem cell-derived 3D brain organoids in a perfusable organ-on-a-chip system. *RSC Adv.* **8**, 1677–1685 (2018).
24. Cho, A. N. *et al.* Microfluidic device with brain extracellular matrix promotes structural and functional maturation of human brain organoids. *Nat. Commun.* **12**, (2021).
25. Karzbrun, E., Kshirsagar, A., Cohen, S. R., Hanna, J. H. & Reiner, O. Human brain organoids on a chip reveal the physics of folding. *Nat. Phys.* **14**, 515–522 (2018).
26. Ao, Z. *et al.* One-Stop Microfluidic Assembly of Human Brain Organoids to Model Prenatal Cannabis Exposure. *Anal. Chem.* **92**, 4630–4638 (2020).
27. Yin, F., Zhu, Y., Wang, Y. & Qin, J. Engineering Brain Organoids to Probe Impaired Neurogenesis Induced by Cadmium. *ACS Biomater. Sci. Eng.* **4**, 1908–1915 (2018).
28. Zhu, Y. *et al.* In situ generation of human brain organoids on a micropillar array. *Lab Chip* **17**, 2941–2950 (2017).

29. Ray, L. A. & Heys, J. J. Fluid flow and mass transport in brain tissue. *Fluids* **4**, (2019).
30. Zirath, H. *et al.* Every Breath You Take: Non-invasive Real-Time Oxygen Biosensing in Two- and Three-Dimensional Microfluidic Cell Models. *Front. Physiol.* **9**, 1–12 (2018).
31. Zirath, H. *et al.* Bridging the academic-industrial gap: Application of an oxygen and pH sensor-integrated lab-on-a-chip in nanotoxicology. *Lab Chip* **21**, 4237–4248 (2021).
32. Kieninger, J., Weltin, A., Flamm, H. & Urban, G. A. Microsensor systems for cell metabolism—from 2D culture to organ-on-chip. *Lab Chip* **18**, 1274–1291 (2018).
33. Burré, J. The synaptic function of α -synuclein. *J. Parkinsons. Dis.* **5**, 699–713 (2015).
34. Jensen, P. H., Nielsen, M. S., Jakes, R., Dotti, C. G. & Goedert, M. Binding of α -synuclein to brain vesicles is abolished by familial Parkinson’s disease mutation. *J. Biol. Chem.* **273**, 26292–26294 (1998).
35. Ghiglieri, V., Calabrese, V. & Calabresi, P. Alpha-synuclein: From early synaptic dysfunction to neurodegeneration. *Front. Neurol.* **9**, (2018).
36. Tsigelny, I. F. *et al.* Role of α -synuclein penetration into the membrane in the mechanisms of oligomer pore formation. *FEBS J.* **279**, 1000–1013 (2012).
37. Lashuel, H. A., Overk, C. R., Oueslati, A. & Masliah, E. The many faces of α -synuclein: From structure and toxicity to therapeutic target. *Nat. Rev. Neurosci.* **14**, 38–48 (2013).
38. Bousset, L. *et al.* Structural and functional characterization of two alpha-synuclein strains. *Nat. Commun.* **4**, (2013).
39. Jarazo, J. *et al.* Parkinson’s Disease Phenotypes in Patient Neuronal Cultures and Brain Organoids Improved by 2-Hydroxypropyl- β -Cyclodextrin Treatment. *Mov. Disord.* 1–16 (2021) doi:10.1002/mds.28810.
40. Soofi, S., Last, J., Liliensiek, J., Nealy, P. & Murphy, C. The elastic modulus of Matrigel™ as determined by atomic force microscopy. **167**, 216–219 (2009).
41. Leipzig, N. D. & Shoichet, M. S. The effect of substrate stiffness on adult neural stem cell behavior. *Biomaterials* **30**, 6867–6878 (2009).
42. Hablitz, L. M. *et al.* Circadian control of brain glymphatic and lymphatic fluid flow. *Nat. Commun.* **11**, (2020).
43. Tithof, J. *et al.* A network model of glymphatic flow under different experimentally-motivated parametric scenarios. *iScience* **25**, (2022).
44. Modamio, J. *et al.* Synaptic decline precedes dopaminergic neuronal loss in human

midbrain organoids harboring a triplication of the SNCA gene. *bioRxiv* 2021.07.15.452499 (2021).

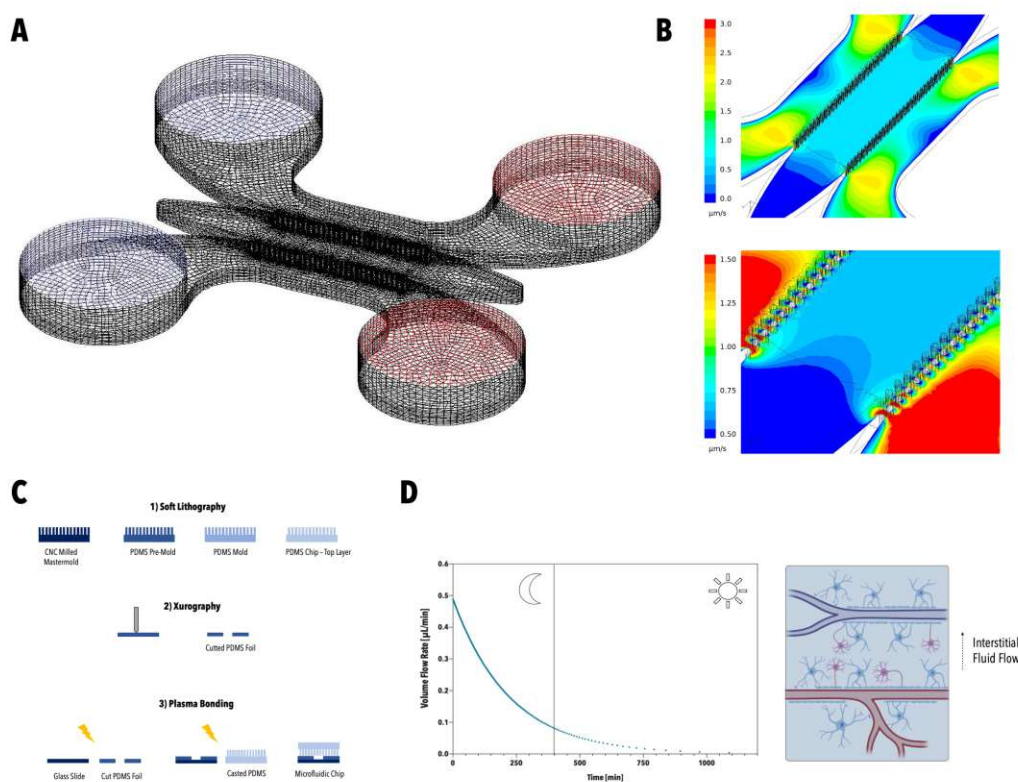
45. Oueslati, A. Implication of Alpha-Synuclein Phosphorylation at S129 in Synucleinopathies: What Have We Learned in the Last Decade? *J. Parkinsons. Dis.* **6**, 39–51 (2016).
46. Jo, J. *et al.* Lewy Body–like Inclusions in Human Midbrain Organoids Carrying Glucocerebrosidase and α -Synuclein Mutations. *Ann. Neurol.* **90**, 490–505 (2021).
47. Jády, A. G. *et al.* Differentiation-Dependent Energy Production and Metabolite Utilization: A Comparative Study on Neural Stem Cells, Neurons, and Astrocytes. *Stem Cells Dev.* **25**, 995–1005 (2016).
48. Takouda, J., Katada, S. & Nakashima, K. Emerging mechanisms underlying astrogenesis in the developing mammalian brain. *Proc. Japan Acad. Ser. B Phys. Biol. Sci.* **93**, 386–398 (2017).
49. Wang, X. *et al.* Pathogenic alpha-synuclein aggregates preferentially bind to mitochondria and affect cellular respiration. *Acta Neuropathol. Commun.* **7**, 41 (2019).
50. Paladini, C. A., Robinson, S., Morikawa, H., Williams, J. T. & Palmiter, R. D. Dopamine controls the firing pattern of dopamine neurons via a network feedback mechanism. *Proc. Natl. Acad. Sci. U. S. A.* **100**, 2866–2871 (2003).
51. Stauffer, W. R. *et al.* Dopamine Neuron-Specific Optogenetic Stimulation in Rhesus Macaques. *Cell* **166**, 1564-1571.e6 (2016).
52. Neufeld, T. P. Autophagy and cell growth - the yin and yang of nutrient responses. *J. Cell Sci.* **125**, 2359–2368 (2012).
53. Lee, H. J. *et al.* Autophagic failure promotes the exocytosis and intercellular transfer of α -synuclein. *Exp. Mol. Med.* **45**, 1–9 (2013).
54. Zagare, A., Gobin, M., Monzel, A. S. & Schwamborn, J. C. A robust protocol for the generation of human midbrain organoids. *STAR Protoc.* **2**, (2021).
55. Song, J. J. *et al.* Cografting astrocytes improves cell therapeutic outcomes in a Parkinson’s disease model. *J. Clin. Invest.* **128**, 463–482 (2018).
56. Berger, E. *et al.* Millifluidic culture improves human midbrain organoid vitality and differentiation. *Lab Chip* **18**, 3172–3183 (2018).
57. Monzel, A. S. *et al.* Derivation of Human Midbrain-Specific Organoids from Neuroepithelial Stem Cells. *Stem Cell Reports* **9**, 667–680 (2017).
58. Sackner-Bernstein, J. Estimates of Intracellular Dopamine in Parkinson’s Disease: A Systematic Review and Meta-Analysis. *J. Parkinsons. Dis.* **11**, 1011–1018 (2021).

59. Klaentschi, K., Brown, J. A., Niblett, P. G., Shore, A. C. & Tooke, J. E. Pressure-permeability relationships in basement membrane: Effects of static and dynamic pressures. *Am. J. Physiol. - Hear. Circ. Physiol.* **274**, 1327–1334 (1998).
60. Hsu, Y. H., Moya, M. L., Hughes, C. C. W., George, S. C. & Lee, A. P. A microfluidic platform for generating large-scale nearly identical human microphysiological vascularized tissue arrays. *Lab Chip* **13**, 2990–2998 (2013).
61. Moreno-Arotzena, O., Meier, J. G., Amo, C. Del & García-Aznar, J. M. Characterization of fibrin and collagen gels for engineering wound healing models. *Materials (Basel)*. **8**, 1636–1651 (2015).
62. Ng, C. P. & Swartz, M. A. Fibroblast alignment under interstitial fluid flow using a novel 3-D tissue culture model. *Am. J. Physiol. - Hear. Circ. Physiol.* **284**, 1771–1777 (2003).
63. Chee, P. N. & Pun, S. H. A perfusable 3D cell-matrix tissue culture chamber for in situ evaluation of nanoparticle vehicle penetration and transport. *Biotechnol. Bioeng.* **99**, 1490–1501 (2008).
64. Madl, C. M. *et al.* Maintenance of neural progenitor cell stemness in 3D hydrogels requires matrix remodelling. *Nat. Mater.* **16**, 1233–1242 (2017).
65. Reinhardt, P. *et al.* Derivation and Expansion Using Only Small Molecules of Human Neural Progenitors for Neurodegenerative Disease Modeling. *PLoS One* **8**, (2013).
66. Njagi, J., Ispas, C. & Andreescu, S. Mixed ceria-based metal oxides biosensor for operation in oxygen restrictive environments. *Anal. Chem.* **80**, 7266–7274 (2008).
67. Zanetti, C. *et al.* Monitoring the neurotransmitter release of human midbrain organoids using a redox cycling microsensor as a novel tool for personalized Parkinson’s disease modelling and drug screening. *Analyst* **146**, 2358–2367 (2021).
68. Mika, J., Schwarz, K., Wanzenböck, H., Scholze, P. & Bertagnolli, E. Simultaneous Electrical Investigation of Isolated Neurites Using a Neurite-Isolation Device as Neurite Regeneration Model. in *9th Int. Meeting on Substrate-Integrated Microelectrode Arrays, 2014* vol. 9 322–323 (2014).
69. Chaure, F. J., Rey, H. G. & Quian Quiroga, R. A novel and fully automatic spike-sorting implementation with variable number of features. *J. Neurophysiol.* **120**, 1859–1871 (2018).
70. Bolognin, S. *et al.* 3D Cultures of Parkinson’s Disease-Specific Dopaminergic Neurons for High Content Phenotyping and Drug Testing. *Adv. Sci.* **6**, 1–14 (2019).

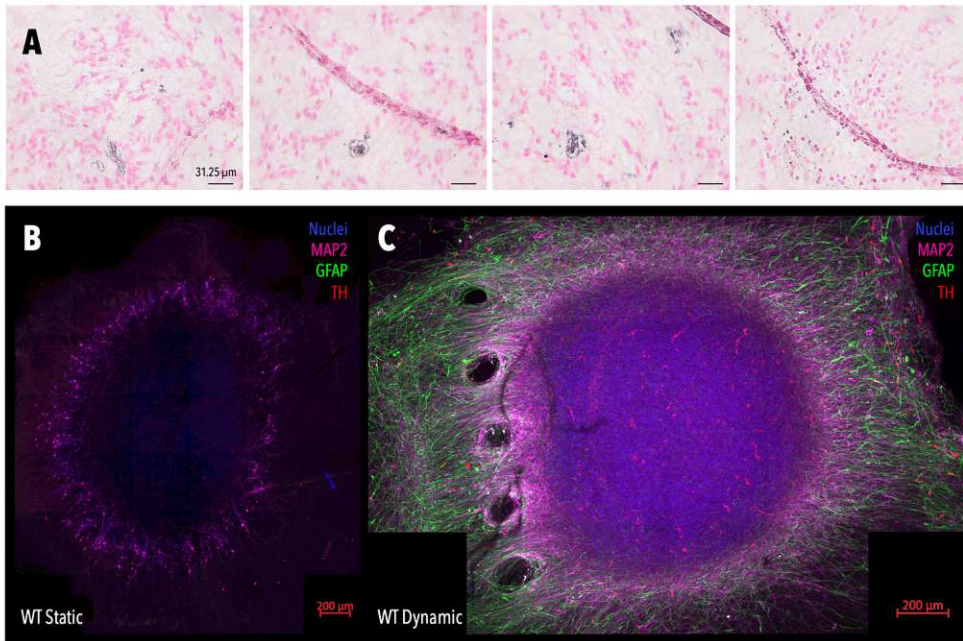
3.7 MANUSCRIPT #4 – SUPPLEMENTARY INFORMATION

Supplementary Information

Development of a multi-sensor integrated midbrain organoid-on-a-chip platform for studying Parkinson's disease



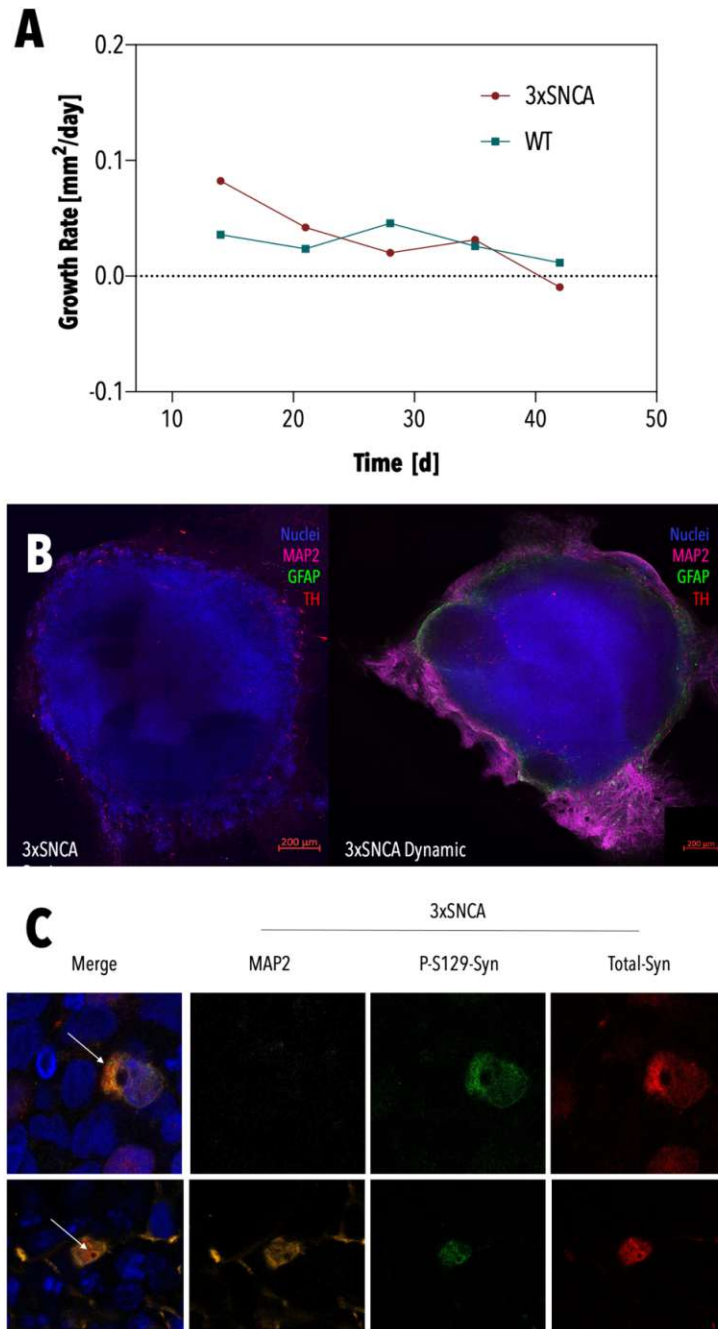
SI Figure 1: Graphical illustration of the hexahedral control volumes applied to the microfluidic device for CFD simulation (A). Overview of the simulated flow profile on chip depicting a highly uniform flow profile within the central hydrogel chamber as well as slightly higher flow rates at the corners of the hydrogel chamber (B). Workflow of the manufacturing process employed for the fabrication of PDMS devices (C). Time-resolved flow profile in the microfluidic device depicting circadian rhythms (D).



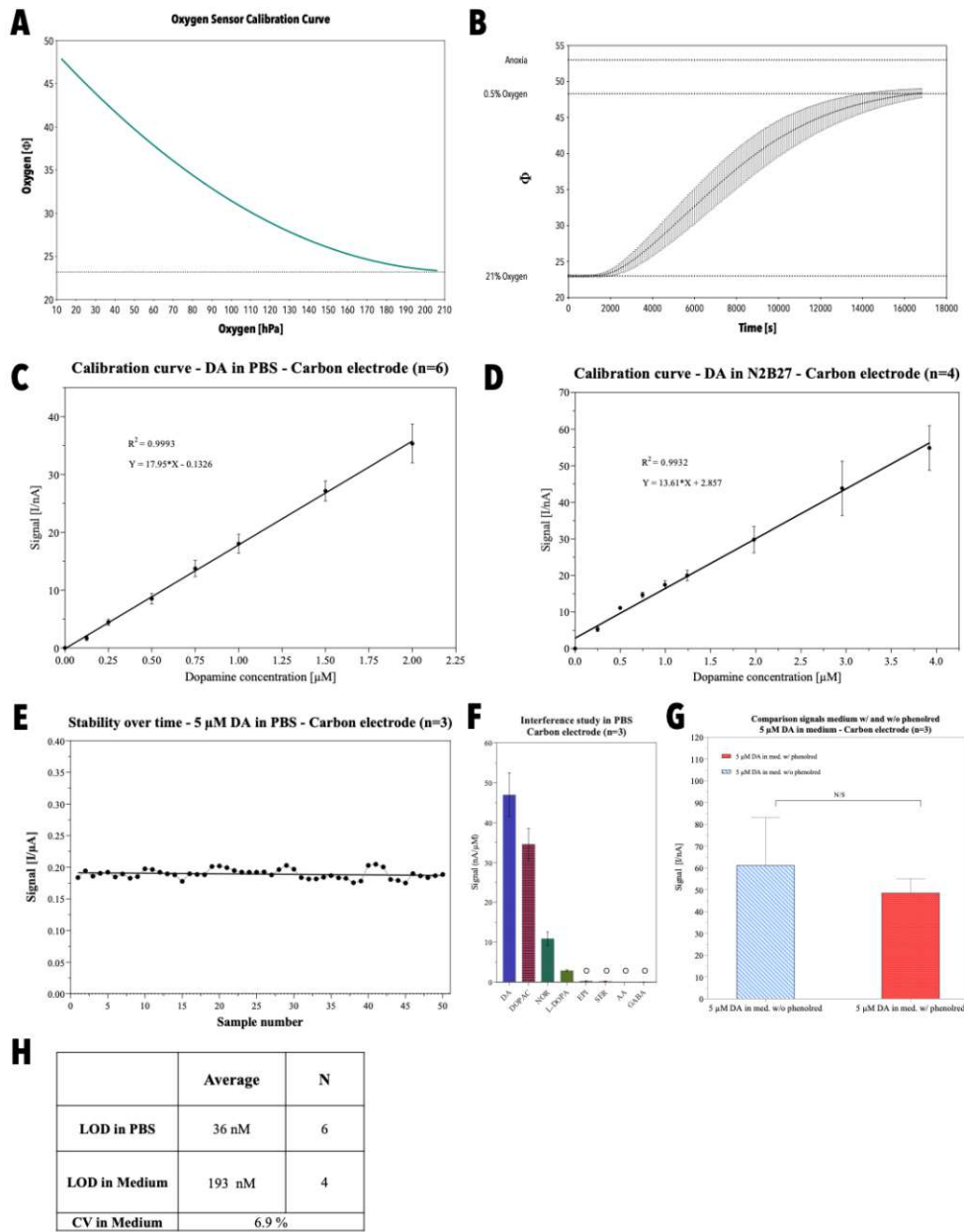
SI Figure 2: Fontana Masson staining of sectioned midbrain organoids revealing intra- and extracellular neuromelanin aggregates (A). Immunohistochemical staining of whole-mounted healthy hMOs cultivated under static culture conditions: TH (red), GFAP (green), MAP2 (magenta), nuclei (blue) (B). Immunohistochemical staining of whole-mounted healthy hMOs cultivated under dynamic culture conditions: TH (red), GFAP (green), MAP2 (magenta), nuclei (blue) (C).

SI Table 1: Comparative analysis of immunohistochemically stained D60 whole-mounted hMOs cultivated under static or dynamic cultivation conditions respectively. Data was retrieved from three individual experiments.

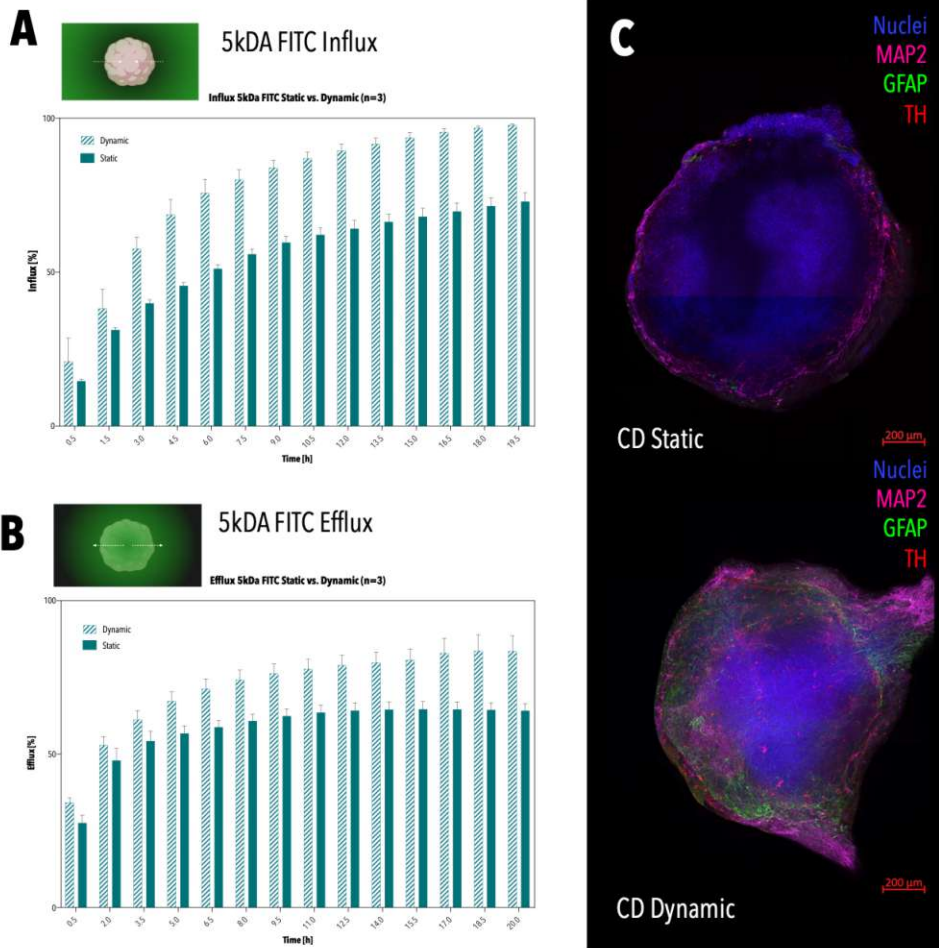
		#1	#2	#3	Average	Dynamic/Static
Dynamic	TH/MAP2 [Px/Px]	0.26116279	0.00420141	0.02983644	0.09840021	
Static	TH/MAP2 [Px/Px]	0.13835968	9.8965E-05	0.00260656	0.04702174	2.092653747
Dynamic	GFAP [Px]	0.26116279	0.00420141	0.02983644	0.09840021	
Static	GFAP [Px]	0.19976123	0.00215019	0.0162215	0.07271097	1.353306201



SI Figure 3: Average growth-rates of healthy and 3xSNCA hMOs ($n=8-10$ from 3 individual organoid batches) (A). Immunohistochemical staining of whole-mounted 3xSNCA hMOs cultivated under static culture conditions: TH (red), GFAP (green), MAP2 (magenta), nuclei (blue) (left panel). Immunohistochemical staining of whole-mounted 3xSNCA hMOs cultivated under dynamic culture conditions: TH (red), GFAP (green), MAP2 (magenta), nuclei (blue) (right panel) (B). Representative images of Lewy-body-like inclusions observed in 100 μm -thick sections of 3xSNCA hMOs (C).



SI Figure 4: Non-linear fit of oxygen sensor calibration curve on-chip (A). Recording of oxygen sensor calibration curve using an O₂-CO₂ controller (B). Dopamine calibration curve in PBS (n=6) and N2B27 (n=4) medium using a three-electrode setup (C/D). Graphical representation of sensor stability over 50 measurements at a dopamine concentration of 5 μM in PBS (n=3) (E). Interference study of common interferents in neurobiology: 3,4-dihydroxyphenylacetic acid (DOPAC), norepinephrine (NOR), levodopa (L-DOPA), epinephrine (EPI), serotonin (SER), ascorbic acid (AA), gamma-aminobutyric acid (GABA) (n=3). Studies were conducted in PBS. Significances were tested using a Welch's t-test *p<0.033, **p<0.002, ***p<0.001 (F). Comparative analysis of 5 μM DA signals retrieved in phenol red and phenol red-free cell culture media (n=3). Significances were tested using a Welch's t-test *p<0.033, **p<0.002, ***p<0.001 (G). Tabular overview of the DA sensor's sensitivity and reproducibility (H).



SI Figure 5: Time-resolved overview of 5kDa FITC transport into hMOs under static and dynamic culture conditions, depicting improved transport under dynamic conditions (n=3) (A). Time-resolved overview of 5kDa FITC transport out of hMOs under static and dynamic culture conditions, depicting enhanced removal of the dextran under dynamic conditions (n=3) (B). Immunohistochemical staining of whole-mounted 3xSNCA hMOs cultivated and treated with HP-β-CD under static culture conditions: TH (red), GFAP (green), MAP2 (magenta), nuclei (blue) (top panel). Immunohistochemical staining of whole-mounted 3xSNCA hMOs cultivated and treated with HP-β-CD under dynamic culture conditions: TH (red), GFAP (green), MAP2 (magenta), nuclei (blue) (bottom panel) (C).

SI Table 2: Overview of used antibodies and respective dilutions.

Target Protein	Dilution	Sample	Company	Catalog Number	RRID
MAP2	1:200	Whole-mount	Millipore	MAB3418	AB_94856
MAP2	1:1000	Section	Abcam	ab92434	AB_2138147
GFAP	1:200	Whole-mount	Millipore	AB5541	AB_177521
TH	1:200 1:1000	Whole-mount Section	Santa Cruz	sc-14007	AB_671397
TUJ1	1:1000	Section	Millipore	AB9354	AB_570918
α -synuclein	1:1000	Section	Novus Biologicals	NBP1-05194	n.a.
p-S129- α -synuclein	1:500	Section	Cell Signalling	23706S	n.a.
TOM20	1:50	Section	Santa Cruz	sc-17764	AB_628381

BIBLIOGRAPHY

1. Parkinson, J. An essay on the Shaking Palsy. *Arch. Neurol.* **20**, 441–445 (1969).
2. Yang, W. *et al.* Current and projected future economic burden of Parkinson's disease in the U.S. *npj Park. Dis.* **6**, (2020).
3. Orozco, J. L. *et al.* Parkinson's disease prevalence, colombiaage distribution and staging in. *Neurol. Int.* **12**, 9–14 (2020).
4. Maserejian, N., Vinikoor-Imler, L. , Dilley, A. Estimation of the 2020 Global Population of Parkinson's Disease (PD). in (MDS Virtual Congress 2020, 2020).
5. Lee, A. & Gilbert, R. M. Epidemiology of Parkinson Disease. *Neurol. Clin.* **34**, 955–965 (2016).
6. Wolters, E. C., Van Der Werf, Y. D. & Van Den Heuvel, O. A. Parkinson's disease-related disorders in the impulsive-compulsive spectrum. *J. Neurol.* **255**, 48–56 (2008).
7. Obeso, J. A. *et al.* Past, present, and future of Parkinson's disease: A special essay on the 200th Anniversary of the Shaking Palsy. *Mov. Disord.* **32**, 1264–1310 (2017).
8. Tolosa, E., Wenning, G. & Poewe, W. The diagnosis of Parkinson's disease. *Lancet Neurol.* **5**, 75–86 (2006).
9. Poewe, W. The natural history of Parkinson's disease. *J. Neurol.* **253**, 2–6 (2006).
10. Hermanowicz, N., Jones, S. A. & Hauser, R. A. Impact of non-motor symptoms in parkinson's disease: A PMDAAlliance survey. *Neuropsychiatr. Dis. Treat.* **15**, 2205–2212 (2019).
11. Obeso, J. A. *et al.* Missing pieces in the Parkinson's disease puzzle. *Nat. Med.* **16**, 653–661 (2010).
12. Fahn, S. The history of dopamine and levodopa in the treatment of Parkinson's disease. *Mov. Disord.* **23**, (2008).
13. DeMaagd, G. & Philip, A. Parkinson ' s Disease and Its Management. *Pharm. Ther.* **40**, 504–511 (2015).
14. Masato, A., Plotegher, N., Boassa, D. & Bubacco, L. Impaired dopamine metabolism in Parkinson's disease pathogenesis. *Mol. Neurodegener.* **14**, 1–21 (2019).
15. Carvey, P. M., Punati, A. & Newman, M. B. Progressive dopamine neuron loss in Parkinson's

disease: The multiple hit hypothesis. *Cell Transplant.* **15**, 239–250 (2006).

16. Meissner, W. G. *et al.* Priorities in Parkinson's disease research. *Nat. Rev. Drug Discov.* **10**, 377–393 (2011).
17. Shulman, J. M., De Jager, P. L. & Feany, M. B. Parkinson's disease: Genetics and pathogenesis. *Annu. Rev. Pathol. Mech. Dis.* **6**, 193–222 (2011).
18. de Lau, L. & Breteler, M. Epidemiology of Parkinson's disease. *Lancet Neurol.* **5**, 525–535 (2006).
19. Dauer, W. & Przedborski, S. Review Parkinson's Disease : Mechanisms and Models. **39**, 889–909 (2003).
20. Goldman, S. M. Environmental toxins and Parkinson's disease. *Annu. Rev. Pharmacol. Toxicol.* **54**, 141–164 (2014).
21. Mappin-Kasirer, B. *et al.* Tobacco smoking and the risk of Parkinson disease: A 65-year follow-up of 30,000 male British doctors. *Neurology* **94**, e2132–e2138 (2020).
22. Hill, C. M. & Mather, M. Tobacco, coffee, and Parkinson's disease. **326**, 561–562 (2004).
23. Tanner, C. M., Goldman, S. M., Ross, G. W. & Grate, S. J. The disease intersection of susceptibility and exposure: Chemical exposures and neurodegenerative disease risk. *Alzheimer's Dement.* **10**, S213–S225 (2014).
24. Tran, J., Anastacio, H. & Bardy, C. Genetic predispositions of Parkinson's disease revealed in patient-derived brain cells. *npj Park. Dis.* **6**, 1–18 (2020).
25. Billingsley, K. J. & Singleton, A. B. Genetic risk factors in Parkinson's disease. 9–20 (2018).
26. Schapira, A. H. & Jenner, P. Etiology and pathogenesis of Parkinson's disease. *Mov. Disord.* **26**, 1049–1055 (2011).
27. MacArthur, J. *et al.* The new NHGRI-EBI Catalog of published genome-wide association studies (GWAS Catalog). *Nucleic Acids Res.* **45**, D896–D901 (2017).
28. Bandres-Ciga, S., Diez-Fairen, M., Kim, J. J. & Singleton, A. B. Genetics of Parkinson's disease: An introspection of its journey towards precision medicine. *Neurobiol. Dis.* **137**, (2020).
29. Rakovic, A. *et al.* Phosphatase and tensin homolog (PTEN)-induced Putative Kinase 1 (PINK1)-dependent ubiquitination of endogenous parkin attenuates mitophagy: Study in

human primary fibroblasts and induced pluripotent stem cell-derived neurons. *J. Biol. Chem.* **288**, 2223–2237 (2013).

30. Zambon, F. *et al.* Cellular α -synuclein pathology is associated with bioenergetic dysfunction in Parkinson's iPSC-derived dopamine neurons. *Hum. Mol. Genet.* **28**, 2001–2013 (2019).
31. Howlett, E. H. *et al.* LRRK2 G2019S-induced mitochondrial DNA damage is LRRK2 kinase dependent and inhibition restores mtDNA integrity in Parkinson's disease. *Hum. Mol. Genet.* **26**, 4340–4351 (2017).
32. Aboud, A. A. *et al.* PARK2 patient neuroprogenitors show increased mitochondrial sensitivity to copper. *Neurobiol. Dis.* **73**, 204–212 (2015).
33. Burbulla, L. F. *et al.* Dopamine oxidation mediates mitochondrial and lysosomal dysfunction in Parkinson's disease. *Science (80-.).* **357**, 1255–1261 (2017).
34. Chung, S. Y. *et al.* Parkin and PINK1 Patient iPSC-Derived Midbrain Dopamine Neurons Exhibit Mitochondrial Dysfunction and α -Synuclein Accumulation. *Stem Cell Reports* **7**, 664–677 (2016).
35. Byers, B. *et al.* SNCA triplication parkinson's patient's iPSC-Derived DA neurons accumulate α -Synuclein and are susceptible to oxidative stress. *PLoS One* **6**, (2011).
36. Imaizumi, Y. *et al.* Mitochondrial dysfunction associated with increased oxidative stress and α -synuclein accumulation in PARK2 iPSC-derived neurons and postmortem brain tissue. *Mol. Brain* **5**, 1–13 (2012).
37. Nguyen, H. N. *et al.* LRRK2 mutant iPSC-derived da neurons demonstrate increased susceptibility to oxidative stress. *Cell Stem Cell* **8**, 267–280 (2011).
38. Schöndorf, D. C. *et al.* iPSC-derived neurons from GBA1-associated Parkinson's disease patients show autophagic defects and impaired calcium homeostasis. *Nat. Commun.* **5**, (2014).
39. Bogetofte, H. *et al.* PARK2 mutation causes metabolic disturbances and impaired survival of human iPSC-derived neurons. *Front. Cell. Neurosci.* **13**, 1–14 (2019).
40. Saroj Chakraborty, Sarah Galla, Xi Cheng, Ji-Youn Yeo, Blair Mell, Vishal Singh, BengSan Yeoh, Piu Saha, Anna V. Mathew, Matam Vijay-Kumar, and B. J. 乳鼠心肌提取 HHS Public Access. *Physiol. Behav.* **176**, 139–148 (2017).
41. Chang, K. H. *et al.* Impairment of proteasome and anti-oxidative pathways in the induced pluripotent stem cell model for sporadic Parkinson's disease. *Park. Relat. Disord.* **24**, 81–88

(2016).

42. Fernandes, H. J. R. *et al.* ER Stress and Autophagic Perturbations Lead to Elevated Extracellular α -Synuclein in GBA-N370S Parkinson's iPSC-Derived Dopamine Neurons. *Stem Cell Reports* **6**, 342–356 (2016).
43. Orenstein, S. J. *et al.* Interplay of LRRK2 with chaperone-mediated autophagy. *Nat. Neurosci.* **16**, 394–406 (2013).
44. Prots, I. *et al.* α -Synuclein oligomers induce early axonal dysfunction in human iPSC-based models of synucleinopathies. *Proc. Natl. Acad. Sci. U. S. A.* **115**, 7813–7818 (2018).
45. Skibinski, G., Nakamura, K., Cookson, M. R. & Finkbeiner, S. Mutant LRRK2 toxicity in neurons depends on LRRK2 levels and synuclein but not kinase activity or inclusion bodies. *J. Neurosci.* **34**, 418–433 (2014).
46. Ludtmann, M. H. R. *et al.* α -synuclein oligomers interact with ATP synthase and open the permeability transition pore in Parkinson's disease. *Nat. Commun.* **9**, (2018).
47. Schwab, A. J. & Ebert, A. D. Neurite Aggregation and Calcium Dysfunction in iPSC-Derived Sensory Neurons with Parkinson's Disease-Related LRRK2 G2019S Mutation. *Stem Cell Reports* **5**, 1039–1052 (2015).
48. Sánchez-Danés, A. *et al.* Disease-specific phenotypes in dopamine neurons from human iPSC-based models of genetic and sporadic Parkinson's disease. *EMBO Mol. Med.* **4**, 380–395 (2012).
49. Devine, M. J. *et al.* Parkinson's disease induced pluripotent stem cells with triplication of the α -synuclein locus. *Nat. Commun.* **2**, (2011).
50. Borgs, L. *et al.* Dopaminergic neurons differentiating from LRRK2 G2019S induced pluripotent stem cells show early neuritic branching defects. *Sci. Rep.* **6**, 1–11 (2016).
51. Jarazo, J. *et al.* Parkinson's Disease Phenotypes in Patient Neuronal Cultures and Brain Organoids Improved by 2-Hydroxypropyl- β -Cyclodextrin Treatment. *Mov. Disord.* 1–16 (2021) doi:10.1002/mds.28810.
52. Beevers, J. E. *et al.* MAPT Genetic Variation and Neuronal Maturity Alter Isoform Expression Affecting Axonal Transport in iPSC-Derived Dopamine Neurons. *Stem Cell Reports* **9**, 587–599 (2017).
53. Kawakami, F. *et al.* LRRK2 phosphorylates tubulin-associated tau but not the free molecule:

LRRK2-mediated regulation of the tau-tubulin association and neurite outgrowth. *PLoS One* **7**, 1–9 (2012).

54. Oliveira, L. M. A. *et al.* Elevated α -synuclein caused by SNCA gene triplication impairs neuronal differentiation and maturation in Parkinson's patient-derived induced pluripotent stem cells. *Cell Death Dis.* **6**, 1–13 (2015).
55. Benjamin Chun-Kit Tong. 乳鼠心肌提取 HHS Public Access. *Physiol. Behav.* **176**, 139–148 (2017).
56. Michel, P. P., Hirsch, E. C. & Hunot, S. Understanding Dopaminergic Cell Death Pathways in Parkinson Disease. *Neuron* **90**, 675–691 (2016).
57. Kouroupi, G. *et al.* Defective synaptic connectivity and axonal neuropathology in a human iPSC-based model of familial Parkinson's disease. *Proc. Natl. Acad. Sci. U. S. A.* **114**, E3679–E3688 (2017).
58. Modamio, J. *et al.* Synaptic decline precedes dopaminergic neuronal loss in human midbrain organoids harboring a triplication of the SNCA gene. *bioRxiv* 2021.07.15.452499 (2021).
59. Sommer, A. *et al.* Th17 Lymphocytes Induce Neuronal Cell Death in a Human iPSC-Based Model of Parkinson's Disease. *Cell Stem Cell* **23**, 123-131.e6 (2018).
60. Beal, M. F. Parkinson's disease: A model dilemma. *Nature* **466**, 8–10 (2010).
61. Adachi-Yamada, T. *et al.* *Drosophila* Models for Human. *Advances in Experimental Medicine and Biology* vol. 1076 (2018).
62. Chia, S. J., Tan, E. & Chao, Y. Historical Perspective : Models of Parkinson ' s Disease. 1–14 (2020).
63. Potashkin, J. A., Blume, S. R. & Runkle, N. K. Limitations of animal models of Parkinson's disease. *Parkinsons. Dis.* **2011**, (2011).
64. Braak, H. B. E. Pathoanatomy of Parkinson ' s disease. 3–10 (2000).
65. Jagmag, S. A., Tripathi, N., Shukla, S. D., Maiti, S. & Khurana, S. Evaluation of models of Parkinson's disease. *Front. Neurosci.* **9**, (2016).
66. Schwarting, R. K. W. & Huston, J. P. The unilateral 6-hydroxydopamine lesion model in behavioral brain research. Analysis of functional deficits, recovery and treatments. *Prog. Neurobiol.* **50**, 275–331 (1996).

67. Jackson-Lewis, V. & Przedborski, S. Protocol for the MPTP mouse model of Parkinson's disease. *Nat. Protoc.* **2**, 141–151 (2007).
68. Sedelis, M., Schwarting, R. K. W. & Huston, J. P. Behavioral phenotyping of the MPTP mouse model of Parkinson's disease. *Behav. Brain Res.* **125**, 109–125 (2001).
69. Cannon, J. R. *et al.* A highly reproducible rotenone model of Parkinson's disease. *Neurobiol. Dis.* **34**, 279–290 (2009).
70. Uversky, V. N. Neurotoxicant-induced animal models of Parkinson's disease: Understanding the role of rotenone, maneb and paraquat in neurodegeneration. *Cell Tissue Res.* **318**, 225–241 (2004).
71. Dawson, T. M., Ko, H. S. & Dawson, V. L. Genetic Animal Models of Parkinson's Disease. *Neuron* **66**, 646–661 (2010).
72. Visanji, N. P. *et al.* α -Synuclein-Based Animal Models of Parkinson's Disease: Challenges and Opportunities in a New Era. *Trends Neurosci.* **39**, 750–762 (2016).
73. Cooper, J. F. & Van Raamsdonk, J. M. Modeling Parkinson's disease in *C. elegans*. *J. Parkinsons. Dis.* **8**, 17–32 (2018).
74. Editor, H. J. R. *Leucine- Rich Repeat Kinase 2*. vol. 2.
75. Gandhi, S. *et al.* Dopamine induced neurodegeneration in a PINK1 model of Parkinson's disease. *PLoS One* **7**, (2012).
76. Zhou, W. *et al.* Phenylbutyrate up-regulates the DJ-1 protein and protects neurons in cell culture and in animal models of Parkinson disease. *J. Biol. Chem.* **286**, 14941–14951 (2011).
77. Jenner, P. Experimental models of Parkinson disease. *Rev. Ecuatoriana Neurol.* **1**, 88–89 (1992).
78. Boucherie, D. M. *et al.* Parkinson's Disease Drug Development since 1999: A Story of Repurposing and Relative Success. *J. Parkinsons. Dis.* **11**, 421–429 (2021).
79. Takahashi, K. & Yamanaka, S. Induction of Pluripotent Stem Cells from Mouse Embryonic and Adult Fibroblast Cultures by Defined Factors. *Cell* **126**, 663–676 (2006).
80. De Souza, N. Organoids. *Nat. Methods* **15**, 23 (2018).
81. Lee, J. *et al.* Generation and characterization of hair-bearing skin organoids from human pluripotent stem cells. *Nat. Protoc.* **17**, 1266–1305 (2022).

82. Matano, M. *et al.* Modeling colorectal cancer using CRISPR-Cas9-mediated engineering of human intestinal organoids. *Nat. Med.* **21**, 256–262 (2015).
83. Mun, S. J. *et al.* Generation of expandable human pluripotent stem cell-derived hepatocyte-like liver organoids. *J. Hepatol.* **71**, 970–985 (2019).
84. Lee, J. *et al.* In vitro generation of functional murine heart organoids via FGF4 and extracellular matrix. *Nat. Commun.* **11**, (2020).
85. Cederquist, G. Y. *et al.* Specification of positional identity in forebrain organoids. *Nat. Biotechnol.* **37**, 436–444 (2019).
86. Valiulahi, P. *et al.* Generation of caudal-type serotonin neurons and hindbrain-fate organoids from hPSCs. *Stem Cell Reports* **16**, 1938–1952 (2021).
87. Monzel, A. S. *et al.* Derivation of Human Midbrain-Specific Organoids from Neuroepithelial Stem Cells. *Stem Cell Reports* **9**, 667–680 (2017).
88. Jo, J. *et al.* Midbrain-like Organoids from Human Pluripotent Stem Cells Contain Functional Dopaminergic and Neuromelanin-Producing Neurons. *Cell Stem Cell* **19**, 248–257 (2016).
89. Berger, E. *et al.* Millifluidic culture improves human midbrain organoid vitality and differentiation. *Lab Chip* **18**, 3172–3183 (2018).
90. Nickels, S. L. *et al.* Reproducible generation of human midbrain organoids for in vitro modeling of Parkinson’s disease. *Stem Cell Res.* **46**, (2020).
91. Sabate-Soler, S. *et al.* Microglia integration into human midbrain organoids leads to increased neuronal maturation and functionality. *Glia* 1–22 (2022) doi:10.1002/glia.24167.
92. Renner, H. *et al.* A fully automated high-throughput workflow for 3d-based chemical screening in human midbrain organoids. *Elife* **9**, 1–39 (2020).
93. Smits, L. M. *et al.* Modeling Parkinson ’ s disease in midbrain-like organoids. 1–8 (2019).
94. Kano, M. *et al.* Reduced astrocytic reactivity in human brains and midbrain organoids with PRKN mutations. *npj Park. Dis.* **6**, 1–9 (2020).
95. Mohamed, N.-V. *et al.* Midbrain organoids with an SNCA gene triplication model key features of synucleinopathy . *Brain Commun.* **3**, (2021).
96. Jo, J. *et al.* Lewy Body–like Inclusions in Human Midbrain Organoids Carrying Glucocerebrosidase and α -Synuclein Mutations. *Ann. Neurol.* **90**, 490–505 (2021).

97. Abbott, N. J., Pizzo, M. E., Preston, J. E., Janigro, D. & Thorne, R. G. The role of brain barriers in fluid movement in the CNS: is there a 'glymphatic' system? *Acta Neuropathol.* **135**, 387–407 (2018).
98. Iliff, J. J. *et al.* A Paravascular Pathway Facilitates CSF Flow Through the Brain Parenchyma and the Clearance of Interstitial Solutes, Including Amyloid beta. **4**, (2012).
99. Zou, W. *et al.* Blocking meningeal lymphatic drainage aggravates Parkinson's disease-like pathology in mice overexpressing mutated α -synuclein. *Transl. Neurodegener.* **8**, 1–17 (2019).
100. Abstract, G., Brief, I. & Numbers, A. Brain-Region-Specific Organoids Using Mini-bioreactors for Modeling ZIKV Exposure Resource Brain-Region-Specific Organoids Using Mini-bioreactors for Modeling ZIKV Exposure. 1238–1254 (2016).
101. Kim, H. *et al.* Modeling G2019S-LRRK2 Sporadic Parkinson's Disease in 3D Midbrain Organoids. *Stem Cell Reports* **12**, 518–531 (2019).
102. Monzel, A. S. *et al.* Machine learning-assisted neurotoxicity prediction in human midbrain organoids. *Park. Relat. Disord.* **75**, 105–109 (2020).
103. Whitesides, G. M. The origins and the future of microfluidics. *Nature* **442**, 368–373 (2006).
104. Rohr, S., Scholly, D. M. & Kleber, A. G. Patterned growth of neonatal rat heart cells in culture. Morphological and electrophysiological characterization. *Circ. Res.* **68**, 114–130 (1991).
105. Sin, A. *et al.* The Design and Fabrication of Three-Chamber Microscale Cell Culture Analog Devices with Integrated Dissolved Oxygen Sensors. *Biotechnol. Prog.* **20**, 338–345 (2004).
106. Viravaidya, K., Sin, A. & Shuler, M. L. Development of a Microscale Cell Culture Analog to Probe Naphthalene Toxicity. *Biotechnol. Prog.* **20**, 316–323 (2004).
107. Viravaidya, K. & Shuler, M. L. Incorporation of 3T3-L1 cells to mimic bioaccumulation in a microscale cell culture analog device for toxicity studies. *Biotechnol. Prog.* **20**, 590–597 (2004).
108. Huh, D. *et al.* Reconstituting organ-level lung functions on a chip. *Science (80-.).* **328**, 1662–1668 (2010).
109. Ma, C., Peng, Y., Li, H. & Chen, W. Organ-on-a-Chip: A New Paradigm for Drug Development. *Trends Pharmacol. Sci.* **42**, 119–133 (2021).
110. Ramadan, Q. & Zourob, M. Organ-on-a-chip engineering: Toward bridging the gap between

lab and industry. *Biomicrofluidics* **14**, (2020).

111. Lee-Montiel, F. T. *et al.* Integrated Isogenic Human Induced Pluripotent Stem Cell–Based Liver and Heart Microphysiological Systems Predict Unsafe Drug–Drug Interaction. *Front. Pharmacol.* **12**, 1–19 (2021).
112. Haase, K. *et al.* Physiologic flow-conditioning limits vascular dysfunction in engineered human capillaries. *Biomaterials* **280**, 121248 (2022).
113. Benam, K. H. *et al.* Small airway-on-a-chip enables analysis of human lung inflammation and drug responses in vitro. *Nat. Methods* **13**, 151–157 (2016).
114. Shah, P. *et al.* A microfluidics-based in vitro model of the gastrointestinal human-microbe interface. *Nat. Commun.* **7**, (2016).
115. Cho, A. N. *et al.* Microfluidic device with brain extracellular matrix promotes structural and functional maturation of human brain organoids. *Nat. Commun.* **12**, (2021).
116. Kasendra, M. *et al.* Development of a primary human Small Intestine-on-a-Chip using biopsy-derived organoids. *Sci. Rep.* **8**, 1–14 (2018).
117. Homan, K. A. *et al.* Flow-enhanced vascularization and maturation of kidney organoids in vitro. *Nat. Methods* **16**, 255–262 (2019).
118. Campisi, M. *et al.* 3D self-organized microvascular model of the human blood-brain barrier with endothelial cells, pericytes and astrocytes. *Biomaterials* **180**, 117–129 (2018).
119. Maoz, B. M. *et al.* A linked organ-on-chip model of the human neurovascular unit reveals the metabolic coupling of endothelial and neuronal cells. *Nat. Biotechnol.* **36**, 865–877 (2018).
120. Occhetta, P. *et al.* Hyperphysiological compression of articular cartilage induces an osteoarthritic phenotype in a cartilage-on-a-chip model. *Nat. Biomed. Eng.* **3**, 545–557 (2019).
121. Ronaldson-bouchard, K. *et al.* *linked by vascular flow*. vol. 6 (2022).
122. Wang, Y., Wang, L., Zhu, Y. & Qin, J. Human brain organoid-on-a-chip to model prenatal nicotine exposure. *Lab Chip* **18**, 851–860 (2018).
123. Ao, Z. *et al.* One-Stop Microfluidic Assembly of Human Brain Organoids to Model Prenatal Cannabis Exposure. *Anal. Chem.* **92**, 4630–4638 (2020).
124. Yin, F., Zhu, Y., Wang, Y. & Qin, J. Engineering Brain Organoids to Probe Impaired Neurogenesis Induced by Cadmium. *ACS Biomater. Sci. Eng.* **4**, 1908–1915 (2018).

125. Park, J. *et al.* Three-dimensional brain-on-a-chip with an interstitial level of flow and its application as an in vitro model of Alzheimer's disease. *Lab Chip* **15**, 141–150 (2015).
126. Karzbrun, E., Kshirsagar, A., Cohen, S. R., Hanna, J. H. & Reiner, O. Human brain organoids on a chip reveal the physics of folding. *Nat. Phys.* **14**, 515–522 (2018).
127. Rifès, P. *et al.* Publisher Correction: Modeling neural tube development by differentiation of human embryonic stem cells in a microfluidic WNT gradient (Nature Biotechnology, (2020), 38, 11, (1265-1273), 10.1038/s41587-020-0525-0). *Nat. Biotechnol.* **38**, 1357 (2020).
128. Fuchs, S. *et al.* In-line analysis of organ-on-chip systems with sensors: Integration, fabrication, challenges, and potential. *ACS Biomater. Sci. Eng.* **7**, 2926–2948 (2021).
129. Vigh, J. P. *et al.* Transendothelial electrical resistance measurement across the blood–brain barrier: A critical review of methods. *Micromachines* **12**, 1–18 (2021).
130. Zoio, P., Lopes-Ventura, S. & Oliva, A. Barrier-on-a-chip with a modular architecture and integrated sensors for real-time measurement of biological barrier function. *Micromachines* **12**, (2021).
131. Odijk, M. *et al.* Measuring direct current trans-epithelial electrical resistance in organ-on-a-chip microsystems. *Lab Chip* **15**, 745–752 (2015).
132. van der Helm, M. W. *et al.* Non-invasive sensing of transepithelial barrier function and tissue differentiation in organs-on-chips using impedance spectroscopy. *Lab Chip* **19**, 452–463 (2019).
133. Yeste, J. *et al.* A compartmentalized microfluidic chip with crisscross microgrooves and electrophysiological electrodes for modeling the blood-retinal barrier. *Lab Chip* **18**, 95–105 (2018).
134. Wu, Q. *et al.* Bionic 3D spheroids biosensor chips for high-throughput and dynamic drug screening. *Biomed. Microdevices* **20**, (2018).
135. Schuller, P. *et al.* Optimized plasma-assisted bi-layer photoresist fabrication protocol for high resolution microfabrication of thin-film metal electrodes on porous polymer membranes. *MethodsX* **6**, 2606–2613 (2019).
136. Schuller, P. *et al.* A lab-on-a-chip system with an embedded porous membrane-based impedance biosensor array for nanoparticle risk assessment on placental Bewo trophoblast cells. *Sensors Actuators, B Chem.* **312**, 127946 (2020).

137. Spira, M. E. & Hai, A. Multi-electrode array technologies for neuroscience and cardiology. *Nat. Nanotechnol.* **8**, 83–94 (2013).
138. Perrier, R. *et al.* Bioelectronic organ-based sensor for microfluidic real-time analysis of the demand in insulin. *Biosens. Bioelectron.* **117**, 253–259 (2018).
139. Lind, J. U. *et al.* Cardiac microphysiological devices with flexible thin-film sensors for higher-throughput drug screening. *Lab Chip* **17**, 3692–3703 (2017).
140. Jin, Z. H., Liu, Y. L., Fan, W. T. & Huang, W. H. Integrating Flexible Electrochemical Sensor into Microfluidic Chip for Simulating and Monitoring Vascular Mechanotransduction. *Small* **16**, 1–5 (2020).
141. Ortega, M. A. *et al.* Muscle-on-a-chip with an on-site multiplexed biosensing system for: In situ monitoring of secreted IL-6 and TNF- α . *Lab Chip* **19**, 2568–2580 (2019).
142. Rothbauer, M. *et al.* Monitoring tissue-level remodelling during inflammatory arthritis using a three-dimensional synovium-on-a-chip with non-invasive light scattering biosensing. *Lab Chip* **20**, 1461–1471 (2020).
143. Dornhof, J. *et al.* Microfluidic organ-on-chip system for multi-analyte monitoring of metabolites in 3D cell cultures. *Lab Chip* **22**, 225–239 (2022).
144. Misun, P. M., Rothe, J., Schmid, Y. R. F., Hierlemann, A. & Frey, O. Multi-analyte biosensor interface for real-time monitoring of 3D microtissue spheroids in hanging-drop networks. *Microsystems Nanoeng.* **2**, (2016).
145. Shin, S. R. *et al.* Label-Free and Regenerative Electrochemical Microfluidic Biosensors for Continual Monitoring of Cell Secretomes. *Adv. Sci.* **4**, 1–14 (2017).
146. Osaki, T., Uzel, S. G. M. & Kamm, R. D. Microphysiological 3D model of amyotrophic lateral sclerosis (ALS) from human iPS-derived muscle cells and optogenetic motor neurons. *Sci. Adv.* **4**, 1–16 (2018).
147. Ando, Y. *et al.* A microdevice platform recapitulating hypoxic tumor microenvironments. *Sci. Rep.* **7**, 1–12 (2017).
148. Matsumoto, S. *et al.* Investigation of the hepatic respiration and liver zonation on rat hepatocytes using an integrated oxygen biosensor in a microscale device. *Biotechnol. Prog.* **35**, 1–13 (2019).
149. Sticker, D. *et al.* Oxygen Management at the Microscale: A Functional Biochip Material with

Long-Lasting and Tunable Oxygen Scavenging Properties for Cell Culture Applications. *ACS Appl. Mater. Interfaces* **11**, 9730–9739 (2019).

150. Rennert, K. *et al.* A microfluidically perfused three dimensional human liver model. *Biomaterials* **71**, 119–131 (2015).
151. Uzel, S. G. M. *et al.* Microfluidic device for the formation of optically excitable, three-dimensional, compartmentalized motor units. *Sci. Adv.* **2**, (2016).
152. Huebsch, N. *et al.* cardiac microtissues on microfluidic chips. **6**, (2022).
153. Qian, F. *et al.* Simultaneous electrical recording of cardiac electrophysiology and contraction on chip. *Lab Chip* **17**, 1732–1739 (2017).
154. Riahi, R. *et al.* Automated microfluidic platform of bead-based electrochemical immunosensor integrated with bioreactor for continual monitoring of cell secreted biomarkers. *Sci. Rep.* **6**, 1–14 (2016).
155. Skardal, A. *et al.* Multi-tissue interactions in an integrated three-tissue organ-on-a-chip platform. *Sci. Rep.* **7**, 1–16 (2017).
156. Aleman, J., Kilic, T., Mille, L. S., Shin, S. R. & Zhang, Y. S. Microfluidic integration of regeneratable electrochemical affinity-based biosensors for continual monitoring of organ-on-a-chip devices. *Nat. Protoc.* **16**, 2564–2593 (2021).
157. Zhang, Y. S. *et al.* Multisensor-integrated organs-on-chips platform for automated and continual in situ monitoring of organoid behaviors. *Proc. Natl. Acad. Sci. U. S. A.* **114**, E2293–E2302 (2017).
158. Mermoud, Y., Felder, M., Stucki, J. D., Stucki, A. O. & Guenat, O. T. Microimpedance tomography system to monitor cell activity and membrane movements in a breathing lung-on-chip. *Sensors Actuators, B Chem.* **255**, 3647–3653 (2018).
159. Ramadan, Q. & Ting, F. C. W. In vitro micro-physiological immune-competent model of the human skin. *Lab Chip* **16**, 1899–1908 (2016).
160. Vatine, G. D. *et al.* Human iPSC-Derived Blood-Brain Barrier Chips Enable Disease Modeling and Personalized Medicine Applications. *Cell Stem Cell* **24**, 995-1005.e6 (2019).
161. Ferrell, N. *et al.* A Microfluidic Bioreactor With Integrated Transepithelial Electrical Resistance (TEER) Measurement Electrodes for Evaluation of Renal Epithelial Cells. *Biotechnol Bioeng.* **107**, 707–716 (2010).

162. Henry, O. Y. F. *et al.* Organs-on-chips with integrated electrodes for trans-epithelial electrical resistance (TEER) measurements of human epithelial barrier function. *Lab Chip* **17**, 2264–2271 (2017).
163. Mattern, K., Beißner, N., Reichl, S. & Dietzel, A. DynaMiTES – A dynamic cell culture platform for in vitro drug testing PART 1 – Engineering of microfluidic system and technical simulations. *Eur. J. Pharm. Biopharm.* **126**, 159–165 (2018).
164. Beißner, N., Mattern, K., Dietzel, A. & Reichl, S. DynaMiTES – A dynamic cell culture platform for in vitro drug testing PART 2 – Ocular DynaMiTES for drug absorption studies of the anterior eye. *Eur. J. Pharm. Biopharm.* **126**, 166–176 (2018).
165. Huebsch, N. *et al.* in silico. (2020).
166. Huebsch, N. *et al.* 2,6,7 ,. (2018).
167. Lai, B. F. L. *et al.* InVADE: Integrated Vasculature for Assessing Dynamic Events. *Adv. Funct. Mater.* **27**, 1–11 (2017).
168. Chen, Y. *et al.* A microfluidic circulatory system integrated with capillary-assisted pressure sensors. *Lab Chip* **17**, 653–662 (2017).
169. Oleaga, C. *et al.* Long-Term Electrical and Mechanical Function Monitoring of a Human-on-a-Chip System. *Adv. Funct. Mater.* **29**, 1–12 (2019).
170. Oleaga, C. *et al.* HHS Public Access. 176–190 (2019)
doi:10.1016/j.biomaterials.2018.07.062.Investigation.
171. Oleaga, C. *et al.* Multi-Organ toxicity demonstration in a functional human in vitro system composed of four organs. *Sci. Rep.* **6**, 1–17 (2016).
172. Bavli, D. *et al.* Real-time monitoring of metabolic function in liver-onchip microdevices tracks the dynamics of Mitochondrial dysfunction. *Proc. Natl. Acad. Sci. U. S. A.* **113**, E2231–E2240 (2016).
173. Ehrlich, A. *et al.* Microphysiological flux balance platform unravels the dynamics of drug induced steatosis. *Lab Chip* **18**, 2510–2522 (2018).
174. Prill, S. *et al.* Real-time monitoring of oxygen uptake in hepatic bioreactor shows CYP450-independent mitochondrial toxicity of acetaminophen and amiodarone. *Arch. Toxicol.* **90**, 1181–1191 (2016).
175. Farooqi, H. M. U., Khalid, M. A. U., Kim, K. H., Lee, S. R. & Choi, K. H. Real-time

physiological sensor-based liver-on-chip device for monitoring drug toxicity. *J. Micromechanics Microengineering* **30**, (2020).

176. Khalid, M. A. U. *et al.* A lung cancer-on-chip platform with integrated biosensors for physiological monitoring and toxicity assessment. *Biochem. Eng. J.* **155**, 107469 (2020).
177. Asif, A., Kim, K. H., Jabbar, F., Kim, S. & Choi, K. H. Real-time sensors for live monitoring of disease and drug analysis in microfluidic model of proximal tubule. *Microfluid. Nanofluidics* **24**, 1–10 (2020).
178. Azizgolshani, H. *et al.* High-throughput organ-on-chip platform with integrated programmable fluid flow and real-time sensing for complex tissue models in drug development workflows. *Lab Chip* **21**, 1454–1474 (2021).
179. Maoz, B. M. *et al.* Organs-on-Chips with combined multi-electrode array and transepithelial electrical resistance measurement capabilities. *Lab Chip* **17**, 2294–2302 (2017).
180. Qian, F. *et al.* Simultaneous electrical recording of cardiac electrophysiology and contraction on chip. *Lab Chip* **17**, 1732–1739 (2017).

SARAH SPITZ



SARAH.SPITZ@TUWIEN.AC.AT

AREAS OF RESEARCH

organ-on-a-chip technology; iPSC-technology; neurobiology; neurodegeneration; tissue engineering; biomaterials research; microfluidics; rapid prototyping; system integration, electrochemistry; biosensing; point-of-care diagnostics

EDUCATION

2019 – 09/2022

VIENNA UNIVERSITY OF TECHNOLOGY

Doctoral Student at the Institute of Chemical Technologies and Analytics, CellChip Group, Prof. Peter Ertl

10/2015 – 11/2018

UNIVERSITY OF NATURAL RESOURCES AND LIFE SCIENCES VIENNA

Master of Science in Biotechnology

Diploma thesis: “Enter the Matrix - Studying the Impact of Matrix Type and Stiffness Based on the Redifferentiation Behavior of Primary Human Chondrocytes”, at the Institute of Chemical Technologies and Analytics, CellChip Group, Prof. Peter Ertl

10/2011 – 09/2015

UNIVERSITY OF NATURAL RESOURCES AND LIFE SCIENCES VIENNA

Bachelor of Science in Food- and Biotechnology

Bachelor Thesis: “Biomaterials in Bone Tissue Engineering - A Suitability Assessment of the Biomaterial Tutoplast® Spongiosa” at the Division of Biotechnology, Prof. Cornelia Kasper

09/2003 – 07/2011

BUNDESGYMNASIUM/BUNDESREALGYMNAISUM KLOSTERNEUBURG

High School Diploma

Page 1 of 7

PROFESSIONAL EXPERIENCE

08/2021 - present	VIENNA UNIVERSITY OF TECHNOLOGY UNIVERSITY ASSISTANT at the Institute of Chemical Technologies and Analytics, CellChip Group, Prof. Peter Ertl
03/2022 – 09/2022	MASSACHUSETTS INSTITUTE OF TECHNOLOGY VISITING SCHOLAR at the Biomedical Engineering Department, Mechanobiology Lab, Prof. Roger Dale Kamm
06/2021 – 08/2021	UNIVERSITY OF LUXEMBOURG VISITING SCHOLAR at the Luxembourg Centre for Systems Biomedicine, Developmental and Cellular Biology Group, Prof. Jens C. Schwamborn
11/2018 – 08/2021	VIENNA UNIVERSITY OF TECHNOLOGY RESEARCH ASSISTANT at the Institute of Chemical Technologies and Analytics, CellChip Group, Prof. Peter Ertl
09/2017 – 04/2018	TRAUMA CARE CONSULT INTERNSHIP (FEMtech) at Trauma Care Consult, Prof. Heinz Redl
08/2015 – 04/2017	UNIVERSITY OF NATURAL RESOURCES AND LIFE SCIENCES VIENNA RESEARCH FELLOW at the University of Natural Resources and Life Sciences, Department of Biotechnology, Prof. Cornelia Kasper
2013	UNIVERSITY OF NATURAL RESOURCES AND LIFE SCIENCES VIENNA INTERNSHIP at the University of Natural Resources and Life Sciences, Department of Biotechnology, Prof. Renate Kunert

TEACHING AND ADMINISTRATIVE EXPERIENCE

- Teaching assistant in the practical course: “General Chemistry Introductory Laboratory (163.006)” at the Vienna University of Technology
- Supervision and training of 1-2 students per year (2019-2021)
- Laboratory management
- Participation in the practical implementation of two international projects: EU Joint Program – Neurodegenerative Disease Research (JPND) project (INTER/ JPND/15/11092422) and M-era. Net project NanoPD (INTER/MERA/17/11760144)
- Project manager of an industry-commissioned project for the development of a point-of-care device

METRICS

- Publications: 17
- Patent applications: 1
- Citations: 260
- h-factor: 8
- Conference contributions: 9

CONFERENCE PRESENTATIONS

08/2021	<u>Spitz, S.</u> ; Bolognin, S.; Brandauer, K.; Schobesbeger S.; Schuller, P.; Mayr, T.; Schwamborn, J. C.; Ertl, P., Austrian Tissue Cluster Meeting, Vienna, Austria, oral presentation
07/2020	<u>Spitz, S.</u> ; Zanetti, C.; Bolognin, S.; Muwanigwa, M. N.; Smits, L.; Berger, E.; Jordan, C.; Harasek, M.; Schwamborn, J. C.; Ertl, P., Midbrain-on-a-Chip, European Organ-on-Chip Conference, EUROoC, 2020, online, oral presentation Zirath, H.; <u>Spitz, S.</u> ; Rothbauer, M.; Müller, B.; Mayr, T.; Ertl, P., A Microfluidic Device for Real-time Nanotoxicity Screening, European Organ-on-Chip Conference, EUROoC, 2020, online, poster presentation
11/2019	<u>Spitz, S.</u> ; 3DPD – Advanced Modelling of Parkinson’s disease with Three-Dimensional Human Midbrain Organoids, JPND / JPco-fuND Symposium, 2019, Brussels, Belgium, poster presentation
07/2019	<u>Spitz, S.</u> ; Zanetti, C.; Marchietti-Deschmann, M.; Schwamborn, J.C.; Ertl, P., Parkinson’s disease-on-a-chip: culturing and

	<p>monitoring human midbrain organoids employing a redox cycling sensor, European Organ-on-Chip Conference, EUROoC, 2019, Graz, Austria, poster presentation – <u>Awarded with poster prize</u></p>
	<p>Rothbauer, M.; Zirath, H.; <u>Spitz, S.</u>; Bachmann, B.; Mayr, T.; Ertl P., Real-time Oxygen Biosensing in Three-dimensional Vascular Organ-on-a-chip Systems, European Organ-on-Chip Conference, EUROoC, 2019, Graz, Austria, poster presentation</p>
	<p>Bachmann, B.; <u>Spitz, S.</u>; Redl, H.; Nürnberger, S.; Ertl, P., Enter the Matrix-Hydrogel Stiffness and its Effects on Chondrocyte Redifferentiation, European Organ-on-Chip Conference, EUROoC, 2019, Graz, Austria, poster presentation</p>
06/2019	<p><u>Spitz, S.</u>; Zanetti, C., Schuller, P.; Schwamborn, J.; Ertl, P., Unravelling the complexity of Parkinson's Disease, Organ-on-a-Chip & Tissue-on-a-Chip Europe, 2019, Rotterdam, the Netherlands, poster presentation</p> <p>Bachmann, B.; <u>Spitz, S.</u>; Redl, H.; Nürnberger, S.; Ertl, P., The Stiffer the Better?, Organ-on-a-Chip & Tissue-on-a-Chip Europe, 2019, Rotterdam, the Netherlands, poster presentation</p>

SCHOLARSHIPS AND AWARDS

07/2021	Marietta Blau Grant 2021 – OeAD GmbH (Austrian Federal Ministry of Education, Science and Research)
05/2021	Marshall Plan Scholarship 2021 – Austrian Marshall Plan Foundation
11/2020	Houska Award for Application Driven Research 2020 – B&C Holding GmbH
10/2019	Herbert Stiller Award 2019 - Doctors Against Animal Experiments Germany
07/2019	Poster Award – EUROoCS 2019
2018	Merit-based Scholarship at the University of Natural Resources and Life Sciences
2017	Merit-based Scholarship at the University of Natural Resources and Life Sciences

SKILLS AND QUALIFICATION

Languages	German (native), English (fluent), French (basic)
Software	MS Office (Word, Excel, Power Point), Adobe Photoshop, Adobe InDesign, Adobe Illustrator, AutoCad, Fusion 360, CFD, ImageJ, Graph Pad Prism, C, C++

PUBLICATION LIST

1. Zirath, H.; Spitz, S.*; Roth, D.; Schellhorn, T.; Rothbauer, M.; Müller, B.; Walch, M.; Kaur, J.; Wörle, A.; Kohl, Y.; Mayr, T.; Ertl, P. Bridging the Academic–Industrial Gap: Application of an Oxygen and PH Sensor-Integrated Lab-on-a-Chip in Nanotoxicology. *Lab Chip* **2021**, 10.1039. D1LC00528F. <https://doi.org/10.1039/D1LC00528F>.
2. Rothbauer, M.; Byrne, R. A.; Schobesberger, S.; Olmos Calvo, I.; Fischer, A.; Reihls, E. I.; Spitz, S.; Bachmann, B.; Sevelde, F.; Holinka, J.; Holnthoner, W.; Redl, H.; Toegel, S.; Windhager, R.; Kiener, H. P.; Ertl, P. Establishment of a Human Three-Dimensional Chip-Based Chondro-Synovial Coculture Joint Model for Reciprocal Cross Talk Studies in Arthritis Research. *Lab Chip* **2021**, 10.1039. D1LC00130B. <https://doi.org/10.1039/D1LC00130B>.
3. Kocsis, Á.; Pasztorek, M.; Rossmann, E.; Djinovic, Z.; Mayr, T.; Spitz, S.; Zirath, H.; Ertl, P.; Fischer, M. B. Dependence of Mitochondrial Function on the Filamentous Actin Cytoskeleton in Cultured Mesenchymal Stem Cells Treated with Cytochalasin B. *Journal of Bioscience and Bioengineering* **2021**, 132 (3), 310–320. <https://doi.org/10.1016/j.jbiosc.2021.05.010>.
4. Rothbauer, M.; Bachmann, B. E. M.; Eilenberger, C.; Kratz, S. R. A.; Spitz, S.*; Höll, G.; Ertl, P. A Decade of Organs-on-a-Chip Emulating Human Physiology at the Microscale: A Critical Status Report on Progress in Toxicology and Pharmacology. *Micromachines* **2021**, 12 (5), 470. <https://doi.org/10.3390/mi12050470>.
5. Goldstein, Y.; Spitz, S.; Turjeman, K.; Selinger, F.; Barenholz, Y.; Ertl, P.; Benny, O.; Bavli, D. Breaking the Third Wall: Implementing 3D-Printing Techniques to Expand the Complexity and Abilities of Multi-Organ-on-a-Chip Devices. *Micromachines* **2021**, 12 (6), 627. <https://doi.org/10.3390/mi12060627>.
6. Bachmann, B.; Spitz, S.; Jordan, C.; Schuller, P.; Wanzenböck, H. D.; Haddadi, B.; Harasek, M.; Redl, H.; Holnthoner, W.; Ertl, P. *Microvasculature-on-a-Chip: Bridging the Interstitial Blood-Lymph Interface via Mechanobiological Stimuli*; preprint; *Bioengineering*, **2021**. <https://doi.org/10.1101/2021.04.08.438936>.

7. Rothbauer, M.; Byrne, R. A.; Schobesberger, S.; Calvo, I. O.; Fischer, A.; Reihls, E. I.; Spitz, S.; Bachmann, B.; Sevelde, F.; Holinka, J.; Holnthoner, W.; Redl, H.; Tögel, S.; Windhager, R.; Kiener, H. P.; Ertl, P. *Establishment of a Human Three-Dimensional Chip-Based Chondro-Synovial Co-Culture Joint Model for Reciprocal Cross-Talk Studies in Arthritis Research*; preprint; Bioengineering, **2021**. <https://doi.org/10.1101/2021.02.19.431936>.
8. Zanetti, C.; Spitz, S.*; Berger, E.; Bolognin, S.; Smits, L. M.; Crepaz, P.; Rothbauer, M.; Rosser, J. M.; Marchetti-Deschmann, M.; Schwamborn, J. C.; Ertl, P. Monitoring the Neurotransmitter Release of Human Midbrain Organoids Using a Redox Cycling Microsensor as a Novel Tool for Personalized Parkinson's Disease Modelling and Drug Screening. *The Analyst* **2021**, 10.1039. D0AN02206C. <https://doi.org/10.1039/D0AN02206C>.
9. Rothbauer, M.; Eilenberger, C.; Spitz, S.*; Bachmann, B.; Pajenda, J.; Schwaighofer, A.; Höll, G.; Helmke, P. S.; Kohl, Y.; Lendl, B.; Ertl, P. FTIR Spectroscopy as a Novel Analytical Approach for Investigation of Glucose Transport and Glucose Transport Inhibition Studies in Transwell in Vitro Barrier Models. *Spectrochim. Acta. A. Mol. Biomol. Spectrosc.* **2020**, 237, 118388. <https://doi.org/10.1016/j.saa.2020.118388>.
10. Bachmann, B.; Spitz, S.*; Schädl, B.; Teuschl, A. H.; Redl, H.; Nürnberger, S.; Ertl, P. Stiffness Matters: Fine-Tuned Hydrogel Elasticity Alters Chondrogenic Redifferentiation. *Front. Bioeng. Biotechnol.* **2020**, 8, 373. <https://doi.org/10.3389/fbioe.2020.00373>.
11. Kratz, S. R. A.; Bachmann, B.; Spitz, S.; Höll, G.; Eilenberger, C.; Goeritz, H.; Ertl, P.; Rothbauer, M. A Compression Transmission Device for the Evaluation of Bonding Strength of Biocompatible Microfluidic and Biochip Materials and Systems. *Sci. Rep.* **2020**, 10 (1), 1400. <https://doi.org/10.1038/s41598-020-58373-0>.
12. Spitz, S.; Zanetti, C.; Bolognin, S.; Muwanigwa, M. N.; Smits, L.; Berger, E.; Jordan, C.; Harasek, M.; Schwamborn, J. C.; Ertl, P. *Cultivation and Characterization of Human Midbrain Organoids in Sensor Integrated Microfluidic Chips*; preprint; Bioengineering, **2019**. <https://doi.org/10.1101/869701>.
13. Eilenberger, C.; Spitz, S.; Bachmann, B. E. M.; Ehmoser, E. K.; Ertl, P.; Rothbauer, M. The Usual Suspects 2019: Of Chips, Droplets, Synthesis, and Artificial Cells. *Micromachines* **2019**, 10 (5), 285. <https://doi.org/10.3390/mi10050285>.
14. Kratz, S. R. A.; Eilenberger, C.; Schuller, P.; Bachmann, B.; Spitz, S.; Ertl, P.; Rothbauer, M. Characterization of Four Functional Biocompatible Pressure-Sensitive Adhesives for Rapid Prototyping of Cell-Based Lab-on-a-Chip and Organ-on-a-Chip Systems. *Sci. Rep.* **2019**, 9 (1), 9287. <https://doi.org/10.1038/s41598-019-45633-x>.

15. Zirath, H.; Rothbauer, M.; Spitz, S.*; Bachmann, B.; Jordan, C.; Müller, B.; Ehgartner, J.; Priglinger, E.; Mühleder, S.; Redl, H.; Holnthoner, W.; Harasek, M.; Mayr, T.; Ertl, P. Every Breath You Take: Non-Invasive Real-Time Oxygen Biosensing in Two- and Three-Dimensional Microfluidic Cell Models. *Front. Physiol.* **2018**, *9*, 815. <https://doi.org/10.3389/fphys.2018.00815>.

16. Bachmann, B.; Spitz, S.*; Rothbauer, M.; Jordan, C.; Purtscher, M.; Zirath, H.; Schuller, P.; Eilenberger, C.; Ali, S. F.; Mühleder, S.; Priglinger, E.; Harasek, M.; Redl, H.; Holnthoner, W.; Ertl, P. Engineering of Three-Dimensional Pre-Vascular Networks within Fibrin Hydrogel Constructs by Microfluidic Control over Reciprocal Cell Signaling. *Biomicrofluidics* **2018**, *12* (4), 042216. <https://doi.org/10.1063/1.5027054>.

17. Egger, D.; Spitz, S.; Fischer, M.; Handschuh, S.; Glösmann, M.; Friemert, B.; Egerbacher, M.; Kasper, C. Application of a Parallelizable Perfusion Bioreactor for Physiologic 3D Cell Culture. *Cells Tissues Organs* **2017**, *203* (5), 316–326. <https://doi.org/10.1159/000457792>.

*...equally contributing first author

P A T E N T S

Spitz S., Ertl P., Schwamborn J., Bolognin S., EPO, App.No.20173702.0-1101, Microfluidic Device, patent pending